UNIVERSITY
OF TASMANIA

PERFORMANCE AND CONTROL OF A COLLECTIVE AND CYCLIC PITCH PROPELLER FOR AN UNDERWATER VEHICLE

by

POOWADOL NIYOMKA

B.Eng. King Mongkut's Institute of Technology North Bangkok (2005)

B.Eng. (Hons) Austalian Maritime College (2009)

Submitted in fulfilment of the requirements for the Degree of Doctor of Philosophy

University of Tasmania

February 2014

Declarations

Statement of Originality

I declare that this thesis contains no material which has been accepted for a degree or diploma by the University or any other institution, except by way of background information and duly acknowledged in the thesis, and to the best of my knowledge and belief no material previously published or written by another person except where due acknowledgement is made in the text of the thesis, nor does the thesis contain any material that infringes copyright.

Authority of Access

This thesis may be made available for loan and limited copying and communication in accordance with the Copyright Act 1968.

Copyright

I warrant that I have obtained, where necessary, permission from the copyright owners to use any third-party copyright material reproduced in the thesis, or to use any of my own published works in which the copyright is held by another party (e.g. publisher, co-author).

Poowadol Niyomka

February 2014

Acknowledgements

There are a number of people I would like to express my deep appreciation for their help and guidance throughout this research. Without their continuous efforts and support, this research would not have been successfully completed.

First of all I would like to express my sincere thank to Professor Neil Bose, my primary supervisor at the Australian Maritime College. With his experience, I always received great advices from him. He is a great listener too. He has expertly guided me through many potential pitfalls.

Second, I would like to thank Dr. Jonathan Binns, my co-supervisor at the Australian Maritime College, for his useful guidance for my experiment and writing. I am always amazed by his critical thinking skills.

Third, I am eternally grateful to Dr. Hung Nguyen, my co-supervisor, for his great support. I received his support many times on weekends and he was very patient with me. Without his help I could not have been able to complete Chapters 2 and 6.I am grateful to all support staffs at the AMC Towing Tank, at Newnham, Tasmania: Gregor Macfarlane, Tim Lilienthal, Kirk Meyer, and Liam Honeychurch, for the support they provided during the difficulty of the test-setup.

I am also grateful to Alan Faulkner and Rowan Frost at the AMC Circulating Water Channel, at Beauty Point, Tasmania, for the support they provided during the difficult test-setups and the intensive tests.

I am very grateful to the AMC technicians: Michael Underhill, Rowan Carins, Jock Ferguson, and Darren Young for their support and I respect for their great technical skills.

From my heart I would like to express my deepest gratefulness to my parents (Ubon and Nopadon Niyomka), for their endless great supports.

My deep gratefulness should go to my lovely fiancée, Chiemi Orihara, for her support and encouragement.

This research is part of the 2010's Institutional Research Grants Scheme (IRGS) funded project. I would like to thank the University of Tasmania, Office of Research Services for funding.

Last but not least, I am very grateful to the Australian Maritime College and the University of Tasmania for the scholarship. It gave me the opportunity to continue my postgraduate and to contribute to this research.

Abstract

Most of the underwater vehicles have control surfaces to enable manoeuvring. The problem with an underwater vehicle with control surfaces is operating it at low speed. At low speed, the control surfaces become inoperative as the magnitude of the generated lift relates to the water speed passing over the control surfaces. A novel device, which is a potential solution to this problem, is the collective and cyclic pitch propeller (CCPP). The CCPP can generate both axial and transverse thrusts in one device.

The research focused on the performance of the CCPP and the performance of an underwater vehicle equipped with the CCPP. The information about the true performance of this CCPP has not been investigated. Assessing the true performance in a straight line of the CCPP was the first objective of this research. The development of the simulation program was the second objective of this research in order to assess the motion control of an underwater vehicle by using the CCPP.

The performance in a straight line of the CCPP behind an underwater vehicle was assessed by using a captive test in the Towing Tank at the Australian Maritime College. In the experiment, the propeller was set at various pitch angles, and it was tested at various advance coefficients. Polynomial equations for estimating the thrust and the torque coefficients of the propeller with the collective pitch setting were established. In addition, the effects of the collective pitch, cyclic pitch, and advance coefficient related to the magnitude and direction of the transverse thrust were studied. Increasing the magnitude of the collective pitch setting caused the direction of the transverse thrust to rotate clockwise when looked at from aft. The magnitude of the transverse thrusts increased as the collective pitch setting increased. Different types of cyclic pitch setting affected the direction of the transverse thrust differently. Increasing the magnitude of the cyclic pitch setting raised the magnitude of the transverse thrust.

According to the experimental information, the direction and the magnitude of the transverse thrust was found to be difficult to control manually. Hence a motion control system of an underwater vehicle equipped with the CCPP was developed in order to assist an operator to control the vehicle. The proportional integral derivative control law was used to develop the control system.

The capability of the motion control system and the manoeuvrability of the underwater vehicle equipped with the CCPP were assessed by using a developed simulation program. In addition, the numerical simulation of an underwater vehicle equipped with the CCPP is an essential tool to develop the CCPP in the future. The simulation program was developed by using the mathematical model of a test underwater vehicle. Furthermore, the forces of the CCPP were modelled by using the experimental results and the performance prediction program. The simulation study has shown that the underwater vehicle equipped with the CCPP has flexible manoeuvrability, and controllability. The CCPP is capable of controlling an underwater vehicle in all directions. For further development, the free running test should be conducted in order to demonstrate the performance of the underwater vehicle and to verify the simulation program.

Table of Contents

List of Figures

List of Tables

List of Abbreviations

ADC	Analog to Digital Converter
AMC	Australian Maritime College
ANOVA	Analysis of Variance
AUVs	Autonomous Underwater Vehicles
BEMT	Blade Element Momentum Theory
BLDC	Brushless Direct Circuit
CCPP	Collective and Cyclic Pitch Propeller
CFD	Computational Fluid Dynamic
CPP	Controllable-Pitch Propeller
C-SOUT	Canadian Self-Contained Off-the-shelf Underwater Test Bed
DAC	Digital to Analog Converter
DAQ	Data Acquisition
DC	Direct Circuit
DOFs	Degrees of Freedom
EMF	Electromagnetic Field
GPS	Global Positioning System
GNSS	Global Navigation Satellite System
IMU	Inertial Measurement Unit
LOS	Line of Sight
MUVs	Manned Underwater Vehicles
NACA	National Advisory Committee for Aeronautics
PID	Proportional Integral Derivative
ROVs	Remotely Operated Vehicles
RSM	Response Surface Methodology
SNAME	Society of Naval Architects and Marine Engineers
TPS	Tandem Propeller System

UUVs Unmanned Underwater Vehicles

List of Notations

Greek Symbols

α Angle between Longitudinal Axis of Vehicle to Inflow and Angular Attack

$\alpha_{(i,\varphi)}$ Total Pitch Angle of Each Blade.

$\alpha_{Col(i)}$ Collective Pitch Angle of a Particular Blade range from –29 deg to +29 deg

$\alpha_{U/D(i)}$ Up/Down Cyclic Pitch Angle of a Particular Blade range from = –20 deg to +20 deg

$\alpha_{R/L(i)}$ Right/Left Cyclic Pitch Angle of a Particular Blade range from = –20 deg to +20 deg

α_{E_n} Effective Angle of Attack

α_f Effective Angle of Attack for Unsteady Leading Edge Pressure

α_n Angle of Attack at Current Time Step

α_1 Breaking Point Angle of Attack corresponding to f=0.7

β Prandtl-Glauert Factor

$\Delta C_n(S)$ Normal Force Coefficient in S domain

Δm Moving distance of First Links

Δs Time Step

Δz Moving distance of Slide Block

$\Delta\alpha$ Step Change of Angle of Attack

$\triangle\varphi$ Azimuth Angle Step

δ Wedge angle of the Slide Block

δT Thrust from the Momentum Theory for each Blade Section

δQ Torque from the Momentum Theory for each Blade Section

δr Thinkness of each Blade Element

$\boldsymbol{\eta}$ Vector of Positions and Orientation Inertial Reference Frame

η	Cross-flow Proportionality Factor
η_{CE}	Vector of Position of the Centre of Effort
$\boldsymbol{\omega}_{\mathbf{b/i}}^{\mathbf{b}}$	Vector of Angular Velocities in Body-Fixed Reference Frame
ω_r	Angular Speed of Motor Rotor
ω_o	Angular Velocity about the Centre of Origin
$\boldsymbol{\psi}$	Angular Position about the z-axis in Inertial Reference Frame
ψ_d	Desired Yaw
φ	Angular Location of Propeller Blade
Φ	Rotation Angle of the Vehicle
ϕ	Angular Position about the x-axis in Inertial Reference Frame
ϕ_{a_i}	Phase Angle for Each Actuator
ρ	Water Density
σ'	Solidity
$\boldsymbol{\tau}_o$	Vectors of the External Forces and Moments acting on an Underwater Vehicle
τ_v	Non-Dimensional Vortex Time Parameter
$\boldsymbol{\Theta}_{\mathbf{ib}}$	Vector of Euler Angles
$\boldsymbol{\theta}$	Angular Position about the y-axis in Inertial Reference Frame

Roman Symbols

A	Wetted Surface of Vehicle [m^2]
A_p	Body Plan-Form Area [m^2]
a	Axial Induction Factor
a’	Swirl Induction Factor
B	Number of Blades
Col	Collective Pitch Setting [%]

$\mathbf{C}$	Position of Centre Point of Circle [m]
$\mathbf{C}_{RB}$	Coriolis and Centrifugal Matrix
C_C	Chord Force Coefficients
C_{C_n}	Circulatory Component of Chord Normal Force
C_C^f	Chord Force Coefficient Including Separation Effects
C_D	2D Foil Section Drag Coefficient
C_{Dc}	Drag Coefficient
C_{DF}	Form Drag Coefficient
C_G	Centre of Gravity
C_L	2D Foil Section Lift Coefficient
C_N	Final Normal Force Coefficient
C_{N_a}	Normal Force Coefficient with Respect to Various Angles of Attack [/deg]
$C_{N_n}^C$	Circulatory Normal Force
$C_{N_n}^I$	Non-Circulatory Loading Component
$C_{N_n}^p$	Total Normal Force Coefficient under Attached Flow Condition
$C_{N_n}^f$	Normal Force Coefficient Including Separation Effects
$C_{N_n}^V$	Vortex Normal Force Coefficient
C_n'	Normal Force Coefficient after Taking Account for Lag in Leading Edge Pressure Response
C_{n1}	Critical Normal Force Coefficient
C_O	Centre of Origin
C_V	Increment in Vortex Lift
c	Element of Chord [m]
D	Diameter of the CCPP [m]

$\mathbf{D}(\mathbf{v})$	Damping Matrix
Df	Deficiency Function due to Trailing Edge Separation
D_n	Deficiency Function due to Pressure Disturbances
D_{P_n}	Deficiency Function due to a Lag in the Leading Edge Pressure Response
d	Cross-Section Diameter of Vehicle [m]
e	Actuating Error
e_1, e_2, e_3	Back EMF of Each Phase [v]
F	Prandlt's Tip-loss Factor
F_x	Propeller Force in x direction [N]
F_y	Propeller Force in y direction [N]
F_z	Propeller Force in z direction [N]
$\mathbf{f_g^b}$	Gravitation Force, Acting throughout the Centre of Gravity [N]
$\mathbf{f_b^b}$	Buoyancy Force, Acting throughout the Centre of Buoyancy [N]
f	Function of Fineness Ratio
f_o	Net External Forces Acting on the Vehicle [N]
f'	Effective Separation Point
f''	Final Delayed Trailing Edge Separation Location
$\mathbf{g}$	Buoyancy and Gravity Vector [N]
I_o	Moments of Inertia with Respect to the Origin Point [Kg m^2]
i_1, i_2, i_3	Phase Currents [A]
J	Inertia of the Motor and Driven Load [Kg cm^2]
J	Advance Coefficient
$\mathbf{J}(\boldsymbol{\eta})$	Transformation Matrix
KT	Thrust Coefficient
KQ	Torque Coefficient

K_D	Derivative Control Gain
K_I	Integral Control Gain
K_P	Proportional Control Gain
K_α	Non-Circulatory Time Constant Multiplier
K_o	Moments about the x-axis (roll) [Nm]
L	Distance from the Centre of the Rotating Swash Plate Plane to the Centre of the Non-Rotating Swash Plate Plane [m]
L_{tot}	Length of Vehicle [m]
L_1	Displacement of Actuator 1 [in]
L_2	Displacement of Actuator 2 [in]
L_3	Displacement of Actuator 3 [in]
l	Vehicle Length [m]
$\mathbf{M_A}$	Hydrodynamic Added Mass
M_o	Moments about the y-axis (pitch) [Nm]
$\mathbf{M}_{RB}$	Rigid-Body Matrix
M_{X_blade}	Total Moment for One Blade about x-axis [Nm]
m_o	Moment of Net External Forces [Nm]
N_o	Moments about the z-axis (yaw) [Nm]
n	Shaft Speed [rps]
$\hat{\mathbf{n}}$	Unit Normal Vector of Non-Rotating Swash Plate
P_{nom}	Nominal Value of the Input Parameter
P_1, P_2, P_3	Position Vectors of Each Joint between Actuators and Non-Rotating Swash Plate [m]
p	Angular Velocity about the x-axis [m/s]
Q_{blade}	Torque for One Blade [Nm]

Q_{X_avg}	Averaged Torque for Propeller about x axis [Nm]
q	Angular Velocity about the y-axis [rad/s]
R	Winding Resistance [ohm]
R	Output Variable (added mass element)
Re	Reynolds Number
R/L	Right/Left Cyclic Pitch Setting [%]
$\mathbf{R}_{\mathbf{b}}^{\mathbf{i}}$	Euler Angle Rotation Matrix of the Linear Velocities
$\mathbf{R}_{\mathbf{i}1}$	Position of Base of Each Actuator [m]
$\mathbf{R}_{\mathbf{i}2}$	Total Length of Each Actuator [m]
$\mathbf{R}_{\mathbf{i}3}$	Position of a Point on Rotating Swash Plate [m]
$\mathbf{R}_{\mathbf{i}4}$	Position of Front End Plate [m]
R_{nom}	Nominal Value of the Output Variable
R_0	Radius of Acceptance [m]
r_G	Distance from the Centre of Gravity to the Centre of Origin [m]
r	Angular Velocity about the z-axis [rad/s]
r	Radius in Middle of Each Blade Element [m]
r_a	Distance from Axis of Propeller Shaft to the Base of Actuator [m]
$\mathbf{r}_{\mathbf{b}}^{\mathbf{b}}$	Vector Location of the centre-buoyancy is defined by the vector with respect to the origin of the body-fixed Frame [m]
$\mathbf{r}_{\mathbf{p}}^{\mathbf{b}}$	Vector of Location of the Propeller Plane [m]
$\mathbf{r}_{\mathbf{g}}^{\mathbf{b}}$	Vector of Location of the Centre of Gravity [m]
$\mathbf{r}_1$	Vertical Vector from the Centre of the Rotating Swash Plate to the Control Rod Slider [m]
$\mathbf{r}_2$	Vector from the Centre of the Rotating Swash Plate to the Joint of the Connecting Linkage [m]
$\mathbf{r}_3$	Vector of Connecting Linkage [m]

$\mathbf{r}_4$	Distance of Eccentricity [m]
S	Sensitivity of Response to the Variation in Geometric Parameter
S_b	Maximum Cross-Sectional Area of Vehicle [m^2]
S1, S2	Static Stall Characteristic
T_{X_avg}	Averaged Thrust for Propeller in x direction [N]
T_{Y_avg}	Averaged Thrust for Propeller in y direction [N]
T_{Z_avg}	Averaged Thrust for Propeller in z direction [N]
T_{N_blade}	Total Thrust for One Blade [N]
T_{X_blade}	Total Thrust for One Blade in x direction [N]
T_{R_blade}	Total Thrust for One Blade in x direction [N]
T_{Y_blade}	Total Thrust for One Blade in y direction [N]
T_{Z_blade}	Total Thrust for One Blade in z direction [N]
T_e	Electromagnetic Torque [Nm]
T_f	Viscous Lag Time Constant
T_P	Pressure Lag Time Constant
T_V	Vortex Lag Time Constant
T_{VL}	Vortex Passage Time Constant [semi-chord]
T_l	Load Torque [Nm]
$\mathbf{T}_\Theta$	Rotation Matrix of the Angular Velocities [rad/s]
t	Time [s]
t_i	Swash Plate Tracking Line [m]
U/D	Up/Down Cyclic Pitch Setting [%]
$\mathbf{U}$	Unit Vector from the Centre of the Circle to Any Point on the Circumference
U_d	Desired Speed [m/s]

u	Linear Velocity in the x direction [m/s]
V	Unit Vector from the Centre of the Circle to Any Point on the Circumference
V_B	Total Volume of Vehicle [m^3]
V_{CE}	Vector of Velocity at Centre of Effort [m/s]
v	Vector of Velocities in Body-Fixed Reference Frame [m/s]
v	Linear Velocity in the y direction [m/s]
$\mathbf{v}^{\mathbf{b}}_{\mathbf{b/i}}$	Vector of Linear Velocities in Body-Fixed Reference Frame [m/s]
v_o	Velocity of the Centre of Origin of the Body-Fixed Reference Frame [m/s]
v_s	Star Point Voltage [v]
v_1, v_2, v_3	Phase Voltages [v]
w	Linear Velocity in the z direction [m/s]
X_m	Position of Pitching Moment Centre, Which Is the Same Position of the Centre of Gravity [m]
X_n, Y_n	Deficiency in Angle of Attack due to Shed Wake Effects and Unsteady Hydrodynamics
X_o	Forces in the x direction [N]
X_p	Position of Centre of the Plan-Form Area [m]
x	Position in the x direction in the Inertial Reference Frame [m]
x_d	Desired Position in the x direction in the Inertial Reference Frame Effects
Y_o	Forces in the y direction [N]
y	Position in the y direction in the Inertial Reference Frame [m]
y_d	Desired Position in the y direction in the Inertial Reference Frame [m]
Z_o	Forces in the z direction [N]
z	Position in the z direction in the Inertial Reference Frame [m]
z_d	Desired Position in the z direction in the Inertial Reference Frame [m]

Chapter 1 Introduction

1.1 Research Background

1.1.1 General Information on an Underwater Vehicle

There are many different applications of underwater vehicles, such as ocean exploration, leisure activities, search and rescue operation, and inspections. The designs of an underwater vehicle tend to be for a specific application; therefore, there are many types of underwater vehicles in operation. Underwater vehicles can be categorized into two main groups according to methods by which they are controlled. The first group is the manned underwater vehicles (MUVs). Most people are familiar with this type of vehicle because it is not a new concept. Back in 1576, William Bourne, a British mathematician, published the first known detailed plan of an underwater navigation vehicle. His vehicle was capable of submerging by decreasing the internal volume. In 1620, Cornelius Van Drebbel, a Dutch inventor, built an underwater vehicle possibly from Bourne's proposals. The vehicle was made of a wooden rowboat tightly wrapped with waterproofed leather. The historical details of submarines can be found in a book titled *The Story of the Submarine* (Field, 2010).

The second group is the unmanned underwater vehicles (UUVs). The UUVs gain popularity in submersible operations because MUVs can be hazardous to life and expensive to operate. Many of the technologies of UUVs were developed by the U.S. Navy in the 1960s and 1970s. The U.S. Navy needed robotic vehicles to recover underwater ordnance lost during testing (PAST Foundation, 2009). UUVs can be categorized into four subtypes based on the method of control and the energy supply. The simplest underwater vehicles are submersibles that are towed behind a ship, and they have several sensors attached to the underwater vehicle's frame or body. Remotely operated vehicles (ROVs) are the second type of unmanned submersible vehicle. In operation, an ROV is attached with a power supply cable and a communication cable, usually from a mother ship, and it is controlled directly by a remote operator. The third type of unmanned submersible is UUV. It is untethered and has its own power supply on board; however, it still needs commands from a remote operator to complete a mission via some types of communication link. The last type is called autonomous underwater vehicle (AUV). It is similar to a UUV as it is untethered and has its own energy supply. The difference between an AUV and a UUV is that an AUV does not require communication during their assigned mission (Blidberg, 2001). An AUV can operate independently without human support and keep human personnel at a safe location on the water surface. In the scientific community, an AUV is becoming a less expensive method of obtaining ocean data compared with manned submersibles and surface science vessels. In addition, researchers can also deploy and monitor several AUVs at the same time to maximize the amount of data in the same expedition. The data from each AUV are transmitted back to a support base.

Regarding AUVs for a survey mission, the survey performance capabilities of these vehicles are usually assessed by their endurance and speed. The limited energy supply is a constraint on the survey performance capability. To enhance their performance, their designs need to have a high-efficiency propulsion system and a hydrodynamically shaped hull form. A torpedo-shaped hull form with a propeller mounted on the stern and control surfaces (sail, rudder, and hydroplanes) for control are the common design of this survey-style AUVs.

As the employment of AUVs increases, the development of their capabilities is also desired. The operators want the vehicle to perform more complex tasks and various types of missions. One of the desired capabilities for survey-style AUVs is low-speed manoeuvrability or station keeping. This ability is advantageous for a mission that requires a longer sampling period or monitoring at a small area. This type of mission is more suitable for ROVs whose energy supply comes from an onshore control station and on a carry surface vessel. However, it is very difficult to accomplish the mission using AUVs with conventional control surfaces because the control surfaces cannot provide sufficient forces to manoeuvre the vehicle when the vehicle is kept stationary or operating at very low speed. The vehicle needs to have sufficient forward speed in order to keep the control surfaces effectively operational.

To manoeuvre an underwater vehicle, there must be forces acting on the vehicle. A conventional control surface generates a lifting force when it is positioned to an angle to the flow. The magnitude of the lifting force depends on the angle of the control surface and the relative velocity of the flow over the control surface. As already mentioned earlier, at low-speed operation, the relative velocity of the flow is too low so that a control surface cannot generate a sufficient amount of lift to manoeuvre an underwater vehicle. Another method is that a vehicle can generate forces by itself. Hence, the vehicle must have a device that generates a sufficient amount of forces in the desired directions. Using multiple thrusters is the simplest method; however, it requires more space, higher energy consumption, and high-resistance hull form. Using multiple thrusters is typically found on ROVs that have a free frame form. An oscillating flexible foil is another device used to generate and control the propulsion and manoeuvring of underwater vehicles. Oscillating flexible foils imitate the movement of fish fins. Many fish robots have been built to demonstrate this technology (Science Daily, 2012). Details of the oscillating propulsion can also be found in a book titled *Marine Powering Prediction and Propulsors* (Bose, 2008, p. 135).

Another device that is suitable for AUVs is a vectored thruster. Instead of using each thruster to provide the manoeuvring force in a particular direction as the propulsion system on ROVs, one vectored thruster can generate and control thrust in any desired direction. A vectored thruster works similar to an azimuthing or podded propulsors (Carlton, 2007, p. 343). The last device with low-speed manoeuvrability for an AUV is a collective and cyclic pitch propeller (CCPP). This research work focuses on the propulsion system of UUVs, the CCPP in particular. This type of the device is a combination of a propulsor and a manoeuvreing device. The development of this type of propeller and more details of the CCPP for this research are presented in the following chapters.

1.1.2 Historic Overview of Development of CCPPs

Although propulsion technology with the capability to generate side forces has been investigated within the surface vehicle industry for a long time, many questions have been left unanswered. In 1963 in Sweden, a ship propeller with separate turntable blades was patented (Lindahl, 1965). The propeller pitch was controlled as a function of the angular position, and it could be selected (Joosen, Manen, and Walle, 1963). Haselton, Wilson, and Rice (1966) conducted tests with a ship propeller model whose pitch angle could be varied in angular position in order to provide steering forces to the ship. Jessup (1976) conducted an experiment to demonstrate the reduction of propeller vibration and cavitation by the cyclic variation of blade pitch. Simonsson (1981) designed a pinnate propeller. The pinnate propeller was a programmable pitch propeller. It had an even number of blades, and the opposing blades were assembled in pairs on axles, which passed through the hub as shown in Figure 1.1. In 1984, Simonsson conducted full-scale tests with the pinnate propellers on a Swedish Navy Patrol boat.

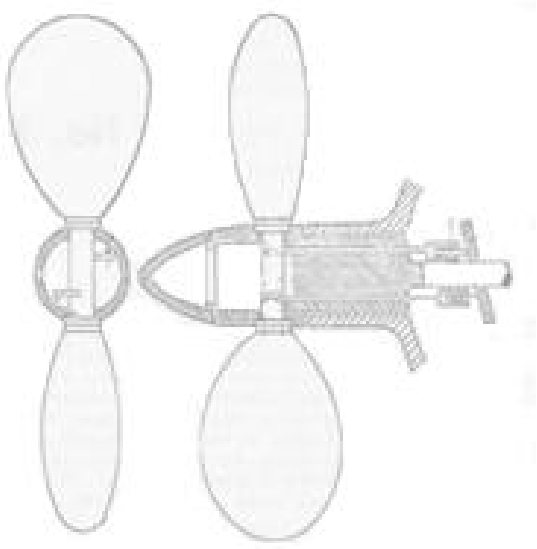

Figure 1.1. Principles of the pinnate propeller (Simonsson, 1981).

In the submersible vehicle field, scientific investigations of the marine environment may use underwater vehicles to monitor, survey, and map the seabed and to collect data. These kinds of missions require time to take samples and to analyse and record the samples locally. Therefore, the underwater vehicle is required to hold its position to complete the tasks. The tandem propeller system (TPS) was proposed for a novel submarine propulsion and control system by Haselton, Wilson, and Rice (1966). The TPS is capable of manoeuvring in all six degrees of freedom (DOFs). It has a pair of CCPPs with one propeller at the bow and another at the stern. The TPS configuration is shown in Figure 1.2.

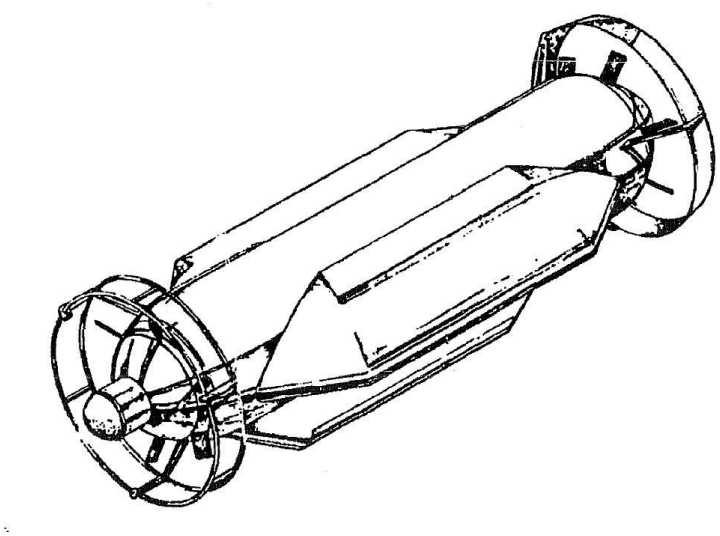

Figure 1.2. The configuration of the TPS (Haselton et al., 1987).

The TPS concept was not extensively developed at the time due to mechanical complexity and control issue (Benjamin et al., 2008). A renewed design of the TPS concept was done by Benjamin et al. (2008) with an advanced control system, electric motors, and electric actuators. Figure 1.3 is the initial demo vehicle.

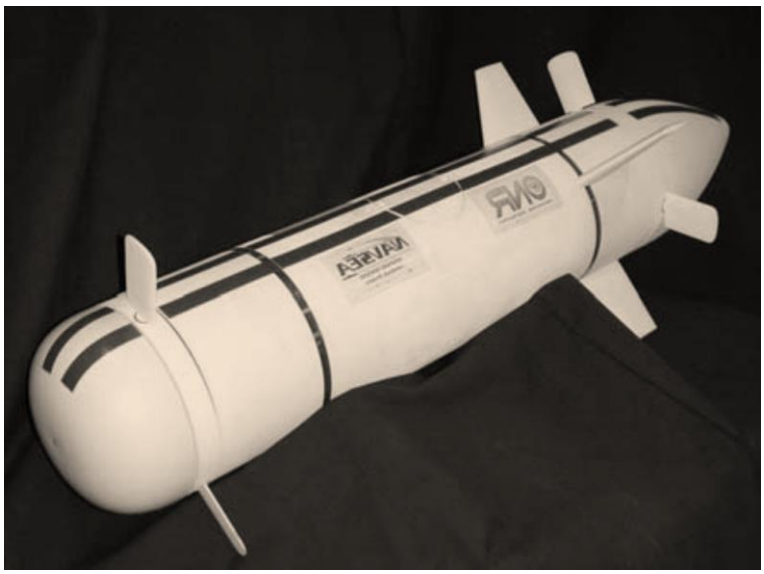

Figure 1.3. Initial demo vehicle (Benjamin et al., 2008).

In Japan, a compact AUV using a variable vector propeller, as shown in Figure 1.4, was developed by Nagashima et al. (2002). The development of this variable vector propeller system utilized radio control helicopter elements of a swash plate and DC servomotors.

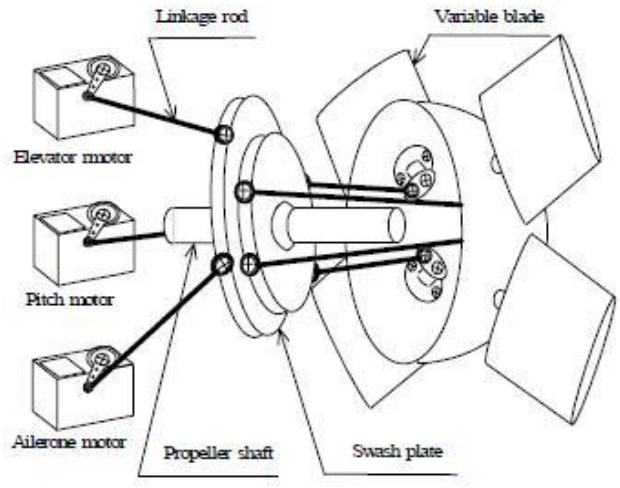

Figure 1.4. Assembly of variable vector propeller (Nagashima et al., 2002).

1.1.3 Introduction to the CCPP for the Research

1.1.3.1 How the CCPP Works

The mechanism of the CCPP allows each angle of the propeller blade to be positioned while the propeller shaft is turning. An operator can change a pitch angle of every propeller blade to a particular angle, as changing the pitch angle of a controllable pitch propeller (CPP). The pitch angles of each propeller blade can also be changed in the function of the angular position, like working a cyclic-pitch propeller. The most notable example of a rotor of this CCPP is a main rotor of a helicopter. The mechanism of the CCPP has a component called a swash plate. It provides an adjustability of the angle of the propeller blades. The swash plate assembly consists of two parts: the nonrotated and the rotated swash plates, as shown in Figure 1.6.

Figure 1.6 shows that the rotated swash plate rotates with the propeller blades and the propeller shaft. The connecting linkages allow the rotated swash plate to change the pitch of the rotor blades. The attached linear actuators change the angle of the nonrotated swash plate. The operator can control the collective and cyclic pitch via linear actuators. The nonrotated and the rotated swash plates are connected with a spherical swash plate bearing between the two plates. The bearing allows the rotated swash plate to spin around the nonrotated swash plate.

The assembly can be explained in the following paragraphs in order to understand the relationship between the collective and cyclic pitch controls and the swash plate. The collective pitch control manipulates the entire swash plate assembly upward or downward. This causes the pitch of all blades to change simultaneously.

The cyclic pitch control tilts the swash plate assembly to one side. This causes the pitch of the blades to change unevenly. The pitch angle of each blade depends on the location of each

blade in the rotation. The result of the uneven pitch of each blade is that more thrust is generated on the greater pitch angled blades on one side, and less thrust is generated on the lesser pitch-angled blades on the opposite side. The cyclic pitch propeller can generate lateral thrust because of this unbalanced thrust and the rake angle of the blades, δ. Blade rake angle influences a generated side thrust, which is illustrated in Figure 1.5. For the propeller on this research work, the blade rake angle is at 20°. The simulation results show that at a rake angle of 20°, the side thrust increases five times, a trade-off of an approximately 12% decrease in the axial thrust. The function of the cyclic pitch control of the CCPP enables an underwater vehicle to dive, surface, or undertake side-to-side motions. The mathematical kinematic of the mechanism of CCPP is presented in Chapter 3.

The blade section is a NACA 0012. The thickness and chord length constantly decrease toward the tip. The pitch distribution progressively increases toward the tip. The rake angle of the blades is 20°. The blades do not have skew. The diameter of the propeller is 0.305 m. The propeller turns counterclockwise.

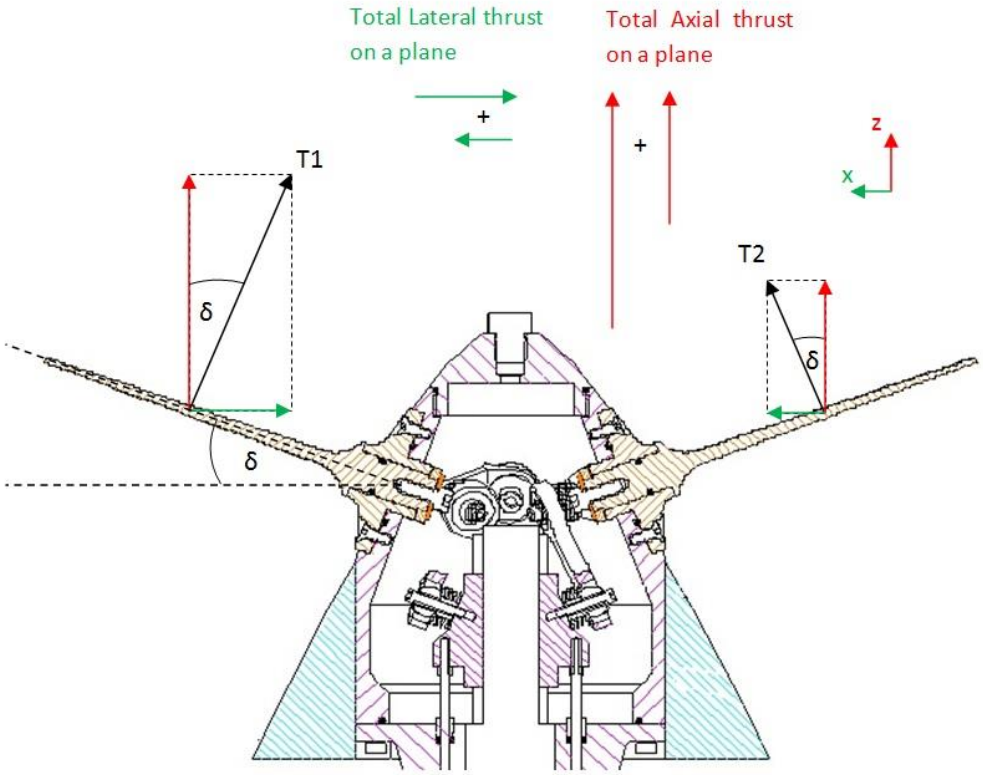

Figure 1.5. Influences of blade rake angle on lateral and axial thrusts.

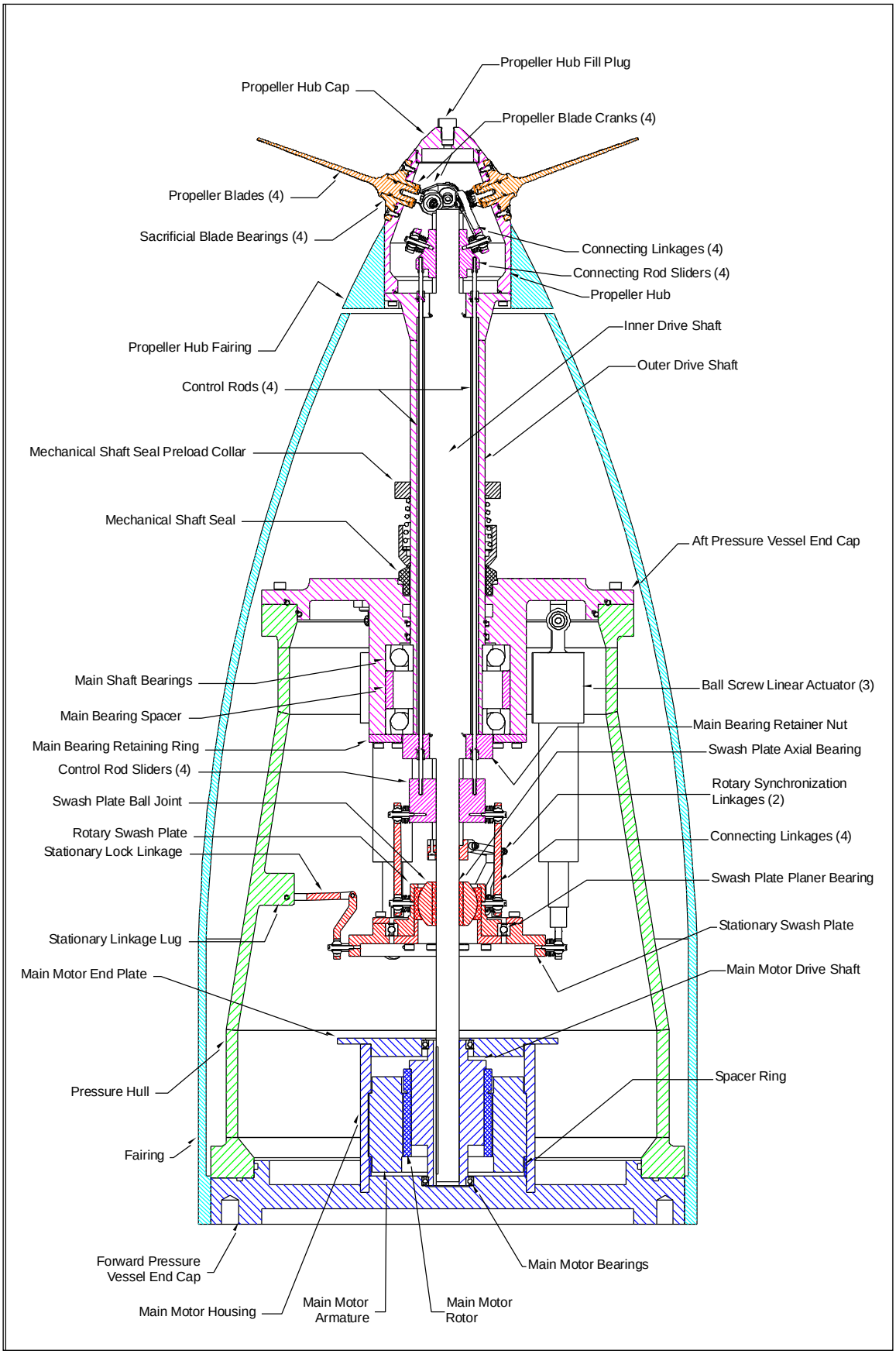

Figure 1.6. Hull-mounted mechanism of the CCPP (Humphrey, 2005).

Table 1.1. Specifications of the CCPP (Humphrey, 2005)

Overall length	838 mm
Propeller diameter	305 mm
Overall diameter	400 mm
Propeller area ratio	0.15
Blade rake angle	20°
Blade angle	±29° collective pitch, ±20° cyclic pitch
Number of blades	4
Main motor power	1.1 HP (800W)
Propeller speed (max)	500 RPM
Main motor voltage	48 VDC
Control voltage	±12 VDC
Control options	TCP/IP, USB, PCI 6036E

The control system of the CCPP was developed to control the Revolution Per Minute (RPM) of the propeller shaft and the pitch angle of the propeller blades to the desired values. A computer was the main processing unit to control the brushless DC main motor and the three linear actuators. The control program was developed in LabVIEW. The computer received and sent signals through a data acquisition (DAQ) card (NI6036E). The signals are the RPM of the propeller shaft and the position of the linear actuators. The details of the control system are presented in Chapter 3.

This propeller was designed and built at the Memorial University of Newfoundland in Canada. This CCPP was considered for the alternative propulsion of the Canadian self-contained off-the-shelf underwater test bed (C-SCOUT) vehicle, and the research of this type of propulsion began in 2001 at the Memorial University, where the feasibility of this technology was investigated (Bijleveld, 2002). The result of the investigation and experiment on a two-bladed propeller showed that this technology was feasible, and it had a high potential to be a combination of propulsion and manoeuvring system for an underwater vehicle. A more in-depth study of this system began in 2002 by Humphrey. He achieved the development of a CCPP prototype, which has been further developed in this research.

1.1.3.2 Applications of the CCPP to the Underwater Industry

The CCPP can generate thrust in the longitudinal and lateral directions. The propeller is suitable for a streamline-shaped underwater vehicle with a high manoeuvrability at low speed. An underwater vehicle propelled by a single CCPP can provide three DOFs (surge, pitch, and

yaw). An underwater vehicle, which is installed two CCPPs at both fore and aft end, could manoeuvre in six DOFs (Benjamin et al. 2008).

The information about the performance of the CCPP is required for the development of a control system of an underwater vehicle. In addition, the development of the simulation program of an underwater vehicle is based on the information and the control system. The desired data to be acquired are the resistance of the vehicle, the magnitudes of thrust and torque at various pitch settings, and the advance coefficients. The details of input variables are in Chapter 4.

1.2 Research Objectives and Scope

The research focused on two main objectives. Each objective had many subtasks to complete in order to achieve the objective. The first main objective was to understand how the CCPP performs. After understanding the performance, the control system of the propeller was developed to have an efficient propulsion and a precise manoeuvring. For the future development of the CCPP, the numerical simulation is an essential tool. The development of the simulation program for an underwater vehicle equipped with the CCPP was the second main objective of this research. The subtasks were used to determine numerically the hydrodynamic characteristics of both the underwater vehicle and the CCPP.

1.3 Research Challenges

The CCPP is a novel propeller, which has useful capabilities such as high manoeuvrability. The CCPP is able to assist an underwater vehicle to perform complex manoeuvres such as up and down, side to side, forward and backward, and pitch and yaw.

The CCPP was built in 2005. The built CCPP was only tested in order to demonstrate that the built CCPP could generate axial and side thrusts. In the test, the CCPP was tested in a bollard pull condition without any underwater vehicle body or fairing. That study did not represent the performance of the CCPP.The first research question arises from the uncertainty of the performance of the CCPP. The true performance of the CCPP was assessed. In the experiment, the CCPP was attached behind an underwater body and to all fairing. Its true propulsion performance in a straight line was conducted in the Towing Tank at the Australian Maritime College. The details of the experiment are presented in Chapter 4.

The second research question is whether the CCPP can be utilized to propel an underwater vehicle. There are several tasks to be completed before the answer is positively confirmed. The most important work is the completion of a control program required to control collective and cyclic pitches and to control the RPM of the main shaft of the propeller.

With only the basic developed control system and many uncertainties of the hydrodynamic characteristics of the CCPP, which may cause the underwater vehicle to be uncontrollable, the following issues may cause difficulties in controlling the CCPP:

- According to Humphrey (2005), if the thrust coefficient, K_T, variation with blade angle was nonlinear, the CCPP could be difficult to control.
- According to Humphrey (2005), the measured thrust directions were not the same as the assumed thrust directions because the oscillating blades of the propeller created an unsteady flow effect. In his preliminary test, the unsteady flow effects were found dependant only on the axial thrust magnitude.
- In addition, a generated torque is inherent when the propeller is operating. A cylinder-shaped underwater vehicle tends to roll if it does not have any devices that can generate torque to counter the generated torques from the propeller.
- When an underwater vehicle is operating, the observation is limited. The operator cannot see the orientation of the vehicle, and the lack of this information could cause a disaster to an underwater vehicle.
- At the current control system, the control signals are simultaneously sent to the actuators. It is the cause of the unsmooth and uncontrollable paths of the direction of the thrust during the transition of the thrust direction.

These issues lead to the third research question, that is, whether an underwater vehicle with the CCPP can be controlled by any operator with only minimal training. In order to shorten the learning period, all mentioned issues must be overcome. The control algorithm of the blade angles must be modified to compensate for the nonlinearity in the response curve of the thrust coefficient, K_T, to provide a linear thrust output for operations of a vehicle. The control algorithm that can provide a linear thrust output is simple and intuitive for an operator to understand the control system. The thrust coefficient, K_T, in various conditions can be quantified by conducting the captive experiments. The experimental data can also be used for the issue of lagging of thrust direction.

The fourth question is whether the performance of the CCPP can be predicted by numerical methods. The blade element method can be used to model the unsteady hydrodynamic effects. The most elementary calculation of blade forces is based on a 2-D thin airfoil theory. This theory does not model the wake from the neighbouring blades; however, it allows convenient analytical mathematical solutions to be incorporated into the rotor analysis. The 2-D thin airfoil theory provides a considerable level of analysis of the problem and good insight into the response of the unsteady behaviour (Leishman, 2006, p. 428). The problem of an oscillating blade was considered. In this problem, the indicial response theory created by Wagner (1925) can provide a solution for the indicial lift on a thin airfoil undergoing a transient step change in an angle of attack in an incompressible flow (Leishman, 2006, p. 446). After the implementation of the prediction performance program, the program was integrated into the simulation program.

A development of an AUV is very expensive and time consuming. A lot of money is spent on hiring a researcher, hiring a support crew, purchasing equipment, and using test facilities. In addition, the development will be a disaster if the research team lost a developed AUV during field testing because of a malfunction of a vital system. Therefore, the numerical simulation software of an underwater vehicle is a valuable tool for a development team. The simulation

program can provide the position, orientation, and velocity of an underwater vehicle. The program utilized information about the performance in a straight line of CCPP assessed in the experiment, the development of the numerical prediction program, and the hydrodynamic coefficients. These hydrodynamic coefficients describe the hydrodynamic forces and moments acting on an underwater vehicle. There are many ways to estimate the hydrodynamic coefficients. A general method to estimate the coefficients of an underwater vehicle is by conducting an experiment using the planar motion mechanism. Another estimating method is semiempirical methods. More details of semiempirical methods can be found in the work of Jones et al. (2000). Another method is to use computational fluid dynamics (CFD) software to estimate the coefficients. This research deploys a semiempirical method.

1.4 Research Outcomes

The research outcomes were as follows:

1. Knowledge and understanding of the true performance of the CCPP. The results of the experiment were used to verify the mathematical model of the control system. In addition, the results can be used as a reference for a future development of the CCPP.

2. Verification of the mathematical model of the control system of the CCPP. The results would be used in the field of simulation of the behaviour of an underwater vehicle with the CCPP as its propulsion. The successful outcomes of the development of the simulation program can reduce the risk of loss of the actual developed vehicle during a field test. Regarding the future development of the control program, the simulation program will be an essential tool in the development of the intelligent control.

1.5 Thesis Organization

The thesis is arranged into six chapters as follows:

Chapter 1 (Introduction) includes the background of the research and the literature review on the development of a CCPP. It also introduces how the CCPP works and how this propeller enhances the manoeuvrability of an underwater vehicle.

Chapter 2 (Modelling of ROV/AUV Equipped with a CCPP) presents the developments of every component in the simulation propeller. It starts with the development of an underwater vehicle body to all equations used in the simulation program.

Chapter 3 (Control of CCPP for an Underwater Vehicle) presents the development of mathematical control model of the CCPP.

Chapter 4 (Experimentation) presents the results of the true performance in a straight line of the CCPP from the experiments presented in this chapter.

Chapter 5 (Numerical Prediction of the Hydrodynamic Performance of the CCPP) presents the development of the prediction program.

Chapter 6 (Simulation Study) presents results of the various operations of an underwater vehicle with the CCPP as its propulsion system.

Chapter 7 (Conclusions and Future Works) concludes the study.

Chapter 2 Modelling of ROV/AUV Equipped with a CCPP

The simulation program is a valuable tool for the development of an underwater vehicle. In this research, the tool used to evaluate the performance was a simulation program. The aims of the simulation program were to predict the response of an underwater vehicle equipped with a collective and cyclic pitch propeller (CCPP), to verify the motion control of the vehicle and to use the predicted results to understand the vehicle's manoeuvrability. In addition, a simulation program can be used to compare the performance of the vehicle with different configurations for future development. The simulation program was developed using LabVIEW. Furthermore, the simulation was modified to improve the designed underwater in this research and to adapt the CCPP. Chapter 2 is divided into two main parts. The first part presents a summary of the mathematical model of an underwater vehicle equipped with a CCPP. The second part is an omnidirectional control system of an underwater vehicle.

2.1 Underwater Vehicle Construction

In this research, a configuration with an axis symmetric streamlined body using the CCPP for a propulsion and manoeuvre device was considered. The propeller was located at the rear of the vehicle. The configuration was a base configuration. It does not have any control surfaces as shown in Figure 2.1. The main particulars of the underwater vehicles equipped with the CCPP are given in Table 2.1.

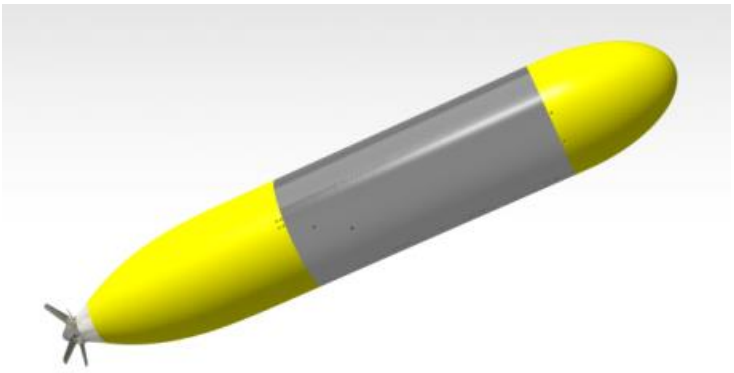

Figure 2.1. Base configuration AMC001.

Table 2.1. Main particulars of the base configuration

Parameters	Base Configuration
Length	2.335 m
Diameter	0.4052 m
Volume	0.16 m^3
Structural Mass (without inside components)	126 kg
Surface area	2.285 m^2

2.2 Reference Frames

The two orthogonal reference frames are the inertial reference frame and the body-fixed reference frame. The inertial reference frame used the same notation as the SNAME (1950) inertial reference frame, and it is a right-handed orthogonal system. The origin G of the body-fixed frame is located at the centre of mass of the vehicle as shown in Figure 2.2. Therefore, the dynamic equations can be simplified. The motion of an underwater vehicle has six DOFs. The motion of the body-fixed frame can be described relative to the inertial frame. The six different motions of the body can be divided into three translational motions along the X_B, Y_B, and Z_B axes and three rotational motions. The surge motion of the vehicle is on the X_B axis. Positive X_B is when the vehicle moves forward. The sway is in the Y_B direction, and positive Y_B is directed to the starboard. The heave motion is in the Z_B direction, and the Z_B is positive downward. The rotation about the X_B, the Y_B, and the Z_B axes are called roll, pitch, and yaw, respectively, as presented in Figure 2.2. Furthermore, the position and orientation of the body can be expressed relative to the inertial frame by x, y, and z and φ, θ, and ψ, respectively, as shown in Table 2.2. The linear and angular velocities of the body with respect to the inertial frame can be expressed by u, v, and w and p, q, and r, respectively.

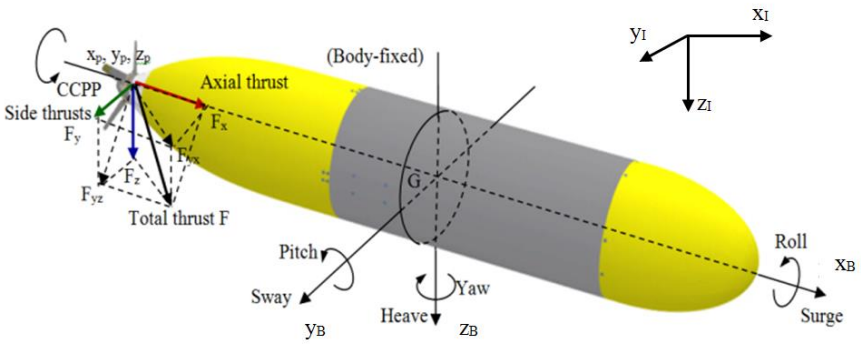

Figure 2.2. Inertial and body-fixed reference frames

Table 2.2. Notation of SNAME for marine vessels

DOF	Forces/Moments	Linear/Angular velocities	Position/Orientation
Motion in the *x* direction (surge)	X_o	u	x
Motion in the *y* direction (sway)	Y_o	v	y
Motion in the *z* direction (heave)	Z_o	w	z
Rotation about the *x* axis (roll)	K_o	p	ϕ
Rotation about the *y* axis (pitch)	M_o	q	θ
Rotation about the *z* axis (yaw)	N_o	r	ψ

2.3 Transformations between the Body-Fixed Frame and the Inertial Frame

In the thesis, the notation for an underwater vehicle is presented in a vectorial notation (Fossen, 1994, 2002). When transforming a vector from one reference frame to another, the notation is adopted as follows:

$$\mathbf{v}^{\text{new\_frame}} = R_{\text{old\_frame}}^{\text{new\_frame}} v^{\text{old\_frame}} . \tag{2.1}$$

In the above-mentioned notation, the velocity vector in the old reference frame, $\mathbf{v}^{\text{old\_frame}}$, is transformed to a new reference frame by applying the rotation matrix, $R_{\text{old\_frame}}^{\text{new\_frame}}$.

The velocity in the body-fixed reference frames can be transformed into the inertial reference frame as expressed in the following equation:

$$\dot{\eta} = J_{\Theta}(\eta) v , \tag{2.2}$$

where the positions and orientation in the inertial reference frame can be expressed as follows:

$$\eta = \left[x, y, z, \phi, \theta, \psi \right]^T . \tag{2.3}$$

The velocities in the body-fixed reference frame is given as follows:

$$v = \begin{bmatrix} v_{\text{b/i}}^{\text{b}} \\ \omega_{\text{b/i}}^{\text{b}} \end{bmatrix} = \begin{bmatrix} u & v & w & p & q & r \end{bmatrix}^T . \tag{2.4}$$

The transformation matrix, $\boldsymbol{J}(\eta)$, can be defined as follows:

$$\boldsymbol{J}(\eta) = \begin{bmatrix} R_{\text{b}}^{\text{i}}(\Theta_{\text{ib}}) & 0_{3\times 3} \\ 0_{3\times 3} & \text{T}_{\Theta}(\Theta_{\text{ib}}) \end{bmatrix}, \tag{2.5}$$

where the Euler angle rotation matrix of the linear velocities can be defined as follows:

$$\boldsymbol{R}_{\text{b}}^{\text{i}}(\Theta_{\text{ib}}) = \begin{bmatrix} c\psi c\theta & -s\psi c\phi + c\psi s\theta s\phi & s\psi s\phi + c\psi c\phi s\theta \\ s\psi c\theta & c\psi c\phi + s\phi s\theta s\psi & -c\psi s\phi + s\theta s\psi c\phi \\ -s\theta & c\theta s\phi & c\theta c\phi \end{bmatrix}. \tag{2.6}$$

The rotation matrix of the angular velocities can be expressed as

$$\boldsymbol{T}_{\Theta}(\boldsymbol{\Theta}_{\text{ib}}) = \begin{bmatrix} 1 & s\phi t\theta & c\phi t\theta \\ 0 & c\phi & -s\phi \\ 0 & s\phi / c\theta & c\phi / c\theta \end{bmatrix}, \tag{2.7}$$

where $\text{s} \equiv \sin(\cdot), \text{c} \equiv \cos(\cdot), \text{t} \equiv \tan(\cdot)$.

The vector of Euler angles is given as

$$\boldsymbol{\Theta}_{\mathrm{ib}} = [\phi, \theta, \psi]^T . \tag{2.8}$$

The rotation matrix differential equation between the body-fixed frame and the inertial frame is given as

$$\dot{\boldsymbol{R}}_{\mathrm{b}}^{\mathrm{i}} = \boldsymbol{R}_{\mathrm{b}}^{\mathrm{n}} S(\omega_{\mathrm{b/i}}^{\mathrm{b}}), \tag{2.9}$$

where

$$S(\omega_{\mathrm{b/i}}^{\mathrm{b}}) = \begin{bmatrix} 0 & -r & q \\ r & 0 & -p \\ -q & p & 0 \end{bmatrix}. \tag{2.10}$$

2.4 Dynamics and Hydrodynamics of the Underwater Vehicle

2.4.1 Underwater Vehicle Equations of Motion

The equations of motion of the underwater vehicle are derived from Newton's laws of linear and angular momentum. Two assumptions are made when deriving the equations of motion: (1) the underwater vehicle is rigid and (2) the inertial frame is fixed in space. The equations of both translation and angular momentum based on Newton's second law are expressed as follows:

$$m\left(\dot{v}_{\mathrm{o}} + \omega_{\mathrm{o}} \times v_{\mathrm{o}} + \dot{\omega}_{\mathrm{o}} \times r_{\mathrm{G}} + \omega_{\mathrm{o}} \times (\omega_{\mathrm{o}} \times r_{\mathrm{G}})\right) = f_{\mathrm{o}}, \tag{2.11}$$

$$m r_{\mathrm{G}} \times \dot{v}_{\mathrm{o}} + m r_{\mathrm{G}} \times (\omega_{\mathrm{o}} \times v_{\mathrm{o}}) + I_{\mathrm{o}} \dot{\omega}_{\mathrm{o}} + \omega_{\mathrm{o}} \times (I_{\mathrm{o}} \omega_{\mathrm{o}}) = \mathrm{m}_{\mathrm{o}}, \tag{2.12}$$

where f_{o} is the net external force acting on the vehicle, m_{o} is the moment of net external forces, m is the mass of the vehicle, I_{o} is the moments of inertia with respect to the origin, v_{o} is the velocity of the centre of origin in the Body-Fixed Reference Frame, ω_{o} is the angular velocity about the centre of origin, and r_{G} is the distance from the centre of gravity, C_{G}, to the centre of origin, C_{O}.

Equation (2.11) is expanded into three equations, and they are written in the notation of SNAME (1950). The three equations represent the translational motion given as follows:

$$m\left[\dot{u} - vr + wq - x_{\mathrm{G}}(\mathrm{q}^2 + \mathrm{r}^2) + \mathrm{y}_{\mathrm{G}}(pq - \dot{r}) + \mathrm{z}_{\mathrm{G}}(\mathrm{pr} + \dot{\mathrm{q}})\right] = X_o, \tag{2.13}$$

$$m\left[\dot{v} - wp + ur - y_{\mathrm{G}}(\mathrm{r}^2 + p^2) + z_{\mathrm{G}}(qr - \dot{p}) + x_{\mathrm{G}}(qp + \dot{r})\right] = Y_o, \tag{2.14}$$

$$m\left[\dot{w} - uq + vp - z_{\mathrm{G}}(p^2 + q^2) + x_{\mathrm{G}}(rp - \dot{q}) + y_{\mathrm{G}}(rq + \dot{p})\right] = Z_o. \tag{2.15}$$

Equation (2.12) is expanded into three equations with the notation of SNAME (1950). The three equations represent the rotational motion given as follows:

$$\begin{aligned} &I_x\dot{p}+\left(I_z+I_y\right)qr-\left(\dot{r}+pq\right)I_{xz}+\left(r^2-q^2\right)I_{yz}+\left(pr-\dot{q}\right)I_{xy}\ldots \\ &+m\left[y_{\mathrm{G}}\left(\dot{w}-uq+vp\right)-z_{\mathrm{G}}\left(\dot{v}-wp+ur\right)\right]=K_{\mathrm{o}}, \end{aligned} \tag{2.16}$$

$$\begin{aligned} &I_y\dot{q}+\left(I_x+I_z\right)rp-\left(\dot{p}+pr\right)I_{xy}+\left(p^2-r^2\right)I_{zx}+\left(qp-\dot{r}\right)I_{yz}\ldots \\ &+m\left[z_{\mathrm{G}}\left(\dot{u}-vr+wq\right)-x_{\mathrm{G}}\left(\dot{w}-uq+vp\right)\right]=M_{\mathrm{o}}, \end{aligned} \tag{2.17}$$

$$\begin{aligned} &I_z\dot{r}+\left(I_y+I_x\right)pq-\left(\dot{q}+rp\right)I_{yz}+\left(q^2-p^2\right)I_{xy}+\left(rq-\dot{p}\right)I_{zx}\ldots \\ &+m\left[x_{\mathrm{G}}\left(\dot{v}-wp+ur\right)-y_{\mathrm{G}}\left(\dot{u}-vr+wq\right)\right]=N_{\mathrm{o}}. \end{aligned} \tag{2.18}$$

Equations (2.13)–(2.18) can be simplified because the considered underwater vehicle is symmetrical with the x_b-z_b plane and the x_b-y_b plane. For this reason, the products of inertia, I_{xy} and I_{yz}, become zero. In addition, an assumption is made that the centre of origin, C_{O}, and the centre of gravity, C_{G}, coincided each other, $r_{\mathrm{G}}=\left[0,0,0\right]^T$. Therefore, these equations can be further simplified. The simplified equations of motion in six DOFs are given as follows:

$$m\left[\dot{u}-vr+wq\right]=X_0, \tag{2.19}$$

$$m\left[\dot{v}-wp+ur\right]=Y_0, \tag{2.20}$$

$$m\left[\dot{w}-uq+vp\right]=Z_0, \tag{2.21}$$

$$I_x\dot{p}+\left(I_z+I_y\right)qr-\left(\dot{r}+pq\right)I_{xz}=K_{\mathrm{o}}, \tag{2.22}$$

$$I_y\dot{q}+\left(I_x+I_z\right)rp+\left(p^2-r^2\right)I_{zx}=M_{\mathrm{o}}, \tag{2.23}$$

$$I_z\dot{r}+\left(I_y+I_x\right)pq+\left(rq-\dot{p}\right)I_{zx}=N_{\mathrm{o}}. \tag{2.24}$$

The six DOF equations (equations (2.19)–(2.24)) can be expressed in a compact form as follows:

$$\mathbf{M}_{\mathrm{RB}}\dot{\mathbf{v}}+\mathbf{C}_{\mathrm{RB}}\left(\mathbf{v}\right)\mathbf{v}=\boldsymbol{\tau}_o, \tag{2.25}$$

where $\mathbf{v}=\left[u\quad v\quad w\quad p\quad q\quad r\right]^T$ is the velocity vector in the body-fixed reference frame and $\boldsymbol{\tau}_{\mathrm{o}}=\left[X_{\mathrm{o}},Y_{\mathrm{o}},Z_{\mathrm{o}},K_{\mathrm{o}},M_{\mathrm{o}},N_{\mathrm{o}}\right]^T$ is the sum of vectors of the external forces and moments acting on an underwater vehicle.

The sum of the vectors of the external forces and moments, $\boldsymbol{\tau}_o$, consists of the following components:

1. Hydrodynamic forces, $\boldsymbol{\tau}_H$
    a. Added mass, $\boldsymbol{\tau}_I$
    b. Hull forces: damping forces, $\boldsymbol{\tau}_D$
2. Propulsive forces, $\boldsymbol{\tau}_P$
3. Restoring forces: gravity and buoyancy forces, $\boldsymbol{\tau}_R$
4. Environmental forces: wave, current, $\boldsymbol{\tau}_E$
5. Umbilical forces, $\boldsymbol{\tau}_U$

Each set of external forces and moments can be estimated separately, and the results are superimposed as follows:

$$\boldsymbol{\tau}_o = \boldsymbol{\tau}_H + \boldsymbol{\tau}_P + \boldsymbol{\tau}_R + \boldsymbol{\tau}_E + \boldsymbol{\tau}_U . \tag{2.26}$$

Each vector component will be explained in details in the forthcoming chapters. However, the environmental and umbilical forces are not considered at this preliminary stage. Therefore, these forces are assumed to be zero.

By using both equations (2.25) and (2.26), the equations of motion in six DOFs (equations (2.19)–(2.24)) are presented in a compact form (Fossen, 1991, 2002, 2011) as follows:

$$\boldsymbol{M}\dot{\mathbf{v}} + \mathbf{C}(\mathbf{v})\mathbf{v} + \mathbf{D}(\mathbf{v})\mathbf{v} + \mathbf{g} = \boldsymbol{\tau} , \tag{2.27}$$

$$\dot{\boldsymbol{\eta}} = \mathbf{J}_{\Theta}(\boldsymbol{\eta})\mathbf{v} , \tag{2.28}$$

where $\mathbf{v} = [\mathrm{u} \;\; \mathrm{v} \;\; \mathrm{w} \;\; \mathrm{p} \;\; \mathrm{q} \;\; \mathrm{r}]^{\mathrm{T}}$, $\boldsymbol{M} = \boldsymbol{M}_{\mathrm{RB}} + \boldsymbol{M}_{\mathrm{A}}$ is the inertial matrix including hydrodynamic added mass, $\mathbf{C}(\mathbf{v})$ is the Coriolis and centrifugal matrix, $\mathbf{D}(\mathbf{v})$ is the damping matrix, $\mathbf{g}$ is the buoyancy and gravity vector, $\boldsymbol{\tau} = \boldsymbol{\tau}_S + \boldsymbol{\tau}_P$ is the input vector, $\eta = [x, y, z, \phi, \theta, \psi]^T$ is the positions and orientation in the inertial reference frame, and $\boldsymbol{J}_{\Theta}$ is the transformation matrix of the previous chapter.

From equation (2.27), the body-fixed acceleration vector, $\dot{\mathbf{v}}$, can be solved as follows:

$$\dot{\mathbf{v}} = \mathbf{M}^{-1}\left[\boldsymbol{\tau} - \mathbf{h}(\mathbf{v})\right] = \mathbf{M}^{-1}\left[\boldsymbol{\tau} - \mathbf{C}(\mathbf{v})\mathbf{v} - \mathbf{D}(\mathbf{v})\mathbf{v} - \mathbf{g}\right]. \tag{2.29}$$

where $\mathrm{h}(\mathbf{v}) = \mathbf{C}(\mathbf{v})\mathbf{v} + \mathbf{D}(\mathbf{v})\mathbf{v} + \mathbf{g}$.

Rigid-Body Matrix

The rigid-body matrix, $\boldsymbol{M}_{\mathrm{RB}}$, is given as

$$\boldsymbol{M}_{\mathrm{RB}} = \begin{bmatrix} m & 0 & 0 & 0 & mz_{\mathrm{G}} & -my_{\mathrm{G}} \\ 0 & m & 0 & -mz_{\mathrm{G}} & 0 & mx_{\mathrm{G}} \\ 0 & 0 & m & -my_{\mathrm{G}} & -mx_{\mathrm{G}} & 0 \\ 0 & -mz_{\mathrm{G}} & my_{\mathrm{G}} & I_x & -I_{xy} & -I_{xz} \\ mz_{\mathrm{G}} & 0 & -mz_{\mathrm{G}} & -I_{xy} & I_y & -I_{yz} \\ -my_{\mathrm{G}} & mx_{\mathrm{G}} & 0 & -I_{xz} & -I_{yz} & I_z \end{bmatrix}$$

The origin of the Earth-fixed reference frame, C_{O}, and the centre of gravity, C_{G}, coincided with each other, $r_G = [0,0,0]^T$. Therefore, the matrix above can be further simplified. The simplified rigid-body matrix is given as follows:

$$\boldsymbol{M}_{\mathrm{RB}} = \begin{bmatrix} m & 0 & 0 & 0 & 0 & 0 \\ 0 & m & 0 & 0 & 0 & 0 \\ 0 & 0 & m & 0 & 0 & 0 \\ 0 & 0 & 0 & I_x & -I_{xy} & -I_{xz} \\ 0 & 0 & 0 & -I_{xy} & I_y & -I_{yz} \\ 0 & 0 & 0 & -I_{xz} & -I_{yz} & I_z \end{bmatrix}$$

The final mass and the final moments of inertia of the considered underwater vehicles were still uncertain because inside components had not been designed. The mass of underwater vehicle is important because it relates to the respond of the vehicle. The mass of the consider underwater vehicle was based on an exsiting underwater vehicle which had a similar shape and size. The dimension of the C-SCOUT vehicle with the base configuration has similar dimensions to the considered underwater vehicle, which has the base configuration. At the preliminary design stage, the mass and the moments of inertia of the vehicle with the base configuration in this research are taken from specification data of C-SCOUT vehicle (Perrault, 2002). The rigid-body matrix of the considered underwater vehicle for the configuration is given as follows:

$$\boldsymbol{M}_{\mathrm{RB}} = \begin{bmatrix} 314.7 & 0 & 0 & 0 & 0 & 0 \\ 0 & 314.7 & 0 & 0 & 0 & 0 \\ 0 & 0 & 314.7 & 0 & 0 & 0 \\ 0 & 0 & 0 & 0.6 & 0 & -0.8 \\ 0 & 0 & 0 & 0 & 150.3 & 0 \\ 0 & 0 & 0 & -0.8 & 0 & 149.6 \end{bmatrix}$$, for the base configuration AMC001.

Hydrodynamic Forces

Added Mass

The fluid around the vehicle is also accelerated, when an underwater vehicle accelerates relative to the fluid around it. The additional energy is needed to accelerate the underwater vehicle through the fluid. The additional energy can be described as the added inertia of the underwater vehicle or added mass. The added mass, $\boldsymbol{M}_{\mathrm{A}}$, is recognized as

$$\boldsymbol{M}_{\mathrm{A}} = \begin{bmatrix} X_{\dot{u}} & X_{\dot{v}} & X_{\dot{w}} & X_{\dot{p}} & X_{\dot{q}} & X_{\dot{r}} \\ Y_{\dot{u}} & Y_{\dot{v}} & Y_{\dot{w}} & Y_{\dot{p}} & Y_{\dot{q}} & Y_{\dot{r}} \\ Z_{\dot{u}} & Z_{\dot{v}} & Z_{\dot{w}} & Z_{\dot{p}} & Z_{\dot{q}} & Z_{\dot{r}} \\ K_{\dot{u}} & K_{\dot{v}} & K_{\dot{w}} & K_{\dot{p}} & K_{\dot{q}} & K_{\dot{r}} \\ M_{\dot{u}} & M_{\dot{v}} & M_{\dot{w}} & M_{\dot{p}} & M_{\dot{q}} & M_{\dot{r}} \\ N_{\dot{u}} & N_{\dot{v}} & N_{\dot{w}} & N_{\dot{p}} & N_{\dot{q}} & N_{\dot{r}} \end{bmatrix}$$

where X, Y, Z are hydrodynamic force components relative to body axes, referred to as longitudinal, lateral, and normal forces, respectively. K, M, N are hydrodynamic moment components relative, pitching, and yawing moments, respectively. The partial derivative of a force or moment component X, Y, Z, K, M or N with respect to a linear or angular velocity or acceleration $u, v, w, p, q, r, \dot{u}, \dot{v}, \dot{w}, \dot{p}, \dot{q}, \dot{r}$ is designated by the force or moment with the velocity or acceleration as a subscript, SNAME (1950).

The added mass matrix only has 21 unique elements because it is symmetrical with the diagonal (Imay, 1961, as cited in Perrault, 2002). Therefore, the added mass matrix becomes

$$\boldsymbol{M}_{\mathrm{A}} = \begin{bmatrix} X_{\dot{u}} & X_{\dot{v}} & X_{\dot{w}} & X_{\dot{p}} & X_{\dot{q}} & X_{\dot{r}} \\ X_{\dot{v}} & Y_{\dot{v}} & Y_{\dot{w}} & Y_{\dot{p}} & Y_{\dot{q}} & Y_{\dot{r}} \\ X_{\dot{w}} & Y_{\dot{w}} & Z_{\dot{w}} & Z_{\dot{p}} & Z_{\dot{q}} & Z_{\dot{r}} \\ X_{\dot{p}} & Y_{\dot{p}} & Z_{\dot{p}} & K_{\dot{p}} & K_{\dot{q}} & K_{\dot{r}} \\ X_{\dot{q}} & Y_{\dot{q}} & Z_{\dot{q}} & K_{\dot{q}} & M_{\dot{q}} & M_{\dot{r}} \\ X_{\dot{r}} & Y_{\dot{r}} & Z_{\dot{r}} & K_{\dot{r}} & M_{\dot{r}} & N_{\dot{r}} \end{bmatrix}$$

The added mass matrix can be simplified because the considered underwater vehicles have symmetrical shapes about the $x_{\mathrm{b}} - z_{\mathrm{b}}$ plane, and there is no force in the *x* direction when the vehicle accelerates in the *z* direction. Therefore, added mass elements $X_{\dot{v}}$, $X_{\dot{w}}$, $X_{\dot{p}}$, $X_{\dot{r}}$, $Y_{\dot{w}}$, $Y_{\dot{q}}$, $Z_{\dot{p}}$, $Z_{\dot{r}}$, $K_{\dot{q}}$, and $M_{\dot{r}}$ are zero. The added mass matrix becomes

$$\boldsymbol{M}_{\mathrm{A}} = \begin{bmatrix} X_{\dot{u}} & 0 & 0 & 0 & X_{\dot{q}} & 0 \\ 0 & Y_{\dot{v}} & 0 & Y_{\dot{p}} & 0 & Y_{\dot{r}} \\ 0 & 0 & Z_{\dot{w}} & 0 & Z_{\dot{q}} & 0 \\ 0 & Y_{\dot{p}} & 0 & K_{\dot{p}} & 0 & K_{\dot{r}} \\ X_{\dot{q}} & 0 & Z_{\dot{q}} & 0 & M_{\dot{q}} & 0 \\ 0 & Y_{\dot{r}} & 0 & K_{\dot{r}} & 0 & N_{\dot{r}} \end{bmatrix}$$

A variation of the values of the added mass elements is upon the geometry of the underwater vehicle. Perrault (2002) investigated the sensitivity of the added mass values to variables in the geometry of the C-SCOUT vehicle. Perrault (2002) used a program called *estimated submarine added masses*, which was developed by George Watt of Canada's Defence Research Establishment Atlantic. The geometric parameters, which were studied, are as follows:

1. the length-to-diameter ratio;
2. the location of the control surfaces in x direction—measured as x_{aqca}, the distance from the nose to the quarter-chord axis of the rear control surface; and
3. the size of the control surfaces.

Table 2.3. Maximum sensitivity of dimensional added masses to change in geometric parameters (Perrault, 2002)

	Hull L/D
$X_{\dot{u}}$	0.818
$Y_{\dot{v}}$	1.252
$Z_{\dot{w}}$	1.252
$K_{\dot{p}}$	1.249
$M_{\dot{q}}$	6.040
$N_{\dot{r}}$	6.040
$X_{\dot{q}}$	0.819
$Y_{\dot{p}}$	1.252
$Y_{\dot{r}}$	1.421
$Z_{\dot{q}}$	1.421
$K_{\dot{r}}$	1.405

The sensitivity, S, of the response to the variation in geometric parameter can be calculated by

$$S = \frac{(R - R_{\mathrm{nom}}) / R_{\mathrm{nom}}}{(P - P_{\mathrm{nom}}) / P_{\mathrm{nom}}}, \qquad (2.30)$$

where R is the output variable (added mass element), R_{nom} is the nominal value of the output variable, P is the input parameter (geometric parameter), and P_{nom} is the nominal value of the input parameter.

The value of sensitivity S is the percentage change in the added mass element for a 1% change in the specific geometric parameter. The sensitivity of each added mass element for each geometric parameter is shown in Table 2.3.

The values of elements of the added mass matrix for the underwater vehicle with the base configuration are given as follows:

$$\boldsymbol{M}_{\text{A}} = \begin{bmatrix} 9.119 & 0 & 0 & 0 & 11.692 & 0 \\ 0 & -146.663 & 0 & 16.035 & 0 & 34.105 \\ 0 & 0 & -146.663 & 0 & 6.362 & 0 \\ 0 & 16.035 & 0 & 14.188 & 0 & 20.152 \\ 11.692 & 0 & 6.362 & 0 & 11.196 & 0 \\ 0 & 34.105 & 0 & 20.152 & 0 & 11.551 \end{bmatrix}$$

In this research, it was assumed that the considered underwater vehicle was deeply submerged. Therefore, the values of the added mass elements can be constant.

Hull Forces

The studies related to calculating the hull forces are those of Munk (1924), Allen and Perkins (1951), Hopkins (1951), and Jorgensen (1973). The hull forces were estimated by using the method of Jorgensen (1973) in this research because the method was recommended and used by Evans (2003) for the simulation of the C-SCOUT vehicle. The method is capable of estimating the hull forces in a wide range of angles of attack. If the underwater vehicle in this research is required to manipulate at low speed or to stop, the simulation must be able to estimate the forces in a wide range of angles of attack. Jorgensen's formulation was modified by Evans (2003) to include the added term in the potential term in the calculation of normal and pitch moment coefficients. The modified Jorgensen's equations are as follows:

$$C_{\text{N}} = (k_2 - k_1)\frac{S_{\text{b}}}{A}\sin 2\alpha' \cos\frac{\alpha'}{2} + \ldots \\ \eta C_{\text{Dc}}\frac{A_{\text{p}}}{A}\sin^2\alpha', \text{ if } 0° \le \alpha \le 180°; \tag{2.31}$$

$$C_{\text{A}} = C_{\text{DF}(\alpha=0°)}\cos^2\alpha', \text{ if } 0° \le \alpha \le 90°; \tag{2.32}$$

$$C_{\mathrm{A}} = C_{\mathrm{DF}(\alpha=180°)} \cos^2 \alpha', \text{ if } 90° \le \alpha \le 180°; \tag{2.33}$$

$$C_{\mathrm{M}} = (k_2 - k_1)\left[\frac{V_{\mathrm{B}} - S_{\mathrm{b}}(l - X_{\mathrm{m}})}{AL_{\mathrm{tot}}}\right]\sin 2\alpha' \cos\frac{\alpha'}{2} + \ldots$$
$$\eta C_{\mathrm{Dc}} \frac{A_{\mathrm{p}}}{A}\left[\frac{X_{\mathrm{m}} - X_{\mathrm{p}}}{L_{\mathrm{tot}}}\right]\sin^2 \alpha', \text{ if } 0° \le \alpha \le 90°; \tag{2.34}$$

$$C_{\mathrm{M}} = -(k_2 - k_1)\left[\frac{V_{\mathrm{B}} - S_{\mathrm{b}} X_{\mathrm{m}}}{AL_{\mathrm{tot}}}\right]\sin 2\alpha' \cos\frac{\alpha'}{2} + \ldots$$
$$\eta C_{\mathrm{Dc}} \frac{A_{\mathrm{p}}}{A}\left[\frac{X_{\mathrm{m}} - X_{\mathrm{p}}}{L_{\mathrm{tot}}}\right]\sin^2 \alpha', \text{ if } 90° \le \alpha \le 180° \tag{2.35}$$

In the above-mentioned equations, S_{b} is the maximum cross-sectional area of the vehicle; A is the reference area for coefficient evaluation, which is the wetted surface of the whole vehicle; A_{p} is the body plan-form area; C_{Dc} is the cross-drag coefficient which is experienced by a circular cylinder section based upon the diameter and the cross component of the velocity and it is a function of the Reynolds number which can be found in Jorgensen (1973); C_{DF} is the form-drag coefficient, and the form-drag coefficients of the hull at an angle of attack of 0° and 180° are assumed to be the same in this implemented simulation; η is the cross-flow proportionality factor, which can be found in Jorgensen (1973); V_{B} is the total volume of the vehicle; X_{m} is the position of the pitching moment centre, which is the same position of the centre of gravity, x_{G}; X_{p} is the position of centre of the plan-form area; L_{tot} is the total length of the vehicle; and α is the angle between the longitudinal axis of the vehicle to the inflow and the angle attack, which is used in equations (2.31), (2.32), (2.34), and (2.35) and can be defined as follows:

$$\alpha' = \alpha, \text{ if } 0° \le \alpha \le 90°, \tag{2.36}$$

$$\alpha' = 180° - \alpha, \text{ if } 90° \le \alpha \le 180°. \tag{2.37}$$

The angle of attack can be estimated from equation (2.38).

$$\alpha = \tan^{-1}\left[\frac{\sqrt{{v_{\mathrm{CE}}}^2 + {w_{\mathrm{CE}}}^2}}{u_{\mathrm{CE}}}\right]. \tag{2.38}$$

The velocity at the centre of effort, $V_{\mathrm{CE}} = \left[u_{\mathrm{CE}}, v_{\mathrm{CE}}, \mathrm{w}_{\mathrm{CE}}\right]^T$, can be calculated using the following equation:

$$V_{\mathrm{CE}} = \mathbf{v}_{\mathrm{b/i}}^{\mathrm{b}} + \boldsymbol{\omega}_{\mathrm{b/i}}^{\mathrm{b}} \times \eta_{\mathrm{CE}}, \tag{2.39}$$

where $\eta_{CE} = [x_{CE}, y_{CE}, z_{CE}]^T$ is the position of the centre of effort. The centre of effort moves along the longitudinal axis because of the symmetrical shape of the vehicle. As the angle of attack increases, the centre of effort moves aft (Jorgensen, 1973). Therefore, the centre of effort becomes

$$\eta_{CE} = [x_{CE}, 0, 0]^T,$$

where the location of centre of effort on the *x* direction can be defined as

$$x_{CE} = L_{tot} \frac{C_M}{C_N}. \tag{2.40}$$

$(k_2 - k_1)$ is the added mass factor and a function of fineness ratio, which is defined as

$$f = \frac{l}{d}, \tag{2.41}$$

where l is the vehicle length and d is the cross-sectional diameter of the vehicle. The value of the added mass factor can be found in Munk (1924).

In the body-fixed reference frame, the hull forces are given as

$$\begin{bmatrix} X_H \\ Y_H \\ Z_H \end{bmatrix} = \frac{1}{2} \rho A V_{CE}^{\ 2} \begin{bmatrix} -1 & 0 & 0 \\ 0 & \sin\Phi & 0 \\ 0 & -\cos\Phi & 1 \end{bmatrix} \begin{bmatrix} C_A \\ C_N \\ 0 \end{bmatrix}, \tag{2.42}$$

where Φ is the rotation angle of the vehicle, which is defined as

$$\Phi = \tan^{-1}\left[\frac{-v_{CE}}{w_{CE}}\right]. \tag{2.43}$$

Propulsive Forces

The CCPP was used to generate propulsive and manoeuvring forces. The propulsive force vector, τ, acts on the propeller plane. The location of the propeller plane is defined by the vector $\mathbf{r}_p^b = \left[x_p, y_p, z_p\right]^T$ with respect to the gravity centre, C_G.

The input vector, including forces and moments generated by the CCPP, is given as

$$\boldsymbol{\tau} = \begin{bmatrix} x_P & y_P & z_P & K_P & M_P & N_P \end{bmatrix}^T$$

or

$$\boldsymbol{\tau} = \begin{bmatrix} F_x \\ F_y \\ F_z \\ -z_p F_y + y_p F_z \\ z_p F_x - x_p F_z \\ -y_p F_x + x_p F_y \end{bmatrix}, \tag{2.44}$$

where the forces in *x*, *y*, and *z* directions, that is, F_x, F_y, and F_z, are functions of pitch settings, ϕ_{col}, ϕ_{c1}, and ϕ_{c2}, and advance coefficient, J, as shown in Figure 2.3. ϕ_{col} is the collective pitch angle, ϕ_{c1} is the right/left cyclic pitch angle, and ϕ_{c2} is the up/down cyclic pitch angle. The advance coefficient, J, is given as

$$J = \frac{v}{nD}, \tag{2.45}$$

where *v* is the vehicle velocity (or water velocity in the captive experiment using the Towing Tank or circulating water channel), *D* is the diameter of the CCPP, and *n* is the shaft speed in revolutions per second.

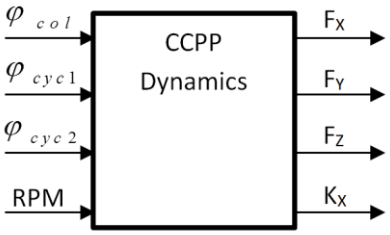

Figure 2.3. Inputs and outputs of the collective and cyclic pitch propeller.

Restoring Forces

The gravitation force, f_g^b, acts throughout the centre gravity, C_G. The location of the centre gravity point is defined by the vector $\mathbf{r}_g^b = \left[x_g, y_g, z_g\right]^T$ with respect to the origin centre of the body-fixed reference frame, C_O. The buoyancy force, f_b^b, acts throughout the centre buoyancy, C_B. The location of the centre buoyancy point is defined by the vector $\mathbf{r}_b^b = \left[x_b, y_b, z_b\right]^T$ with respect to the origin centre, C_O. The gravitation force, f_g^i, and the buoyancy force, f_b^i, act in a vertical plane in the inertial reference frame, and they can transform into the body-fixed frame by the following expressions:

$$f_g^b = R_b^i(\Theta_{ib})^{-1} f_g^n = R_b^i(\Theta_{ib})^{-1} \begin{bmatrix} 0 \\ 0 \\ mg \end{bmatrix}, \tag{2.46}$$

$$f_b^b = R_b^i(\boldsymbol{\Theta}_{ib})^{-1} f_b^n = R_b^i(\boldsymbol{\Theta}_{ib})^{-1} \begin{bmatrix} 0 \\ 0 \\ \rho g \nabla \end{bmatrix}, \tag{2.47}$$

where m is the mass of the vehicle, ∇ is the volume of fluid displaced by the vehicle, g is the acceleration of gravity, and ρ is the density of water.

The restoring force ad moment vector can be expressed in the body-fixed reference frame as follows:

$$g(\eta) = -\begin{bmatrix} f_g^b + f_b^b \\ \mathbf{r}_g^b \times f_g^b + \mathbf{r}_b^b \times f_b^b \end{bmatrix}. \tag{2.48}$$

And the full expansion of the restoring force is given as

$$g(\eta) = \begin{bmatrix} (mg - \rho g \nabla)\sin(\theta) \\ -(mg - \rho g \nabla)\cos(\theta)\sin(\phi) \\ -(mg - \rho g \nabla)\cos(\theta)\cos(\phi) \\ -(y_g mg - y_b \rho g \nabla)\cos(\theta)\cos(\phi) + (z_g mg - z_b \rho g \nabla)\cos(\theta)\sin(\phi) \\ (z_g mg - z_b \rho g \nabla)\sin(\theta) + (x_g mg - x_b \rho g \nabla)\cos(\theta)\cos(\phi) \\ -(x_g mg - x_b \rho g \nabla)\cos(\theta)\sin(\phi) - (y_g mg - y_b \rho g \nabla)\sin(\theta) \end{bmatrix}. \tag{2.49}$$

In this research, in order to simplify the mathematical model, the following assumptions are made. The origin of the body-fixed reference frame, C_O, is at the same location of the centre of gravity, C_G. The vehicle is symmetrical with both the vertical axis z and the lateral axis y. The vehicle is symmetrical with the midplane. In addition, the vehicle has a neutral buoyancy, and the mass distribution of the vehicle is homogeneous throughout the vehicle.

Therefore, the mathematical model of the restoring force can be reduced as follows:

$$g(\eta) = \begin{bmatrix} 0 \\ 0 \\ 0 \\ (z_b \rho g \nabla)\cos(\theta)\sin(\phi) \\ (z_b \rho g \nabla)\sin(\theta) + (x_b \rho g \nabla)\cos(\theta)\cos(\phi) \\ -(x_b \rho g \nabla)\cos(\theta)\sin(\phi) \end{bmatrix}. \tag{2.50}$$

2.5 Omnidirectional Control of the Underwater Vehicle

The CCPP were used for omnidirectional control of the underwater vehicle. The manoeuvrability of the underwater vehicle was assessed by using the computer simulation as presented in chapter 5. The following manoeuvres were performed:

1. Turning circle
2. Zigzag tests

3. Turning and diving manoeuvre
4. Yaw control
5. Depth control
6. Speed control
7. Trajectory tracking control

In order to perform the mentioned manoeuvres, the control system of the underwater vehicle equipped with the CCPP was established. Turning circle, zigzag test, and Helix manoeuvre can be performed by using an open-loop control system. The open-loop control system does not require feedback signal to correct the output as illustrated in Figure 2.4. An operator can assign the desired thrust and torque to the CCPP controller. The controller transforms the desired commands into the pitch angle, setting and the shaft speed. The mechanism components inside of the CCPP were adjusted according to the pitch angle setting and the shaft speed. The thrust and the torque were generated and used to manoeuvre the underwater vehicle.

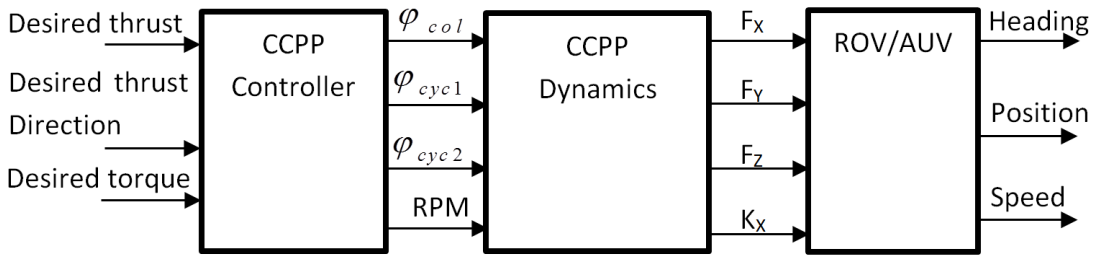

Figure 2.4. Open-loop control system of the underwater vehicle equipped with CCPP.

Yaw control, depth control, and speed control are a closed-loop control system. The closed-loop control system has feedback signals that are compared with the desired signals to detect error signals as shown in Figure 2.7. For the case of a real underwater vehicle, the feedback signals are provided from many kinds of sensors such as Inertial Measurement Unit (IMU), Global Positioning System (GPS), and a pressure sensor. In this research, the underwater vehicle performed in the simulation program. The feedback signal in the simulation program can be calculated from equations (2.29) and (2.2). For simplicity, the multicontrollers used in the simulation study were designed based on the conventional Proportional Integral Derivative (PID) control law as follows:

$$u_{\mathrm{c}} = K_{\mathrm{P}} e(t) + K_{\mathrm{I}} \int_0^t e(t)\,\mathrm{d}t + K_{\mathrm{D}} \frac{\mathrm{d}e(t)}{\mathrm{d}t}, \qquad (2.51)$$

where u_{c} is the control signal (for yaw control, speed control, and depth control); K_{P}, K_{I}, and K_{D} are control gains; and $e(t)$ is the actuating error.

Figure 2.5 shows the fully automated control system for the trajectory tracking.

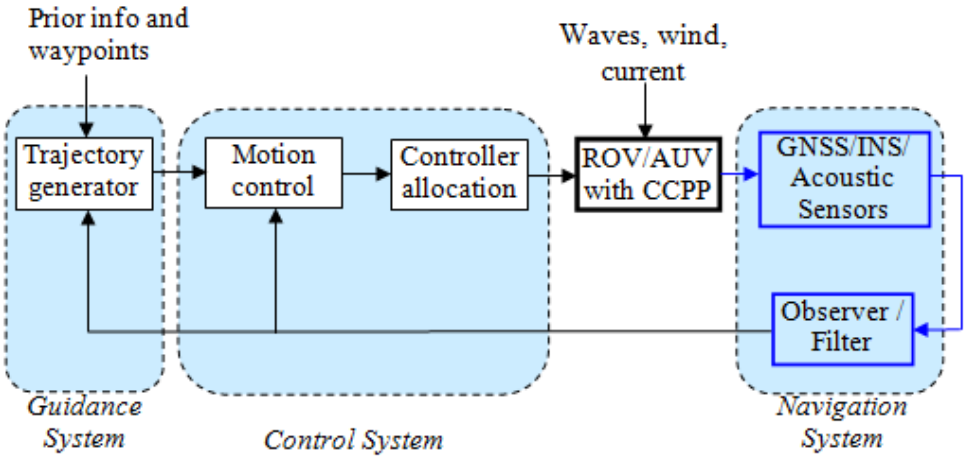

Figure 2.5. Guidance, navigation, and control systems for the ROV/AUV equipped with the CCPP.

Shown in Figure 2.5 are three subsystems: the guidance system, the navigation system, and the control system. The details of the control system of the underwater vehicle with the CCPP are shown in Figure 2.6. The presented block diagram of the control system consists of several parts such as trajectory control, motor control, and pitch control. The highlighted control blocks were presented in this chapter. Block 1 is the underwater vehicle's dynamics. Block 2 is the navigation system, including position sensors (GPS) and motion sensors (IMU). Block 3 is a guidance system where a desired trajectory is generated based on known information. Block 4 is a controller unit (including many controllers). Block 5 is an actuation/control allocation unit/motion control system, including motors and blade actuators. Only the motion control system, which uses the CCPP, is explained in this chapter. The CCPP controller is in block 5, and it will be explained in Chapter 3.

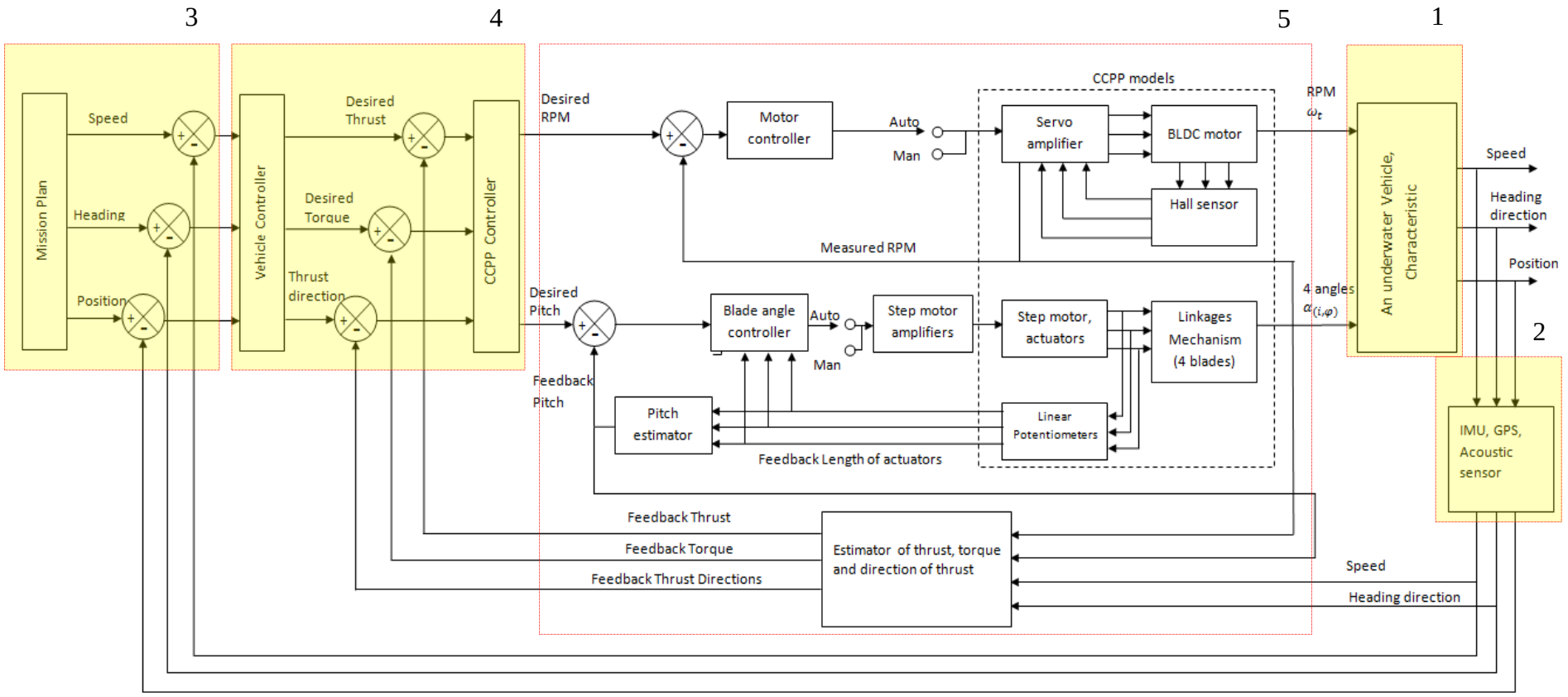

Figure 2.6. Full control system of the underwater vehicle with the CCPP.

The function of each subsystem is as follows:

The guidance system is used to generate a desired trajectory, including the desired yaw (ψ_{d}), speeds $(u_{\mathrm{d}},\ v_{\mathrm{d}},\ w_{\mathrm{d}})$, depth (z_{d}), and position $(x_{\mathrm{d}},\ y_{\mathrm{d}},\ z_{\mathrm{d}})$. The waypoint and line-of-sight (LOS) method is used to generate the desired trajectory (Fossen, 2011).

The desired waypoint positions are as follows:

wpt.pos: $\{(x_0, y_0, z_0),\ (x_1, y_1, z_1),\ \ldots\ (x_{\mathrm{k}}, y_{\mathrm{k}}, z_{\mathrm{k}})\}$

The desired speeds between waypoints are as follows:

wpt.speeds: $U_{\mathrm{d}} = \{u_0,\ u_1,\ \ldots u_{\mathrm{k}}\}$

The desired heading angles are as follows:

wpt.heading: $\psi_{\mathrm{d}} = \{\psi_{\mathrm{d1}}, \psi_{\mathrm{d2}}, \ldots, \psi_{\mathrm{dk}}\}$

The desired heading angles, ψ_{d}, is calculated using the LOS technique (Fossen, 2011) as follows:

$$\psi_{\mathrm{dk}} = \operatorname{atan2}\left(\frac{y_{\mathrm{los}} - y}{x_{\mathrm{los}} - x}\right). \tag{2.52}$$

The x axis of the underwater vehicle aligns the LOS vector, which points to a desired waypoint. A heading control system of the PID type is given as follows:

$$\boldsymbol{\tau} = -K_{\mathrm{P}}\tilde{\psi}(\mathrm{t}) - K_{\mathrm{D}}\frac{\mathrm{d}\tilde{\psi}(t)}{\mathrm{d}t} - K_{\mathrm{I}}\int_0^t \tilde{\psi}(t)\,\mathrm{d}t\ , \tag{2.53}$$

where $\tilde{\psi} = \psi - \psi_{\mathrm{dk}}$.

When the underwater vehicle is moving along the desired trajectory, a switch mechanism for selecting the next waypoint (with a new heading angle and new depth) is necessary. The next waypoint $(x_{k+1},\ y_{k+1},\ z_{k+1})$ is selected when the underwater vehicle lies within a sphere (3-D) or circle (2-D) of acceptance with a radius R_0 around the current waypoint (x_k, y_k, z_k) as shown in Figure 2.7:

$$\sqrt{(x_k - x)^2 + (y_k - y)^2 + (z_k - z)^2} \le R_0\,. \tag{2.54}$$

The value of R_0 is often chosen as two vehicle lengths, that is, $R_0 = 2L$ (Fossen, 2011; Chen et al., 2013; Nguyen, 2008). Otherwise, it is chosen by the control system designer.

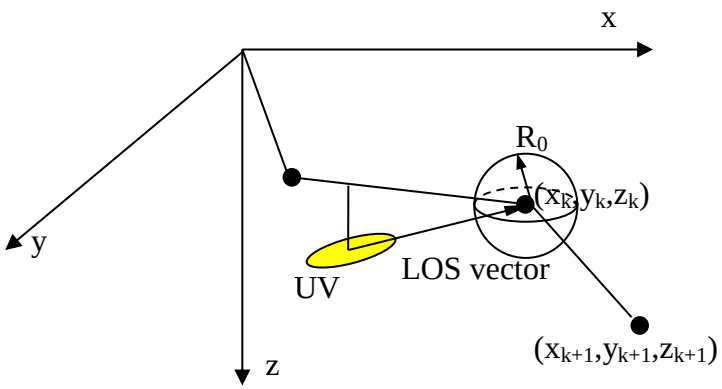

Figure 2.7. LOS technique.

Navigation system is required when the ROV/AUV operates in the real world. It includes a GNSS/IMU sensor when the ROV/AUV operates on the surface, underwater acoustic sensors when it operates underwater, and observer and filter for eliminating noise from the sensors' data.

Chapter Summary

The dynamic models of the underwater vehicle equipped with the CCPP were developed. The vehicles with the base configurations have not been fully built; therefore, some particulars of the vehicles were based on the C-SCOUT vehicle, such as the total mass, the centre of gravity, and the centre of buoyancy. The added mass of the test underwater vehicle was calculated by using the sensitivity, S, of the response to the variation in geometric parameter. The hull forces were determined by using the method of Jorgensen (1973). Furthermore, the forces of the CCPP were determined by using the experimental results and the prediction program.

The motion control system of an underwater vehicle equipped with the CCPP was described. A motion control system was developed in order to control the underwater vehicle to follow a prescribed path. Yaw controller, depth controller, speed controller, and path-following controller were designed by using a theory based on the conventional PID control law. The LabVIEW application was used to develop the simulation program.

Chapter 3 Control of CCPP for an Underwater Vehicle

A collective and cyclic pitch propeller applied in a helicopter generates both axial thrust and side thrusts by manipulating blade angles. If these axial and transverse thrusts can be controlled as desired, it is possible to apply the CCPP for propelling and manoeuvring an AUV. The main purposes of this chapter are as follows:

- to describe a control system of the CCPP,
- to model the motor and the servo drive of the CCPP using a relevant theory,
- to model the kinematics of mechanism of the CCPP,
- to develop the tracking control of the position and orientation of the swash plate, and
- to develop a simulation program for controlling the CCPP.

This study is organized as follows. Section 1 introduces the background, scope, and purposes of the study. Section 2 gives a brief description of the control system of the CCPP. Section 3 is about the theoretical modelling of the motor and its servo drive of the CCPP. Section 4 is about a kinematic model of the mechanism of the CCPP. Section 5 describes a computer simulation of the CCPP. Section 6 is about the control program of the real CCPP program. Finally, section 7 highlights some concluding remarks.

3.1 Control System of the CCPP

The CCPP consists of the following components as shown in Figure 3.1: a brushless DC motor drive, three stepper motor drives, three stepper motor-driven linear actuators, and a data acquisition (DAQ) card.

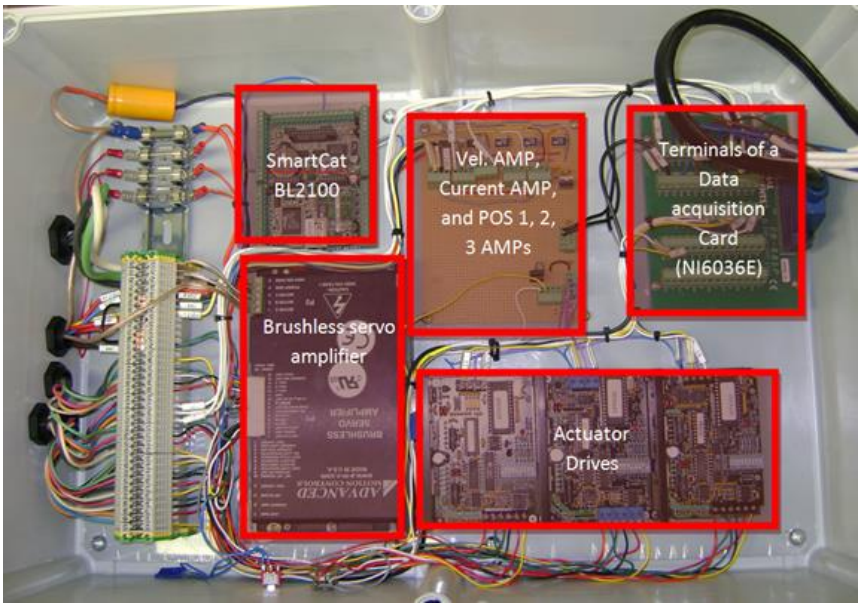

Figure 3.1. Electronics of the control system of the CCPP.

Figure 3.2 shows a functional block diagram of the CCPP with various components. For the development of the control programs, the output variables are the motor shaft speed and four blade angles.

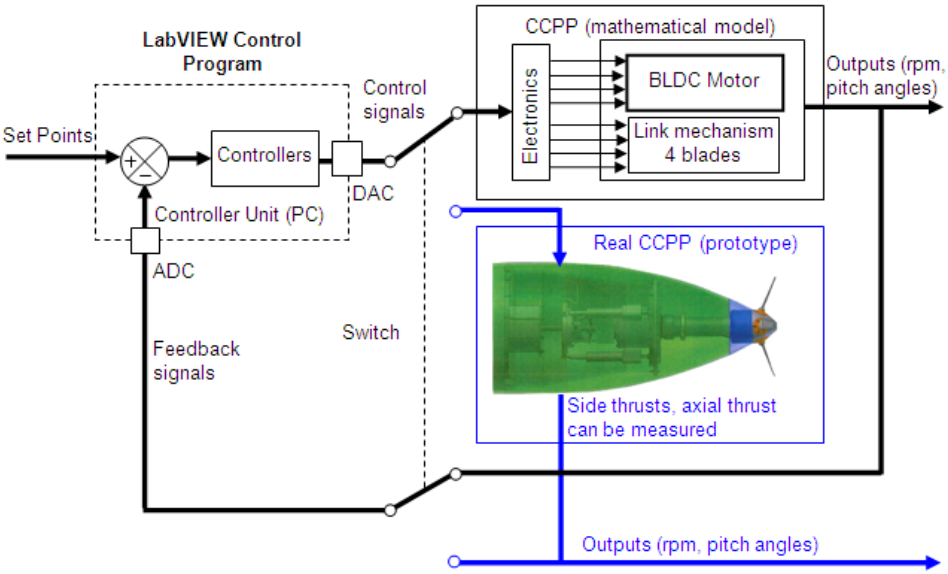

Figure 3.2. Functional block diagram of the CCPP—a conceptual diagram of the simulator and real control system program.

3.2 Definitions of Pitch Setting Parameters

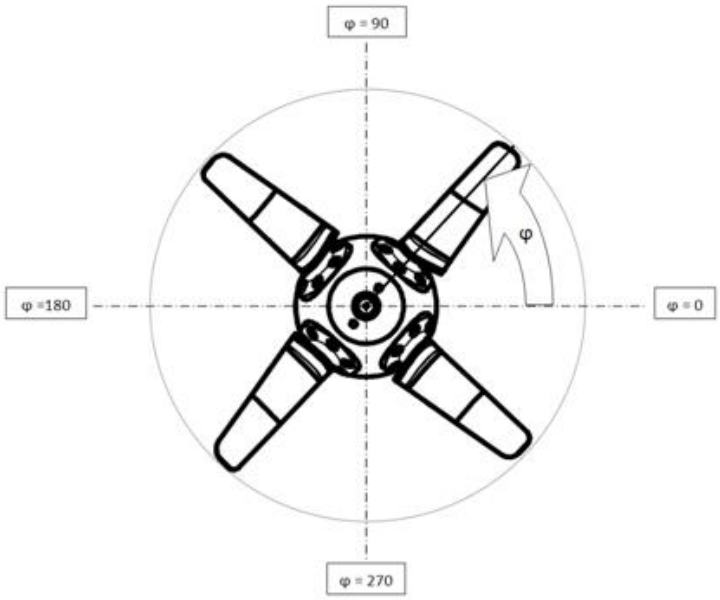

Figure 3.3. Rotation of the CCPP.

The pitch angle at any particular angular position of the propeller plane can be expressed by equation (3.1). Equation (3.1) was developed to estimate the instantaneous angles of each propeller blade at any pitch settings. The change of the angle of the propeller blades is

sinusoidal for a cyclic pitch setting because the swash plate controls the movement of the control rods. The equation is presented as follows:

$$\alpha_{(i,\varphi)} = \alpha_{\mathrm{Col}(i)} + \alpha_{\mathrm{U/D}(i)} \sin(\varphi + 180) + \alpha_{\mathrm{R/L}(i)} \cos(\varphi + 180), \qquad (3.1)$$

where subscript i (1, 2, 3, and 4) is the blade number, subscript φ (0°–360°) is the location of the propeller blade, $\alpha_{(i,\varphi)}$ is the total pitch angle of each blade, and $\alpha_{\mathrm{Col}(i)}$ is the assigned collective pitch angle of a particular blade ($\alpha_{\mathrm{Col}(i)}$ = –29° to +29°).

The two parameters for controlling cyclic pitch are as follows: $\alpha_{\mathrm{U/D}(i)}$, the maximum up/down cyclic pitch angle of a particular blade ($\alpha_{\mathrm{U/D}(i)}$ = –20° to +20°), and $\alpha_{\mathrm{R/L}(i)}$, the maximum right/left cyclic pitch angle of a particular blade ($\alpha_{\mathrm{R/L}(i)}$ = –20° to +20°).

The cyclic variables, $\alpha_{\mathrm{R/L}(i)}$ and $\alpha_{\mathrm{U/D}(i)}$, are explained in following examples.

The blade has a minimum pitch angle at the top position, φ = 90°, when $\alpha_{\mathrm{U/D}(i)}$ is positive and $\alpha_{\mathrm{R/L}(i)}$ is zero, as shown in Figure 3.4. The maximum pitch angle is in the bottom position, φ = 270°.

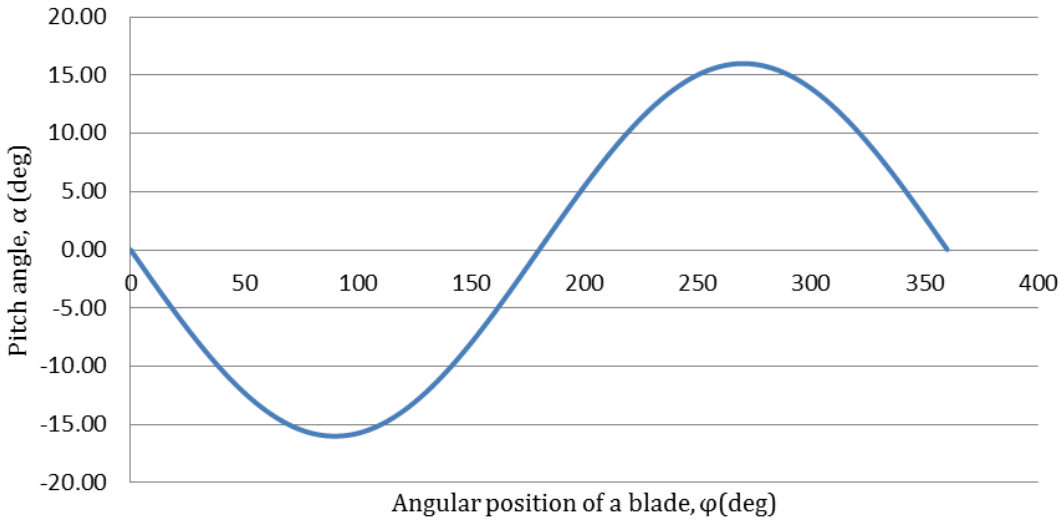

Figure 3.4. Pitch angle of a blade at each angular position for pitch setting is α_{Col} = 0°, $\alpha_{\mathrm{U/D}}$ = 16°, and $\alpha_{\mathrm{R/L}}$ = 0°.

The blade has a maximum pitch angle at the port position, φ = 180°, when $\alpha_{\mathrm{U/D}(i)}$ equals zero and $\alpha_{\mathrm{R/L}(i)}$ is positive, as shown in Figure 3.5. The minimum is in the starboard position, φ = 0°.

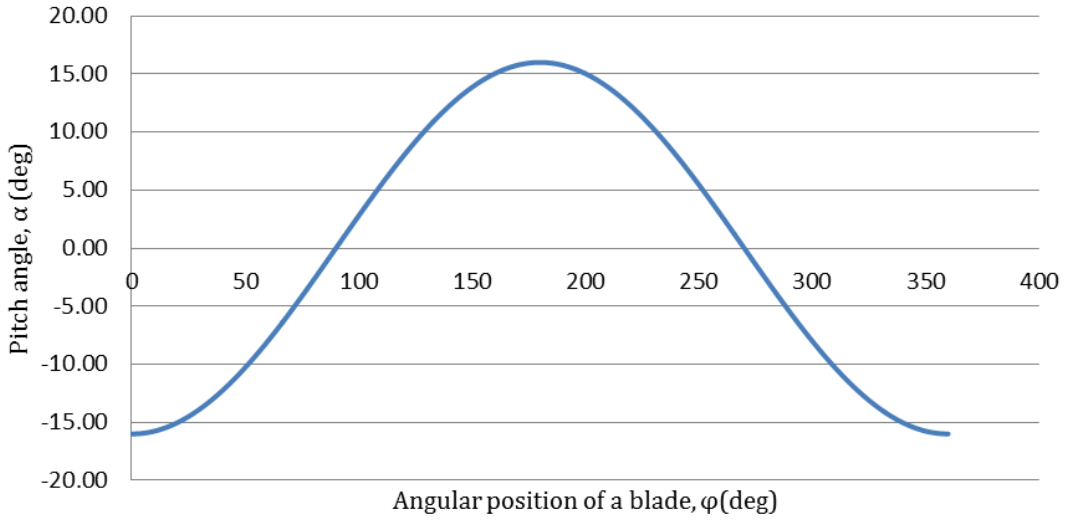

Figure 3.5. Pitch angle of a blade at each angular position for pitch setting is α_{Col}= 0°, $\alpha_{U/D}$ = 0°, and $\alpha_{R/L}$ =16°.

The blade has a maximum pitch angle at the port position, φ = 180°, when α_{Col} is positive and $\alpha_{R/L(i)}$ is positive, as shown in Figure 3.6. The minimum is in the starboard position, φ = 0°. The magnitude of the pitch angle of the port position is an addition of amplitude of cyclic pitch and an amplitude of collective pitch. In addition, positive collective produces forward thrust.

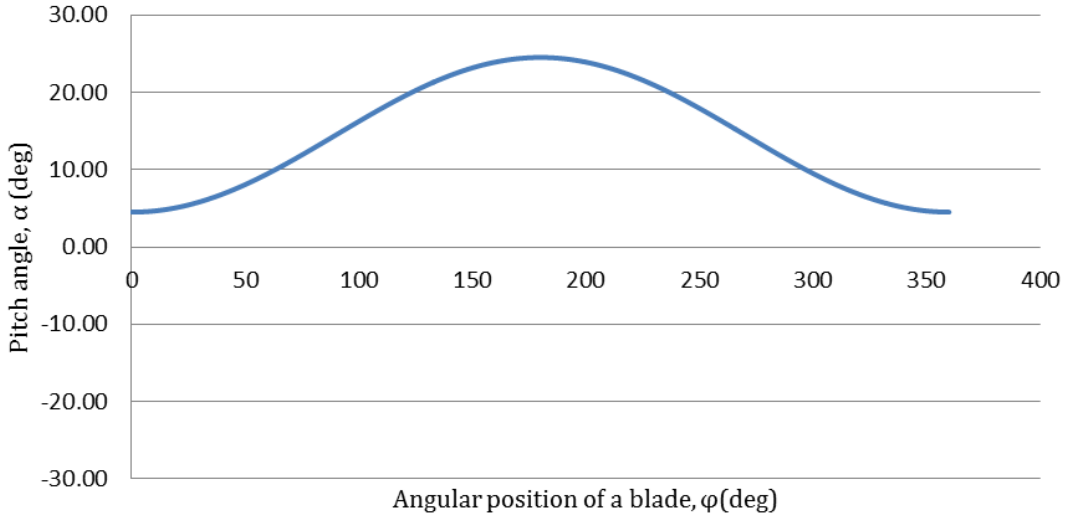

Figure 3.6. Pitch angle of a blade at each angular position for pitch setting is α_{Col} = 14.5°, $\alpha_{U/D}$ = 0°, and $\alpha_{R/L}$ = 10°

For ease of the development of the control system, the pitch angle parameters were converted into percentage number. For instance, a collective pitch angle was set to +100%, which is equal to +29°. In addition, an up/down cyclic pitch angle, $\alpha_{U/D(i)}$, was set to –50%, which is equal to –10°.

3.3 Converting a Blade Angle in Degrees into a Percentage of Maximum Range

The angle of propeller blade was converted into a percentage number for ease of control. It is assumed that the relationship between the blade angle and the thrust is linear in the control and simulation programs.

The collective pitch angle is converted to the percentage number as follows:

$\alpha_{\text{Call(i)}}$ (–29° to +29°) $\rightarrow$ $\alpha_{\text{Call(i)}}$ (–100% to +100%)

$$\alpha^{\text{P}}_{\text{Coll(i)}} = \alpha_{\text{Coll(i)}}\left[\frac{100\% - (-100\%)}{29^\circ - (-29^\circ)}\right]. \tag{3.2}$$

The converting constant (sensitivity) of a collective pitch angle is as follows:

$$K_{\text{Coll}} = \frac{200}{58}\left[\frac{\%}{^\circ}\right] = 3.44838\left[\frac{\%}{^\circ}\right]. \tag{3.3}$$

Superscript P indicates the angle in the form of a percentage. The converting constant of cyclic pitch angle was determined as follows:

$$K_{\text{Cyc1}} = \frac{\alpha^{\text{P}}_{\text{Cyc1(i)}}}{\alpha_{\text{Cyc1(i)}}} = \frac{100\% - (-100\%)}{20^\circ - (-20^\circ)} = 5\left[\frac{\%}{^\circ}\right]. \tag{3.4}$$

Similarly, the following converting constant is obtained:

$$K_{\text{Cyc2}} = \frac{\alpha^{\text{P}}_{\text{Cyc2(i)}}}{\alpha_{\text{Cyc2(i)}}} = \frac{100\% - (-100\%)}{20^\circ - (-20^\circ)} = 5\left[\frac{\%}{^\circ}\right]. \tag{3.5}$$

3.4 Converting a Blade Angle in Percentage to Displacement of Each Actuator

Humphrey (2005) conducted an experiment to find the relationship of the moving distance of the actuators with the angle of the propeller. The developed equations are presented as follows:

$$a_j = \frac{\alpha^{\text{P}}_{\text{Coll}}}{100}, \tag{3.6}$$

$$b_j = \left[\sin\left(\tan^{-1}\left(\frac{\alpha^{\text{P}}_{\text{Cyc2}}}{\alpha^{\text{P}}_{\text{Cyc1}}}\right)\right) \times \left(\frac{\alpha^{\text{P}}_{\text{Cyc2}}}{100}\right)\right], \tag{3.7}$$

if and are not equal to 0

$$b_j = \left(\frac{\alpha^{\mathrm{P}}_{\mathrm{Cyc2}}}{100} \right), \text{if or is equal to } 0 \tag{3.8}$$

$$c_j = \left[\cos\left(\tan^{-1}\left(\frac{\alpha^{\mathrm{P}}_{\mathrm{Cyc2}}}{\alpha^{\mathrm{P}}_{\mathrm{Cyc1}}} \right) \right) \times \left(\frac{\alpha^{\mathrm{P}}_{\mathrm{Cyc1}}}{100} \right) \right], \tag{3.9}$$

if and are not equal to 0

$$c_j = \left(\frac{\alpha^{\mathrm{P}}_{\mathrm{Cyc1}}}{100} \right) \text{ if } \alpha^{\mathrm{P}}_{\mathrm{Cyc1}} \text{ or } \alpha^{\mathrm{P}}_{\mathrm{Cyc2}} \text{ is equal to } 0 \tag{3.10}$$

Subscript *j* is the actuator number (*j* = 1, 2, 3).

The displacement of each actuator is estimated by substituting the value of a_j, b_j, and c_j into the following equations:

The displacement of actuator 1

$$\begin{aligned} L_1 = {} & p_{10} + p_{11}a_1 + p_{12}b_1 + p_{13}c_1 + p_{14}a_1^2 + p_{15}b_1^2 + p_{16}c_1^2 \\ & + p_{17}a_1c_1 + p_{18}b_1c_1 + p_{19}c_1^3 + p_{110}a_1^2c_1 + p_{111}a_1^2c_1 + p_{112}b_1^2c_1 \end{aligned} . \tag{3.11}$$

The displacement of actuator 2

$$\begin{aligned} L_2 = {} & p_{20} + p_{21}a_2 + p_{22}b_2 + p_{23}c_2 + p_{24}a_2^2 + p_{25}b_2^2 + p_{26}c_2^2 \\ & + p_{27}a_2b_2 + p_{28}a_2c_2 + p_{29}b_2c_2 + p_{210}b_2^3 + p_{211}c_2^3 + p_{212}a_2^2b_2 \\ & + p_{213}a_2^2c_2 + p_{214}b_2^2c_2 + p_{215}b_2c_2^2 \end{aligned} . \tag{3.12}$$

The displacement of actuator 3

$$\begin{aligned} L_3 = {} & p_{30} + p_{31}a_3 + p_{32}b_3 + p_{33}c_3 + p_{34}a_3^2 + p_{35}b_3^2 + p_{36}c_3^2 \\ & + p_{37}a_3b_3 + p_{38}a_3c_3 + p_{39}b_3c_3 + p_{310}b_3^3 + p_{311}c_3^3 + p_{312}a_3^2b_3 \\ & + p_{313}a_3^2c_3 + p_{314}b_3^2c_3 + p_{315}b_3c_3^2 \end{aligned} . \tag{3.13}$$

Numerical values of coefficients $p_{1\mathrm{i}}, p_{2\mathrm{i}}, p_{3\mathrm{i}}$ can be found in Appendix A6.2.

The actuators are the linear stepping motors. The stepping motor amplifiers are set to move the stepping motors 1 inch for every 3,200 pulses.

The displacement of each actuator is converted to the number of pulses as follows:

$$\text{Number of pulses} = L_i \frac{1}{3,200} = 3.125 \times 10^{-4} L_i \tag{3.14}$$

Feedback Signals

Inside each linear actuator is a linear potentiometer. The feedback signal is in the form of an amount of voltage Va_i (see Figure 3.7):

The displacement of actuator 1, $L_1 = 0.2359\ Va_1$ (3.15)

The displacement of actuator 2, $L_2 = 0.2359\ Va_2$ (3.16)

The displacement of actuator 1, $L_3 = 0.2359\ Va_3$ (3.17)

The Resolution

The resolution of the DAQ system is 16 bits, and the measuring range is between 0 and 10 V.

The resolution in volts = $\frac{10}{2^{16}}\text{V} = \frac{10}{65536}\text{V} = 0.000152588\ \text{V}$ (3.18)

And the resolution in displacement = 0.000035996 inches (3.19)

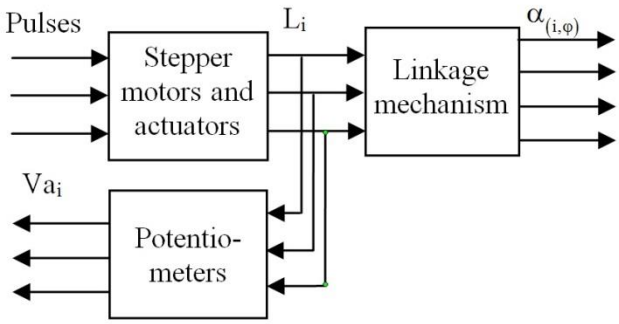

Figure 3.7. Block diagram of the actuators and linkage mechanism with potentiometers.

3.5 Description and Modelling of BLDC Motor and Drive Used in the CCPP

The frameless Brushless Direct Current (BLDC) motor (of Bayside/Parker Motion Group) used in the CCPP is shown in Figure 3.8.

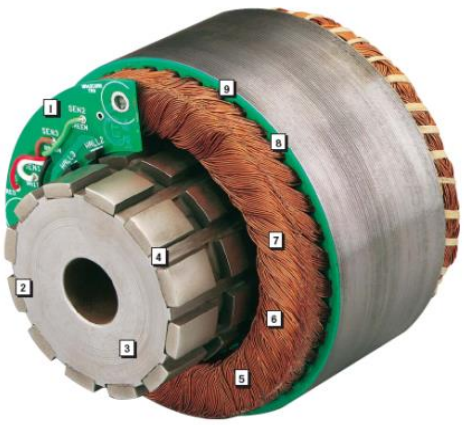

1. Pre-installed integral commutation board
2. Rare earth magnets
3. Rotor assembly
4. Machined groves
6. High-density copper winding
7. Minimized end turns
8. Skewed laminations
9. Optimized slot fill

Figure 3.8. Frameless BLDC motor used for the CCPP (Parker Motion, 2011).

The frameless BLDC motor is controlled by a brushless servo amplifier (Advanced Motion Controls) as illustrated by a block diagram in Figure 3.9.

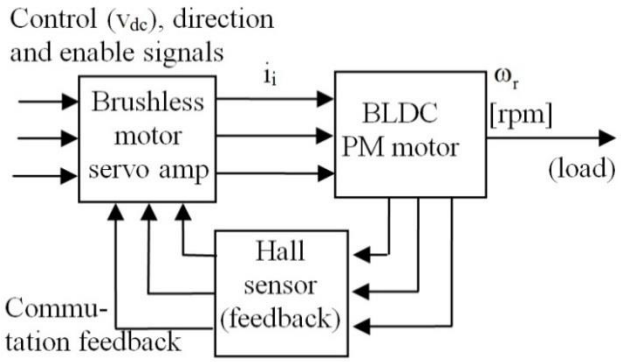

Figure 3.9. Block diagram of the brushless DC pm motor system.

An equivalent diagram for the BLDC motor system with its servo amplifier and Hall sensor is shown in Figure 3.10.

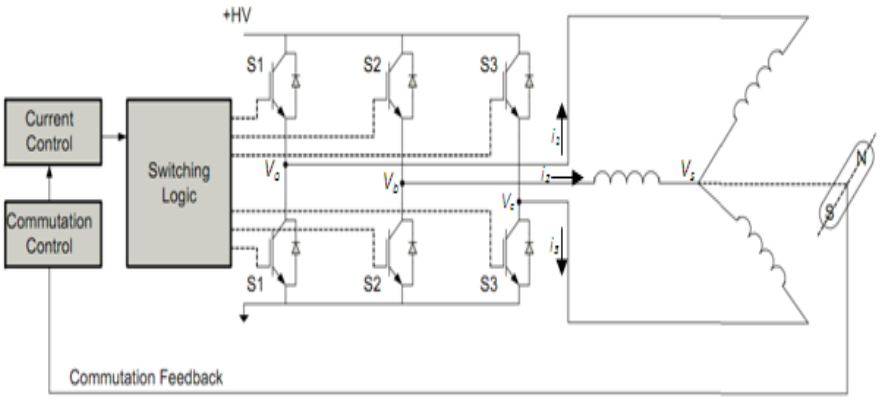

Figure 3.10. BLDC motor system with the servo amplifier and Hall sensor (Advanced Motion Controls, 2011).

Referring to Figure 3.10, the equations for the BLDC motor system are summarized as follows:

Estimation of the voltage values at the star point is given as

$$v_s = \left(\frac{v_a + v_b + v_c}{3}\right) - \left(\frac{e_1 + e_2 + e_3}{3}\right), \qquad (3.20)$$

where $e_1, e_2,$ and e_3 are the back electromagnetic fields (EMF) of each phase; v_s is the star point voltage; and $v_a, v_b,$ and v_c are the voltages at terminals *a*, *b*, and *c*, respectively. It is equal to $\pm V_{dc}/2$ (V_{dc} is the BLDC motor input voltage).

The phase voltages for a brushless DC motor were expressed in matrix form as shown in the following equation:

$$\begin{bmatrix} v_1 \\ v_2 \\ v_3 \end{bmatrix} = \begin{bmatrix} R & 0 & 0 \\ 0 & R & 0 \\ 0 & 0 & R \end{bmatrix} \begin{bmatrix} i_1 \\ i_2 \\ i_3 \end{bmatrix} + \begin{bmatrix} L & 0 & 0 \\ 0 & L & 0 \\ 0 & 0 & L \end{bmatrix} \frac{\mathrm{d}}{\mathrm{d}t} \begin{bmatrix} i_1 \\ i_2 \\ i_3 \end{bmatrix} + \begin{bmatrix} e_1 \\ e_2 \\ e_3 \end{bmatrix}, \tag{3.21}$$

where v_1, v_2, and v_3 are the phase voltages; R is the winding resistance; i_1, i_2, and i_3 are the phase currents; L is the winding inductance; and e_i (i = 1, 2, 3) is the back emf of each phase.

The phase voltages are estimated by the following equation:

$$v_1 = v_\mathrm{a} - v_\mathrm{s}$$

$$v_2 = v_\mathrm{b} - v_\mathrm{s}$$

$$v_3 = v_\mathrm{c} - v_\mathrm{s}$$

The equation used to estimate the electromagnetic torque is presented by Nesimi (2002) as

$$T_\mathrm{e} = \frac{1}{\omega_\mathrm{r}} \left(e_1 i_1 + e_2 i_2 + e_3 i_3 \right). \tag{3.22}$$

Furthermore, the equation used to study the transient behaviour of the brushless DC motor is presented as

$$T_\mathrm{e} - T_\mathrm{l} = J \frac{\mathrm{d}\omega_\mathrm{r}}{\mathrm{d}t}, \tag{3.23}$$

where T_e is the electromagnetic torque, T_l is the load torque, J is the inertia of the motor and the driven load and ω_r is the angular speed of the rotor.

Interested readers can find more details of information on the mathematical models of a brushless DC motor in Nesimi (2002), Baldursson (2005), and MathWorks (2013).

3.6 Kinematics of Mechanism of CCPP

The mechanism of CCPP has a vital role in motion control of the angles of the propeller blades. The study of kinematic analysis of the control mechanism of CCPP is to obtain a mathematical model. This mathematical model can be utilized in the simulation program for the pitch angle control. The simulation program for the pitch angle control is a part of the simulation program of an underwater vehicle with the CCPP.

3.6.1 Swash Plate Plane Equation

A general field point, $P = \left[x, y, z \right]^T$, lies on the swash plate plane. The centre of the rotating swash plate plane is the same position as the centre of the swash plate ball joint as shown in

Figure 3.11. The position vectors of each joint between the actuators and the nonrotating swash plate, P_1, P_2, P_3, are on the nonrotating swash plate plane. The equation of the rotation swash plate plane can be determined by using the positions of three points on the plane. Therefore, the positions of three points need to be determined first.

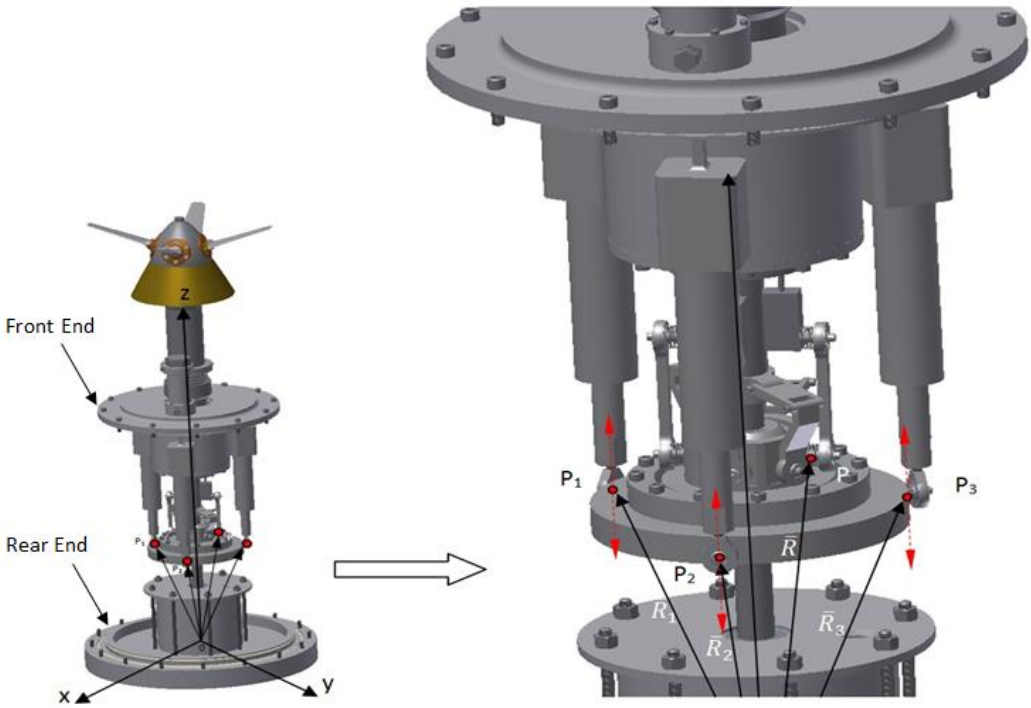

Figure 3.11. Swash plate plane geometry.

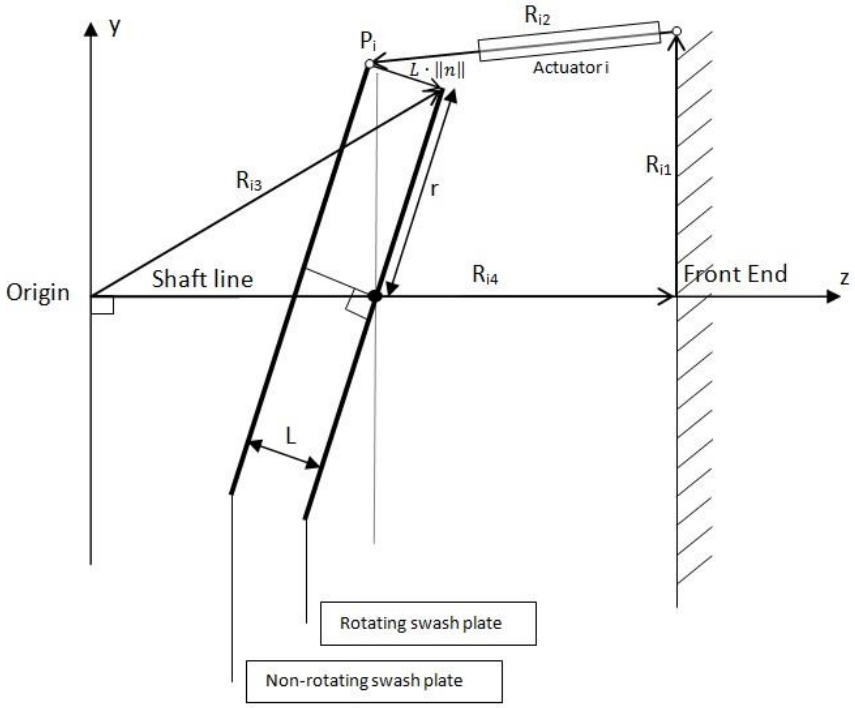

Figure 3.12**.** Skeleton of the swash plate and actuators.

The position vector of the joint between an actuator and the rotating swash plate, R_{i3}, can be determined by using the following equation:

$$R_{i3} = R_{i4} + R_{i1} + R_{i2} + L \cdot \hat{\mathbf{n}}, \tag{3.24}$$

where R_{i1} is the position of the base of an actuator *i* (*x*,*y*, 0) radius (88.9 mm) from the axis of the propeller shaft, R_{i2} is the total length of each actuator, R_{i3} is the position of a point on the rotating swash plate, R_{i4} is the position of a front end plate (449.995 mm), $\hat{\mathbf{n}}$ is the unit normal vector of the nonrotating swash plate, and *L* is the distance from the centre of rotating swash plate plane to the centre of nonrotating swash plate plane.

The calculation of a position of the base of an actuator, R_{i1}, can be determined by using equations (3.25) and (3.26) as follows:

$$x = r_{\mathrm{a}} \cos\left(\phi_{\mathrm{a}_i}\right), \tag{3.25}$$

$$y = r_{\mathrm{a}} \sin\left(\phi_{\mathrm{a}_i}\right), \tag{3.26}$$

$$z = 0, \tag{3.27}$$

where r_{a} is a distance from the axis of the propeller shaft to the base of an actuator and ϕ_{a_i} is the phase angle for the each actuator, which is given as

$$\phi_{\mathrm{a}_i} = (i-1)\left(\frac{360}{N}\right) \text{for } i = 1, 2, \ldots, N, \tag{3.28}$$

where N is the number of actuators and i is the *i*th actuator.

A calculation of the position of a point on the rotating swash plate, R_{i3}, requires to determine a vector, which is perpendicular to the plane of the swash plate and has the same magnitude as the distance from the centre of rotating swash plate plane to the centre of the nonrotating swash plate plane as shown in Figure 3.12. A normal vector is obtained by the cross product of two vectors that lie perfectly on the plane of the nonrotating swash plate.

$$\mathbf{n} = (\mathbf{P}_2 - \mathbf{P}_1) \times (\mathbf{P}_3 - \mathbf{P}_1) = (a, b, c), \tag{3.29}$$

where $\mathbf{P}_1$ is the end point position of actuator 1, $\mathbf{P}_2$ is the end point position of actuator 2, and $\mathbf{P}_3$ is the end point position of actuator 3.

A unit normal vector of the nonrotating swash plate is defined as

$$\hat{\mathbf{n}} = \frac{\mathbf{n}}{|\mathbf{n}|}. \tag{3.30}$$

3.6.2 Vertical Movement of Any Point on the Rotating Swash Plate Plane

A general point, $P(x, y, z)$, that lies on the rotating swash plate plane (see Figure 3.11) can be defined by

$$\left(\overline{\mathbf{R}} - \overline{\mathbf{R}}_{13}\right) \cdot \left[\left(\overline{\mathbf{R}}_{23} - \overline{\mathbf{R}}_{13}\right) \times \left(\overline{\mathbf{R}}_{33} - \overline{\mathbf{R}}_{13}\right)\right] = \mathbf{0} \quad . \tag{3.31}$$

The position of points on the swash plate can be presented in terms as follows:

$$\mathbf{R} = OP = x\hat{i} + y\hat{j} + z\hat{k}$$

$$\mathbf{R}_{13} = OP_1 = x_1\hat{i} + y_1\hat{j} + z_1\hat{k}$$

$$\mathbf{R}_{23} = OP_2 = x_2\hat{i} + y_2\hat{j} + z_2\hat{k}$$

$$\mathbf{R}_{33} = OP_3 = x_3\hat{i} + y_3\hat{j} + z_3\hat{k}$$

The position of points on the rotating swash plate can be used to determine the total length of each actuator, R_{i2}, in equation (3.24).

The vertical position of a general point on the rotating swash plate is defined by equation (3.9). The equation is expressed at a single time step. The details of deriving this equation are found in Leyland (1993).

$$z = \left(A_1 + B_1 y + C_1\right) z_1 + \left(A_2 + B_2 y + C_2\right) z_2 + \left(A_3 + B_3 y + C_3\right) z_3 , \tag{3.32}$$

where

$$A_1 = \frac{-\left(y_3 - y_2\right)}{C_z}$$

$$B_1 = \frac{-\left(x_2 - x_3\right)}{C_z}$$

$$C_1 = \frac{\left(x_2 y_3 - x_3 y_2\right)}{C_z}$$

$$A_2 = \frac{-\left(y_1 - y_3\right)}{C_z}$$

$$B_2 = \frac{-\left(x_3 - x_1\right)}{C_z}$$

$$C_2 = \frac{(x_2 y_1 - x_1 y_3)}{C_z}$$

$$A_1 = \frac{-(y_2 - y_1)}{C_z}$$

$$B_1 = \frac{-(x_1 - x_2)}{C_z}$$

$$C_1 = \frac{(x_1 y_2 - x_2 y_1)}{C_z}$$

$$C_z = (x_2 - x_1)(y_3 - y_1) - (x_3 - x_1)(y_2 - y_1)$$

In order to estimate the vertical position of a general point as a function of time, a general point on the rotating swash plate is needed to be defined with respect to time. Reference points, $\mathbf{P_i}$ on joints between each connecting linkage and the rotating swash plate can be expressed by defining the *x* and *y* coordinates in a polar coordinate system as seen in a circle equation (3.33). By substituting results (*x*, *y*) from equation (3.33) into equation (3.32), the vertical movement for each reference point can be defined as follows:

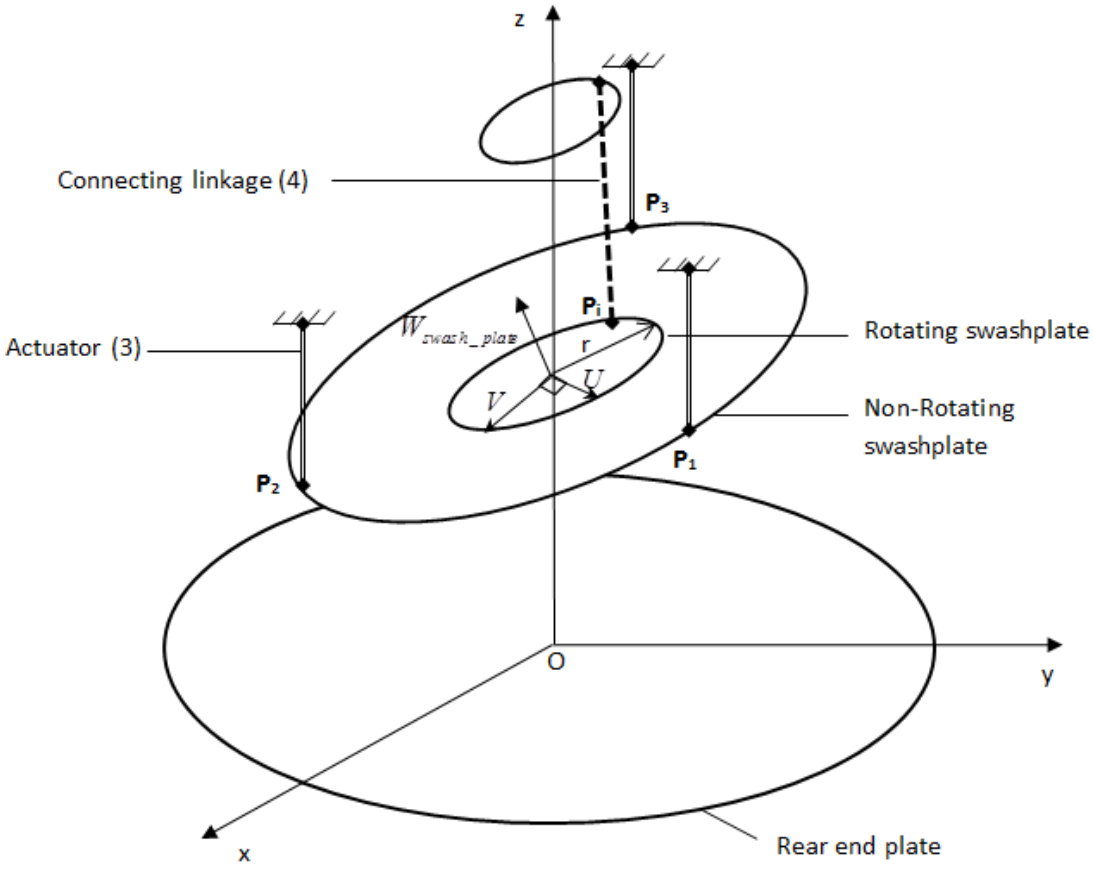

Figure 3.13. Circle equation is on the swash plate plane.

$$\mathbf{P_i}(t) = r\cos(\Omega t + \varnothing_s)\cdot\mathbf{U} + r\sin(\Omega t + \varnothing_s)\cdot\mathbf{V} + C\,, \qquad (3.33)$$

where t is the time, $\mathbf{P_i}$ is the position of a reference point on the circle, C is the position of a centre point of the circle, $\mathbf{W}_{\text{swash plate}} = \hat{\mathbf{n}}_{\text{swash plate}}$ (a unit normal vector of the swash plate plane), $\mathbf{U}$ is a unit vector from the centre of the circle to any point on the circumference, $\mathbf{U} = \mathbf{W}_{\text{swash plate}} \times \hat{i}$ or $\mathbf{W}_{\text{swash\_plate}} \times \hat{j}$ if the angle $\mathbf{W}_{\text{swash plate}}$ is parallel to $\hat{i}$, $\mathbf{V}$ is the unit vector from the centre of the circle to any point on the circumference; $\mathbf{V} = \mathbf{W}_{\text{swash plate}} \times \mathbf{U}$, r is the radius of the circle, Ω is the shaft rotation speed, and $\varnothing_{s_i}$ is the phase angle for the ith blade, which is calculated as follows:

$$\varnothing_{s_i} = (i-1)\left(\frac{360}{N}\right) \text{for } i = 1, 2, \ldots, N\,, \qquad (3.34)$$

where N is the number of blades on the propeller and i is the ith blade.

3.6.3 Movement of the Control Rods

A mechanism for controlling movement of the control rod is an offset slider-crank mechanism. The components for the control can be seen in Figure 3.14. The four control rods are parallel to the propeller shaft. The control rods connect to the control rod slides. Each control rod slider connects to a connecting linkage. Each connecting linkage connects to the rotating swash plate.

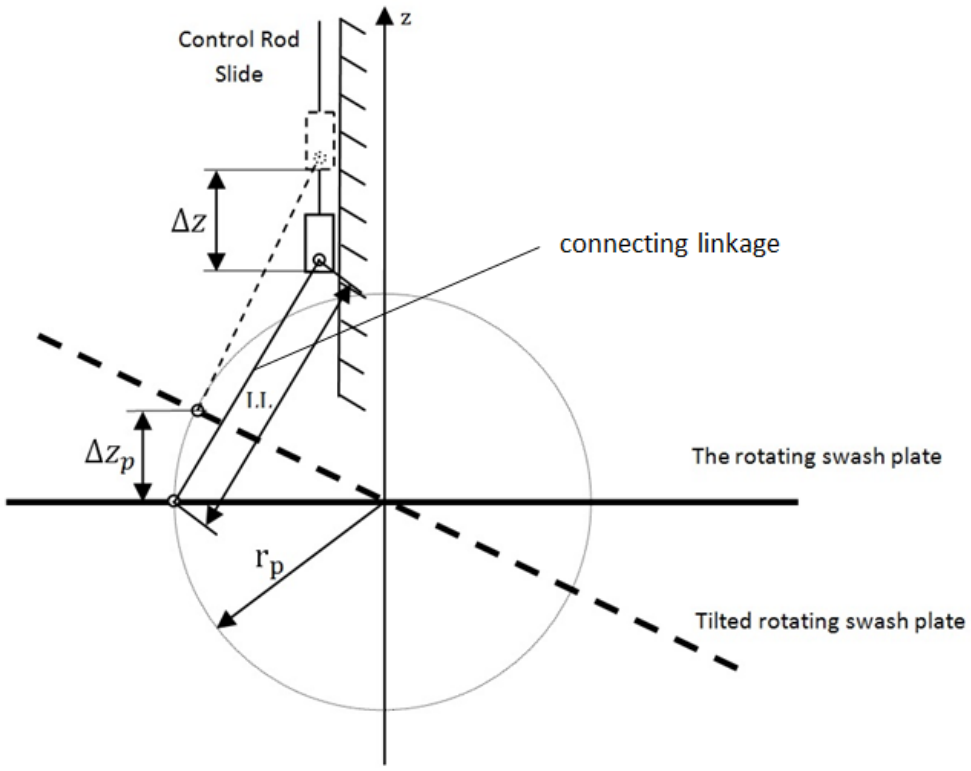

Figure 3.14. Skeleton of the rotating side view of the swash plate and a control rod.

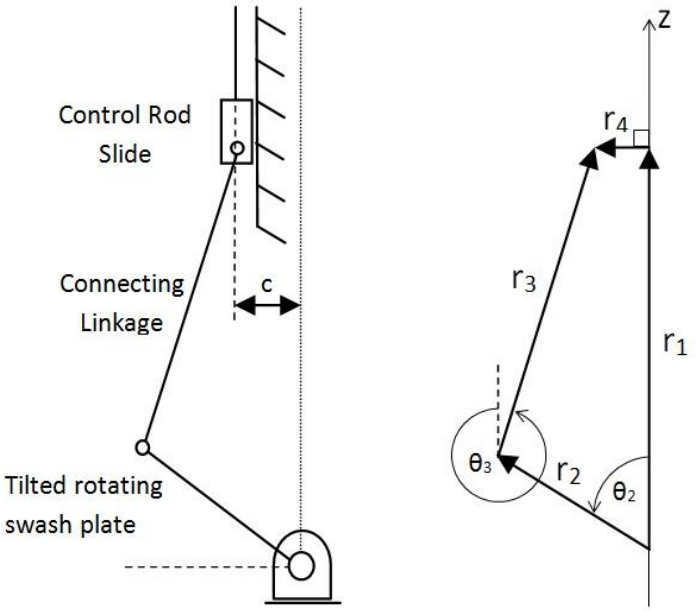

Figure 3.15. An offset slider-crank mechanism of a control rod (left) and its vector representation (right).

The mathematical representation of the vector diagram is the sum of all vectors in the loop. The result of the sum must be equal to zero as seen in equation (3.35).

$$\sum_{i=1}^{4}\mathbf{r}_i = \mathbf{r}_2 + \mathbf{r}_3 = \mathbf{r}_1 + \mathbf{r}_4, \tag{3.35}$$

where $\mathbf{r}_1$ is the vertical vector from the centre of the rotating swash plate to the control rod slider, $\mathbf{r}_2$ is the vector from the centre of the rotating swash plate to the joint of the connecting linkage, $\mathbf{r}_3$ is the vector of the connecting linkage, and $\mathbf{r}_4$ is the eccentricity.

Each vector can be represented in the following form:

$$\mathbf{r}_i = \mathbf{r}_i\left(\cos\theta_i, \sin\theta_i\right)^T. \tag{3.36}$$

Therefore, equation (3.36) can be rewritten in the following form:

$$\mathbf{r}_2\left(\cos\theta_2, \sin\theta_2\right)^T + \mathbf{r}_3\left(\cos\theta_3, \sin\theta_3\right)^T = \mathbf{r}_1\left(\cos\theta_1, \sin\theta_1\right)^T \ldots + \mathbf{r}_4\left(\cos\theta_1, \sin\theta_1\right)^T. \tag{3.37}$$

This equation is a vector equation comprising two scalars, the vector magnitudes and their corresponding direction angles.

A unit vector, $\hat{\mathbf{u}}_{\mathrm{m}} = \left(\cos\theta_1, \sin\theta_1\right)^T$, is utilized to transform the variables θ_2 and θ_3 into variables $\theta_1 - \theta_2$ and $\theta_1 - \theta_3$. The transformation is achieved by multiplying equation (3.37) by the unit vector perpendicular to the vector $\mathbf{r}_1$, $\left(\sin\theta_1, \cos\theta_1\right)^T$. The result is as follows:

$$\mathbf{r}_2 \sin\left(\theta_1 - \theta_2\right) - \mathbf{r}_4 + \mathbf{r}_3 \sin\left(\theta_1 - \theta_3\right) = 0 . \tag{3.38}$$

In addition, The transformation is achieved by multiplying equation (3.37) by the unit vector parallel to the vector $\mathbf{r}_1$, $\left(\cos\theta_1, \sin\theta_1\right)^T$. The result is as follows:

$$\mathbf{r}_2 \cos\left(\theta_1 - \theta_2\right) + \mathbf{r}_3 \cos\left(\theta_1 - \theta_3\right) - \mathbf{r}_1 = 0 . \tag{3.39}$$

Squaring and rearranging equation (3.37) using the trigonometric identity, $\sin^2\left(\theta_1 - \theta_2\right) + \cos^2\left(\theta_1 - \theta_2\right) = 1$, results in the following equation:

$$\begin{aligned} &\mathbf{r}_3^2\left(\cos^2\left(\theta_1 - \theta_2\right) + \sin^2\left(\theta_1 - \theta_2\right)\right) = \mathbf{r}_1^2 + \ldots \\ &\mathbf{r}_2^2\left(\cos^2\left(\theta_1 - \theta_2\right) + \sin^2\left(\theta_1 - \theta_2\right)\right) - \ldots \\ &2\mathbf{r}_1\mathbf{r}_2\cos\theta_2 + \mathbf{r}_4^2 - 2\mathbf{r}_4\mathbf{r}_2\sin\theta_2 = 0 \end{aligned} \tag{3.40}$$

$$\mathbf{r}_1^2 - \left(2\mathbf{r}_2\cos\theta_2\right)\mathbf{r}_1 + \mathbf{r}_2^2 + \mathbf{r}_4^2 - \mathbf{r}_3^2 - 2\mathbf{r}_4\mathbf{r}_2\sin\theta_2 = 0 . \tag{3.41}$$

Equation (3.41) is a quadratic equation, and the vector $\mathbf{r}_1$ can be determined by equation (3.42) as follows:

$$\mathbf{r}_1 = \frac{-b \pm \sqrt{b^2 - 4c}}{2}, \tag{3.42}$$

where

$$b = -2\mathbf{r}_2\cos\theta_2 \tag{3.43}$$

$$c = \mathbf{r}_2^2 + \mathbf{r}_4^2 - \mathbf{r}_3^2 - 2\mathbf{r}_4\mathbf{r}_2\sin\theta_2 . \tag{3.44}$$

3.6.4 Blade Pitch

A mechanism for controlling blade pitch adopts a slider-crank mechanism used in a car engine. The components inside of the propeller hub can be seen in Figure 3.16. The four pitch link rods are parallel to the propeller shaft. The pitch link rods connect to the slide blocks. The slide blocks were shaped like a wedge in order to accommodate the desired rake angle, 20°. Each slide block connects to a first link. Each first link connects to the second links, which connects directly to the blade.

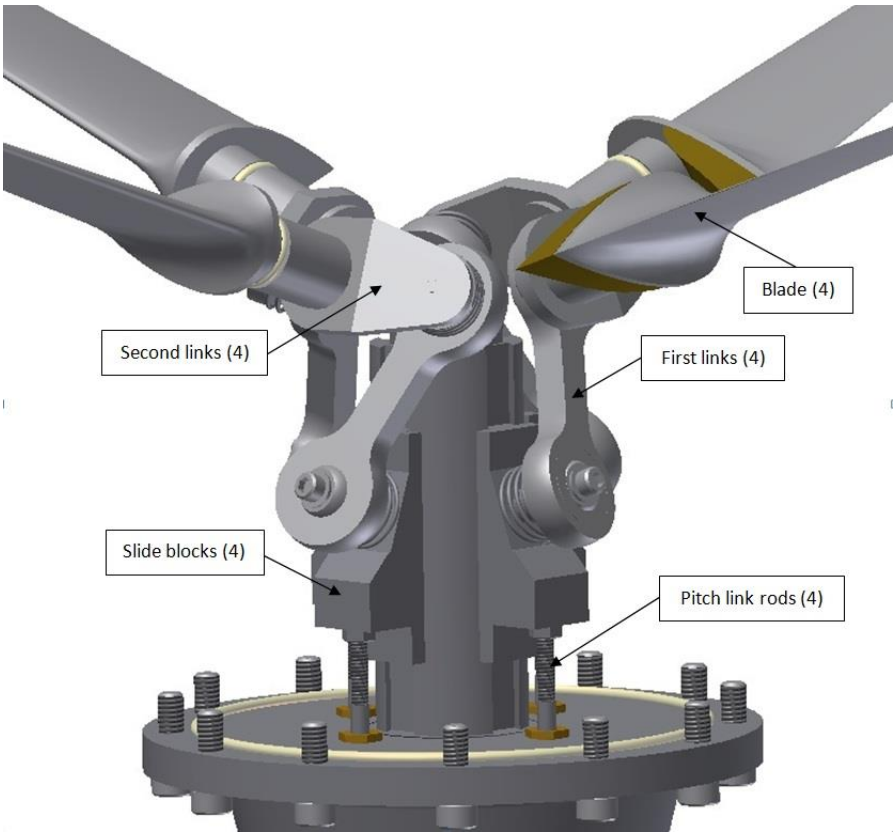

Figure 3.16. Mechanical components in a CCPP hub.

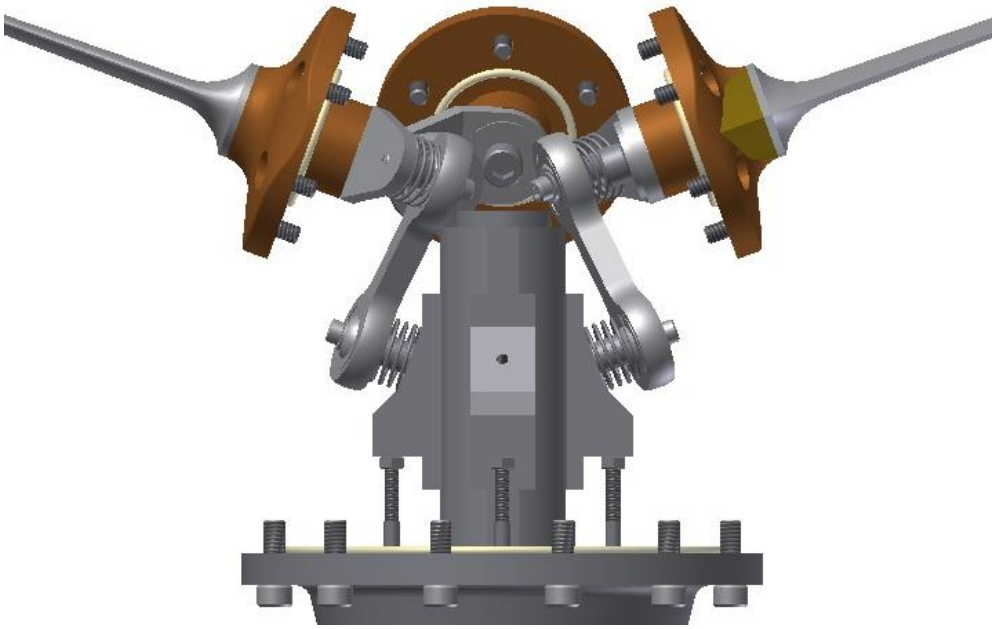

Figure 3.17. The 3-D model of slide-crank mechanism in side view.

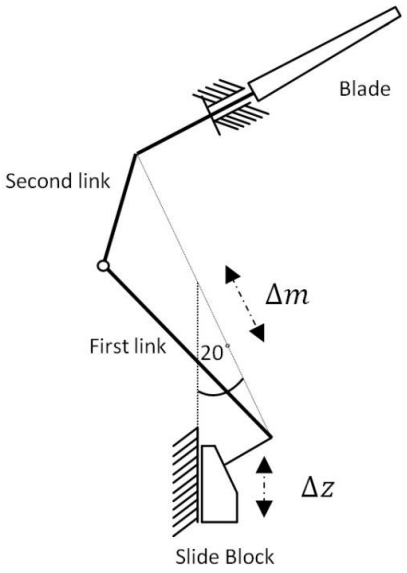

Figure 3.18. Skeleton of a slide-crank mechanism in side view.

The motion of the slide block is on a different plane from the motion of the first link because of the wedge-shaped slide block. The moving distance of the slide block can be converted into its moving distance on the same plane as the motion of the first links as shown in equation (3.45).

$$\Delta m = \Delta z \cos(\delta), \tag{3.45}$$

where Δm is the moving distance of the first link, Δz is the moving distance of the slide block, and δ is the wedge angle of the slide block.

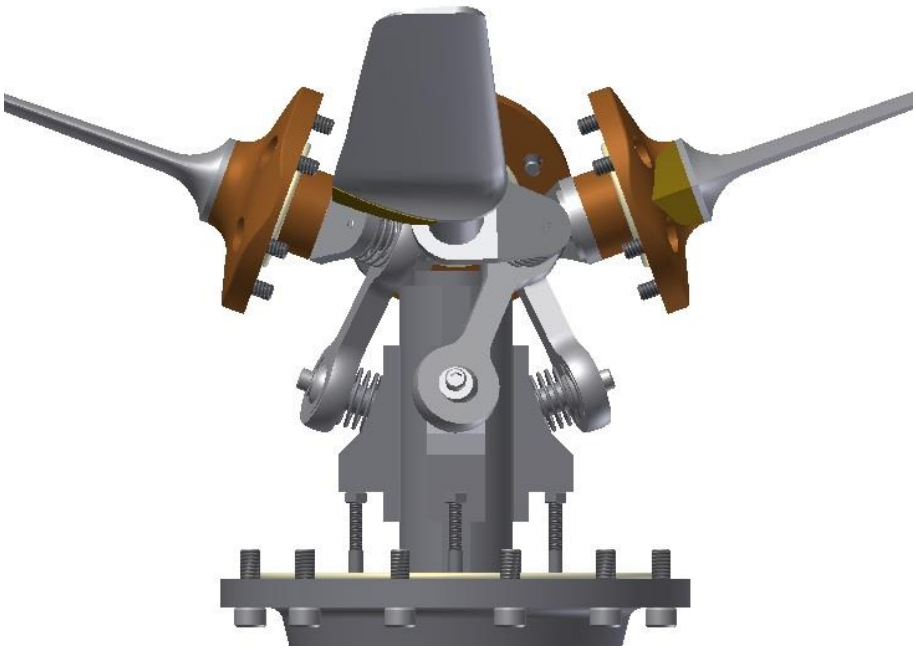

Figure 3.19. The 3-D model of slide-crank mechanism in front view.

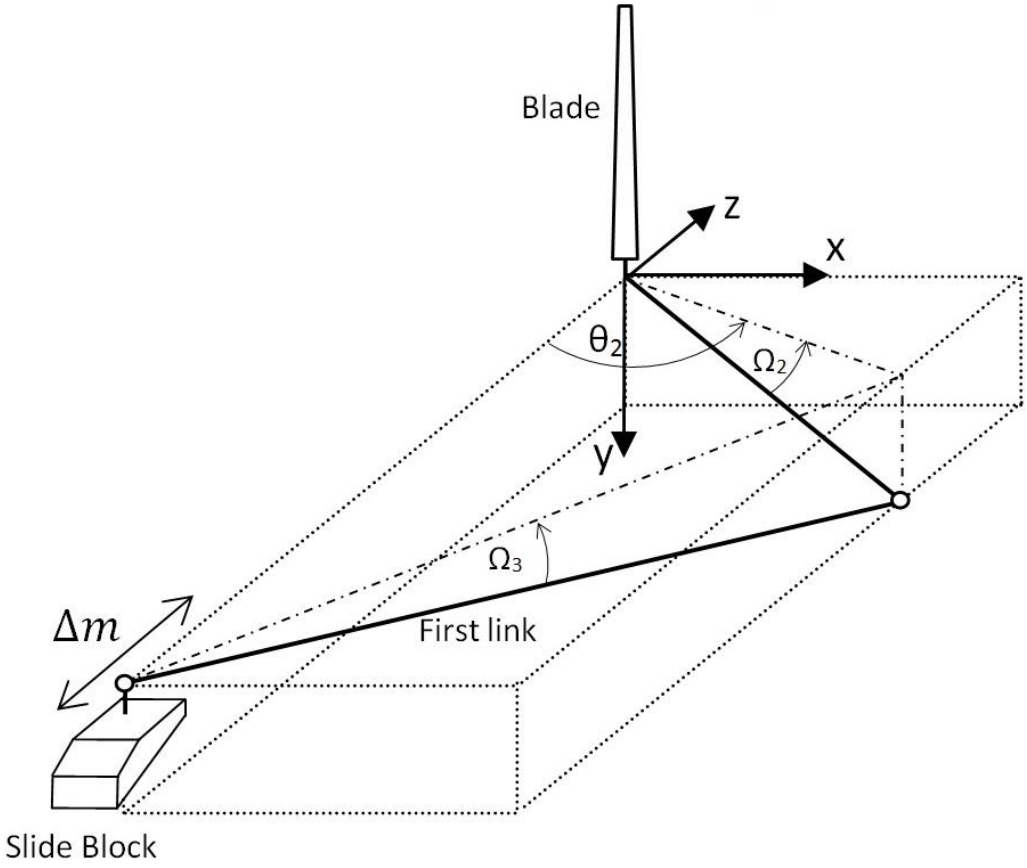

Figure 3.20. Skeleton of slider-crank mechanism.

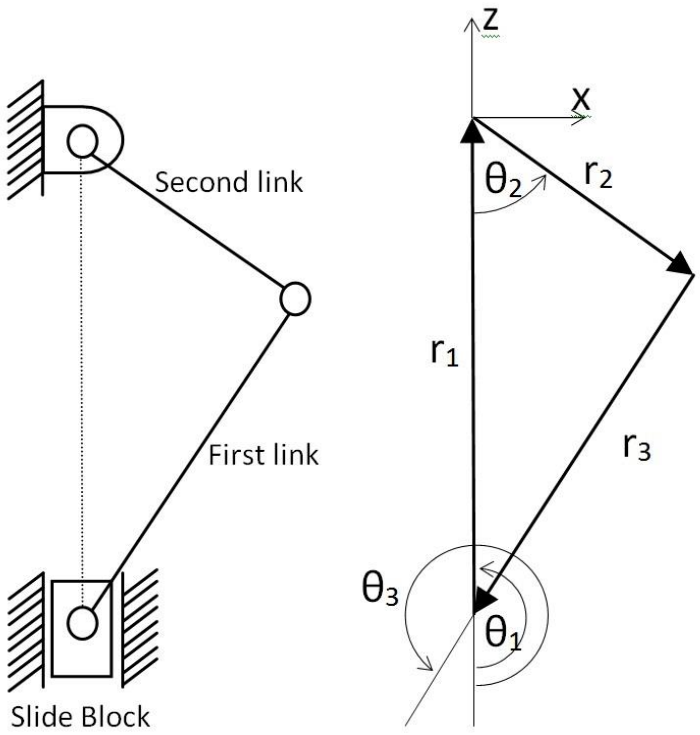

Figure 3.21. Skeleton of slider-crank mechanism on the top view (left) and its vector representation (right).

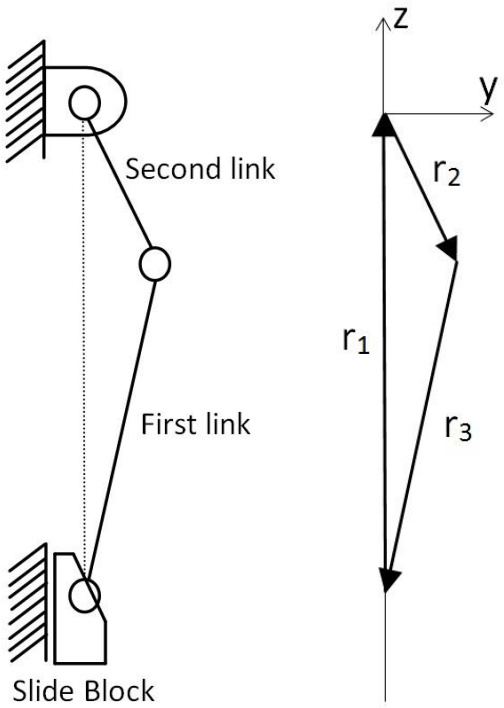

Figure 3.22. Skeleton of slider-crank mechanism on the side view (left) and its vector representation (right).

Skeleton diagrams of the control mechanism of the blade pitch in various views are shown in Figures 3.20–3.22. The *z* axis coincides with the axis of the slide block. The skeletons are also represented in a vector diagram. The magnitudes of these vectors are the length of the links. The lengths of the first link and the second link are projected onto a plane, which is perpendicular to the axis of a blade. The magnitudes of the projected vectors can be determined by the following equation:

$$\mathbf{r}_{i\mathrm{p}} = \mathbf{r}_i \cos\left(\Omega_i\right). \tag{3.46}$$

The mathematical representation of the vector diagram is the sum of all vectors in the loop. The result of the sum must be equal to zero as seen in equation (3.47) as follows:

$$\sum_{i=1}^{3} \mathbf{r}_{i\mathrm{p}} = \mathbf{r}_{1\mathrm{p}} + \mathbf{r}_{2\mathrm{p}} + \mathbf{r}_{3\mathrm{p}} = 0. \tag{3.47}$$

Each vector can be represented in the form

$$\mathbf{r}_{i\mathrm{p}} = \mathbf{r}_{i\mathrm{p}} \left(\cos\theta_i, \sin\theta_i\right)^T. \tag{3.48}$$

Therefore, equation (3.48) can be rewritten in the form

$$\mathbf{r}_1 p(\cos\theta_1, \sin\theta_1)^T + \mathbf{r}_2 p(\cos\theta_2, \sin\theta_2)^T + \mathbf{r}_3 p(\cos\theta_3, \sin\theta_3)^T = 0. \tag{3.49}$$

This equation is a vector equation comprising two scalars: the vector magnitudes and their corresponding direction angles. The equation can be solved for only two unknowns; therefore, the given and the unknown parameters should be identified.

Figure 3.18 shows the blade pitch control mechanism. The motion of the slide block at any given time is given as

$$\mathbf{r}_{\mathbf{1p}} = \mathbf{r}_{\mathbf{1p}}(t) = \Delta m(t). \tag{3.50}$$

The length of the first link and the second link can be measured; thus, the magnitude of vectors $\mathbf{r}_{2\mathrm{p}}$ and $\mathbf{r}_{3\mathrm{p}}$ are identified. The direction of the slide block, θ_1, also is identified. Therefore, there are two unknowns: angles θ_2 and θ_3. All known vector is moved to the right-hand side, so equation (3.49) is rearranged in the following form:

$$\mathbf{r}_{2\mathrm{p}}(\cos\theta_2, \sin\theta_2)^T + \mathbf{r}_{3\mathrm{p}}(\cos\theta_3, \sin\theta_3)^T = m(\cos\theta_1, \sin\theta_1)^T. \tag{3.51}$$

A unit vector, $\hat{\mathbf{u}}_{\mathrm{m}} = (\cos\theta_1, \sin\theta_1)^T$, is utilized to transform the variables θ_2 and θ_3 into variables $\theta_1 - \theta_2$ and $\theta_1 - \theta_3$. The transformation is achieved by multiplying equation (3.51) by the unit vector perpendicular to the vector $\mathbf{m}$, which is $(\sin\theta_1, \cos\theta_1)^T$. The resulting equation is as follows:

$$\mathbf{r}_{2\mathrm{p}}\sin(\theta_1 - \theta_2) + \mathbf{r}_{3\mathrm{p}}\sin(\theta_1 - \theta_3) = 0. \tag{3.52}$$

Then, the transformation is achieved by multiplying equation (3.52) by the unit vector parallel to the vector $\mathbf{m}$, which is $(\cos\theta_1, \sin\theta_1)^T$. The resulting equation is as follows:

$$\mathbf{r}_{2\mathrm{p}}cos(\theta_1 - \theta_2) + \mathbf{r}_{3\mathrm{p}}cos(\theta_1 - \theta_3) = m. \tag{3.53}$$

Rearranging equation (3.53) using the trigonometric identity, $\sin^2(\theta_1 - \theta_2) + \cos^2(\theta_1 - \theta_2) = 1$, yields the following equation:

$$\mathbf{r}_{2\mathrm{p}}\sqrt{1 - \left(\frac{\mathbf{r}_{3\mathrm{p}}}{\mathbf{r}_{2\mathrm{p}}}\right)^2 \sin^2(\theta_1 - \theta_3)} = -\mathbf{r}_{3\mathrm{p}}\cos(\theta_1 - \theta_3) + m. \tag{3.54}$$

Equation (3.54) is rearranged by squaring both sides and then leaving $\cos(\theta_1 - \theta_3)$ to one side. The arranged equation is as follows:

$$\cos(\theta_1 - \theta_3) = \frac{m^2 - \mathbf{r}_{2\mathrm{p}}^2 + \mathbf{r}_{3\mathrm{p}}^2}{2m\mathbf{r}_{3\mathrm{p}}} = A. \tag{3.55}$$

θ_2 can be determined by substituting $\cos(\theta_1 - \theta_3) = A$ into equations (3.52) and (3.53) and solve for $\cos(\theta_1 - \theta_2)$ and $\sin(\theta_1 - \theta_2)$. The following equations can be used to determine θ_2:

$$\cos(\theta_1 - \theta_2) = B, \tag{3.56}$$

$$\sin(\theta_1 - \theta_2) = C, \tag{3.57}$$

where

$$B = \frac{m - \mathbf{r}_{3p} A}{\mathbf{r}_{2p}}, \tag{3.58}$$

$$C = \pm \frac{\mathbf{r}_{3p}}{\mathbf{r}_{2p}} \sqrt{1 - A^2}\ . \tag{3.59}$$

If the value of C is used to acquire a unique solution to the angle θ_2, the sign of B and C should be considered using the following equation:

$$\theta_2 = \begin{Bmatrix} \theta_2 & \text{if } B > 0 \text{ and } C \geq 0 \\ \pi - \theta_2 & \text{if } B < 0 \text{ and } C \geq 0 \\ \pi + \theta_2 & \text{if } B < 0 \text{ and } C \leq 0 \\ 2\pi - \theta_2 & \text{if } B > 0 \text{ and } C \leq 0 \end{Bmatrix}. \tag{3.60}$$

Angle θ_2 is not pitch angle of the blade. The pitch angle can be determined as follows:

$$\text{Pitch angle} = -90 + \theta_2. \tag{3.61}$$

Table 3.1. Summary of dimension of the propeller

Parameters	Units	Values
Radial position of actuators	mm	88.752
Radial position of pitch links (original)	mm	40.068
Length of the first link	mm	37.338
Length of the second link	mm	13.71988
Ω_3	°	5.4881
Ω_2	°	15.0866

3.7 Tracking the Orientation of the Swash Plate

Before developing a new pitch angle control program, the control program commanded the blades to the final pitch setting as fast as possible. With this control strategy, the direction of the generated thrust was not considered while the blades were changing their pitch angle setting to a new pitch angle setting. Consequently, the direction of the thrust moved randomly while the pitch angle of the blades were changed. In order to reduce random movement of the thrust direction, the movement of the thrust direction was required to be tracked. The CCPP did not have any force transducer to use as a feedback signal. Therefore, the movement of the thrust direction could not be tracked directly. In this research, the relationship between the pitch angle and the position and orientation of the swash plate was utilized for tracking the movement of the thrust direction. In addition, the unsmooth changing of pitch angle affects the direction of the generated thrusts. Without a control during the transition of the pitch angle, this also caused the unsmooth transition of the swash as shown in Figure 3.23. Therefore, the position and orientation of the swash plate was necessary to be tracked in order to change the pitch angle smoothly.

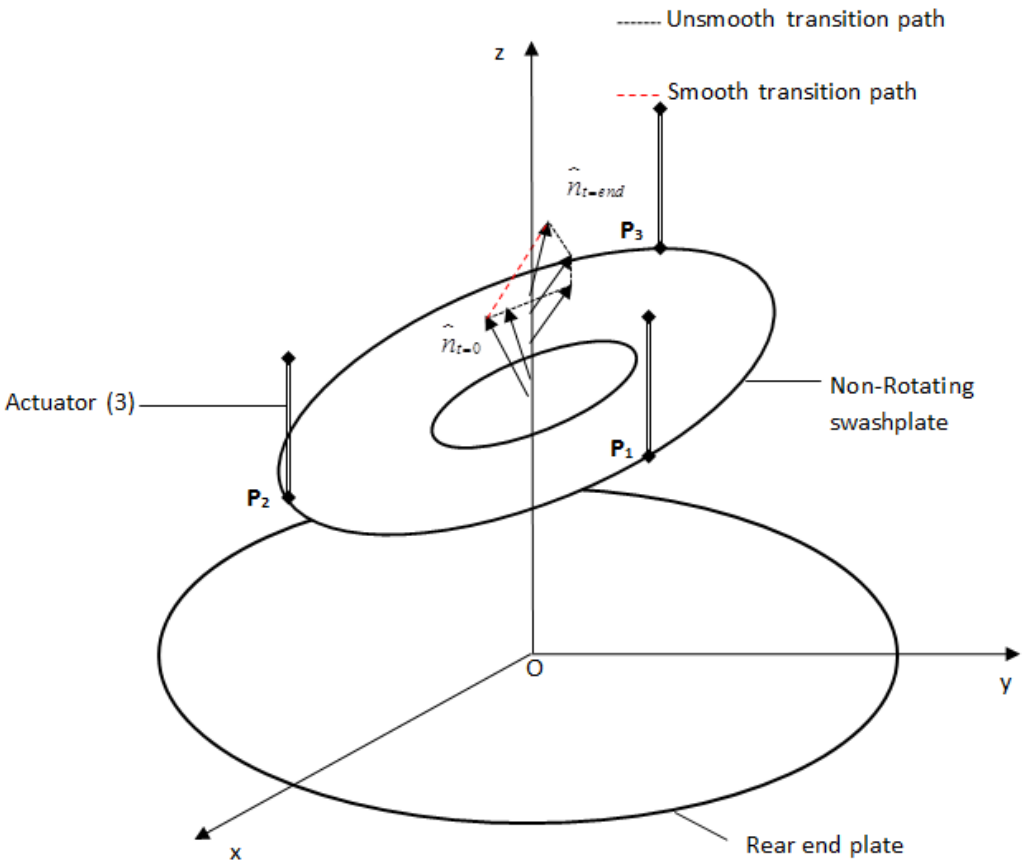

Figure 3.23. Transition movements of the swash plate.

3.7.1 The Orientation of the Swash Plate

The top end point of the normal vector of the swash plate needs to be acquired to be used in the program for tracking the orientation of the swash plate.

The point and the normal vectors can be described as a plane as shown in the following equation:

$$\left(\mathbf{r}-\mathbf{r}_0\right)\cdot\mathbf{n}=0, \tag{3.62}$$

where $\mathbf{n}$ is a normal vector, $\mathbf{r}_0$ is a vector from the origin to a point on the plane, and

$\mathbf{r}$ is another vector from the origin to a point on the plane.

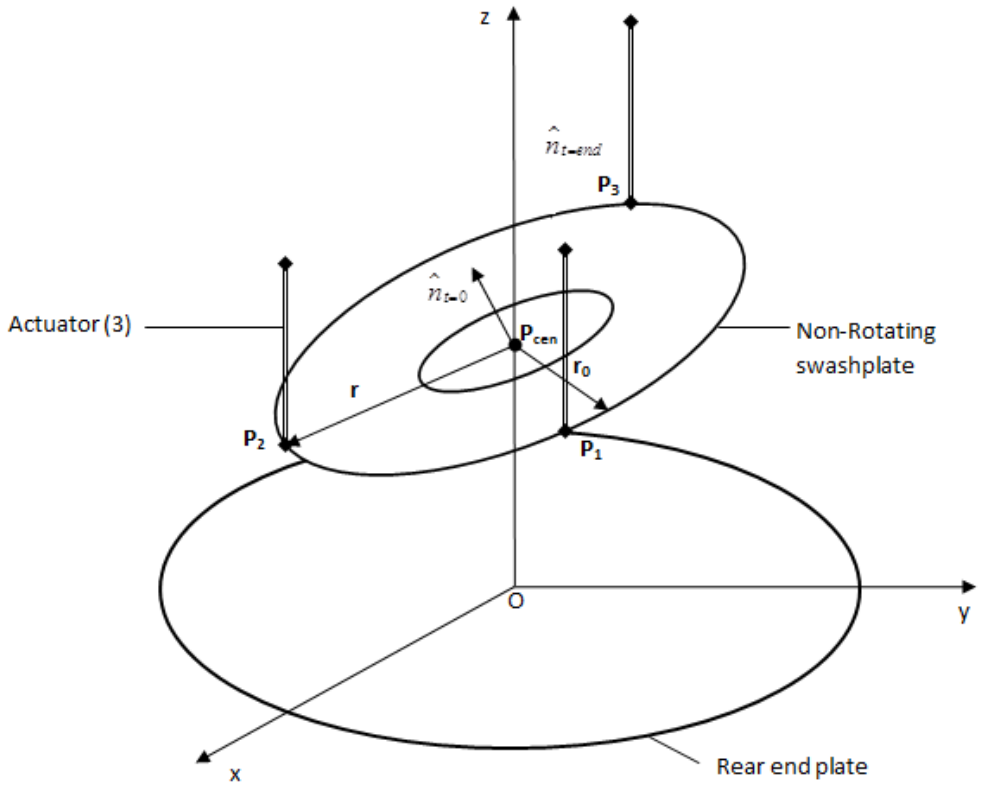

Figure 3.24. The orientation of the swash plate represented by a point.

A normal vector is obtained by the cross product of two vectors that lie perfectly on the plane, shown as follows:

$$\mathbf{n}=\left(p_2-p_1\right)\times\left(p_3-p_1\right)=\left(a,b,c\right), \tag{3.63}$$

where p_1 is the end point position of actuator 1, p_2 is the end point position of actuator 2, and p_3 is the end point position of actuator 3.

Substituting the position of p_1 and the values of a, b, and c in the general form of a plane equation determines the following plane equation:

$$a\left(x-x_{p1}\right)+b\left(y-y_{p1}\right)+c\left(z-z_{p1}\right)=0 \tag{3.64}$$

After acquiring the equation of the plane, substitute $x = 0$ and $y = 0$ in the plane equation. The result of the substitution gives the centre position of the swash plate where the axis line of the shaft intersecting with the swash plate.

The top end point of the normal vector of the swash plate can be determined by adding the normal vector to a vector of the centre of the swash plate as follows:

$$\mathbf{P}_{\text{top end}} = \mathbf{P}_{\text{cen}} + \mathbf{n} = \begin{bmatrix} 0 \\ 0 \\ z_{\text{cen}} \end{bmatrix} + \begin{bmatrix} a \\ b \\ c \end{bmatrix}. \tag{3.65}$$

3.7.2 Manipulation of Three Actuators by Using a Single Point

The single point can be represented by the desired orientation of the swash plate as mentioned in the previous chapter. The end positions of each actuator need to change to acquire the desired orientation of the swash plate. The end position of each actuator is determined from a desired point as follows.

First, determine the intersection between the axis of the propeller shaft and the surface of a sphere. The sphere has a centre position at the desired point and a radius of $\|\mathbf{n}\|$. Although, there are two intersections on the axis line, there is only one intersection, which is the actual centre of the swash plate. The position of real intersection is the one that has z component closer to the origin (0, 0, 0) as seen in Figure 3.25.

A point on the axis of the propeller shaft can be described by two points: the original point, $\mathbf{P}_{\text{origin}}\left(x_{\text{origin}}, y_{\text{origin}}, z_{\text{origin}}\right) = (0,0,0)$, and the end point, $\mathbf{P}_{\text{end}}\left(x_{\text{end}}, y_{\text{end}}, z_{\text{end}}\right)$.

$$\mathbf{P}_{\text{inter}} = \mathbf{P}_{\text{origin}} + \mathbf{m}\left(\mathbf{P}_{\text{end}} - \mathbf{P}_{\text{origin}}\right). \tag{3.66}$$

Equation (3.66) can be described in each coordinate as follows:

$$x = x_{\text{origin}} + m\left(x_{\text{end}} - x_{\text{origin}}\right), \tag{3.67}$$

$$y = y_{\text{origin}} + m\left(y_{\text{end}} - y_{\text{origin}}\right), \tag{3.68}$$

$$z = z_{\text{origin}} + m\left(z_{\text{end}} - z_{\text{origin}}\right). \tag{3.69}$$

The centre of the sphere is at $P\left(x_{\text{sphere}}, y_{\text{sphere}}, z_{\text{sphere}}\right)$, with the radius, $r = \|\mathbf{n}\|$, described as follows:

$$\left(x - x_{\text{sphere}}\right)^2 + \left(y - y_{\text{sphere}}\right)^2 + \left(z - z_{\text{sphere}}\right)^2 = r^2 = \|\mathbf{n}\|^2. \tag{3.70}$$

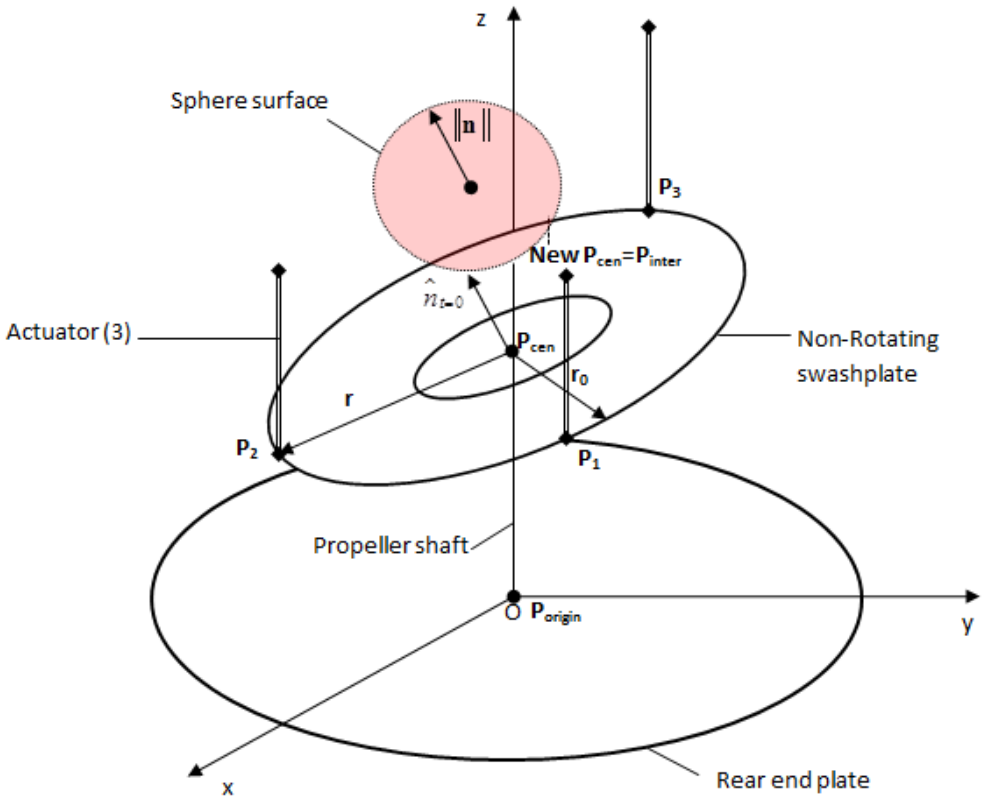

Figure 3.25. A sphere intersects an axis of the propeller shaft.

Substituting the equation of the line into the sphere equation gives a quadratic equation of the following form:

$$am^2 + bm + c = 0, \tag{3.71}$$

where

$$a = \left(x_{\text{end}} - x_{\text{origin}}\right)^2 + \left(y_{\text{end}} - y_{\text{origin}}\right)^2 + \left(z_{\text{end}} - z_{\text{origin}}\right)^2, \tag{3.72}$$

$$b = 2\begin{bmatrix}\left(x_{\text{end}} - x_{\text{origin}}\right)\left(x_{\text{origin}} - x_{\text{sphere}}\right) + \left(y_{\text{end}} - y_{\text{origin}}\right)\left(y_{\text{origin}} - y_{\text{sphere}}\right)\ldots \\ + \left(z_{\text{end}} - z_{\text{origin}}\right)\left(z_{\text{origin}} - z_{\text{sphere}}\right)\end{bmatrix} \tag{3.73}$$

$$\begin{aligned} c = {} & x_{\text{sphere}}^2 + y_{\text{sphere}}^2 + z_{\text{sphere}}^2 + x_{\text{origin}}^2 + y_{\text{origin}}^2 + z_{\text{origin}}^2 \ldots \\ & -2\left[x_{\text{sphere}}x_{\text{origin}} + y_{\text{sphere}}y_{\text{origin}} + z_{\text{sphere}}z_{\text{origin}}\right] - r^2 \end{aligned} . \tag{3.74}$$

Solve equation (3.71) by using the following:

$$m = \frac{-b \pm \sqrt{b^2 - 4ac}}{2a}. \tag{3.75}$$

The value in the square root in equation (3.75) is as follows:

$$i = b^2 - 4ac \,. \tag{3.76}$$

The number of intersection points can be acquired by considering the solution to equation (3.76) as follows:

If the value of i is less than 0, then there is not any intersection.

If the value of i equals 0, then there is a single intersection.

If the value of i is more than 0, then there are two intersections.

After acquiring *m* values, the value of *m* is substituted into equations (3.67), (3.68), and (3.69) to solve for the position of the intersection or the value of P_{inter}. If there are two intersection points, solve for P_{inter1} and P_{inter2}. Furthermore, select the real centre point of the swash plate by considering the *z* component of P_{inter1} and P_{inter2}. The position that has *z* component closer to the origin (0, 0, 0) is to be selected.

The equation of the plane that represents the swash plate can be determined by using a component of the normal vector of the swash-plate plane as follows:

$$\mathbf{n}_{\text{swash plate}} = \overrightarrow{P_{\text{inter}} P_{\text{sphere}}} = \left(x_{\text{sphere}} - x_{\text{inter}}, y_{\text{sphere}} - y_{\text{inter}}, z_{\text{sphere}} - z_{\text{inter}} \right), \tag{3.77}$$

$$\mathbf{n}_{\text{swash plate}} = \left(a_{\text{swash plate}}, b_{\text{swash plate}}, c_{\text{swash plate}} \right). \tag{3.78}$$

Substituting components of the normal vector into the general plane equation, the equation for the plane of the swash plate can be acquired as follows:

$$\text{plane}_{\text{swash plate}} = \begin{pmatrix} a_{\text{swash plate}} \left(x - x_0 \right) + b_{\text{swash plate}} \left(y - y_0 \right) \ldots \\ + c_{\text{swash plate}} \left(z - z_0 \right) \end{pmatrix}. \tag{3.79}$$

The determination of the circle equation of the swash plate plane can be completed by using equation (3.80). The results of the equation will be used for the determination of the total length of each actuator.

$$\mathbf{P_i} \left(\phi_{ai} \right) = r\cos\left(\phi_{ai} \right) \cdot \mathbf{U} + r\sin\left(\phi_{ai} \right) \cdot \mathbf{V} + \mathbf{C}, \tag{3.80}$$

where ϕ_{a_i} is the phase angle for each blade, which can be defined by using equation (3.28); $\mathbf{P}_i$ is the position of each end point of the actuator on the swash plate plane; $\mathbf{C}$ is the position of a centre point of the swash plate, which has been determined from the previous section; $\mathbf{W}_{\text{swash plate}} = \hat{\mathbf{n}}_{\text{swash plate}}$ (a unit normal vector of the swash plate plane, which is from equation (3.77); $\mathbf{U}$ is a unit vector from the centre of the circle to any point on the circumference, $\mathbf{U} = \mathbf{W}_{\text{swash plate}} \times \hat{i}$ or $\mathbf{W}_{\text{swash plate}} \times \hat{j}$ if the angle $\mathbf{W}_{\text{swash plate}}$ is parallel to $\hat{i}$; $\mathbf{V}$ is a unit vector from the centre of the circle to any point on the circumference, $\mathbf{V} = \mathbf{W}_{\text{swash plate}} \times \mathbf{U}$; and *r* is a radius of the swash plate.

3.7.3 Determination of the Total Length of Each Actuator

By rearranging equation (3.24), the total length of each actuator can be obtained using equation (3.81). The results of equation (3.81) will be used as a feedback signal to the actuator control block as follows:

$$R_{i2} = R_{i3} - R_{i4} - R_{i1} - L \cdot \left\| \mathbf{n} \right\|, \tag{3.81}$$

where R_{i1} is the position of an actuator i; R_{i2} is the total length of each actuator; R_{i3} is the position of a tip actuator on the rotating swash plate plane, $\mathbf{P_i}(\mathbf{t})$, which is from equation (3.80); R_{i4} is a position of a front end plate; $\left\| \mathbf{n} \right\|$ is a unit normal vector of the nonrotating swash plate; and L is a distance from the centre of rotating swash plate plane to the centre of nonrotating swash plate plane.

3.7.4 Transition Path of the Changing Orientation of the Swash Plate

The transition path can be defined by using two positions and orientations of the swash plate: the first one is the old position and orientation of the swash plate and the new desired position and orientation of the swash plate as shown in Figure 3.23. The position and orientation of the swash plate can be defined by using the top end point of the normal vector of the swash plate, which is obtained using equation (3.65). The shortest path between the two points is a straight line. The parametric equation of the line passing the two points is described in matrix form as follows:

$$\mathbf{P}_{\text{top end\_target}}(t_i) = \begin{bmatrix} x_{\text{top end\_old}} + t_i(x_{\text{top end\_new}} - x_{\text{top end\_old}}) \\ y_{\text{top end\_old}} + t_i(\mathrm{y}_{\text{top end\_new}} - y_{\text{top end\_old}}) \\ z_{\text{top end\_old}} + t_i(\mathrm{z}_{\text{top end\_new}} - z_{\text{top end\_old}}) \end{bmatrix}. \tag{3.82}$$

3.7.5 Tracking Method

After the equation of the path of the top end point is acquired, the line can be divided into several shorter lines as desired. Each shorter line can be defined by substituting t_i into equation (3.82):

$$t_i = \frac{1}{N} i, i = (1, 2, 3, ..., N), \tag{3.83}$$

where N is the number of shorter lines and i is the order of target points.

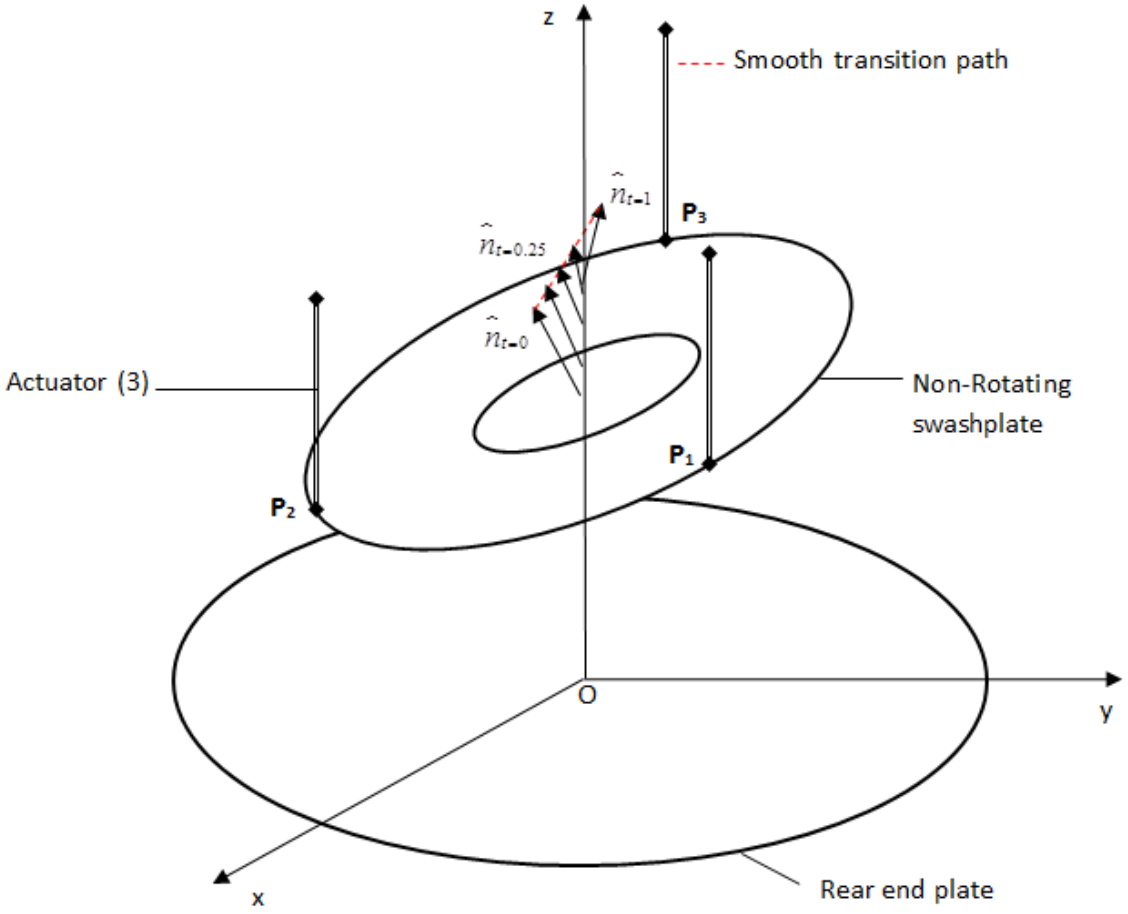

Figure 3.26. Tracking smooth path.

The target position of the top end point of the normal vector of the swash plate can be acquired from equation (3.82). The actuators must manipulate the position and orientation of the swash plate to reach the target points in order as shown in Figure 3.26. The position and orientation of the swash plate reach the target when the distance between the top end point and the target point is less than the desired error. In order to reach the final target point, the new target point is updated when the current top end point reaches the old target, and then the process repeats until the final target point is reached.

3.8 Computer Simulation Program of the CCPP Using LabVIEW

3.8.1 Diagram of Computer Simulation Program for Controlling the CCPP

A computer simulation program was implemented with LabVIEW. In the investigation of the CCPP dynamics, the simulation program was developed based on the block diagram as shown in Figure 3.27, in which there are two controllers. The rpm and blade angles were controlled by two modes: auto (closed loop) and man (open loop).

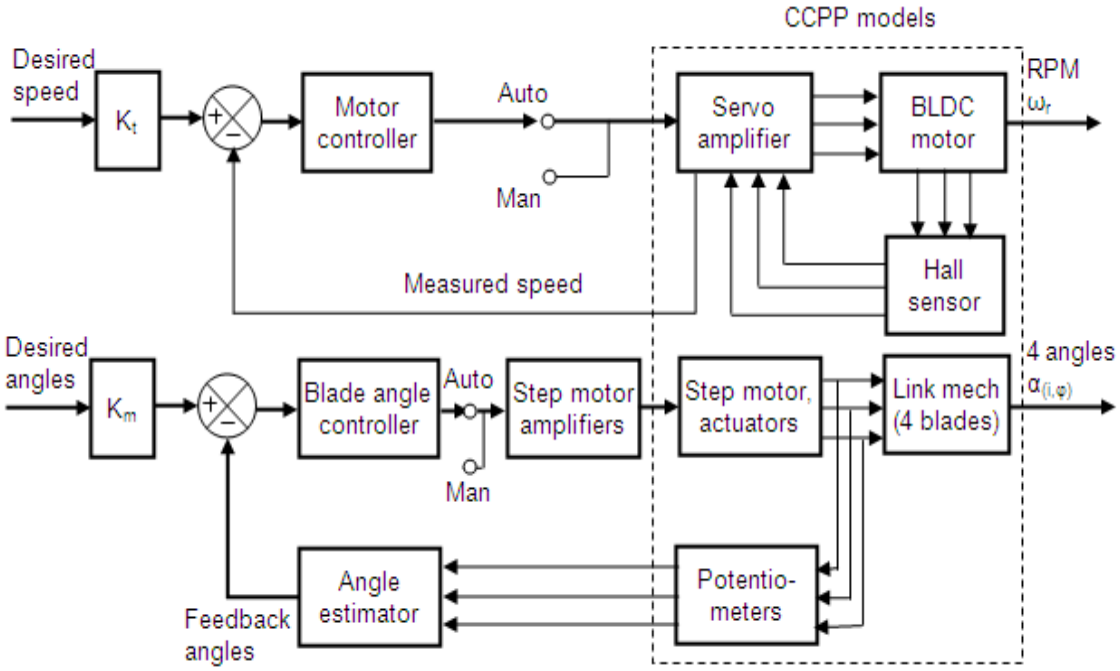

Figure 3.27. Block diagram of the simulation program.

In the simulation program, two controllers were designed based on the conventional PID control law:

$$u = K_{\mathrm{P}} e(t) + K_{\mathrm{I}} \int e(t)\,\mathrm{d}t + K_{\mathrm{D}} \frac{\mathrm{d}(t)}{\mathrm{d}t}, \qquad (3.84)$$

where e is error between the feedback signal and the desired signal.

3.8.2 Simulation Programs of Control System of the CCPP

The simulation program is divided into two main parts. The first part is for controlling the brushless DC motor. The objective of the simulation program for controlling the brushless motor was to study the dynamics and also the steady-state performance at various loading conditions. The main user interface of the simulation program is given in Figure 3.28. There were six inputs, which could be assigned: the load torque, the moment of inertia, the sampling rate, the reference speed of the motor, the reference current, and the motor and drive parameters. The load torque is from the calculating performance of the CCPP. There were also several outputs, including the total electromagnetic torque, the current motor speed, an electrical position of the rotor, phase voltages, phase current, and phase back emf. Figure 3.29 shows simulated results of controlling the shaft speed.

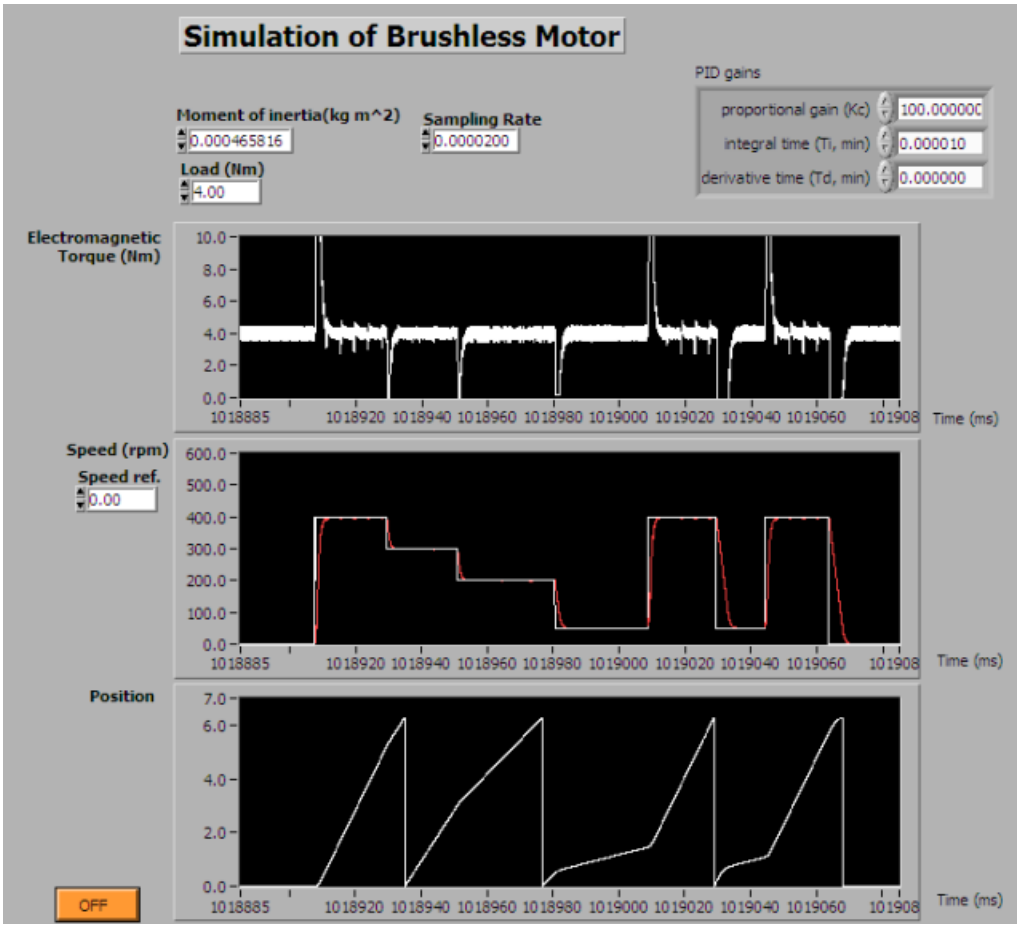

Figure 3.28. The main user interface of the main motor simulation.

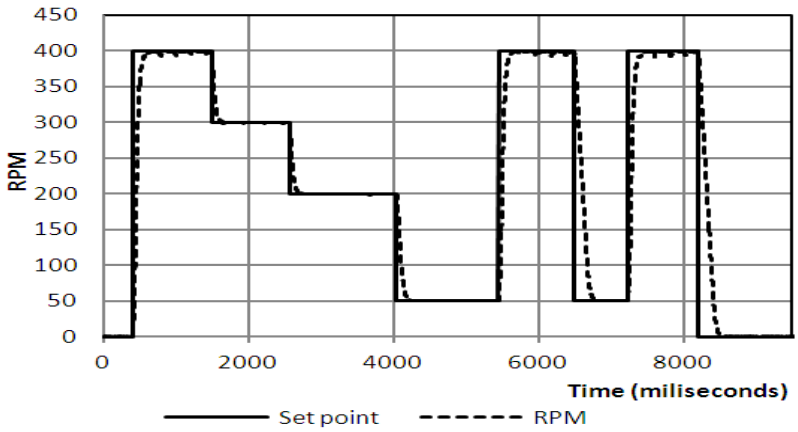

Figure 3.29. The result of the automatic RPM control.

The second part of the simulation is for controlling the pitch angle. The objectives were to study an algorithm of the control program and to use the estimated pitch angle to feed into the performance prediction program. The program can simulate automatic and manual control of the propeller pitch. The main user interface of the pitch control part is given in Figure 3.30. Figure 3.31 shows a result of automatic pitch control for a collective pitch angle of 29° and cyclic pitch angles of –20° and 0°.

Furthermore, the pitch control part in the simulation program also allows the operator to adjust the speed of the actuator. The adjustment of the speed of the actuator is implemented by changing the pulse rate, the sampling rate, and the resolution. The simulation program in the pitch control pad allows the operator to manually manoeuvre each actuator control.

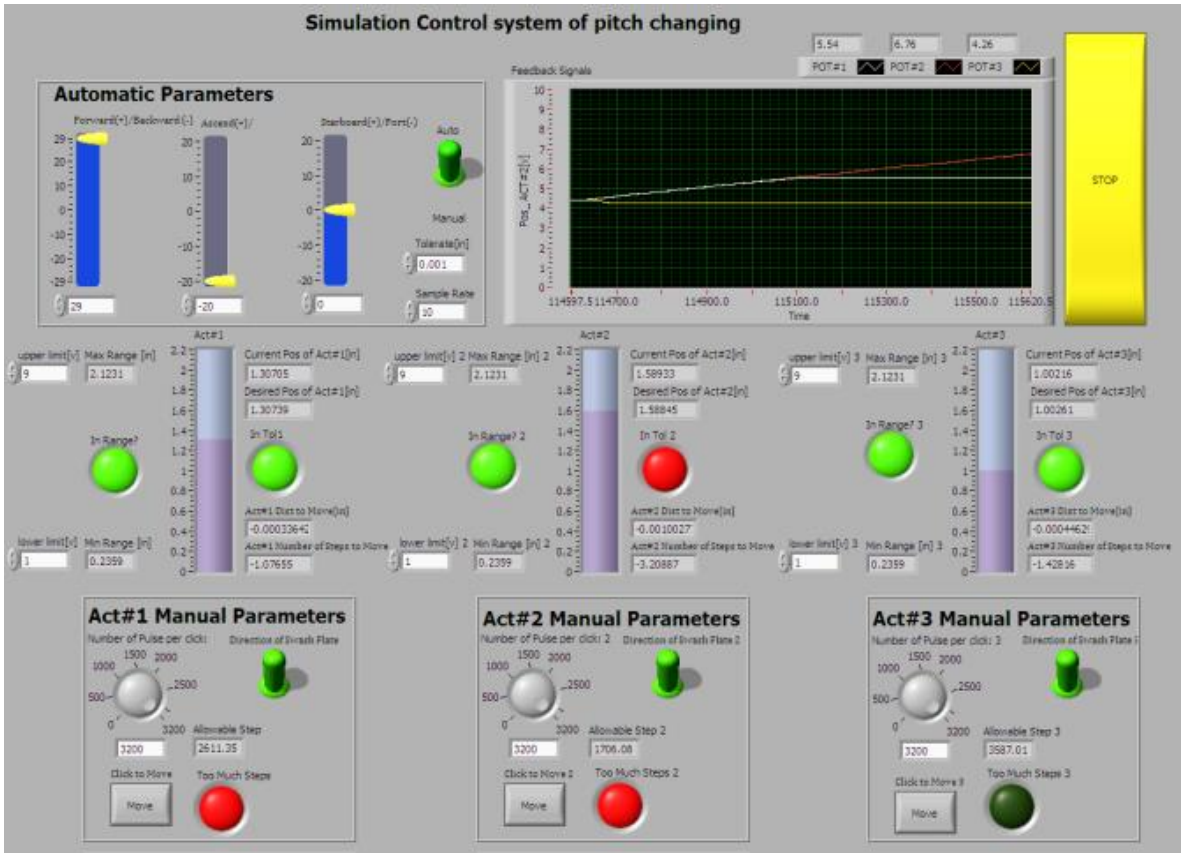

Figure 3.30. The main user interface of the pitch control simulation.

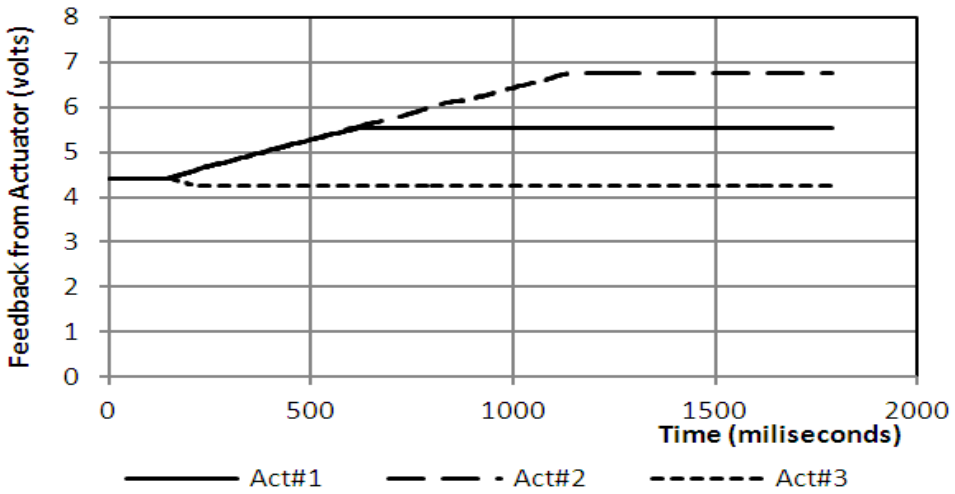

Figure 3.31. The result of automatic pitch control for a pitch setting of 29° collective pitch and –20° cyclic pitch.

The CCPP does not have an internal device to measure the pitch angle directly. However, the pitch angle at any angular position can be estimated by using the kinematic model of the mechanism and the relationship between the pitch angle and the displacement of the actuators. In this research, the pitch angles of each blade at various pitch settings were measured by a digitizer. The details and the procedure of measuring the pitch angle of the CCPP are presented in Appendix A1. The comparison results between the estimation of pitch angle and the measured pitch angle are shown in Figures 3.32 and 3.33. The estimated pitch angle is slightly different from the measured pitch angle. The input parameters of the kinematic model were measured from the virtual 3-D model of the CCPP. The different dimension of each component in the virtual 3-D model and the real CCPP is the cause of difference of estimated pitch angle to the measured pitch angle.

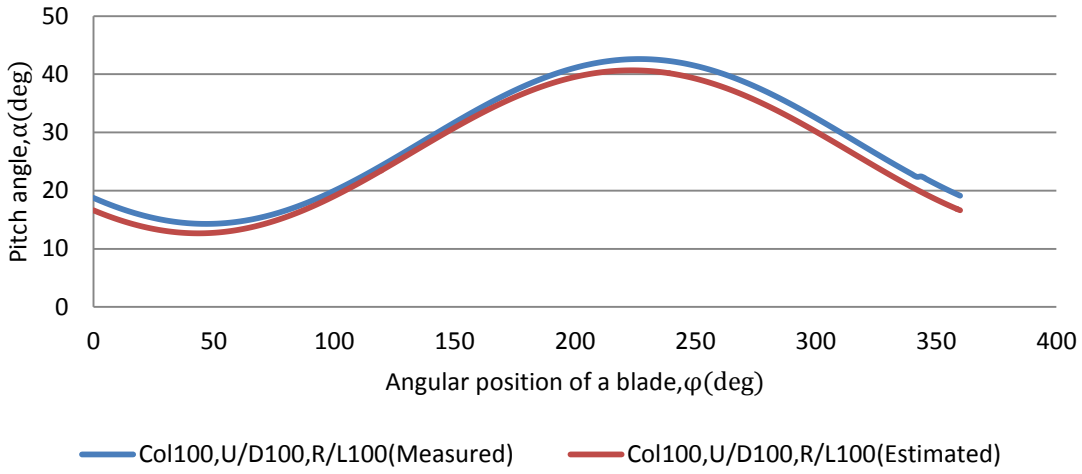

Figure 3.32. The comparison between the estimated pitch angles and the measure pitch angles: the collective pitch setting = 100%, the cyclic pitch setting (up/down) = 100%, and the cyclic pitch setting (right/left) = 100%.

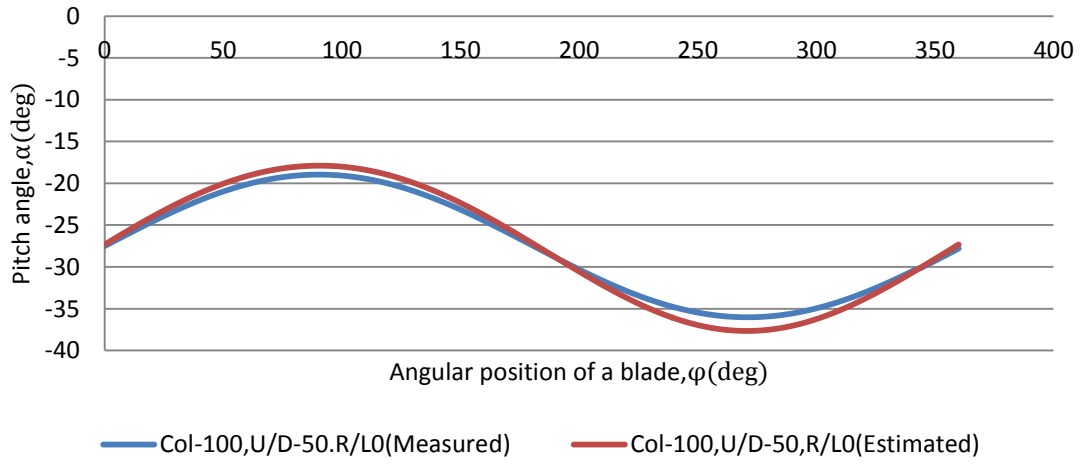

Figure 3.33. The comparison between the estimated pitch angles and the measure pitch angles: the collective pitch setting = –100%, the cyclic pitch setting (up/down) = –50%, and the cyclic pitch setting (right/left) =0%.

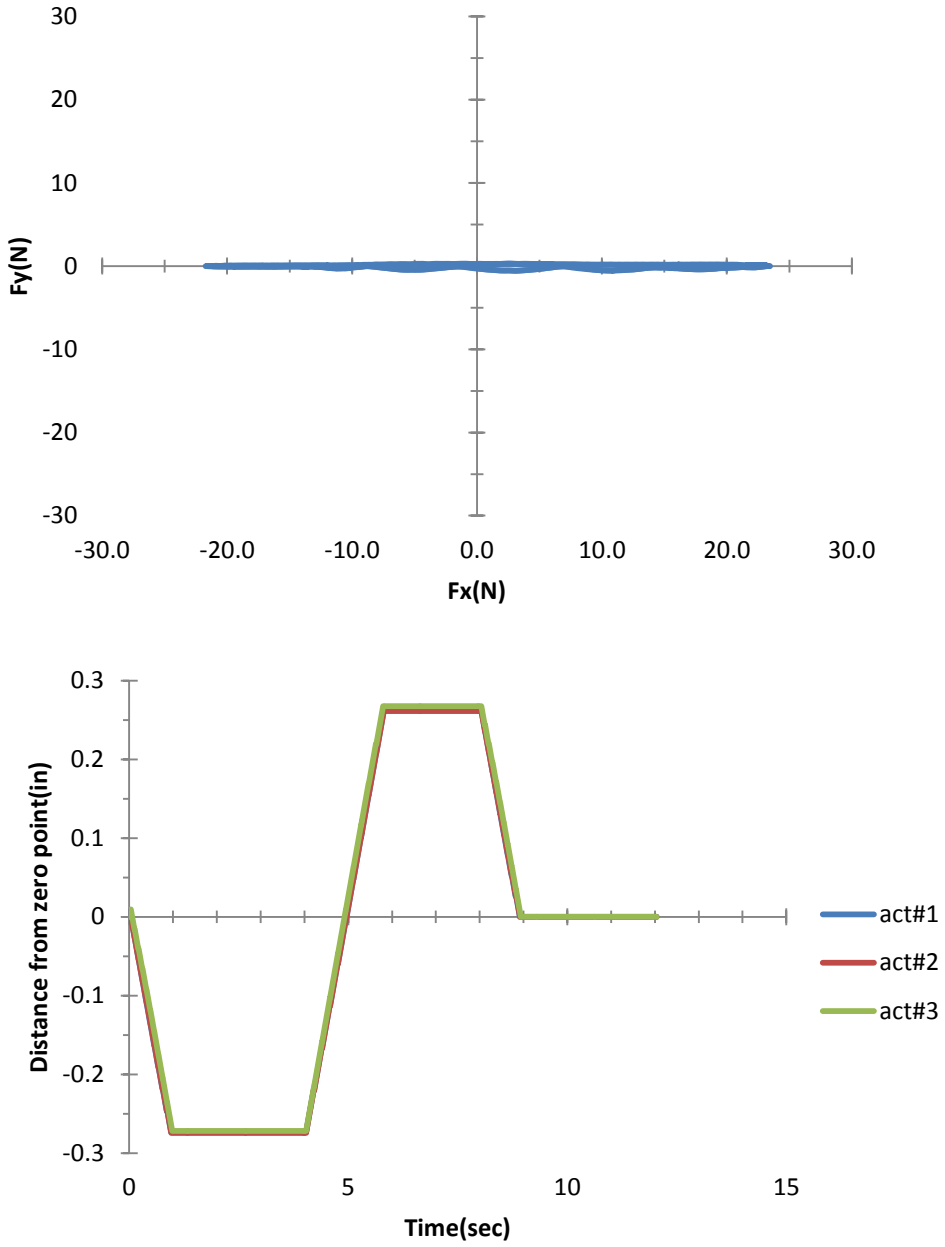

Figure 3.34. The simulated results of the program with the tracking capability and the profile of the pitch setting starting from the collective pitch at 0% → 100% → –100% → 0%.

The implemented simulation program for the pitch angle control was also able to track the position and orientation of the swash plate. Because of the tracking capability, the simulation program can control the direction of the generated thrust. The paths of the thrust direction at various pitch angle settings were simulated. The simulated results showed the benefit of the tracking capability. The simulated results with the tracking capability and without the tracking capability are shown in Figures 3.34–3.39. Figures 3.34 and 3.35 show the results of the changing collective pitch angle setting (0% → 100% → –100% → 0%). Comparing these two figures, the paths of the thrust direction of both figures are slightly different. Both figures show the change in the thrust direction from a straight line in the *x* direction.

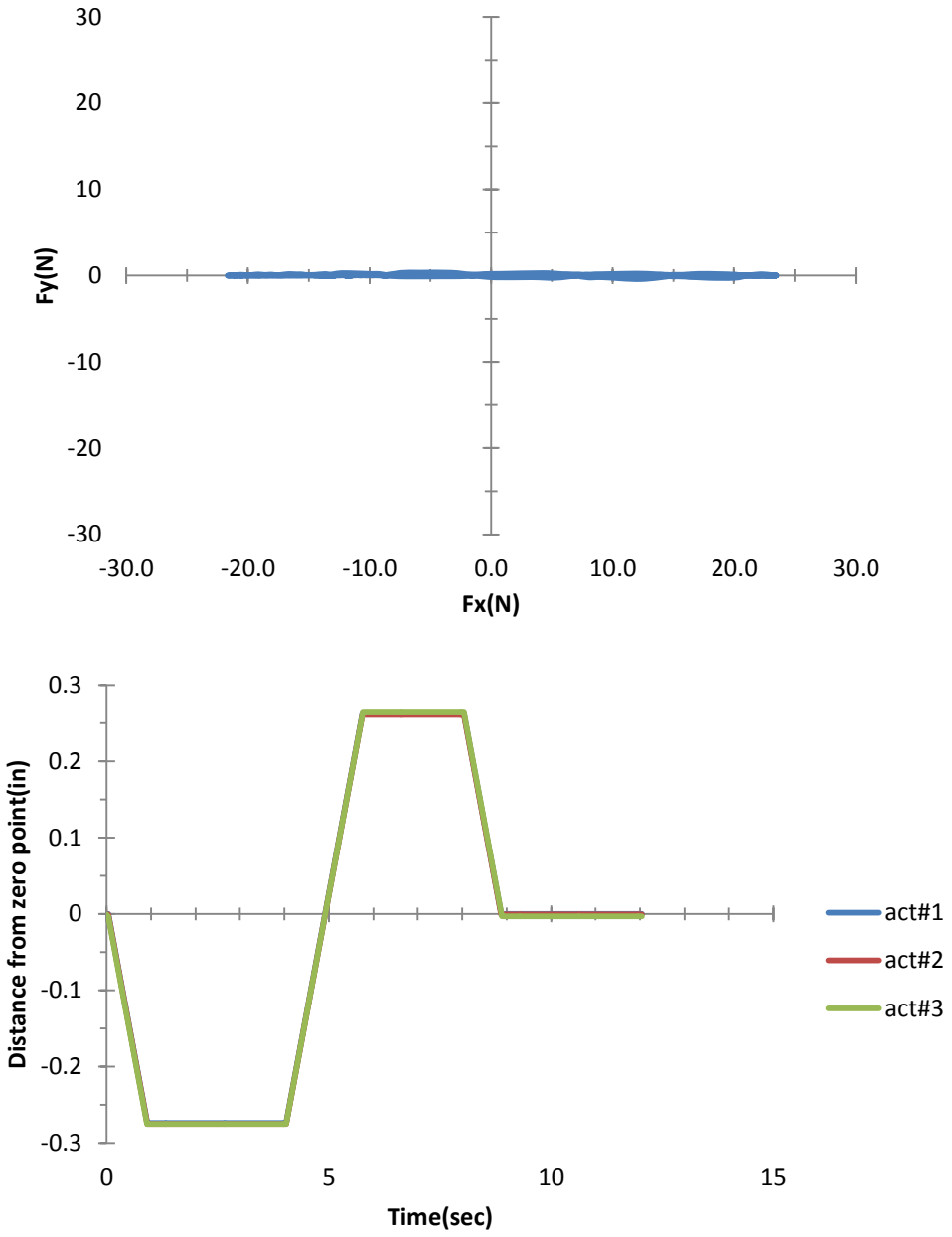

Figure 3.35. The simulated results of the program without the tracking capability and the profile of the pitch setting starting from the collective pitch at 0% → 100% → –100% → 0%.

The simulated result with the tracking capability of changing collective pitch does not show any advantage. However, the simulated results of changing cyclic pitch show the benefit of adding the tracking capability into the simulation program as shown in Figures 3.36 and 3.37. The simulated results in both figures are for changing the up/down cyclic pitch setting, which starts from at 0% → 50% → –50% → 0%. The simulated result of the program with the tracking capability showed that the path of the thrust direction was a straight line and on the vertical axis (*z* direction). In contrast, the result of the program without the tracking capability showed that the thrust direction only moved vertically while changing cyclic pitch setting from 0% to 50% and from –50% to 0%. The thrust direction moved sideways while changing

cyclic pitch setting from 50% to –50%. The sideways movement of the thrust direction could cause the underwater vehicle to move sideways as well. The simulated result of movement of the actuators showed that the actuators reach the target position faster for the program without the tracking capability.

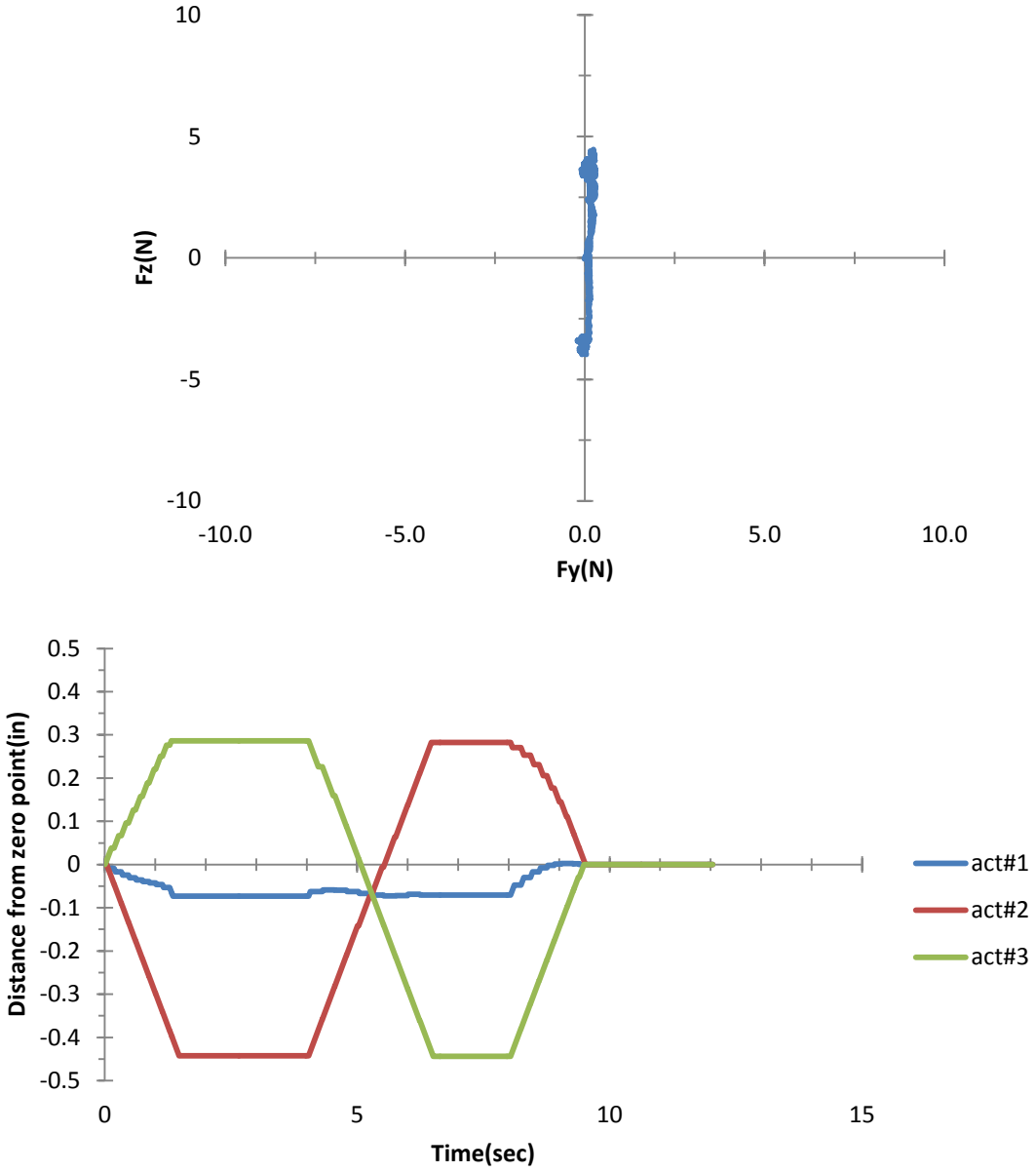

Figure 3.36. The simulated results of the program with the tracking capability and the profile of the pitch setting starting from up/down cyclic pitch at 0% → 50% → –50% → 0%.

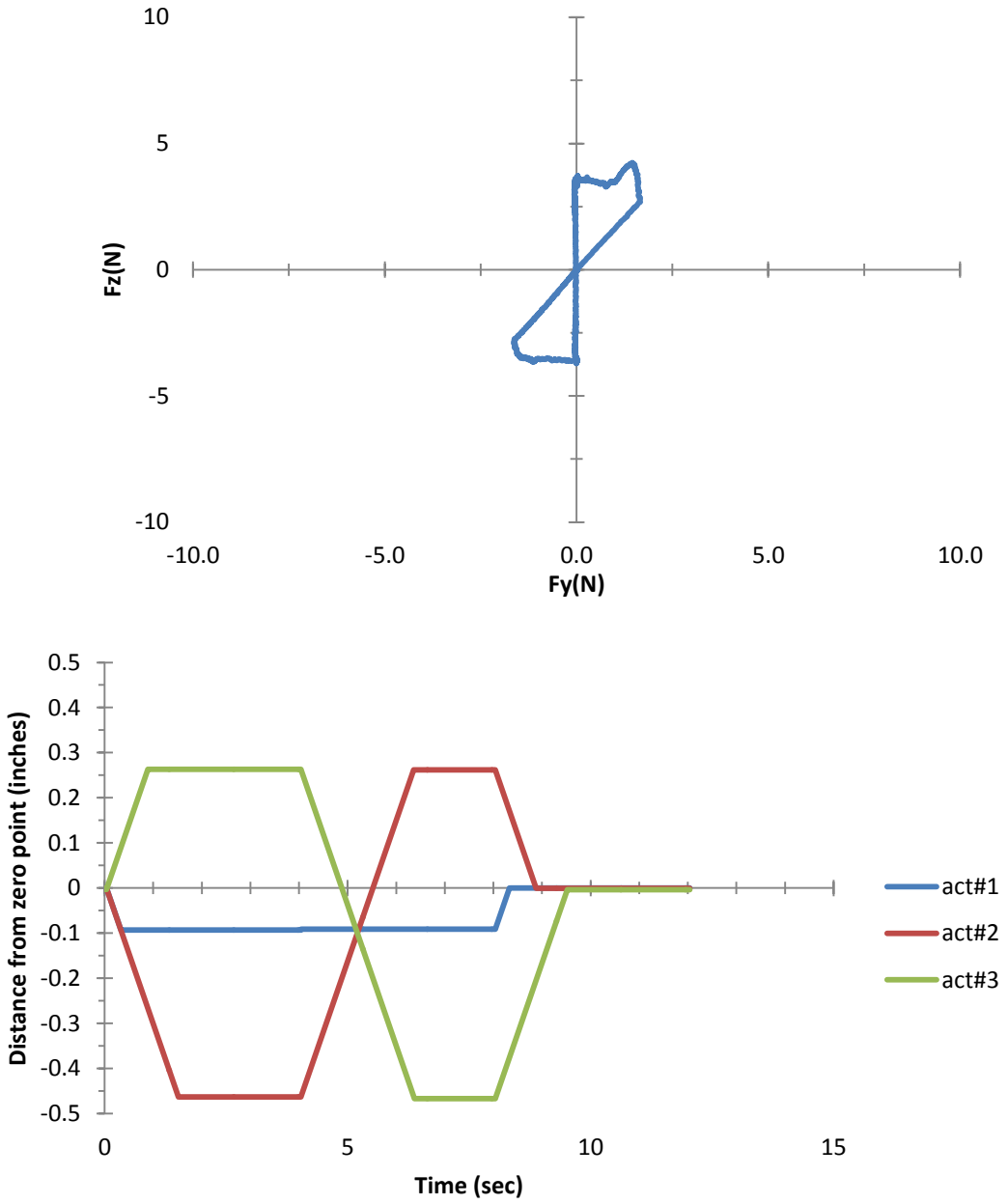

Figure 3.37. The simulated results of the program without the tracking capability and the profile of the pitch setting starting from the up/down cyclic pitch at 0% → 50% → –50% → 0%.

The simulated results in Figures 3.38 and 3.39 are a combination of the up/down cyclic pitch setting and the right/left cyclic pitch setting. Cyclic pitch setting started changing right/left cyclic pitch setting from 0% → 50% → –50% → 0% with a combination of up/down pitch from 0% → 50% → 50% → 0%. The simulated result of the program with the tracking capability showed that the path of the thrust direction was a semicircle when the right/left cyclic pitch setting was changed from 50% to –50%. In contrast, the result of the program without the tracking capability showed that the thrust direction moved randomly while changing the right/left cyclic pitch setting from 50% to –50%. The thrust direction moved

sideways while changing cyclic pitch setting from 50% to –50%. The random movement of the thrust direction could cause instability of the underwater vehicle.

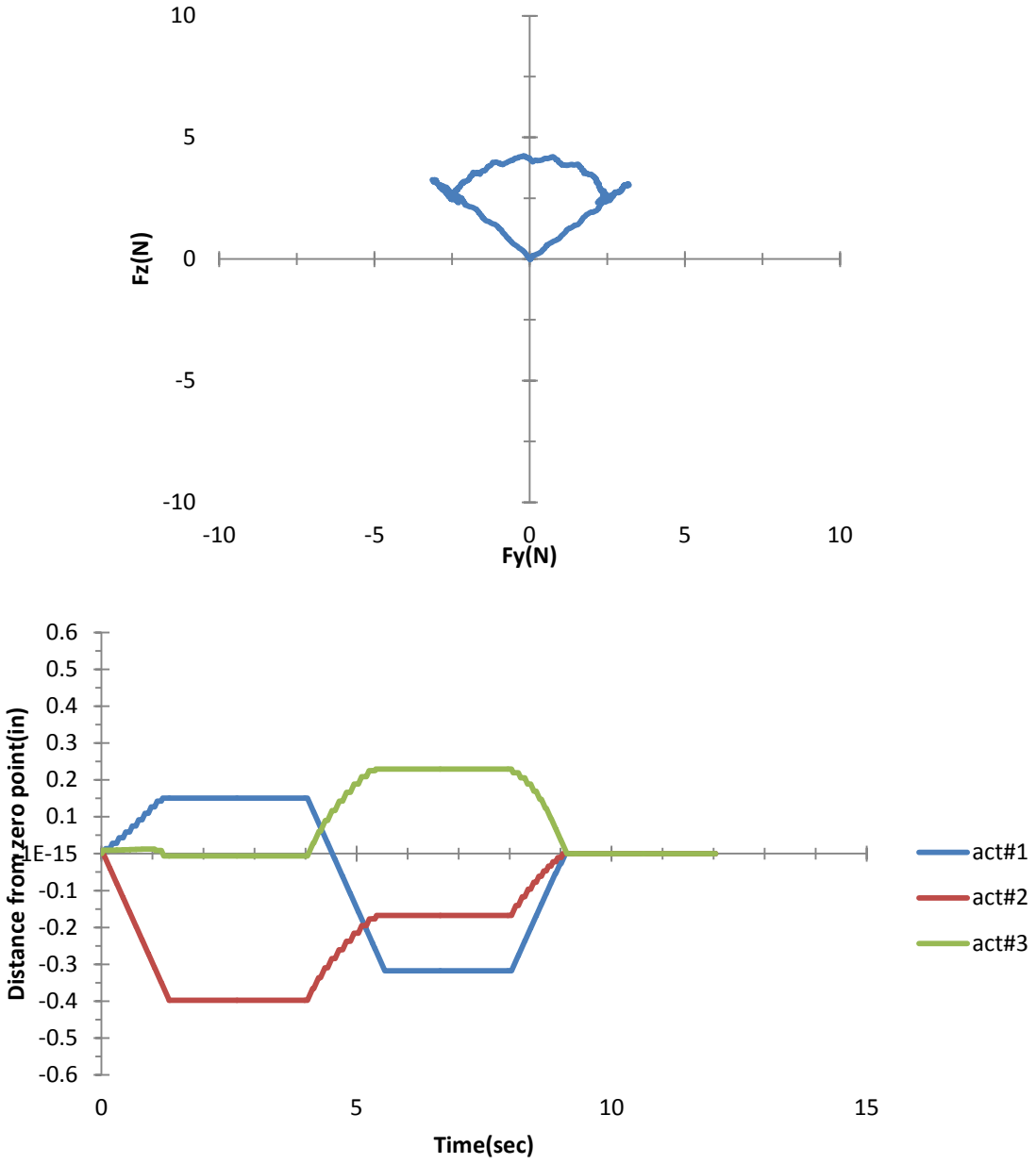

Figure 3.38. The simulated results of the program with the tracking capability and the profile of the pitch setting of the right/left cyclic pitch from 0% → 50% → –50% → 0% with a combination of the up/down cyclic pitch from 0% → 50% → 50% → 0%.

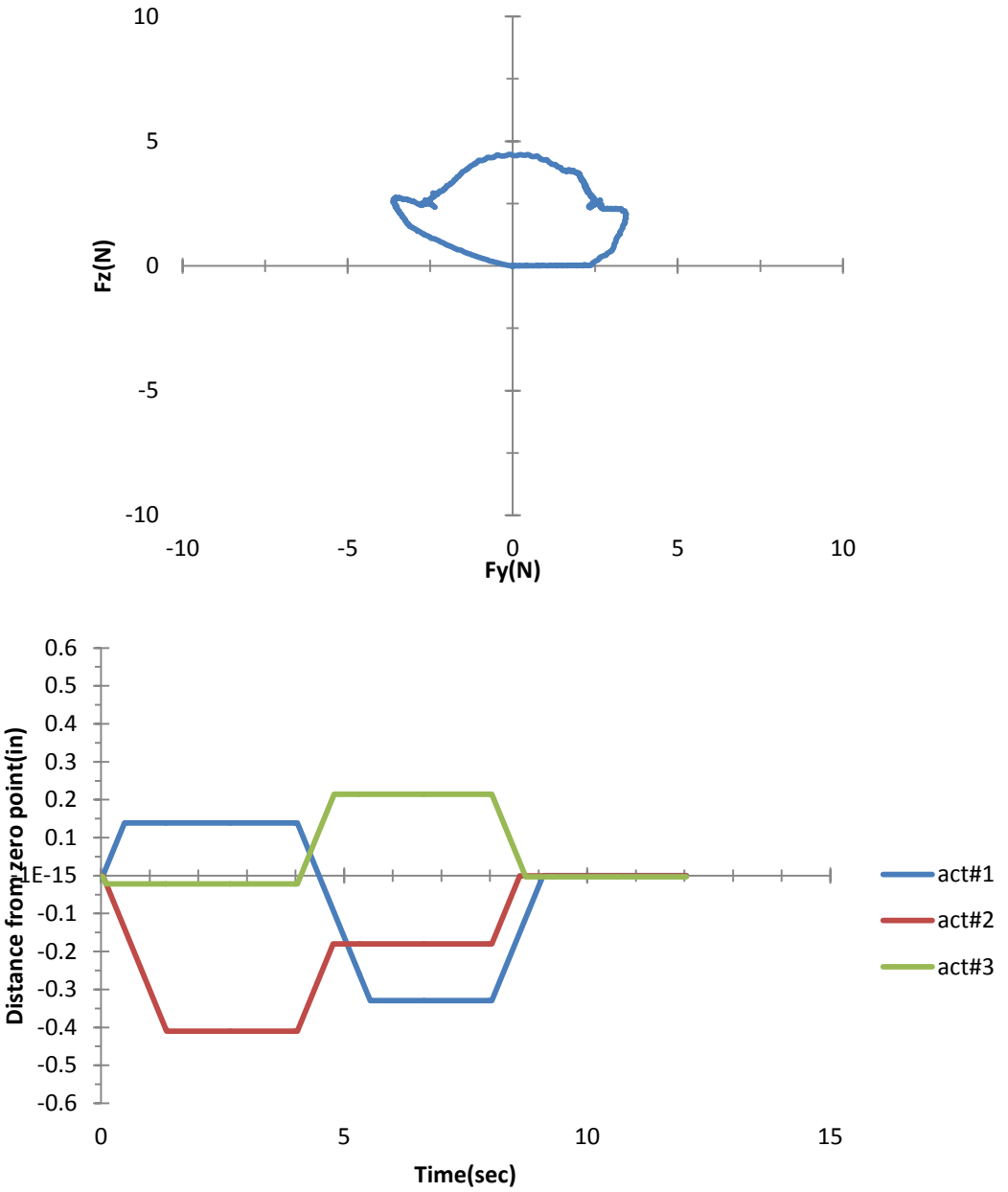

Figure 3.39. The simulated results of the program without the tracking capability and the profile of the pitch setting of the right/left cyclic pitch from 0% → 50% → –50% → 0% with a combination of the up/down cyclic pitch from 0% → 50% → 50% → 0%.

The tracking capability of the simulation program can be developed further. As mentioned in the kinematic model section, the current tracking function generated the shortest straight-line path to guide the movement of the swash plate. A possible future tracking function is to use a combination of multiple straight lines as the tracking path for the swash plate. With new tracking capability, control of the thrust direction will be more flexible. For instance, the thrust can be reduced to zero before changing its direction.

3.9 Control Program of the Real CCPP

The objective of the program was to control the collective and cyclic pitch propeller. The program was divided into two parts. The first part was to control the angle of the propeller. Controlling the angle of the propeller blades can be done manually or automatically. Manual control was implemented by setting the number of pulses to be sent to each actuator and the moving direction of each actuator. The current position of each actuator was measured by the linear potentiometer. The automatic control system utilized the on-off control method with the feedback signals from the linear potentiometers. A toggle switch was used to switch the manual system to an automatic system. The manipulation of the angles of the propeller blade can be done by simply changing the setting value of the slide bars. The first slide bar was for changing the angle of all propeller blades simultaneously. This slide bar was used to command the propeller to generate the forward or backward thrusts. The other two slide bars were to control the side thrusts. One slide was for changing the thrust vector vertically. Another one was for changing the thrust vector horizontally. The user interface window on the angle control program is given in Figure 3.40.

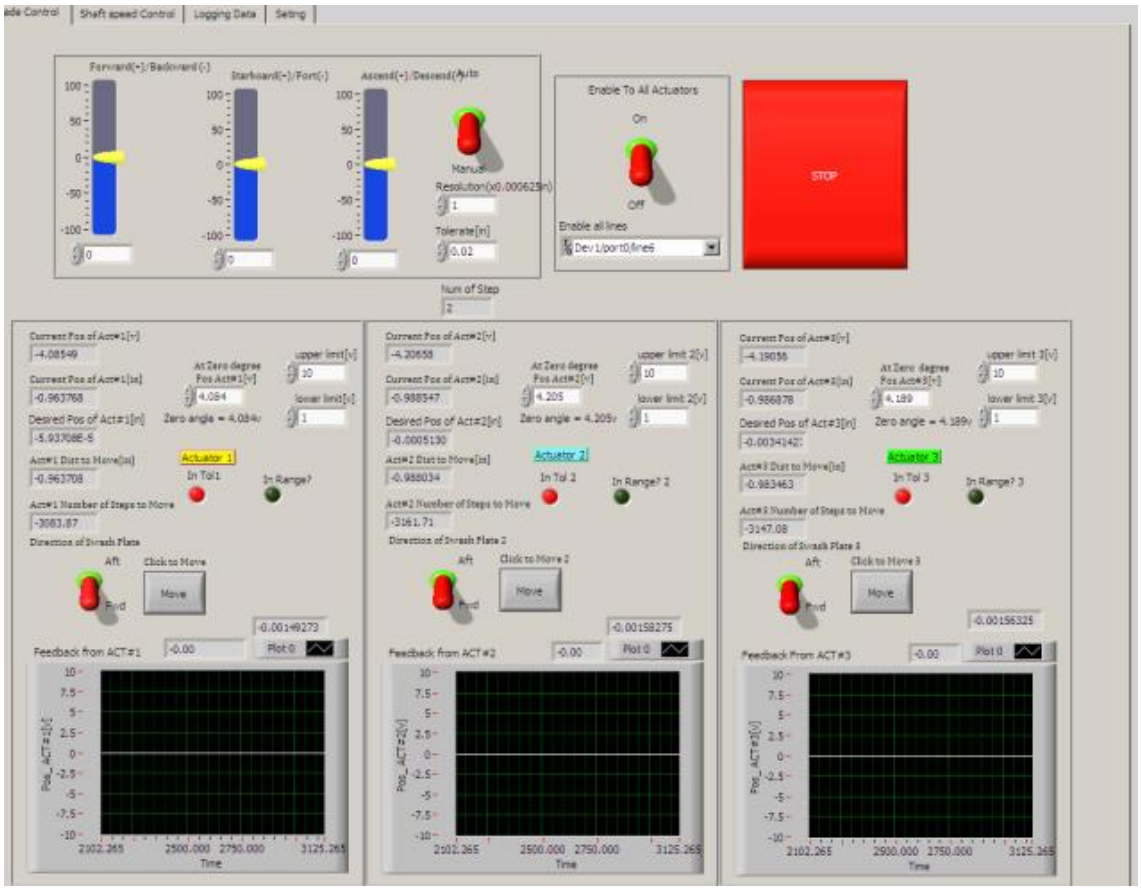

Figure 3.40. The user interface window of the pitch control program.

The second part of the program was for controlling the speed of the main motor. The motor could be controlled manually or automatically. Controlling the motor manually was undertaken by turning the knob to adjust the value of the reference voltage at the brushless servo amplifier. The range of the reference voltage is from 0 to 10 V. The PID control

method was selected for automatically controlling the speed of the motor. The feedback signal was from the hall-effect sensors. The operator could adjust the desired speed. The user interface window of the speed control program is shown in Figure 3.41.

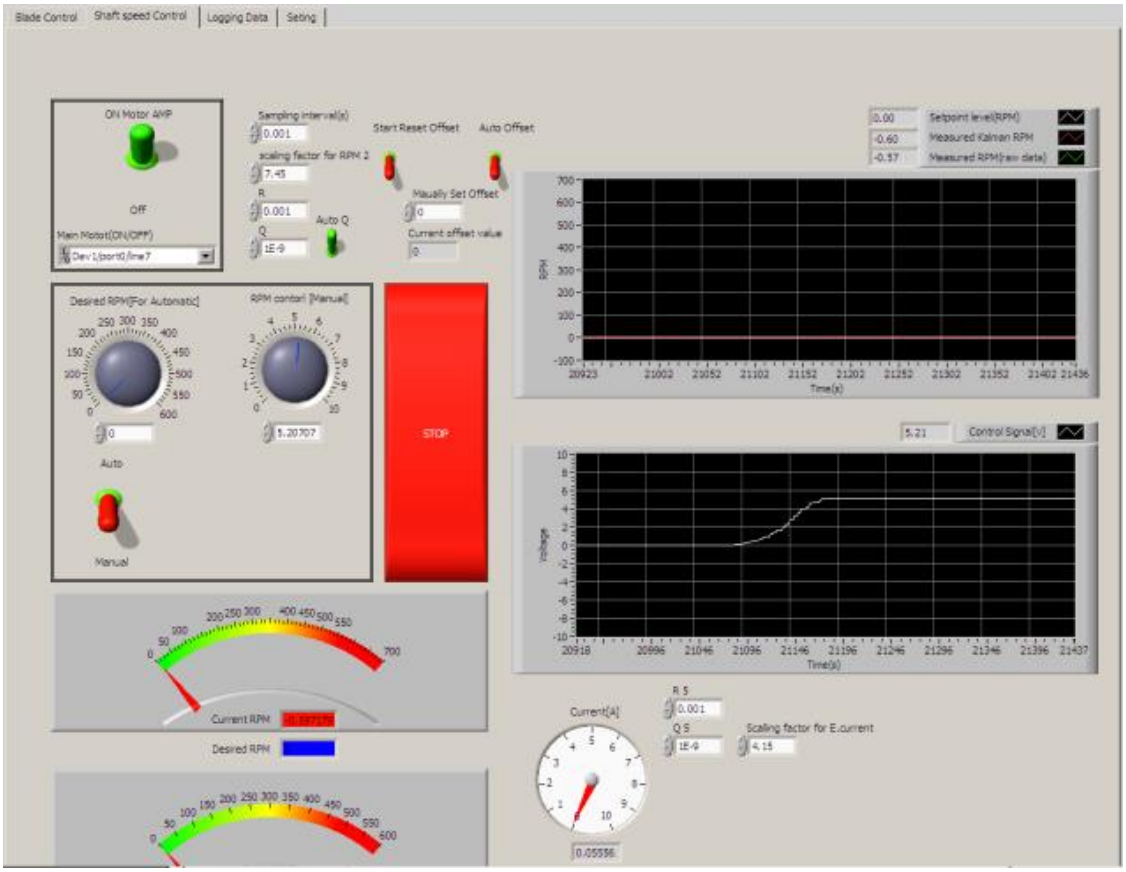

Figure 3.41. The user interface (Front Panel) window of the speed control program.

Chapter Summary

The simulation program for controlling a collective and cyclic pitch propeller was developed to control the pitch of the propeller blades and the RPM of the propeller shaft.

The relationship between pitch angles and the displacement of the actuators was established. The kinematics of the mechanism of the CCPP was modelled. Therefore, the simulation of the pitch control was developed by using the kinematic model and the relationship between the pitch angles and the displacement of the actuators. The simulation program for controlling pitch angle was included in the tracking function. The tracking function was based on the developmental kinematic model. The tracking function can guide the position and orientation of the swash plate. The simulation program with the tracking capability can reduce the random movement of the thrust direction. The program with tracking capability can also reduce the instability of the underwater vehicle.

The simulation of the brushless DC motor was also developed to estimate the electrical parameters such as the phase voltages, the phase current, and the back emf. The shaft velocity was successfully controlled with the PID control law.

Chapter 4 Experimentation

The collective and cyclic pitch propeller (CCPP) was designed to assist an underwater vehicle to perform complex manoeuvres at low speed. The CCPP was built in 2005. The built CCPP was only tested in order to demonstrate that the built CCPP could generate axial and side thrusts. In the test, the CCPP was tested in a bollard pull condition without any underwater vehicle body or fairing. That study did not represent the performance of the CCPP. As discussed in Chapter 1, the uncertainty of the performance of the CCPP was still unknown. In addition, the basic control system and the many uncertainties of the hydrodynamic characteristics of the CCPP may cause the underwater vehicle to be uncontrollable. Therefore, the true performance of the CCPP must be assessed. In this chapter, the true performance in a straight line of the CCPP behind an underwater vehicle is estimated empirically.

4.1 Test Objectives

The experiments had two primary objectives: to clarify many uncertainties of the hydrodynamic characteristics of the CCPP and to determine the true propulsion performance in a straight line of the CCPP behind an underwater vehicle at various conditions. The true performance of the CCPP behind a vehicle included the interaction between the vehicle and the CCPP, which affects the propulsive efficiency. Other secondary objectives were to improve the numerical prediction program and to improve the algorithm of the control system program by utilizing the experimental results.

4.2 Methods and Experiment

In order to clarify the uncertainties of the hydrodynamic characteristics of the CCPP, the performance in a straight line of the CCPP was assessed. The CCPP was attached behind an underwater vehicle. Then the performance measurements of the CCPP behind the vehicle were conducted by using a captive test. The captive test was selected because it is the simplest test, and it can assess the performance in a straight line of the propeller in various desired conditions. In addition, an ease of controlling independent variables was another reason of selecting the captive test.

The experiment was divided into three sections. The first test section was for a collective pitch setting only. In this test, the axial thrusts and torques were measured at various pitch angle settings and at various advance coefficients. The second test section was for a combination of a collective pitch, a cyclic pitch (up/down), and a cyclic pitch (right/left). In this test, the capability of the CCPP in terms of generating the transverse thrusts was assessed. Knowing this capability of the CCPP can indicate the limitation of the CCPP to manoeuvre an underwater vehicle. The third test section was a resistance test of the underwater vehicle. This test can be used to validate the hydrodynamic coefficients, which were mentioned in

chapter 2. The range of advance coefficients is presented in Table 4.1. The range of the pitch settings for each advance coefficient is shown in Table 4.2.

Table 4.1. Range of advance coefficients

Determine RPM for J values at various water speeds						
J v[m/s] →	0	0.25	0.5	0.75	1	1.25
0 ↓	300.00	N/A	N/A	N/A	N/A	N/A
0.1	N/A	490.20	980.39	1470.59	1960.78	2450.98
0.2	N/A	245.10	490.20	735.29	980.39	1225.49
0.3	N/A	163.40	326.80	490.20	653.59	816.99
0.4	N/A	122.55	245.10	367.65	490.20	612.75
0.5	N/A	98.04	196.08	294.12	392.16	490.20
0.6	N/A	81.70	163.40	245.10	326.80	408.50
0.7	N/A	70.03	140.06	210.08	280.11	350.14
0.8	N/A	61.27	122.55	183.82	245.10	306.37
0.9	N/A	54.47	108.93	163.40	217.86	272.33
1	N/A	49.02	98.04	147.06	196.08	245.10
1.1	N/A	44.56	89.13	133.69	178.25	222.82
1.2	N/A	40.85	81.70	122.55	163.40	204.25
1.3	N/A	37.71	75.41	113.12	150.83	188.54
1.4	N/A	35.01	70.03	105.04	140.06	175.07
1.5	N/A	32.68	65.36	98.04	130.72	163.40

Colour Code
Physical limit
Possible range
Selected RPM

Table 4.2. Range of the pitch settings for each advance coefficient.

Collective Pitch (%)	Up/Down Cyclic Pitch (%)	Left/Right Cyclic Pitch (%)
−100 (Not in the combined pitch setting tests)	−100 (Some extra tests)	−100 (Some extra tests)
−80	−80	−80
−60 (Not in the combined pitch setting tests)	−60 (Some extra tests)	−60 (Some extra tests)
−40	−40	−40
−20 (Not in the combined pitch setting tests)	−20 (Some extra tests)	−20 (Some extra tests)
0	0	0
+20 (Not in the combined pitch setting tests)	+20 (Some extra tests)	+20 (Some extra tests)
+40	+40	+40
+60 (Not in the combined pitch setting tests)	+60 (Some extra tests)	+60 (Some extra tests)
+80	+80	+80
+100 (Not in the combined pitch setting tests)	+100 (Some extra tests)	+100 (Some extra tests)

4.3 Facility

The experiment was conducted at the Towing Tank facility of the Australian Maritime College. The dimension of the tank is 100 m long and 3.55 m wide, with a maximum water depth of 1.5 m. The towing carriage speed has a maximum speed of 4.6 m/s. The test facility is shown in Figure 4.1.

Figure 4.1. Towing Tank facility of the Australian Maritime College, Launceston, Tasmania. The tested underwater vehicle was about to be installed to the big force balance.

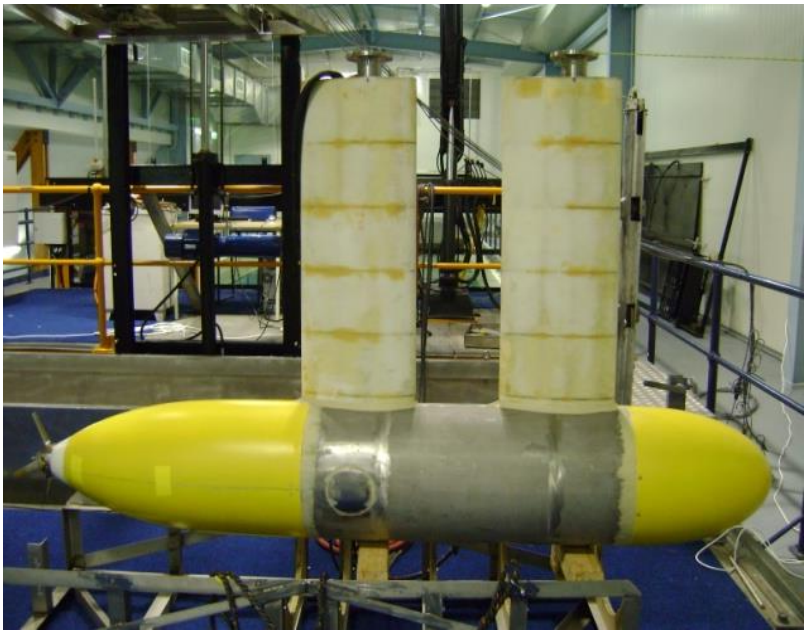

Figure 4.2. Photo of the tested underwater vehicle equipped with the collective and cyclic pitch propeller.

4.4 Instrumentation

4.4.1 Force Transducers

Two force balances were used in the experiment. The first one was a small 6-DOF force transducer, and the second one was a big 6-DOF force balance.

The small 6-DOF force transducer directly measured the propeller thrusts and torques. The small force transducer was calibrated over a range of 0 to 5 kg of thrust and 0 to 1.25 kgf·m.

The big force balance measured total forces acting on the underwater vehicle, including the resistance and the thrusts generated by the CCPP. The resistance data need to be separated from the measured forces in order to acquire only the thrusts and torques generated by the CCPP. However, the uncertainty of the performance data from the big force balance was large.Measuring the generated thrust and torque by the big force balance was indirect. The number of uncertainty sources increased. For instant, the uncertainty sorces of the resistance test of the underwater vehicle need to be included. Furthermore, measuring thrust and torque of the propeller by using the big force balance, the test must be conducted at least two times in the same condition. Therefore, the thrust and torque measurements were performed using the small force transducer. The big force balance was calibrated over a range of 0 to 7 kg. The calibrations of both devices were checked after the completion of experiments in order to confirm the repeatability of the data.

4.4.2 Speed Probes

The speed of the propeller shaft was measured by three hall-effect sensors, which were attached to the main motor. The shaft speed sensor was calibrated by using the optical tachometer. The speed of the vehicle was taken as the speed of the carriage. The speed of the carriage could be set on the carriage. The speed of the carriage was varied according to the desired advance coefficients.

4.4.3 Data Acquisition

Two DAQ systems were used. The first DAQ was a carriage-borne system used to acquire the signals from the force transducers and the carriage speed. The second DAQ was used to capture the shaft speed and the pitch angle setting. Data from both DAQ systems were saved on a computer running a LabVIEW program. A DAQ program was specifically developed by using LabVIEW. Sample rates were set to 100 Hz for the small force transducer and to 2,000 Hz for the big force balance, the shaft speed, and the carriage speed. The measured forces from each measurement device were averaged at the end of recording, and then it was subtracted from the no-load condition.

4.5 Experimental Setup

The big force balance was attached onto the carriage. The top ends of two steel pipes were fastened to the attachment points of the big force balance. The bottom ends of the two steel

pipes were clamped onto the underwater vehicle. The two steel pipes were covered with the hydrofoil-shaped fairing in order to prevent unsteady flow forward to the propeller. The small force transducer was attached between the middle vehicle body and the CCPP unit as shown in Figure 4.5. The small force transducer was installed in a housing to prevent any damage from water ingress. The tail fairing was built to prevent unsteady flow forward to the propeller. The CCPP unit was covered within the tail fairing. In addition, the tail fairing was used to ensure that the small force transducer measured the forces from the CCPP only, not the forces from the water flow strike against the CCPP unit. The centre of the underwater vehicle was 0.9 m below the water surface. The layout of the experimental setup is shown in Figures 4.3–4.5.

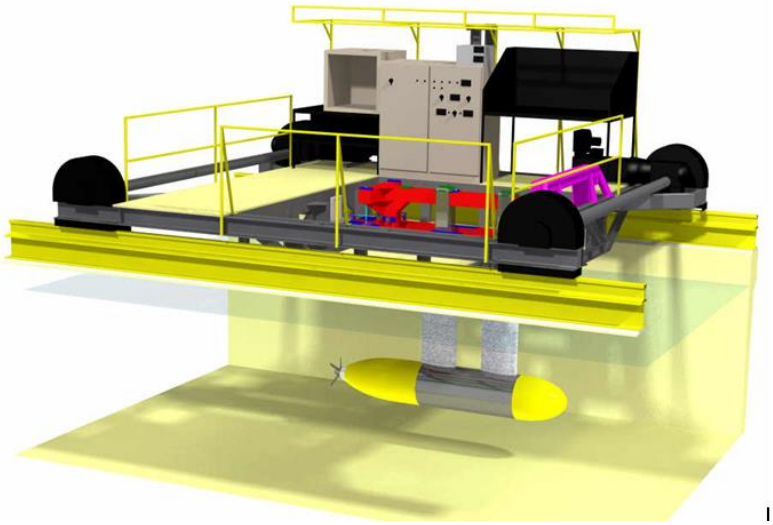

Figure 4.3. Setup configuration of the experiment in 3-D.

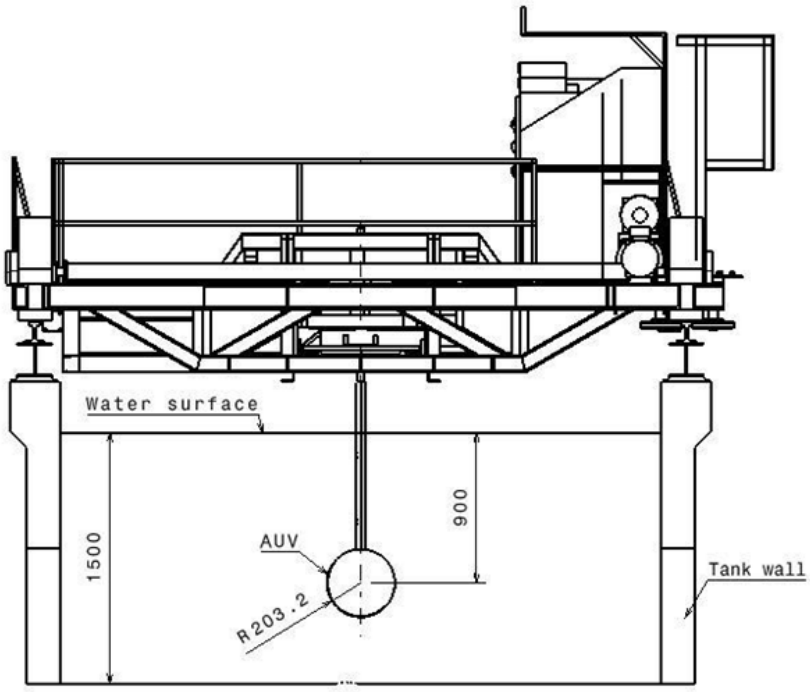

Figure 4.4. Setup configuration, front view.

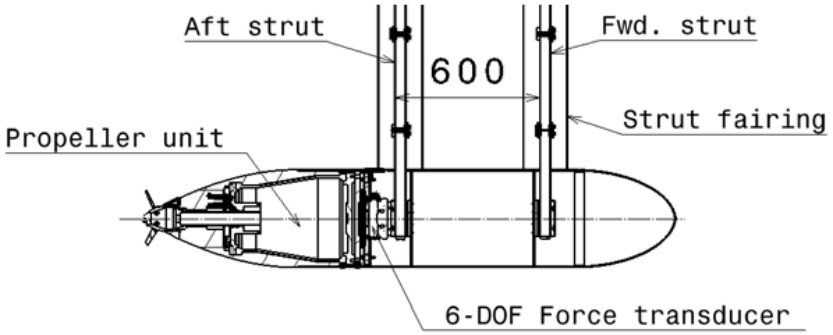

Figure 4.5. Setup configuration, cross-sectional view.

4.6 Experimental Procedure

4.6.1 Propulsion Tests

Each condition was established by setting the speed of the carriage and propeller RPM to achieve a desired advance coefficient. The propeller pitch was set to the desired parameter. At the beginning of each test run, the data of no-load conditions of each measurement device were recorded. After that, the speed of the propeller shaft was ramped up to a desired RPM. Then the carriage was accelerated to the desired speed. When the speed of the carriage was constant, the measurement devices began recording for 80 seconds. After each run, there was a break for 10 minutes to let the water settle down.

4.6.2 Resistance Tests

The speed of the carriage was set to desired values. The propeller blade was set to be in line with the water flow. At the beginning of each test run, the data of no-load conditions of each measurement device were recorded. The carriage was accelerated to the set speed. When the speed of the carriage was constant, the measurement devices began recording for 80 seconds. After each run, there was a break for 10 minutes to let the water settle down.

4.7 Experimental Results and Discussion

4.7.1 Results of Propulsion Tests

4.7.1.1 Collective Pitch Test

The thrust and the torque coefficients of the CCPP are presented as a function of the advance coefficient in Figures 4.6 and 4.7 for a positive collective pitch setting and a forward speed. In a condition of a negative collective pitch setting and a forward speed, Figures 4.8 and 4.9 present the thrust and the torque coefficients, respectively. The pitch angle setting was a percentage of the maximum pitch attainable as explained in Chapter 3 Section 3.2. The propeller with a positive collective pitch setting produces a lower thrust in comparison with the negative pitch because the hydrodynamic angle of attack of the propeller blades is smaller with a positive collective pitch setting. The torque of the positive collective pitch settings was larger than the torque of the negative pitch settings. The maximum torque occurred at +100%,

–100% collective pitch angle (+29°, –29°). The maximum torque was approximately 2.1 N·m (0.214 kgf·m). The efficiency of the propeller for positive pitch is presented in Figure 4.10. The efficiency plot was generated from the experimental data up to the highest advance coefficient of 0.8. Therefore, the highest efficiency of the 100% collective pitch cannot be certain as this occurred at a J value greater than 0.9. The maximum efficiency of positive pitch settings is approximately 70% on the 60% collective pitch angle (17.4°) at about an advance coefficient of 0.6. The information on the efficiency of the propeller can be used to find an optimized pitch angle for a required load and a speed of the underwater vehicle. In Figure 4.10, the performance of the propeller with 60% collective pitch angle setting has high efficiency for a wide range of advance coefficient. Therefore, the pitch angle setting of 60% can be used as an ideal pitch angle setting in many advance coefficients. This can reduce the movement of the actuators, and extend the life of the actuators and internal components.The performance of the CCPP was similar to a conventional controllable pitch propeller (CPP). The performance of a CPP can be seen in a typical CPP characteristic curve (Carlton, 2007, pp. 94). Pitch angle needs to be matched to the required loads and advance coefficients in order to maximize efficiency. This is the same method as the one that is used to optimize a fixed pitch propeller.

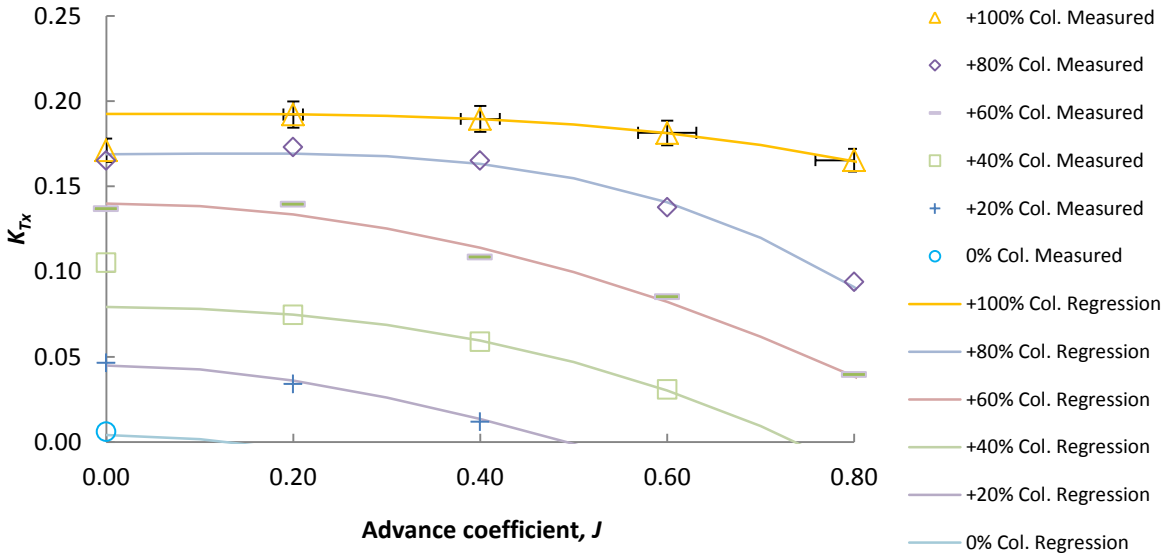

Figure 4.6. Thrust coefficient, K_T, versus advance coefficient, J, for positive collective pitch setting.

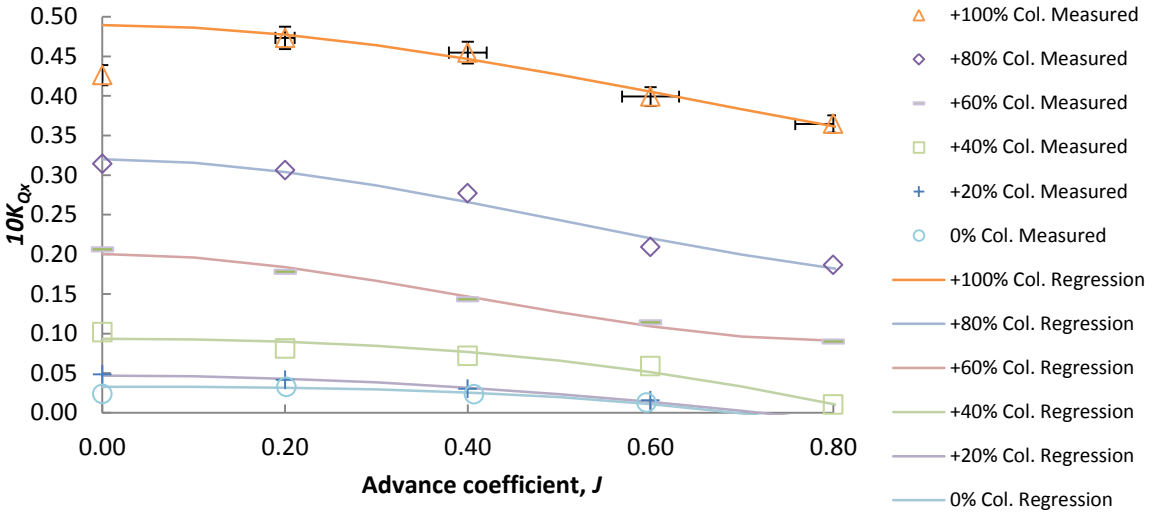

Figure 4.7. Torque coefficient, K_Q, versus advance coefficient, J, for positive collective pitch.

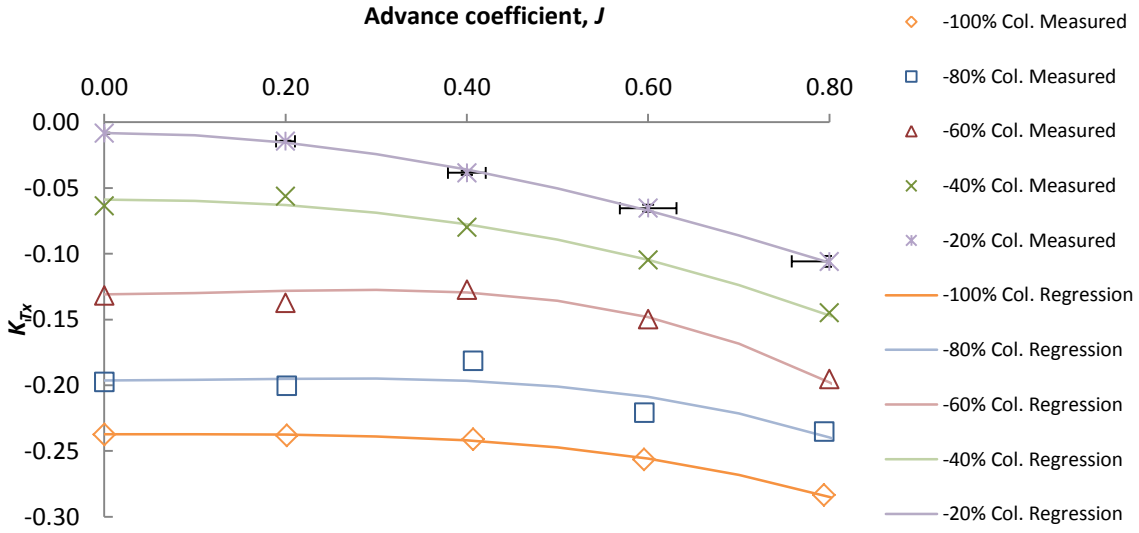

Figure 4.8. Thrust coefficient, K_T, versus advance coefficient, J, for negative collective pitch.

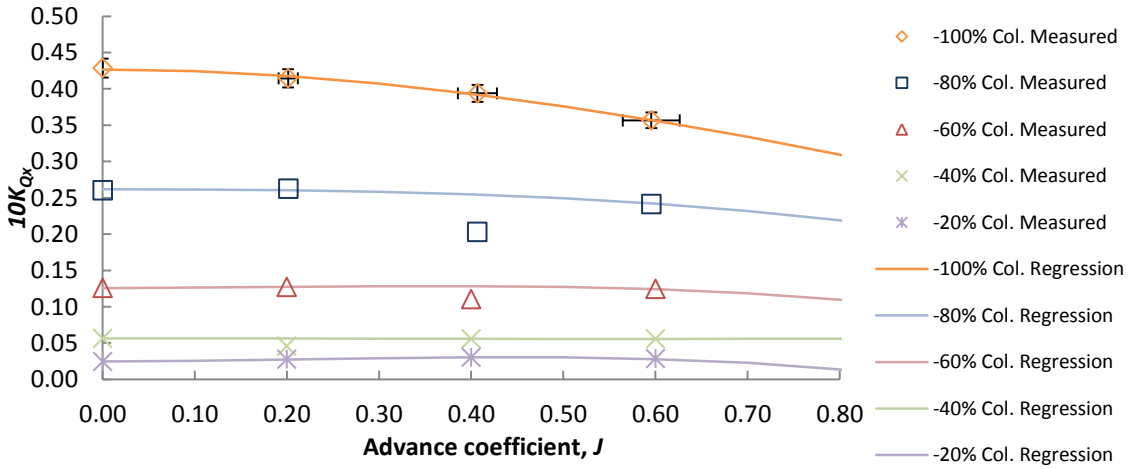

Figure 4.9. Torque coefficient, K_Q, versus advance coefficient, J, for negative collective pitch.

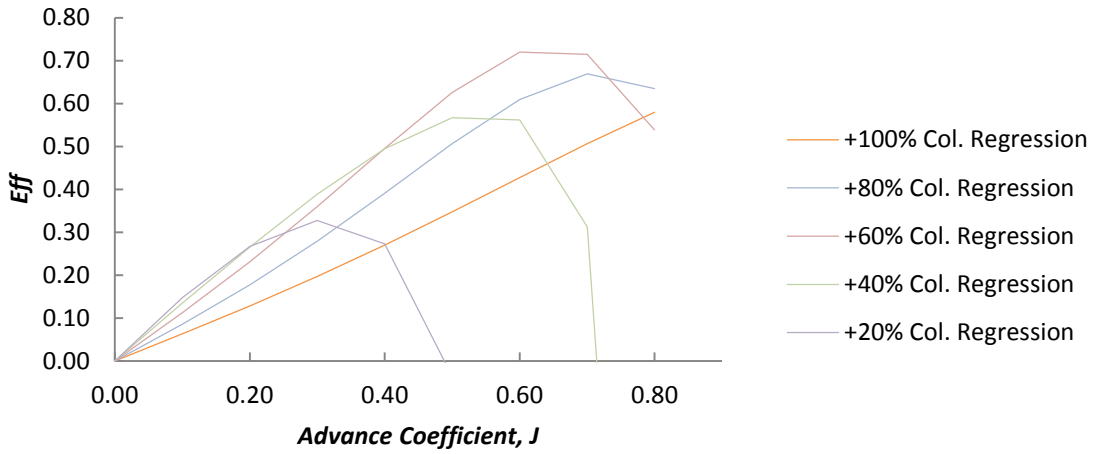

Figure 4.10. Efficiency versus advance coefficient for positive collective pitch setting.

4.7.1.2 Generation of Thrust and Torque Coefficient Equations of the Collective Pitch Test

The experimental data of the collective pitch were analysed to determine the interactions of the input parameters by using analysis of variance (ANOVA). For the collective pitch test, there were two input parameters that varied, which were the collective pitch angle in a percentage number format and the advance coefficients. The thrust coefficient equation and the torque coefficient equation were developed to estimate the thrust and the torque coefficients in other conditions besides the test conditions. The equations were formed in polynomial equations as follows:

$$K_{Ti} = \sum_{n=1}^{N} \mathrm{C}_n \mathrm{J}^{(s_n)} \left(\frac{\varphi_{\mathrm{col}}}{100}\right)^{(t_n)}, \tag{4.1}$$

$$10K_{Qi} = \sum_{n=1}^{N} C_n J^{(s_n)} \left(\frac{\varphi_{\mathrm{col}}}{100}\right)^{(t_n)}, \tag{4.2}$$

where the subscripts and the superscripts are defined as follows: i is the force directions (x, y, and z), n is the order of polynomial terms, N is the number of polynomial terms, s_n is the power of advance coefficient, t_n is the power of collective pitch terms, and J is the advance coefficient that is a function of shaft speed (n, rps).

Table 4.3 lists the polynomial coefficients and the power for each input in a tabular format. The first column in the table is the index of the polynomial terms. The next column is the polynomial coefficients for each polynomial term. The next two columns are the power for each input parameter.

By using equations (4.1) and (4.2), the propulsion forces and moments can be acquired at various conditions by substituting the thrust and the torque services in the following equations:

Thrust on *x* direction, $T_x = K_{Tx}\rho n^2 D^4$. (4.3)

Torque on *x* axis, $Q_x = K_{Qx}\rho n^2 D^5$. (4.4)

where the subscripts are as follows: ρ is the water density (kg/m^3), *n* is the shaft speed (rps), and *D* is the diameter of the propeller (m).

Table 4.3. Polynomial equation of thrust and torque coefficients for the collective pitch test

Polynomial Equations of Thrust and Torque Coefficients							
Thrust K_T				Torque $10*K_Q$			
n	C_n	s_n	t_n	n	C_n	s_n	t_n
1	1.6957042E−02	0	0	1	2.2764215E−02	0	0
2	1.2468124E−01	0	1	2	7.9253688E−02	0	1
3	−5.3544249E−02	1	0	3	3.4127619E−02	1	0
4	7.6568599E−02	1	1	4	−1.2338995E−02	1	1
5	−3.3752762E−02	0	2	5	3.2439889E−01	0	2
6	−9.9282306E−02	2	0	6	−7.2437981E−02	2	0
7	4.6479383E−01	1	2	7	−2.9624669E−01	1	2
8	−1.6213267E−01	2	1	8	−4.7403621E−01	2	1
9	3.3967224E−01	0	3	9	−1.0462502E−01	0	3
10	2.0907729E−02	3	0	10	−3.0834496E−02	3	0
11	−3.7106267E−01	2	2	11	9.8512592E−02	2	2
12	−3.1792032E−01	1	3	12	5.1232714E−02	1	3
13	1.3242512E−01	3	1	13	3.4715353E−01	3	1
14	−6.2975865E−02	0	4	14	2.2358741E−01	0	4
15	−2.9976131E−12	4	0	15	−1.3473281E−12	4	0
16	1.6319914E−01	2	3	16	3.9323791E−01	2	3
17	−1.9892813E−01	3	2	17	1.9883623E−01	3	2
18	−4.6479383E−01	1	4	18	2.9624669E−01	1	4
19	5.0161669E−13	4	1	19	3.8319444E−13	4	1
20	−2.5226009E−01	0	5	20	5.8136434E−02	0	5
21	2.5968457E−12	5	0	21	1.2556394E−12	5	0
22	−1.2466204E−01	3	3	22	−2.6209673E−01	3	3
23	6.2159948E−01	2	4	23	−3.9558835E−01	2	4
24	1.3423946E−14	4	2	24	1.5831501E−14	4	2
25	2.5098973E−01	1	5	25	−4.0446880E−02	1	5
26	−1.9619665E−13	5	1	26	−1.5564134E−13	5	1
27	5.9994545E−02	0	6	27	−1.1431287E−01	0	6
28	−8.4959744E−13	6	0	28	−4.3498303E−13	6	0

4.7.1.2 Combination of Collective and Cyclic Pitch Setting Test

In this test, the collective pitch and two cyclic pitches were varied at various advance coefficients. The blades sinusoidally oscillate when a cyclic pitch setting is applied. All experimental data presented in Figures 4.11, 4.12, 4.15, and 4.16 were conducted with an advance coefficient of 0.2.

Figures 4.11 and 4.12 present the magnitude and the direction of the transverse forces in various combinations of pitch angle settings. The figures show that the propeller with a positive right/left and a negative right/left cyclic pitch setting generates a force in the port side and starboard side, respectively. A collective pitch setting and a right/left cyclic pitch setting were fixed to a positive value, and then an up/down cyclic pitch setting was varied. The direction of the transverse force turned clockwise while decreasing the amplitude of the up/down cyclic pitch setting from +100% to 0% (20° to 0°) or from –100% to 0%. Each pitch setting is distinct from each other by the types and colours of rectangles. For instance, in Figure 4.11, a black rectangle is for a +80% right/left pitch angle setting. A square dot, a long dash dot, and a double square dot are for the +80%, +40%, and 0% collective pitch angle settings, respectively. The unit of the forces is in kilogram. A red arrow in the figure represents a vector of a transverse force. All charts are plotted in the *yz* plane, which is the same view as looking forward to the propeller.

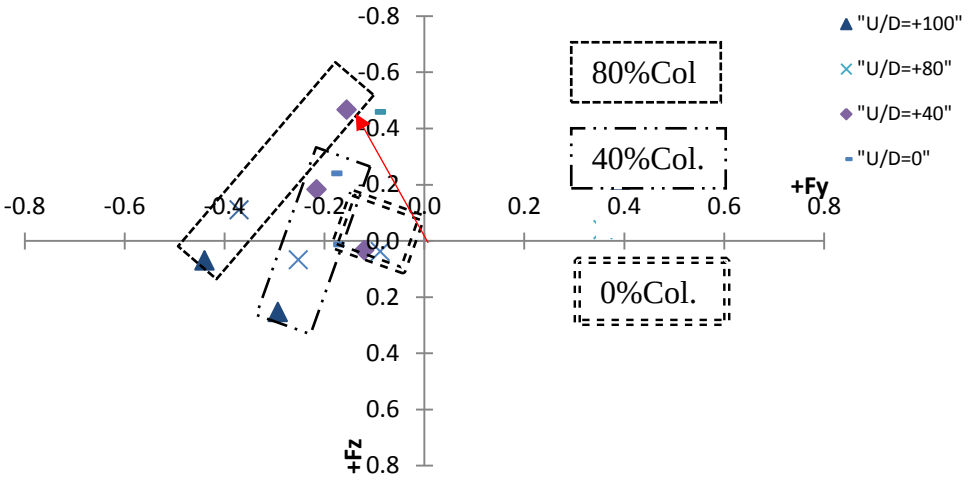

Figure 4.11. Magnitude and direction of transverse forces acting on the small 6-DOF force transducer with various up/down pitches on a constant pitch of +80%, +40%, and 0% collective pitch angle settings and 80% right/left pitch angle setting.

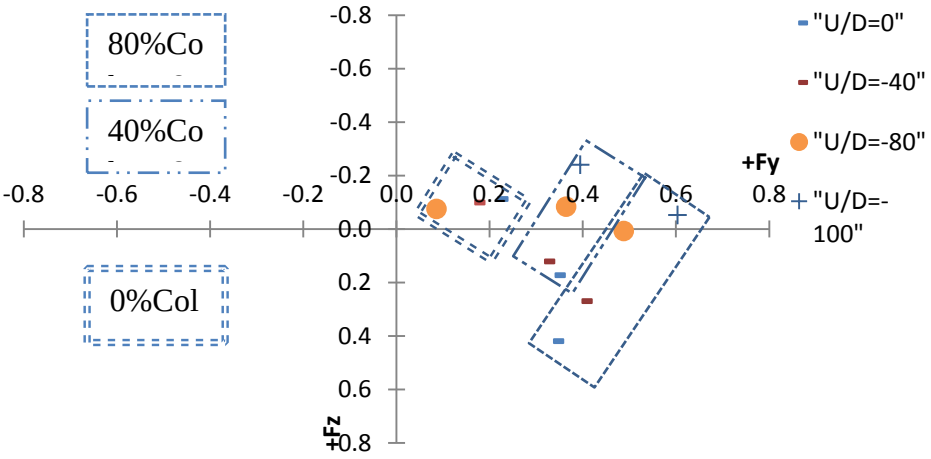

Figure 4.12. Magnitude and direction of transverse forces acting on the small 6-DOF force transducer with various up/down pitches on a constant pitch of +80%, +40%, and 0% collective pitch angle settings and 80% right/left pitch angle setting.

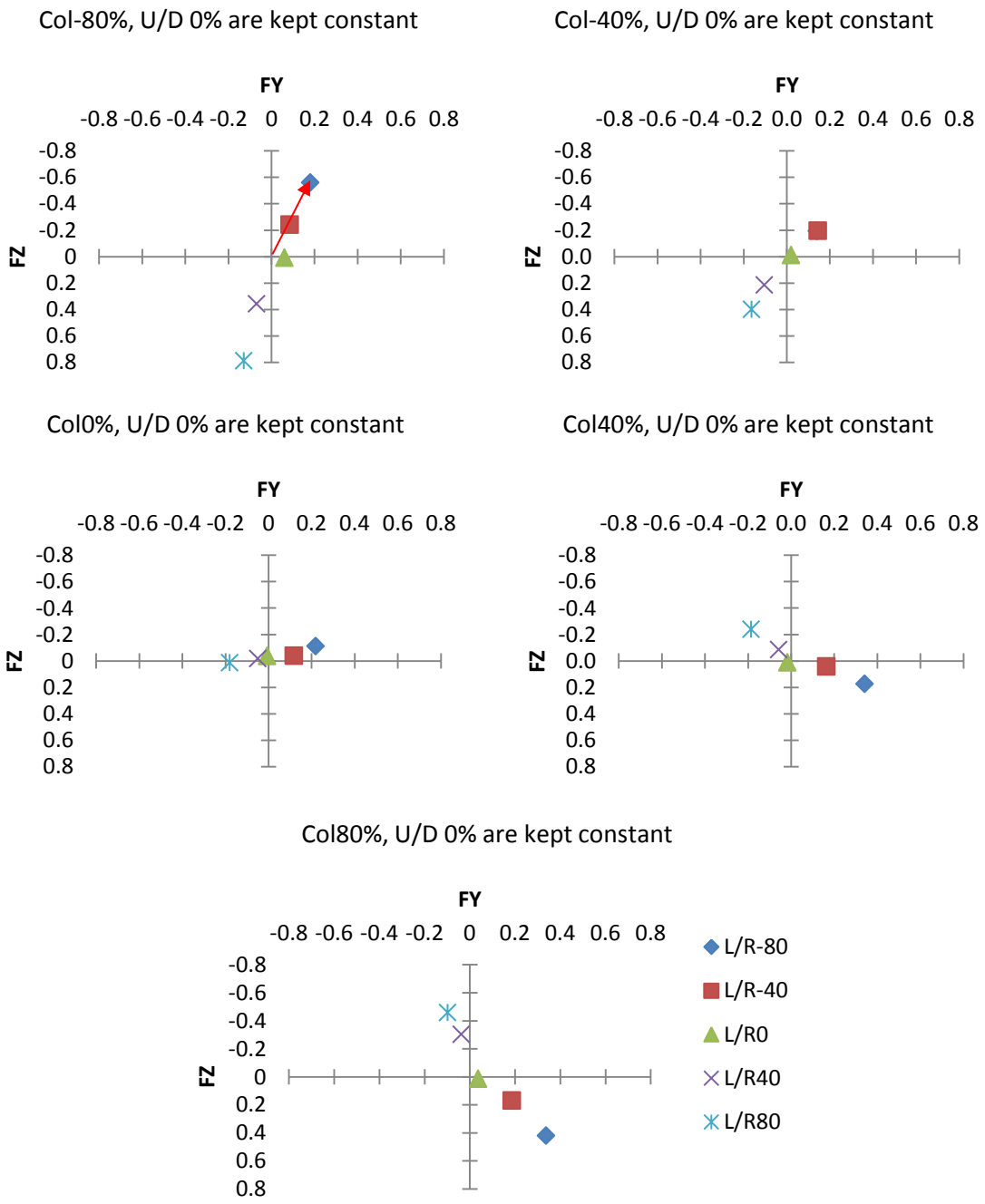

Figure 4.13. The effects of collective pitch on the transverse forces at various right/left pitch setting.

Figures 4.13 and 4.14 clearly show the effects of the collective pitch on the transverse forces in both their magnitudes and directions. When the collective pitch setting was increased, the magnitude of the transverse forces also increased. However, as the collective pitch setting increases, the direction of a generated transverse force rotates. By comparing the plot that has a zero collective pitch setting with other plots that have a positive pitch setting, a transverse force rotates clockwise as the magnitude of the collective pitch setting increases. In contrast, by comparing the plot that has a zero collective pitch setting with other plots that have a

negative pitch setting, a transverse force rotates counterclockwise as the magnitude of the collective pitch increases. Furthermore, in the plots that have a collective setting of 80%, the propeller with the life/right pitch setting makes an up/down force and the propeller with the up/down pitch setting makes a left/right force.

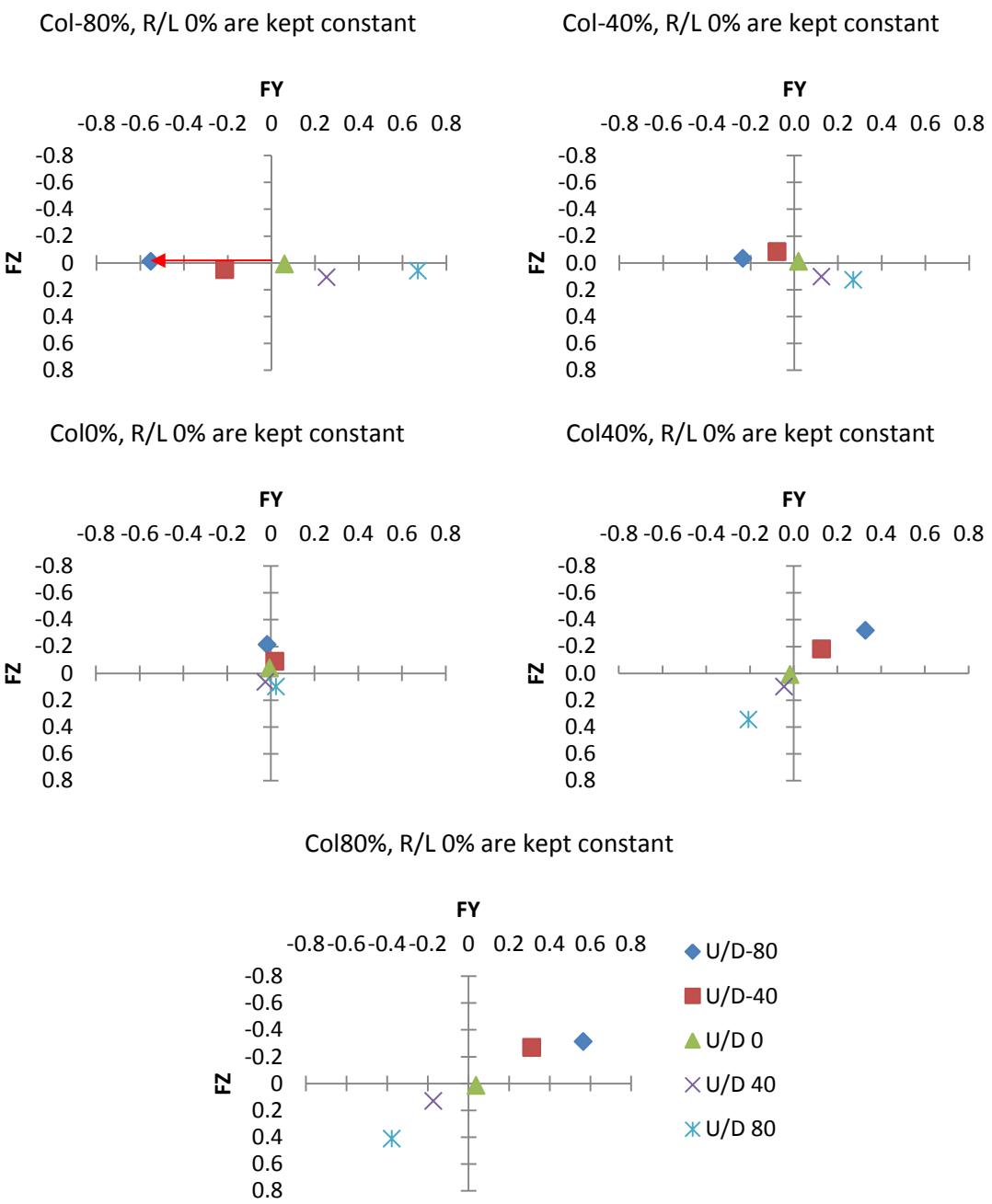

Figure 4.14. The effects of collective pitch on the transverse forces at various up/down pitch setting.

Regarding directional control, if a collective pitch setting is not zero, a pure right/left force was able to be generated by combining an up/down cyclic pitch setting and a right/left cyclic pitch setting. For instance, the propeller with a +80% collective pitch setting and a –80% right/left cyclic pitch setting can produce a pure right force by adding +80% up/down cyclic

pitch setting. If a collective pitch setting is zero, the propeller can generate a pure right/left force by applying only right/left cyclic pitch setting. However, with the zero collective pitch setting, the magnitude of the transverse thrusts were low, approximately 5 N at ±100 right/left cyclic pitch setting. In addition, in the case of a collective pitch setting of zero, the propeller can generate a pure up/down force by applying only up/down cyclic pitch setting as shown in Figure 4.13.

In the case of a propeller with a collective pitch setting of 0% and non-zero cyclic pitch settings, the maximum angle of attack is insufficient to cause separation. As the magnitude of the collective pitch setting increases to 40% and a cyclic pitch setting of 40%, the maximum angle of attack is just sufficient to cause leading edge separation. The blades experience light dynamic stall phenomennon. The dynamic stall phenomenon causes the shift in the direction of a transverse force. In Figures 4.13 and 4.14, at the first and the last plots, a propeller with a collective pitch setting of 80%, the strong dynamic stall occurs. Therefore, the direction of a transverse force shifted to almost 90°. The details of the dynamic stall can be found in Chapter 5.

Figure 4.15 presents the magnitude and direction of the transverse forces of the propeller when a positive up/down pitch setting was fixed at +80% (16°). The propeller generated a force in the port direction when the right/left cyclic pitch setting was positive. In contrast, the propeller generated a force in starboard direction when the right/left cyclic pitch setting was negative.

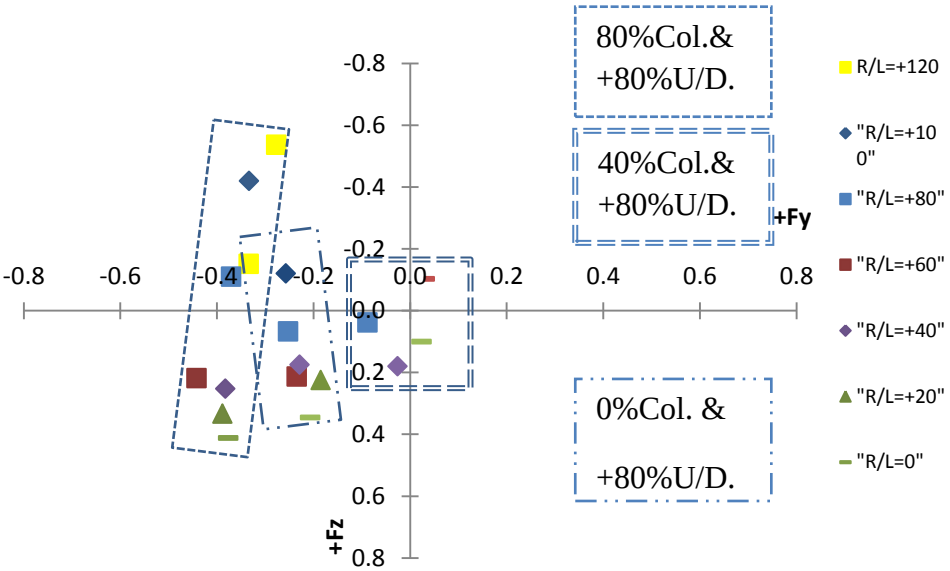

Figure 4.15. Magnitude and direction of forces acting on the small 6-DOF force transducer with various right/left pitches on a constant pitch of +80%, +40%, and +0% collective pitch angle settings and +80% up/down pitch angle setting.

Figure 4.16 presents the magnitude and direction of the transverse forces of the propeller when a positive up/down pitch setting was fixed at –80% (–16°). The propeller generated a force in a starboard direction when the right/left cyclic pitch setting was negative. A collective pitch setting and an up/down cyclic pitch setting were fixed, and then a right/left

cyclic pitch setting was varied. The direction of the transverse force turned counterclockwise as decreasing the right/left cyclic pitch setting from +100% to 0% (20° to 0°). However, as the right/left cyclic pitch setting decreasing from 0% to −100%, the transverse force turned clockwise.

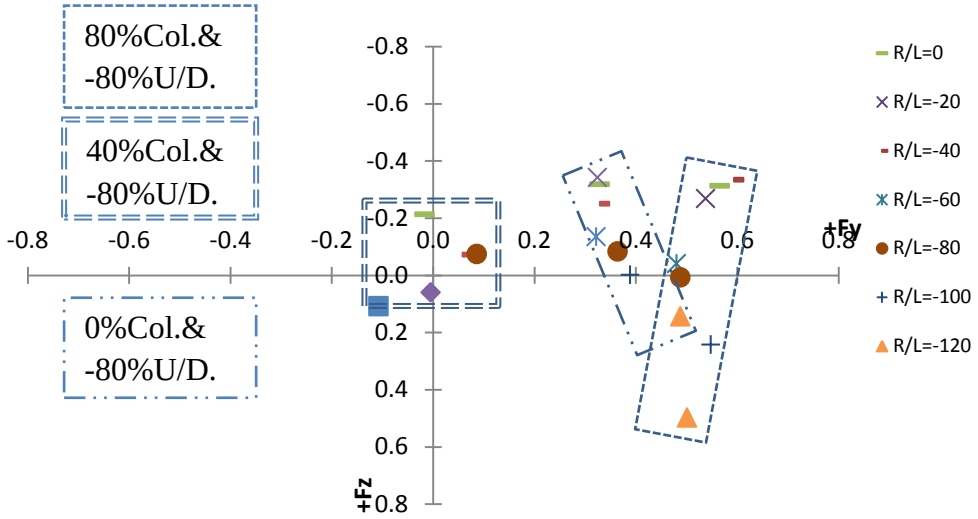

Figure 4.16. Magnitude and direction of transverse forces acting on the small 6-DOF force transducer with various right/left pitches on a constant pitch of +80%, +40%, and 0% collective pitch angle settings and −80% up/down pitch angle setting.

The maximum torque occurred at a combination of +100% collective, +100% up/down, and +100% right/left cyclic pitch settings. The torque was approximately 2.7 N·m (0.275 kgf·m). The data of torque will be used to design an antiroll device to an underwater vehicle for the future works.

4.7.2 Results of Resistance Tests

The big force balance measured the total resistance, including the underwater vehicle and the hydrofoil-shaped struts. To acquire the resistance of the underwater vehicle, the resistance of the hydrofoil-shaped struts is subtracted from the total resistance. The resistance of the vehicle for forward velocities up to 1.2 m/s is presented in Figure 4.17. The drag coefficient of the base configuration vehicle can be calculated by using the following equation :

$$C_{\mathrm{DF}(\alpha=0^\circ)} = \frac{2F_d}{\rho v^2 A}, \qquad (4.5)$$

where F_d is the drag force, from the experimental results, ρ is the mass density of the water, v is the speed of the underwater vehicle relative to the water, and A is the wetted area of the vehicle. The calculated drag coefficient, $C_{\mathrm{DF}(\alpha=0^\circ)}$ was not constant but varies as a function of the speed of the vehicle, size of vehicle, water density and water viscosity. Kinematic viscosity of the water, the speed of the vehicle and a length scale of the vehicle are incorporated into a dimensionless quantity called the Reynolds numbers, Re. Therefore, the drag coefficient was plotted as a function of Re as shown in Figure 4.18. It can be seen from

Figure 4.18 that at low Reynolds numbers, the underwater vehicle exhibits a roughly constant drag with a C_{DF} value, approximately 0.00135. At high Reynolds numbers, the vehicle exhibits the value of the drag coefficient from 0.0006 to 0.0009. When the Reynolds numbers is greater than approximately 480,000, the decrease in drag occurs. This occurrence indicates an abrupt change in the flow from separated laminar to separated turbulent flow. The values of the calculated drag coefficient at various Reynolds numbers were used in the modified Jorgensen's equations (2.32) and (2.33) to improve the accuracy of the simulation program.

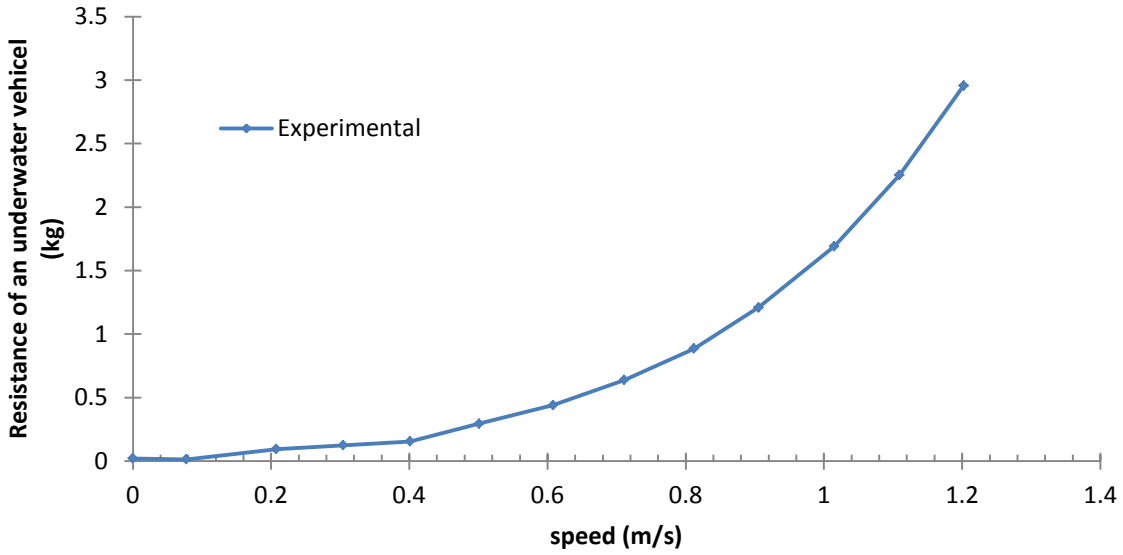

Figure 4.17. Resistance of the underwater vehicle.

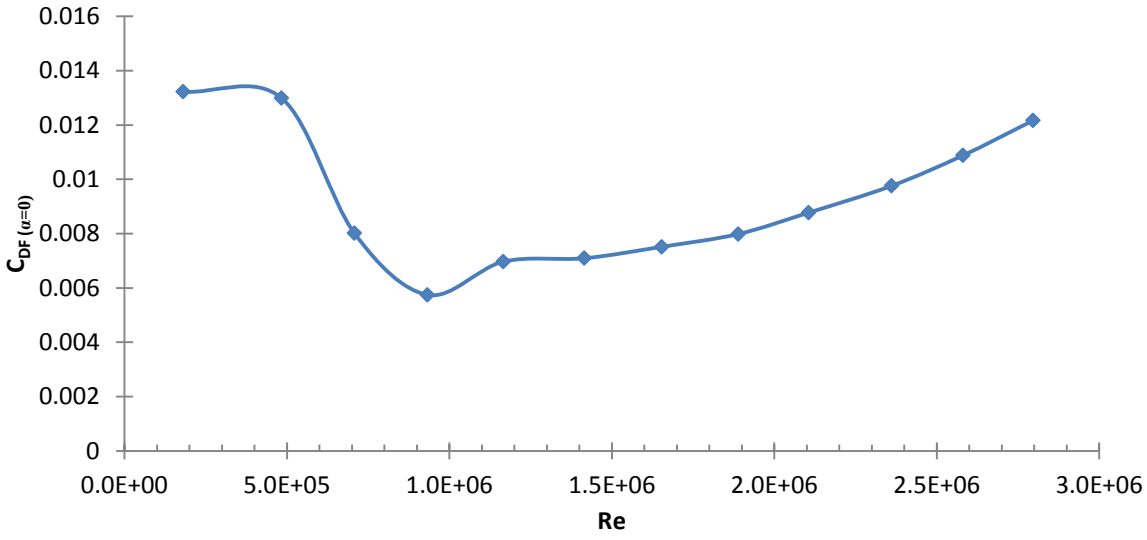

Figure 4.18. Drag coefficient, $C_{DF(\alpha=0°)}$ as a function of Reynolds number *Re*.

With available resistance data, the collective pitch and the shaft speed can be optimized. If the resistance, the constant shaft speed, and the propeller diameter are given, the thrust coefficient can be acquired by substituting the resistance into the required thrust, *T*, in the following equation:

$$K_T = \frac{T}{\rho n^2 D^4}. \quad (4.6)$$

Then the advance coefficient, *J*, can be calculated from the required vehicle speed.

The relationship between the thrust coefficients and advance coefficients at various pitch settings was established and expressed in equation (4.1). The optimized collective pitch angle can be estimated by varying the collective pitch angle in equation (4.1) until the efficiency reaches the maximum at the given advance coefficient, *J*. The details of the optimization of the shaft speed can be found in a book, *Ship Resistance and Propulsion*, by Molland, Turnock, and Hudson (2011).

Chapter Summary

The performance of the CCPP with a collective pitch setting was similar to a conventional CPP. The propeller with a positive collective pitch setting created a force to propel the underwater vehicle forward. The propeller with a negative collective pitch setting created a force to propel the underwater vehicle backward. The experimental results of the performance of the CCPP only with the collective pitch setting were formed in polynomial equations. The thrusts and the torques for the collective pitch setting can be easily estimated from the polynomial equations.

Increasing collective pitch setting will also increase the magnitude of the transverse forces and cause the direction of the transverse forces to rotate clockwise when looking from the aft.

The CCPP with a positive right/left cyclic pitch setting generated force in the port direction. The propeller with a negative right/left cyclic pitch setting generated force in the starboard direction. In addition, different types of cyclic pitch setting affect the direction of the transverse thrust differently. The direction of the transverse force turned counterclockwise while decreasing the magnitude of the right/left cyclic pitch setting towards 0%.

Furthermore, the propeller with a positive up/down cyclic pitch setting produced force in a downward direction. A collective pitch setting and a right/left cyclic pitch setting were fixed to a positive value, and then an up/down cyclic pitch setting was varied. The results of the combined pitch settings showed that the direction of the transverse force turned clockwise while decreasing the magnitude of the up/down cyclic pitch setting towards 0%.

The magnitude of the transverse thrust directly varies the magnitude of the cyclic pitch setting increases.

With these effects, the combination of cyclic pitch must be adjusted to compensate the change in the direction of the transverse forces. A simple change in pitch setting does not always result in a simple change in forces. The manual control of the direction of transverse forces is too complicated because a combination of pitch setting is not intuitive. Therefore, the CCPP requires the development of a control system in order to automatically correct combination of pitch.

Chapter 5 Numerical Prediction of the Hydrodynamic Performance of the CCPP

The hydrodynamic behaviour of the collective and cyclic pitch propeller (CCPP) is complex because the angle of the propeller blades oscillates when the cyclic pitch setting is applied. The aim of this chapter was to develop a program to predict the characteristics of the propeller. The understanding may lead to a greater performance in both propelling and manoeuvring. The first part details a prediction of the performance of the collective and cyclic propeller. It includes an explanation of relevant theories for the prediction and the implementation of the prediction program. The second part presents a comparison between the numerical prediction results and the experimental results. The details of the experiment, such as a testing setup, results, and discussion, are presented in the previous chapter.

5.1 Development of the Prediction Program

A numerical prediction program was required to predict the side thrusts and moments on the CCPP. The prediction program can be used as a part of the computer simulation program of an underwater vehicle with the CCPP. In addition, the prediction program can be used to improve the design of the control system of the propeller.

The prediction program was based on the blade element momentum theory (BEMT) code, which required a small amount of computational resources. The CCPP often experiences unsteady effects because of the oscillation of the angle of attack of the blades. Therefore, the successful design of the performance prediction program of the CCPP requires the ability to predict the unsteady hydrodynamic characteristics of the propeller undergoing dynamic stall. Dynamic stall is a complex phenomenon. Dynamic stall occurs when the angle of attack of the oscillating blade becomes large enough. The detailed information on the dynamic stall phenomenon is found in this chapter.

The nonlinear hydrodynamic effects can be predicted by CFD. However, it requires very high computational time and resources. Therefore, a desired prediction method requires an appropriate compromise between accuracy and computational requirements. Many researchers have investigated the dynamic stall phenomenon via experiments, such as MaCroskey (1976, 1981) and Wilby (1979). Many semiempirical models were established to model the phenomenon, such as the works of Carta et al. (1970), Gormont (1973), Gangwani (1983), Johnson (1974), Trung (1996), and Leishman and Beddoes (1989). Leishman and Beddoes (1989) developed a simple semiempirical model of dynamic stall. The model represents well the physics of the dynamic stall. The model can effectively compromise between quality estimates for lift, drag and pitching moment, and computational requirements. The Leishman-Beddoes dynamic stall model was a subroutine of the BEMT. The dynamic stall model was only used to determine the normal force and chord force coefficients.

5.1.1 Blade Element Momentum Theory

The blade element momentum theory (BEMT) is a simple method used to predict propeller performance. The principle of the BEMT is based on two theories: the blade element theory (Froude, 1878) and the momentum theory (Rankine, 1865; Froude, 1889).

5.1.1.1 Description of Program CCPP_BEMT

CCPP_BEMT is a BEMT code developed in this research using LabVIEW software. The code was only designed for axial inflow. However, the CCPP inherently operated in unsteady conditions and large angle of attack. Only the BEMT cannot predict the hydrodynamic loads accurately. Therefore, the BEMT was needed to be modified to compensate the unsteady conditions. Basic BEMT was improved in order to calculate the induced coefficients and 2-D static hydrofoil data accurately.

The local induced velocities at the blades vary from the annular averaged induced velocities when the cyclic pitch setting was applied. Therefore, the development of the calculation of the induced coefficients was required. In addition, the BEMT was modified to be able to calculate an axial- and tangential-induced velocity at each azimuth position of the blades. The step size of azimuth angles can be assigned and converted into a time step size. The modified BEM is a time-based numerical solution.

The azimuth angle step, $\triangle\varphi$, can be converted into a time step as follows:

$$\Delta s = \frac{2U_{\mathrm{R}}\left(\Delta\varphi\right)\left(\dfrac{\pi}{180\omega}\right)}{c}, \tag{5.1}$$

where Δs is the time step, U_{R} is the velocity components of a blade element, c is the chord length, and ω is the rotation frequency of the propeller shaft.

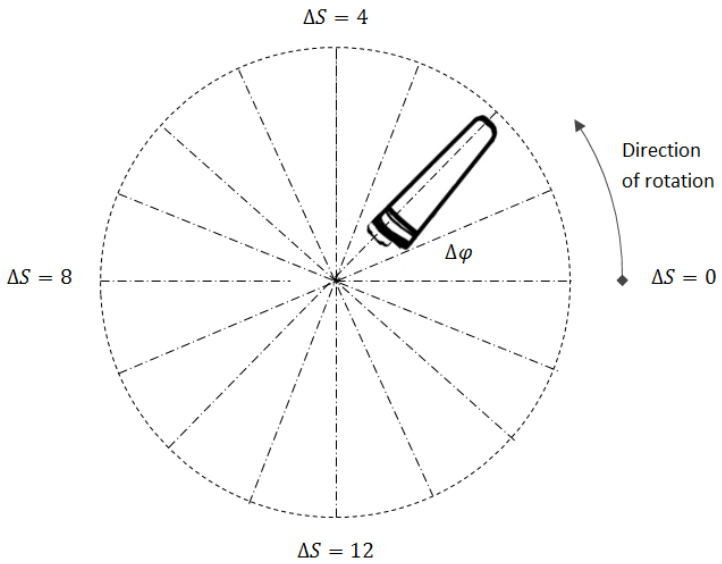

Figure 5.1. A fixed amount of azimuth angle steps.

In the blade element theory, a blade is divided into many small elements as in Figure 5.1.

The theory assumes that each element of a blade is independent of other elements, and each element is analysed as a 2-D hydrofoil section as shown in Figure 5.2.

Velocity components of a blade element are given as follows:

$$U_{\mathrm{R}} = \sqrt{U_{\infty}^{2}\left(1+a\right)^{2} + r^{2}\omega^{2}\left(1-a'\right)^{2}}\,, \tag{5.2}$$

$$\alpha = \theta - \tan\varnothing = \frac{U_{\infty}\left(1+a\right)}{r\omega\left(1-a'\right)}, \tag{5.3}$$

$$U_{\mathrm{R}}\sin\varnothing = U_{\infty}\left(1+a\right), \tag{5.4}$$

$$U_{\mathrm{R}}\cos\varnothing = \omega r\left(1-a'\right), \tag{5.5}$$

where a is the axial induction factor, a' is the swirl induction factor, c is an element of chord, δr is the width of a radius, and r is the radius in the middle of each element.

The thrust and the torque from the blade element theory are given as follows:

$$\delta T = B\frac{1}{2}\rho U_{\mathrm{R}}^{2}\left(C_{\mathrm{L}}\cos\varnothing - C_{\mathrm{D}}\sin\varnothing\right)c\delta r\,, \tag{5.6}$$

$$\delta Q = B\frac{1}{2}\rho U_{\mathrm{R}}^{2}\left(C_{\mathrm{L}}\sin\varnothing + C_{\mathrm{D}}\cos\varnothing\right)cr\delta r\,, \tag{5.7}$$

where B is the number of blades, ρ is the water density, C_{L} is the 2-D foil section lift coefficient, and C_{D} is the 2-D foil section drag coefficient.

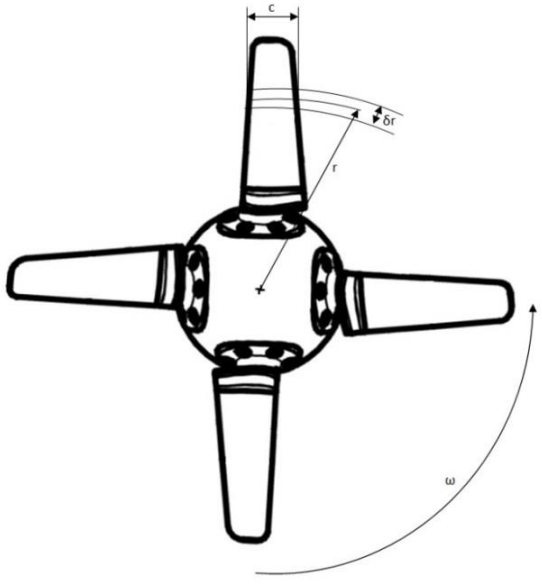

Figure 5.2. Formulation of the blade element theory from consideration of an annulus of flow and associated blade element.

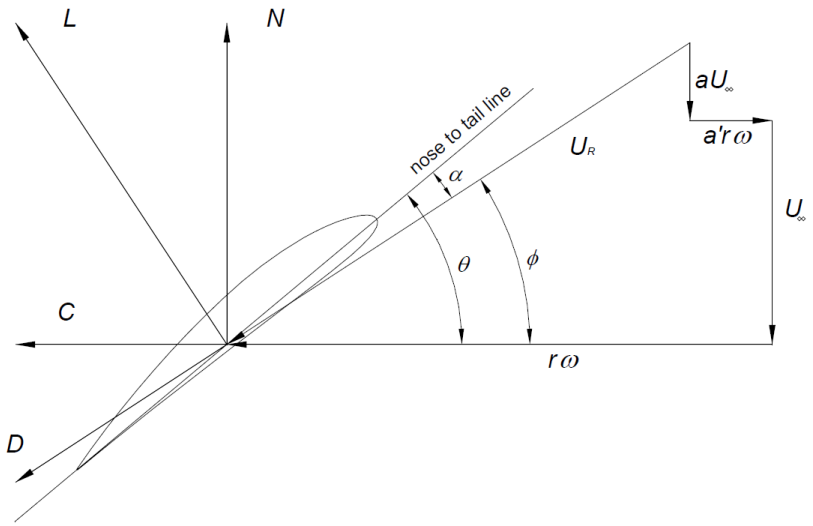

Figure 5.3. Velocity and free body diagram for blade element (Paul Brandner, 2007).

However, the lift and the drag coefficients need to be improved because the blades of the CCPP experienced unsteady hydrodynamic effects, when the cyclic pitch setting is applied. The details of improvement of the lift and the drag coefficients can be found in the next section.

The thrust and the torque from the momentum theory are given as follows:

$$\delta T = 4\pi\rho U_\infty^2 (1+a) a \delta r , \tag{5.8}$$

$$\delta Q = 4\pi r^3 \rho U_\infty \omega (1-a) a' \delta r . \tag{5.9}$$

Finding the induction coefficients by comparing equations (5.6) and (5.7) with equations (5.8) and (5.9) and using equations (5.4) and (5.5) forms the following equations:

The average axial induction coefficient,

$$a = \left[1 - \frac{4F\sin^2 \varnothing}{\sigma' \left(C_{\mathrm{L}} \cos\varnothing + C_{\mathrm{D}} \sin\varnothing \right)} \right]^{-1} . \tag{5.10}$$

The average tangential induction coefficient,

$$a' = \left[1 + \frac{4F\sin\varnothing\cos\varnothing}{\sigma' \left(C_{\mathrm{L}} \sin\varnothing + C_{\mathrm{D}} \cos\varnothing \right)} \right]^{-1} , \tag{5.11}$$

where solidity, σ', is computed as follows:

$$\sigma' = \frac{Bc(r)}{2\pi r} , \tag{5.12}$$

and Prandlt's tip-loss factor, *F*, is computed as follows:

$$F = \frac{2}{\pi}\cos^{-1}e^{-f}, \tag{5.13}$$

$$f = \frac{B}{2}\left(\frac{R-r}{r\sin\phi}\right). \tag{5.14}$$

After the induced coefficients have converged, the thrust and the torque of each blade can be calculated by the integration of the thrust and the torque of each element over the propeller blade as follows:

$$T_{N\_\text{blade}} = \int_{R_{\text{hub}}}^{R} \partial T_N(r), \tag{5.15}$$

$$Q_{\text{blade}} = \int_{R_{\text{hub}}}^{R} \partial Q(r). \tag{5.16}$$

After the thrust and the torque of a blade are calculated, the thrust is decomposed into T_{X_blade} and T_{R_blade}. They can be determined using equations (5.17) and (5.18). Substituting T_{R_blade} into equations (5.19) and (5.20), the thrusts in the *y* and *z* directions, respectively, can be determined.

$$T_{X\_\text{blade}} = T_{N\_\text{blade}}\cos(\delta), \tag{5.17}$$

$$T_{R\_\text{blade}} = T_{N\_\text{blade}}\sin(\delta), \tag{5.18}$$

$$T_{Y\_\text{blade}} = T_{R\_\text{blade}}\cos(\gamma), \tag{5.19}$$

$$T_{\text{Z\_blade}} = T_{\text{R\_blade}}\sin(\gamma), \tag{5.20}$$

$$M_{X\_\text{blade}} = Q_{\text{blade}}. \tag{5.21}$$

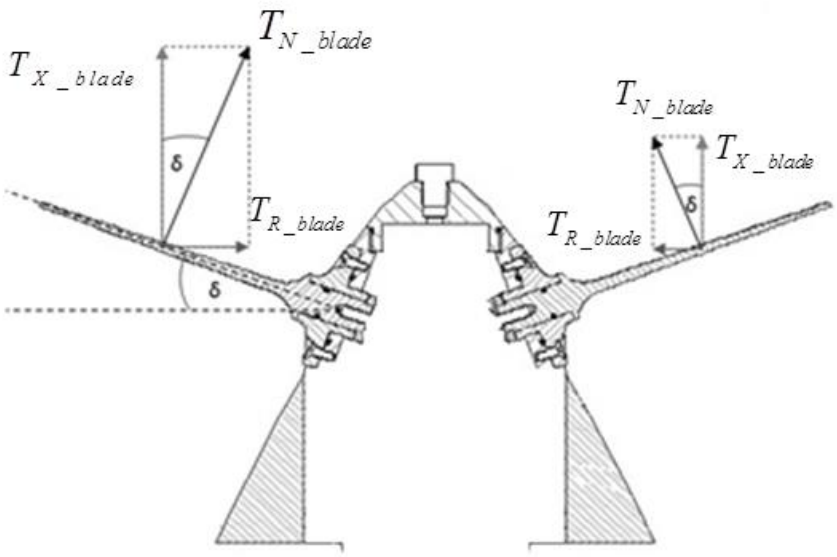

Figure 5.4. Decomposition of the normal thrust.

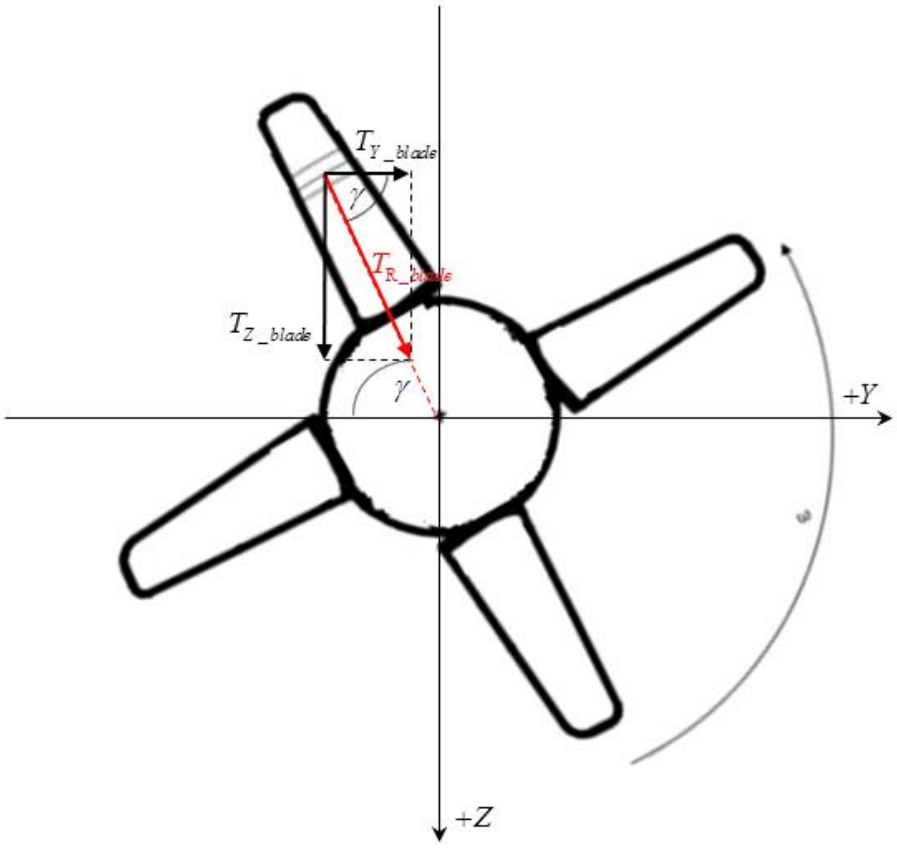

Figure 5.5. Decomposition of the radial thrusts into *y* axis and *z* axis.

Total thrust in each axis at one time step can be calculated using equations (5.22)–(5.24). The total thrust in each axis is averaged over time by calculating equations (5.25)–(5.27).

$$T_{X\_t} = T_{X\_\text{blade}1} + T_{X\_\text{blade}2} + T_{X\_\text{blade}3} + T_{X\_\text{blade}4}, \qquad (5.22)$$

$$T_{Y\_t} = T_{Y\_\text{blade}1} + T_{Y\_\text{blade}2} + T_{Y\_\text{blade}3} + T_{Y\_\text{blade}4}, \tag{5.23}$$

$$T_{Z\_t} = T_{Z\_\text{blade}1} + T_{Z\_\text{blade}2} + T_{Z\_\text{blade}3} + T_{Z\_\text{blade}4}, \tag{5.24}$$

$$T_{X\_\text{avg}} = \frac{\sum_{0}^{N} T_{X\_t}}{N}, \tag{5.25}$$

$$T_{Y\_\text{avg}} = \frac{\sum_{0}^{N} T_{Y\_\text{t}}}{N}, \tag{5.26}$$

$$T_{Z\_\text{avg}} = \frac{\sum_{0}^{N} T_{Z\_\text{t}}}{N}. \tag{5.27}$$

The total torque in the *x* axis at one time step can be calculated using equation (5.28). The total torque is averaged over time by calculating from equation (5.29).

$$Q_{X\_t} = Q_{\text{blade}1} + Q_{\text{blade}2} + Q_{\text{blade}3} + Q_{\text{blade}4}, \tag{5.28}$$

$$Q_{\text{X\_avg}} = \frac{\sum_{0}^{N} Q_{X\_\text{t}}}{N}. \tag{5.29}$$

5.1.2 Leishman-Beddoes Dynamic Stall Model

The Leishman-Beddoes dynamic stall model was used in the BEMT code. The dynamic stall model is a semiempirical model. The model consists of three submodules: an attached flow module, a separated flow module, and a vortex shedding module for unsteady hydrodynamic loads. Each module sequentially computes the unsteady loads. The unsteady attached force coefficients are estimated in the attached flow module. These estimated coefficients are then used as the input for the separated flow module. In the separated flow module, the unsteady attached force coefficients are recalculated by considering the effects of the pressure lag and the boundary layer lag. The outputs of the separated flow module become the inputs for the next module. The vortex shedding phenomena do not always occur. Therefore, a criterion is needed to determine whether the vortex has occurred or not. If the vortex has occurred, the vortex shedding module would yield the forces that include the effect of the vortex passing over the blade. The outputs of the vortex shedding module are added to the outputs of the separated flow model to generate the final normal force coefficient of the blade. The interaction of each module is illustrated in Figure 5.6.

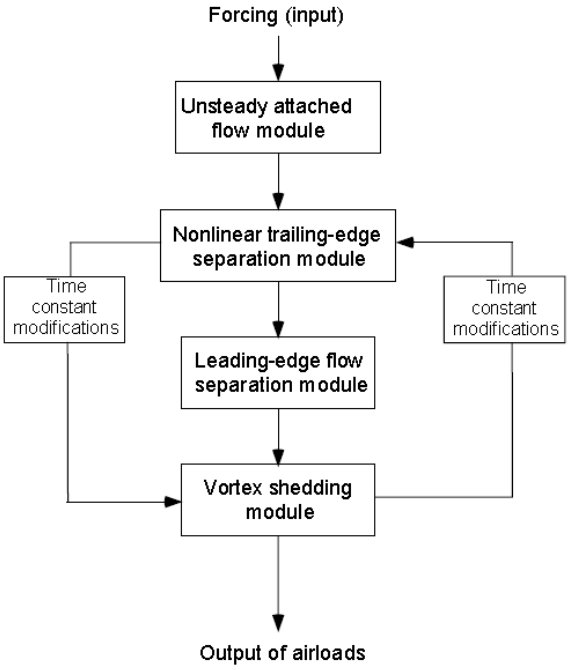

Figure 5.6. Diagram of data flow of the Leishman-Beddoes dynamic stall model (Leishman, 2002).

More details of each module are explained in the following sections.

5.1.2.1 Attached Flow Module

The flow on the blade section is fully attached. The lift slopes of the unsteady and static are almost the same. An unsteady motion of the blade section can delay the onset of the stall and increase lift compared with a static blade. The relationship between the dynamic lift and the angle of attack is linear. The attached flow behaviour is accurately formulated in terms of indicial response. The indicial response are assumed to be composed of the sum of two parts: a circulatory loading component and a noncirculatory loading component (impulsive load), Leishman (1989).

Equation (5.30) is for the normal force coefficient, which is written in the *S* domain as follows:

$$\Delta C_n(S) = \left[C_{N_a}(M)\phi_\alpha^C(S,M) + \frac{4}{M}(\phi_\alpha^I(S,M) \right] \Delta\alpha \quad , \qquad (5.30)$$

where nondimensional time $S = \frac{2Vt}{c}$.

The first term of equation (5.30) is a circulatory part and the second term is the noncirculatory part.

Circulatory Loading Component
The circulatory normal force can be determined using

$$C_{N_n}^{C} = C_{N_a}(M)\alpha_{(E_n)} = C_{N_a}(M)(\varepsilon_n - X_n - Y_n), \tag{5.31}$$

where *n* denotes the current sample, α_n is the angle of attack at the current time step, and α_{E_n} is a lagged effective angle of attack.

The values of C_{N_a} were estimated using Xfoil6.97 at a range of Reynolds number from 10,000 to 1,000,000. The slope of normal force coefficients with respect to the various angles of attack was fit in the polynomial equation as follows:

$$C_{n_a} = sign(angle)\begin{pmatrix}(5E\text{-}26)\,\mathrm{Re}^4 - (1E\text{-}19)\,\mathrm{Re}^3 \ldots \\ +(1E\text{-}13)\,\mathrm{Re}^2 - (2E\text{-}08)\,\mathrm{Re} + 0.1034\end{pmatrix}, \tag{5.32}$$

where Re is the Reynolds number.

The deficiency functions, X_n and Y_n, represent the deficiency in the angle of attack due to the shed wake effects and unsteady hydrodynamic effects. The deficiency functions are given as follows:

$$X_n = X_{n-1}\exp\left(-b_1\beta^2\Delta S\right) + A_1\Delta\alpha_n \exp\left(\frac{-b_1\beta^2\Delta S}{2}\right), \tag{5.33}$$

$$Y_n = Y_{n-1}\exp\left(-b_2\beta^2\Delta S\right) + A_2\Delta\alpha_n \exp\left(\frac{-b_2\beta^2\Delta S}{2}\right), \tag{5.34}$$

where the nondimensional time, ΔS, is given as $\Delta S = \frac{2V\Delta t}{c}$; $\Delta\alpha$ is the step change of angle of attack, $\Delta\alpha = \alpha_n - \alpha_{n-1}$; β is the Prandtl-Glauert factor, $\beta = \sqrt{1-M^2}$; and A_1 = 0.3, A_2 = 0.7, b_1 = 0.14, and b_2 = 0.53 are the constants of the indicial function as given by Leishman and Beddoes (1989).

Noncirculatory Loading Component

The noncirculatory loading component can be determined by using the following equations from the piston theory:

$$C_{N_n}^{I} = \frac{4K_\alpha T_1}{M}\left(\frac{\Delta\alpha_n}{\sum t} - D_n\right), \tag{5.35}$$

where $T_1 = \frac{c}{M}$ is the deficiency function and D_n accounts for the pressure disturbances, given as

$$D_n = D_{n-1}\exp\left(\frac{-\Delta t}{K_\alpha T_1}\right)+\left(\frac{\Delta\alpha_n - \Delta\alpha_{n-1}}{\Delta t}\right)\exp\left(\frac{-\Delta t}{2K_\alpha T_1}\right), \quad (5.36)$$

where K_α is the noncirculatory time constant multiplier. It is a function of Mach number. The multiplier becomes closer to 0.75 when the Mach number is close to 0:

$$K_\alpha = \frac{0.75}{(1-M)+\pi\beta^2 M^2\left(A_1 b_1 + A_2 b_2\right)}. \quad (5.37)$$

The total normal force coefficient under attached flow condition, $C_{N_n}^p$, is given as

$$C_{N_n}^p = C_{N_n}^I + C_{N_n}^C. \quad (5.38)$$

For the circulatory component of the chord normal force, the force is put in terms of an effective angle of attack and an empirically determined normal force curve slope, C_{N_n}:

$$C_{C_n} = C_{N_n}\tan\left(\alpha_{E_n}\right) \quad (5.39)$$

5.1.2.2 Trailing Edge Separated Flow Module

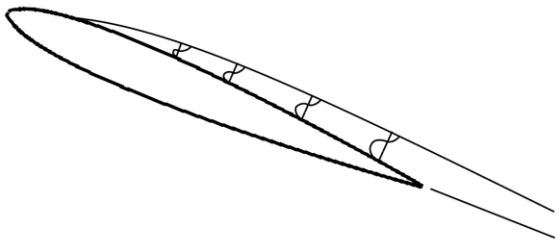

Figure 5.7. Airfoil exceed static stall angle, and flow reversals take place in the boundary layer (Leishman, 2002).

In Figure 5.7, the flow starts to reverse within the boundary layer. The progressive trailing edge separation is evident before most hydrofoils experience dynamic stall. The trailing edge separation introduces a nonlinear force and moment because of the loss of circulation. The normal force coefficient is the same as the normal force coefficient in the attached flow module, except the circulatory component is scaled by a trailing edge separation point. The movement of the separation point induces a dynamic delay. The effect of the delay can be modelled by the Kirchhoff method. The normal force coefficient including separation effects is given as

$$C_{N_n}^f = C_{N_\alpha}\left(\frac{1+\sqrt{f''}}{2}\right)^2 \alpha_{E_n} + C_{N_n}^I. \quad (5.40)$$

The chord force coefficient including the separation effects is given as

$$C_C^f = \eta C_{N_\alpha} \alpha_{E_n}{}^2 \sqrt{f''} + C_{N_n}^I , \tag{5.41}$$

where C_{N_α} is the normal force curve slope, f'' is the final delayed trailing edge separation location, and α_{E_n} is the effective angle of attack.

The final delay trailing edge separation, f'', is given as follows:

$$f'' = f' - \mathrm{Df} , \tag{5.42}$$

$$\mathrm{Df}_n = \mathrm{Df}_{n-1} \exp\left(\frac{-\Delta s}{T_\mathrm{f}}\right) + \left(f'_n - f'_{n-1}\right) \exp\left(\frac{-\Delta s}{2T_\mathrm{f}}\right), \tag{5.43}$$

where f' is the effective separation point, Df is the deficiency function, and T_f is the viscous lag time constant (semichords).

The effective separation point, f', is given as follows:

$$f' = 1 - 0.3 \exp\left(\frac{|\alpha_\mathrm{f}| - \alpha_1}{S_1}\right), \text{ if } |\alpha_\mathrm{f}| \le \alpha_1 , \tag{5.44}$$

$$f' = 0.04 - 0.66 \exp\left(\frac{\alpha_1 - |\alpha_\mathrm{f}|}{S_2}\right), \text{ if } |\alpha_\mathrm{f}| > \alpha_1 , \tag{5.45}$$

where α_f is the effective angle of attack for unsteady leading edge pressure, α_1 is the breaking point corresponding to $f = 0.7$, and S_1 and S_2 define the static stall characteristic. α_1, S_1, and S_2 can be determined from the static lift data.

The effective angle of attack for the unsteady leading edge pressure can be determined using the following equation:

$$\alpha_\mathrm{f} = \frac{C_n'}{C_{N_\alpha}}, \tag{5.46}$$

where C_n' is the normal force coefficient of after taking account for a lag in the leading edge pressure response. C_n' can be determined using equation (5.47) as follows:

$$C_n' = \mathrm{C}_{N_n} - D_{P_n}, \tag{5.47}$$

$$D_{P_n} = D_{Pn-1} \exp\left(\frac{-\Delta s}{T_\mathrm{P}}\right) + \left(C_{Nn}^p - C_{Nn-1}^p\right) \exp\left(\frac{-\Delta s}{2T_\mathrm{P}}\right), \tag{5.48}$$

where D_{P_n} is a deficiency function and T_P is the pressure lag time constants.

5.1.2.3 Vortex Shedding Module

In this module, the normal forces from the previous module add the vortex effect into account. The formation of a vortex appears near the leading edge of the blade section as shown in Figure 5.8. The lift curve shows nonlinear behaviour, and the pitching moment curve of unsteady flow exhibits divergence from the moment curve of the static flow (Leishman, 2002).

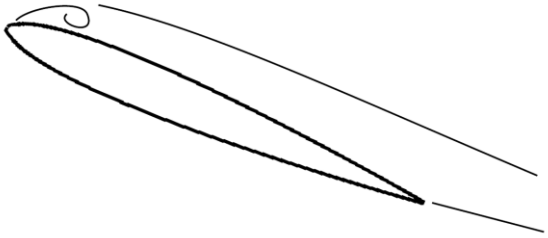

Figure 5.8. Flow separation at the leading edge, followed by the formation of a spilled vortex, moment stall (Leishman, 2002).

The vortex starts to detach and move over the blade surface as shown in Figure 5.9. The sharp drop in the moment coefficient curve occurs when the centre of pressure moves rearward (Leishman, 2002). There is an extra lift due to the vortex convect over the blade surface, and the lift force is maximum when the vortex reaches the trailing edge.

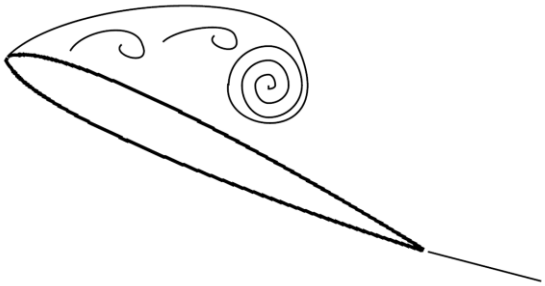

Figure 5.9. Vortex convects over chord (Leishman, 2002).

The phenomenon affects the normal force. The vortex lift force coefficient can be calculated using the following equations:

$$C_{N_n}^V = C_{N_{n-1}}^V \exp\left(\frac{-\Delta S}{T_V}\right) + \left(C_{Vn} - C_{V_{n-1}}\right)\exp\left(\frac{-\Delta S}{2T_V}\right), \text{ if } \tau_v \le T_{vl}, \qquad (5.49)$$

$$C_{N_n}^V = C_{N_{n-1}}^V \exp\left(\frac{-\Delta S}{T_V}\right), \text{ if } \tau_v > T_{vl}, \qquad (5.50)$$

where T_V is the vortex lag time constant; T_{vl} is the vortex passage time constant; τ_v is the nondimensional vortex time parameter, which is used to track the position of the vortex; $\tau_v = 0$ occurs at the onset of separation condition ($C_n' > C_{n1}$); C_{n1} is a critical normal force

coefficient, which is determined by the breaking point of a chord force coefficient from a plot of a chord force coefficient against the normal force coefficient; and C_{V} is the increment in vortex lift, and it can be determined using equation (5.51) as follows:

$$C_{\mathrm{V}} = C_{N_n}^{c}(1-K_{N_n}), \tag{5.51}$$

where K_{N_n} is the unsteady nonlinear lift, and it can be determined by the Kirchhoff approximation as follows:

$$K_{N_n} = \frac{\left(1+\sqrt{f''}\right)^2}{4}. \tag{5.52}$$

The final normal force and chord force coefficients can be obtained using the following equations:

$$C_N = C_N^f + C_N^V, \tag{5.53}$$

$$C_C = \eta C_N{}^2\sqrt{f''}, \text{ if } C_N' < C_{N1}, \tag{5.54}$$

$$C_C = \eta C_N{}^2 f', \text{ if } C_N' > C_{N1}. \tag{5.55}$$

The lift and the drag coefficients, which are used in the BEMT, can be calculated using the following equations:

$$C_d = C_N\sin(\alpha) - C_C\cos(\alpha), \tag{5.56}$$

$$C_l = C_N\cos(\alpha) + C_C\sin(\alpha). \tag{5.57}$$

5.1.3 Validation of the Leishman-Beddoes Model in the Implemented Program

First, the Leishman-Beddoes dynamic stall model was validated to ensure that the dynamic stall model was implemented correctly. The prediction results were compared with the results of oscillating NACA 0012 airfoil at Mach number of 0.4 from Leishman (1989). The parameters of the dynamic stall model for this validation at various mean pitch settings are presented in Table 5.1.

Table 5.1. Parameters of the dynamic stall model

Airfoil Type	Reduce Frequency (k)	Mean Pitch Angle (°)	Amplitude of Oscillating Pitch Angle (°)	$C_{n\alpha}$	α_1	S_1	S_2	T_P	T_f	T_V	T_{VL}
NACA12	0.075	0	8	0.13	11.2	1.5	4.0	2.0	2.5	6.0	11.0
NACA12	0.075	9	8	0.13	11.2	1.5	4.0	2.0	2.5	6.0	11.0
NACA12	0.075	12	8	0.13	11.2	1.5	4.0	2.0	2.5	6.0	11.0
NACA12	0.075	15	8	0.13	11.2	1.5	4.0	2.0	2.5	6.0	11.0

The results of the current implementation of the dynamic stall model were overlaid on the results from the reference at various pitch settings as shown in Figures 5.10–5.13. In these figures, Leishman's results are presented in green lines.

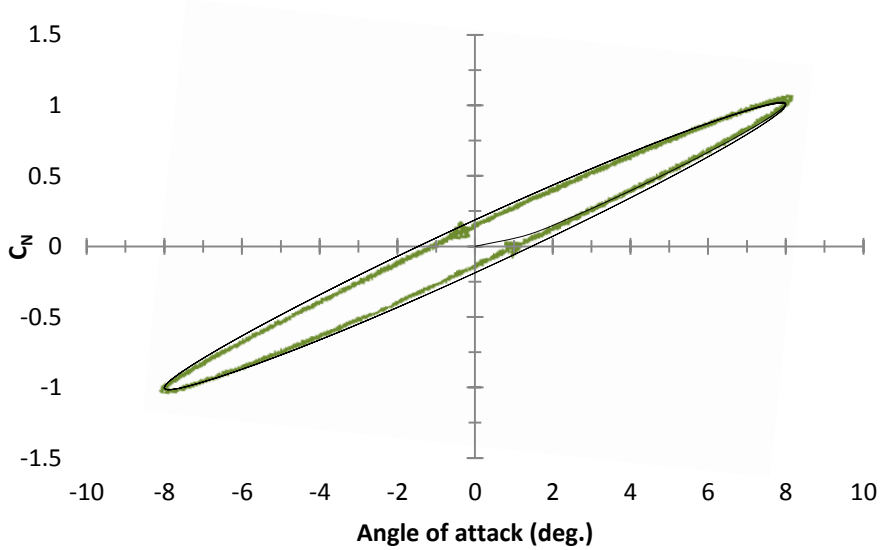

Figure 5.10. Comparison between the normal force coefficient from Leishman's results and the normal force coefficient from the results of the current implemented program at a pitch setting of mean pitch = 0° and cyclic pitch =8°.

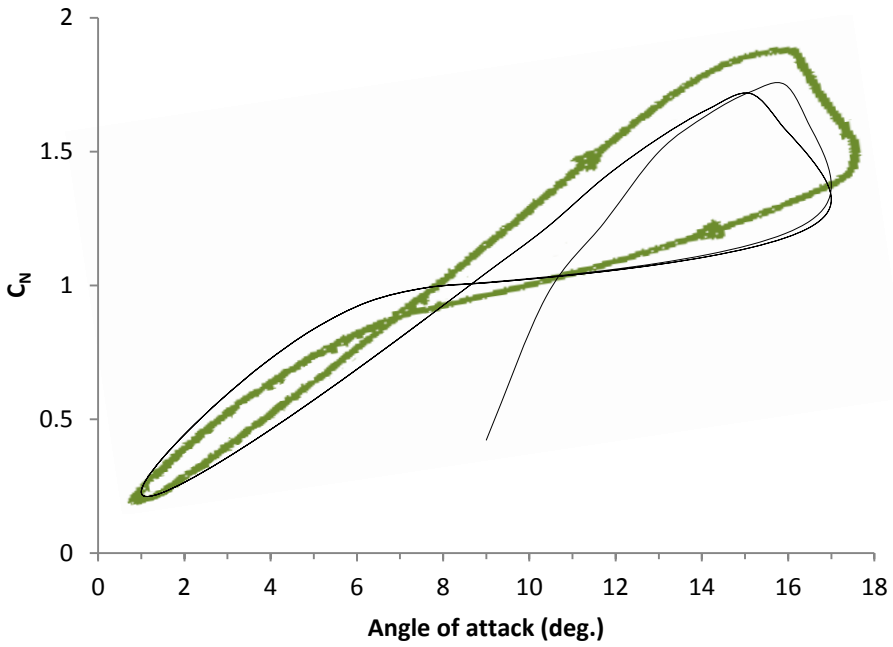

Figure 5.11. Comparison between the normal force coefficient from Leishman's results and the normal force coefficient from the results of the current implemented program at a pitch setting of mean pitch = 9° and cyclic pitch = 8°.

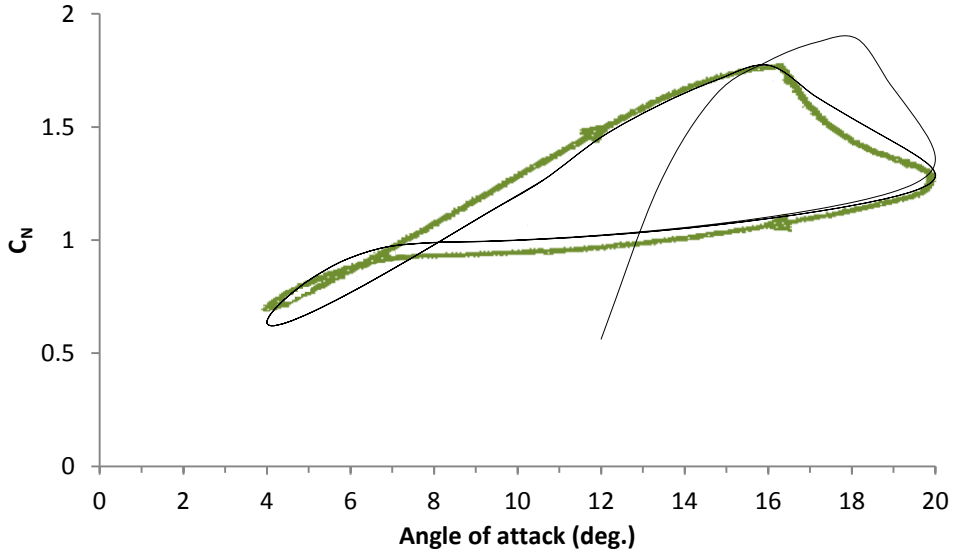

Figure 5.12. Comparison between the normal force coefficient from Leishman's results and the normal force coefficient from the results of the current implemented program at a pitch setting of mean pitch = 12° and cyclic pitch =8°.

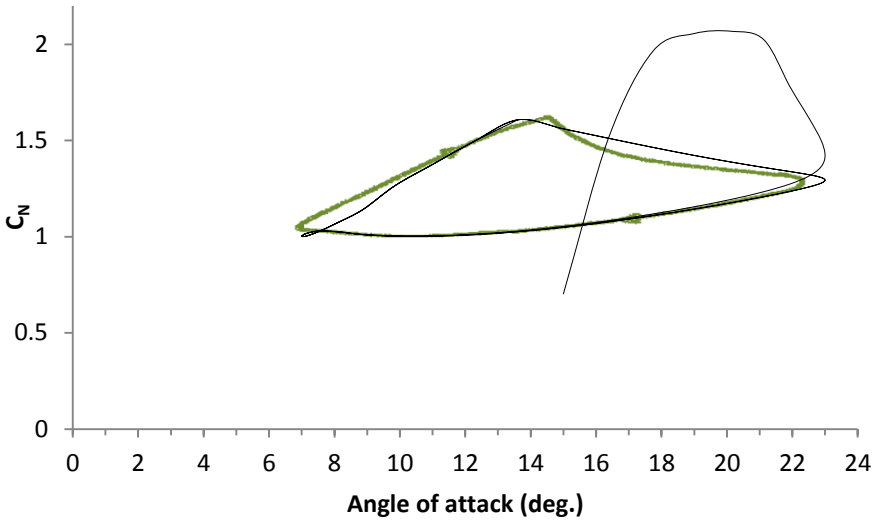

Figure 5.13. Comparison between the normal force coefficient from Leishman's results and the normal force coefficient from the results of the current implemented program at a pitch setting of mean pitch = 15° and cyclic pitch = 8°.

The dynamic stall model was programmed to predict the normal force coefficient. The model uses Duhamel's integral to construct the cumulative effect in the time history of oscillating pitch angle. Therefore, the predicted results of the first shaft revolution must be erased. For instance, the predicted normal force coefficient at the beginning of the plot does not go together with the rest as shown in Figure 5.10. The predicted normal force coefficients from the implemented prediction program correlate well with the coefficient from the Leishman's prediction as shown in Figures 5.10–5.13. The slight discrepancy of both results comes from the differences of the step size of the azimuth angle and the time constant. The step size of azimuth angle was studied and presented in the next section. Modification of the time constants is presented in the section on optimizing the time constants.

5.1.4 Grid Independence Study

The factors, which influence the convergence of the implemented program, are several elements in the spanwise direction, a step size of an azimuth angle and several shaft revolutions. The factors were studied in order to determine a value of each factor. The condition for the study was set to a vehicle speed of 0.2 m/s, a shaft speed of 245 RPM, a mean pitch setting of 20°, and an oscillating pitch of 18°.

5.1.4.1 Number of Elements in the Spanwise Direction

The range of the considered number of elements was from 5 to 20. During the study, the effect of the number of elements and the step size of an azimuth angle is 10°. The forces in the *x*, *y*, and *z* directions were calculated at the difference of the number of elements, and the forces are plotted in Figure 5.14.

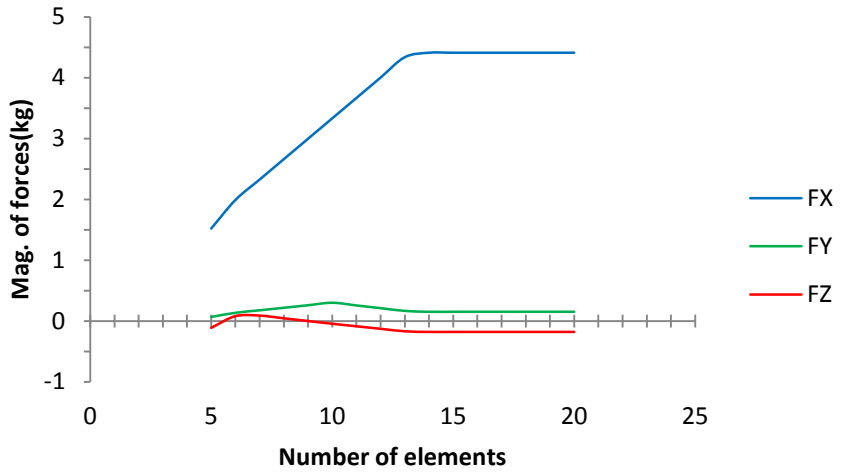

Figure 5.14. The forces in *x*, *y*, and *z* axes with several elements.

It is clear that the number of elements influences the forces. In addition, after the number of elements beyond 15, the magnitude of forces did not change. It has therefore been assumed that a grid-independent solution was obtained for all grids with more than 15 elements.

5.1.4.2 Step Size of Azimuth Angles

The range of the step size of azimuth angles, which was considered, was from 30 to 2. During the study of the effect of the step size of azimuth angles, the number of elements in a spanwise direction is 15. The forces in the *x*, *y*, and *z* directions were calculated at the difference of the step size, and the forces were plotted in Figure 5.15.

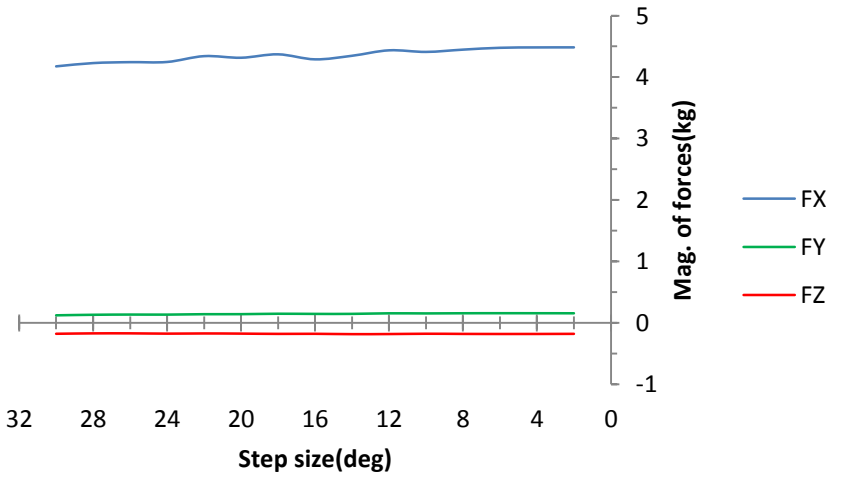

Figure 5.15. The forces in *x*, *y*, and *z* axes with a difference in step size of azimuth angles.

The step size of the azimuth angles has an influence on the forces. After the step size is less than 8°, the magnitude of forces does not change significantly.

5.1.4.3 Number of Shaft Revolution

As mentioned in the section on the validation of the dynamic stall model, the model uses Duhamel's integral to construct the cumulative effect in the time history of oscillating pitch angle. The predicted results of the first revolution must be erased before the average thrust is calculated. The influence of the number of shaft revolution is considered. The range of the number of revolutions is from 1 to 8. The number of elements in a spanwise direction, and the step size of the azimuth angle are 15° and 8°, respectively.

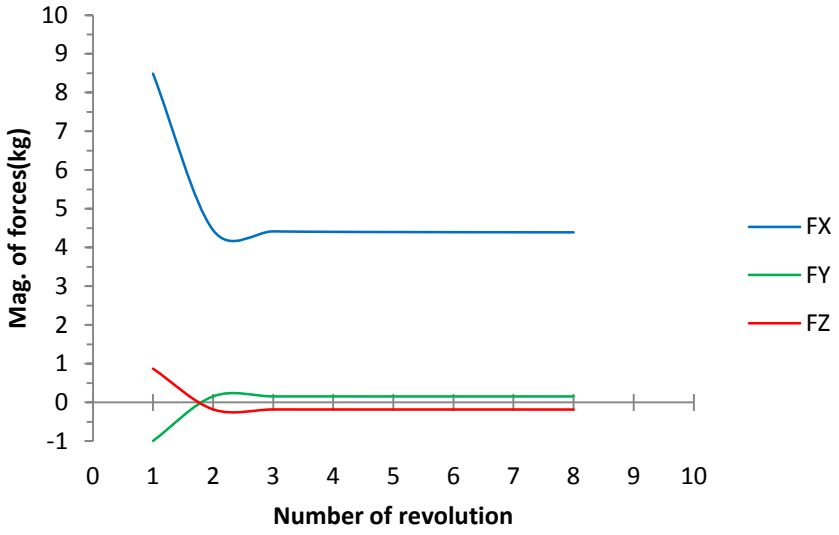

Figure 5.16. The forces in the *x*, *y*, and *z* axes with several shaft revolutions.

The number of shaft revolution insignificantly influences the forces as shown in Figure 5.16. Therefore, the number of revolution of 3 is suitable, and it requires the least computation resources.

5.1.5 Optimizing the Time Constants of the Leishman-Beddoes Dynamic Stall Model

The Leishman-Beddoes dynamic stall uses the semiempirical time constants. The predicted results for unsteady cases depend on the semiempirical time constants T_f, T_p, T_V, and T_{vl}. To improve the accuracy of the prediction program, the time constraints were modified.

5.1.5.1 Methodology

The Leishman-Beddoes dynamic stall model was implemented as a computer program in LabVIEW application. The program carries out the simulation of the forces and moments generated by the CCPP. In this research, the value of each time constant was optimized. The optimization problem was to minimize the total difference between the experimental data and the predicted data, which are based on the dynamic stall model. The function, which is minimized, is defined as follows:

$$f_1 = \sum_{i=1}^{k}\left[\left(Fx_{i_{\text{pred}}}(T_j) - Fx_{i_{\text{exp}}}(T_j)\right)^2\right] + \sum_{i=1}^{k}\left[\left(Fy_{i_{\text{pred}}}(T_j) - Fy_{i_{\text{exp}}}(T_j)\right)^2\right] \ldots + \sum_{i=1}^{k}\left[\left(Fz_{i_{\text{pred}}}(T_j) - Fz_{i_{\text{exp}}}(T_j)\right)^2\right] \quad (5.58)$$

where k is the number of test cases; Fx, Fy, and Fz are the forces in the x, y, and z axes, respectively; and T_j is the time parameter.

In each experimental condition, the values of time constants were varied according to the full factorial design. The ranges of time constants are shown in Table 5.2.

Table 5.2. Range of time constants to be optimized

Parameters	Initial Value	Final Value	Increment
$T_{\text{f}}, T_{\text{P}}, T_{\text{V}}, T_{\text{vl}}$	0.0001	20.0001	2

The experiment was also based on the full factorial design. It means that one parameter was varied while keeping the other parameter fixed. The experimental conditions, which are used in the optimization process, are presented in Table 5.3. The full details of the experiment are presented in Chapter 4.

Table 5.3. Test matrix

Parameters (Pitch Setting)	Level				
	–1	–0.5	0	+0.5	+1
Collective pitch	–80%	–40%	0%	+40%	+80%
Cyclic pitch (up/down)	–80%	–40%	0%	+40%	+80%
Cyclic pitch (right/left)	–80%	–40%	0%	+40%	+80%

In the optimization process of the time constants, the analysis procedure in each experimental condition was as follows:

1. Select the experimental condition.
2. Predict the forces and moments for the experimental condition.
3. Calculate the difference between the experimental data and the prediction data.
4. Model relationships between the input parameters (time constraints) and the response variables (the calculated result in the second step) using the response surface methodology (RSM). The details of RSM can be found in a work of Myers, Montgomery, and Anderson-Cook (2011).
5. Search for the extreme point for this experimental condition.
6. Repeat from step 1 to step 5.
7. Search for the global solution.

The process of the optimization techniques is shown in Figure 5.17.

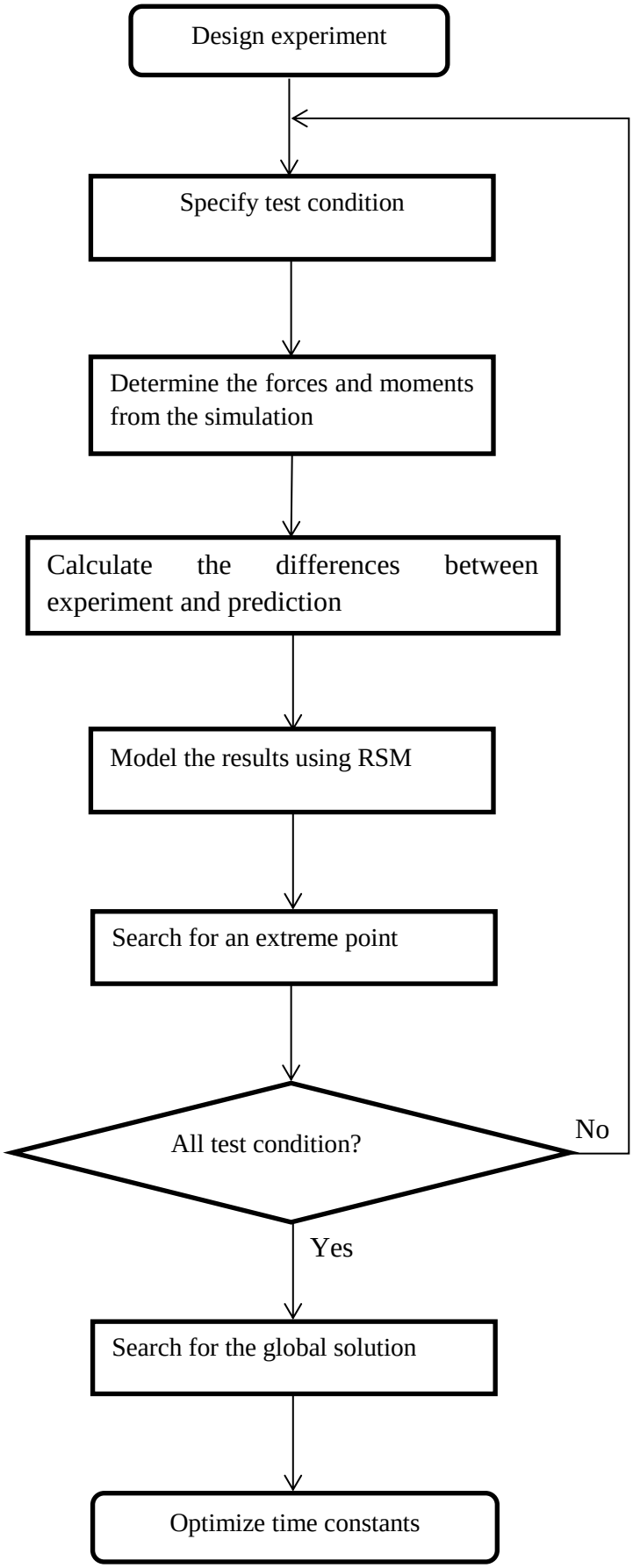

Figure 5.17. Optimization process.

5.1.5.2 Optimization Results

The different pitch settings and the corresponding values for optimized time constants are shown in Table A3.0.1. The main effect plots for each time constant are used in conjunction with ANOVA to assess differences of the time constants with variations in pitch settings. The mean of the time constants is shown by a horizontal line in Figures 5.18–5.21.

A main effects plot shows a time constant for each pitch setting level connected by lines. If the line is horizontal, no main effect is present. If the line is not horizontal then there is a main effect, and different levels of the pitch setting affect the time constant differently. The steeper the line's slope, the greater the magnitude of the effect. For instance, the collective pitch setting (Col) affects the viscous lag time constant, T_f as presented in Figure 5.18. The collective pitch setting significantly affects T_f because the steepness of the trend line of T_f is high. The trend lines of T_f for the other factors—up/down and right/left cyclic pitch settings—are less steep than the trend lines of T_f for the collective pitch setting. It means that the other factors are less statistically significant than the collective pitch factor. The trend lines of the pressure lag time constant (T_P), the vortex lag time constant (T_V), and the vortex passage time constant (T_{VL}) for the collective pitch setting in Figures 5.19–5.21 show that the collective pitch setting significantly affects the other time constants. The trend lines of each time constants for the other factors indicate that they do not significantly influence the time constants. However, the main effect plot for T_{VL} presents that the up/down and right/left pitch settings are significant.

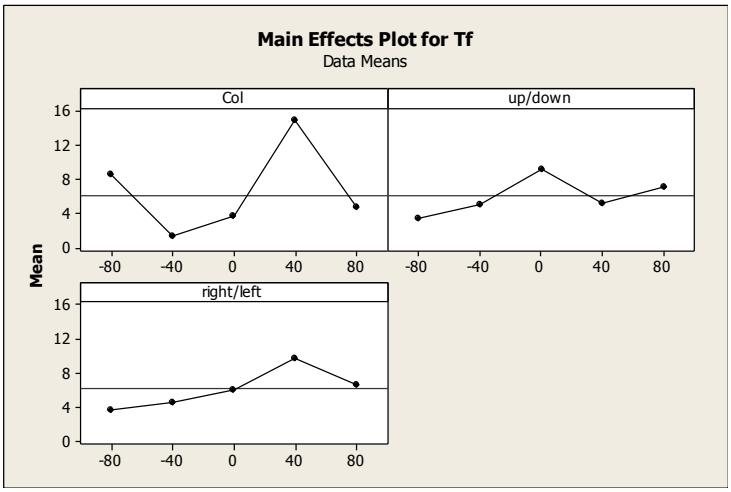

Figure 5.18. The main effect plot for the viscous lag time constant, T_f.

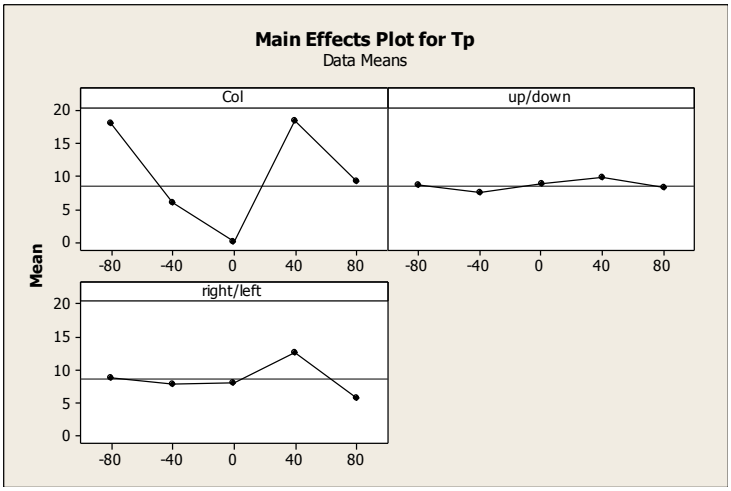

Figure 5.19. The main effect plot for the pressure lag time constant, T_P.

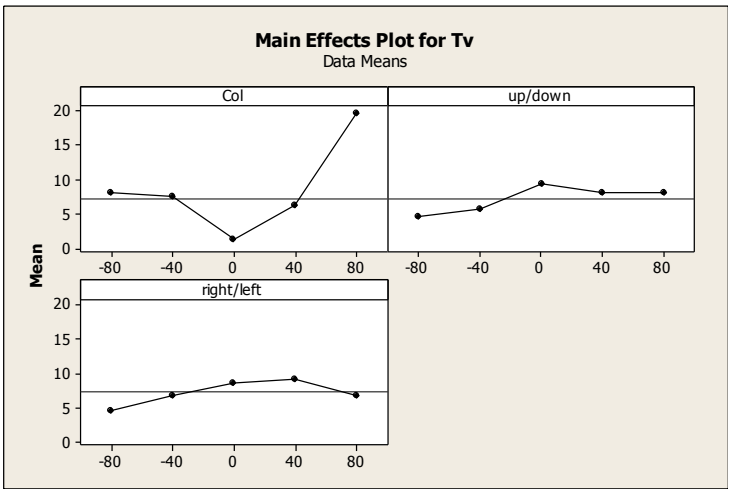

Figure 5.20. The main effect plot for the vortex lag time constant, T_V.

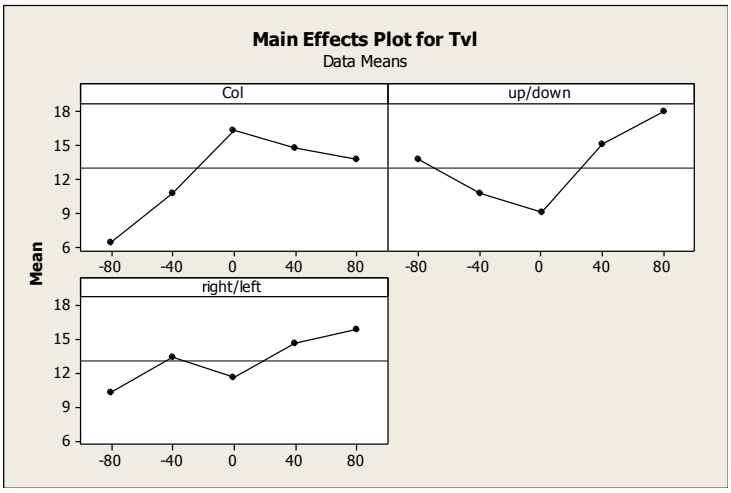

Figure 5.21. The main effect plot for the vortex passage time constant, T_{VL}.

The analysis presented that the optimized value of each time constant does not have a single value for all pitch settings. Therefore, the optimized values of each time constant for different

pitch setting are fit in response surface plots as shown in the following figures. Figures 5.22, 5.24, 5.26, and 5.28 are the surface plot of T_{VL}, T_P, T_V, and T_f, respectively. Each surface plot can be expressed in a polynomial equation with three variables, as shown in Table 5.4. The table lists the equations for each time constant in a tabular format. The index for the polynomial coefficients is shown in the first column in the table. The next four columns are the polynomial coefficients for each time constant. Each optimized time constant equation can be established by multiplying the polynomial coefficients with the parameters found in the sixth column. The coded parameter (Col) represents the percent of the collective pitch setting. The second coded parameter (Up) represents the percent of the up/down cyclic pitch setting. Similarly, the coded parameter (Right) represents the percent of the right/left cyclic pitch setting.

Contour plots of T_{VL}, T_P, T_V, and T_f are plotted in Figures 5.23, 5.25, 5.27, and 5.29, respectively. The contour plots show the contribution of two pitch settings simultaneously, and the other pitch setting is kept at its average level. The optimized time constants for a different pitch setting can be found in the contour plots. For example, Figure 23 presents the contour plot of the optimized T_{VL} as a function of the collective and the up/down cyclic pitch settings.

Table 5.4. Table of time constant equations.

Inde	Coefficients				
	T_f	T_P	T_V	T_{VL}	
0	6.61202E+00	–1.84067E+0	4.32082E+00	1.30191E+00	*1
1	2.61539E–01	3.01630E–01	5.09228E–02	3.89126E–03	*Col
2	–1.90623E–0	8.43675E–06	5.23333E–05	1.79058E–02	*Up
3	–3.89962E–0	–2.56550E–0	–1.95364E–0	4.95539E–04	*Right
4	2.48253E–19	–5.80034E–1	2.48253E–19	–1.90309E–1	*Col * Up
5	1.48952E–19	–4.81141E–1	2.17222E–19	–1.43951E–1	*Col * Right
6	1.48952E–19	–7.00382E–2	2.48253E–19	–2.45416E–1	*Up * Right
7	1.00892E–04	1.05897E–02	1.96010E–03	–1.21511E–0	*Col^2
8	–1.65020E–0	–5.01748E–0	–2.73352E–0	5.01397E–03	*Up^2
9	–2.65880E–0	1.93627E–03	–5.19000E–0	6.93598E–03	*Right^2
10	–5.32111E–2	–6.14396E–2	0.00000E+00	–1.35496E–2	*Col * Up * Right
11	9.01220E–07	8.74210E–09	0.00000E+00	–8.69983E–0	*Col^2 * Up
12	7.15986E–09	–2.39169E–1	0.00000E+00	–2.32288E–0	*Col^2 * Right
13	5.24585E–07	–6.44665E–0	0.00000E+00	4.90490E–07	*Col * Up^2
14	–4.40146E–0	–1.81578E–0	0.00000E+00	5.00740E–06	*Col * Right^2
15	7.15986E–09	–2.39169E–1	0.00000E+00	–2.32288E–0	*Up^2 * Right
16	8.84954E–07	–8.86459E–0	0.00000E+00	–8.15538E–0	*Up * Right^2
17	–4.26049E–0	–4.34379E–0	0.00000E+00	3.96928E–06	*Col^3
18	2.08231E–06	–5.07851E–0	0.00000E+00	–1.94179E–0	*Up^3
19	–4.20311E–0	5.09585E–13	0.00000E+00	–5.41988E–0	*Right^3
20	0.00000E+00	–1.42969E–0	0.00000E+00	–7.37658E–0	*Col^2 * Up^2
21	0.00000E+00	1.85450E–22	0.00000E+00	2.78175E–22	*Col^2 * Up*
22	0.00000E+00	–1.85102E–0	0.00000E+00	–3.92842E–0	*Col^2 * Right^2
23	0.00000E+00	–9.27249E–2	0.00000E+00	2.20222E–22	*Col * Up^2*

24	0.00000E+00	0.00000E+00	0.00000E+00	2.41085E–22	*Col * Up*
25	0.00000E+00	1.29190E–07	0.00000E+00	–1.80205E–0	*Up^2 * Right^2
26	0.00000E+00	2.22232E–22	0.00000E+00	1.87483E–22	*Col^3 * Up
27	0.00000E+00	2.32738E–22	0.00000E+00	1.35764E–22	*Col^3 * Right
28	0.00000E+00	–5.17195E–2	0.00000E+00	1.16369E–22	*Col * Up^3
29	0.00000E+00	–2.58597E–2	0.00000E+00	7.23264E–23	*Col * Right^3
30	0.00000E+00	–3.87896E–2	0.00000E+00	2.32738E–22	*Up^3 * Right
31	0.00000E+00	6.46493E–24	0.00000E+00	1.55158E–22	*Up * Right^3
32	0.00000E+00	–1.14982E–0	0.00000E+00	2.60467E–07	*Col^4
33	0.00000E+00	7.19676E–08	0.00000E+00	–4.66360E–0	*Up^4
34	0.00000E+00	–3.09918E–0	0.00000E+00	–7.28124E–0	*Right^4
Col indicates collective pitch setting; Up, up/down cyclic pitch setting; Right, right/left					

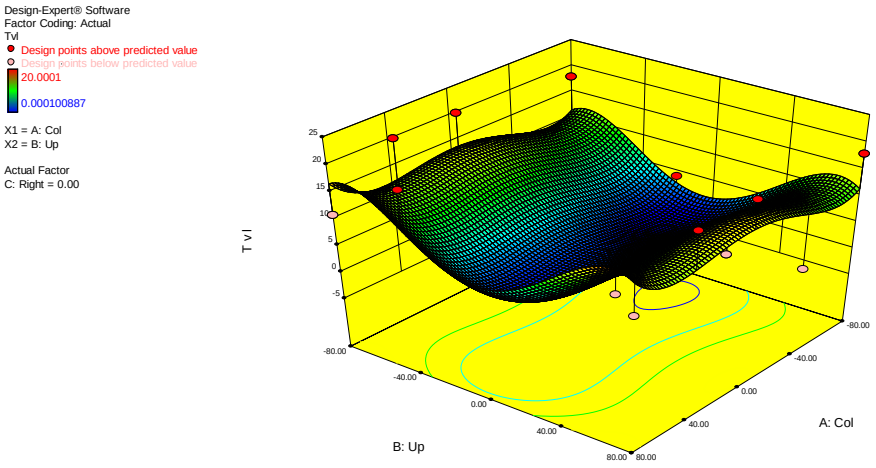

Figure 5.22. The respond surface plot of T_{VL} for various collective and up/down pitch settings which can be represented by the quartic polynomial equation with two variables .

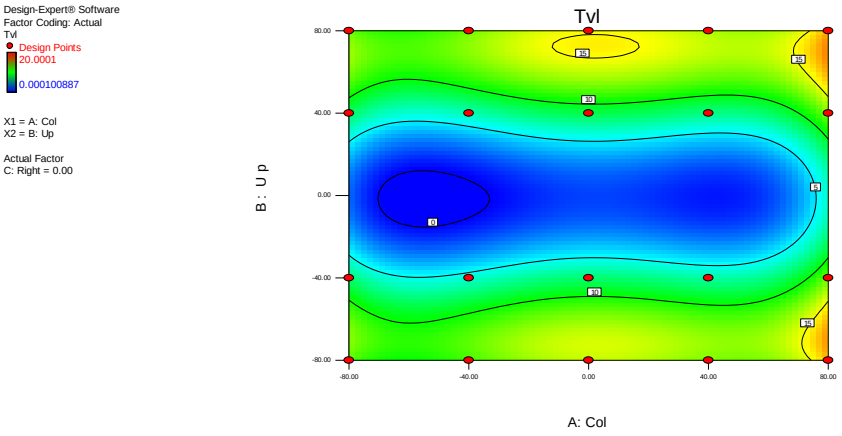

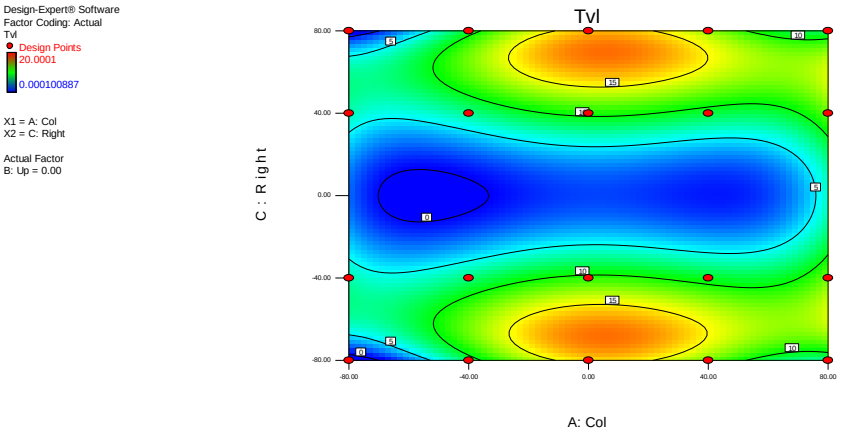

Figure 5.23. The contour plot of T_{VL} for various collective pitch setting, up/down pitch setting (top), and right/left pitch setting (bottom).

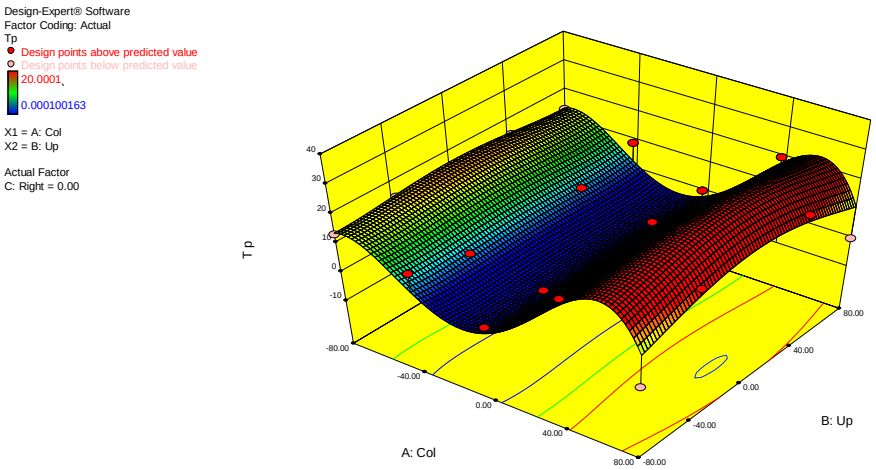

Figure 5.24. The respond surface plot of T_P for various collective and up/down pitch settings which can be represented by the quartic polynomial equation with two variables.

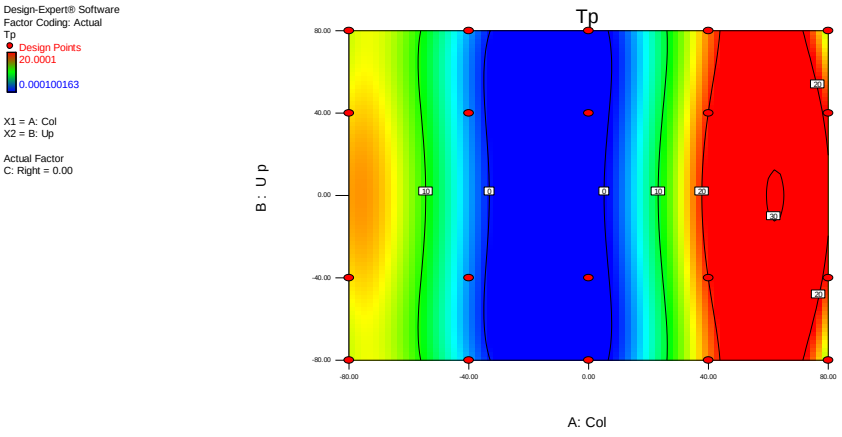

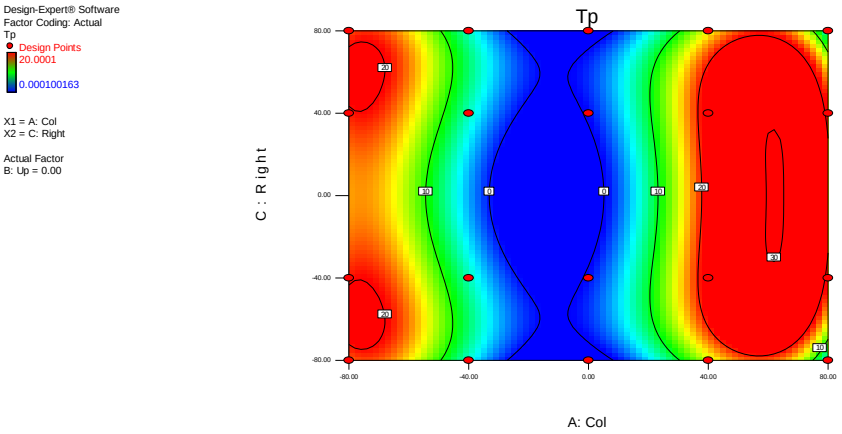

Figure 5.25. The contour plot of T_P for various collective pitch setting, up/down pitch setting (top), and right/left pitch setting (bottom).

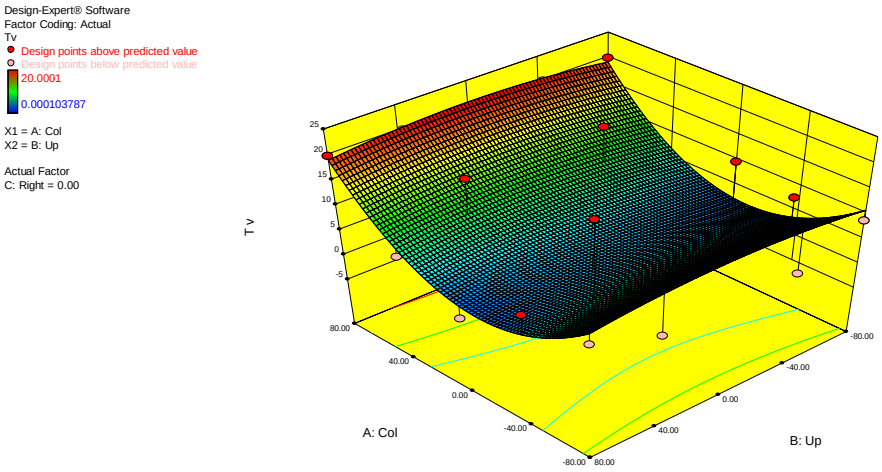

Figure 5.26. The respond surface plot of T_V for various collective and up/down pitch settings which can be represented by the quadratic polynomial equation with two variables.

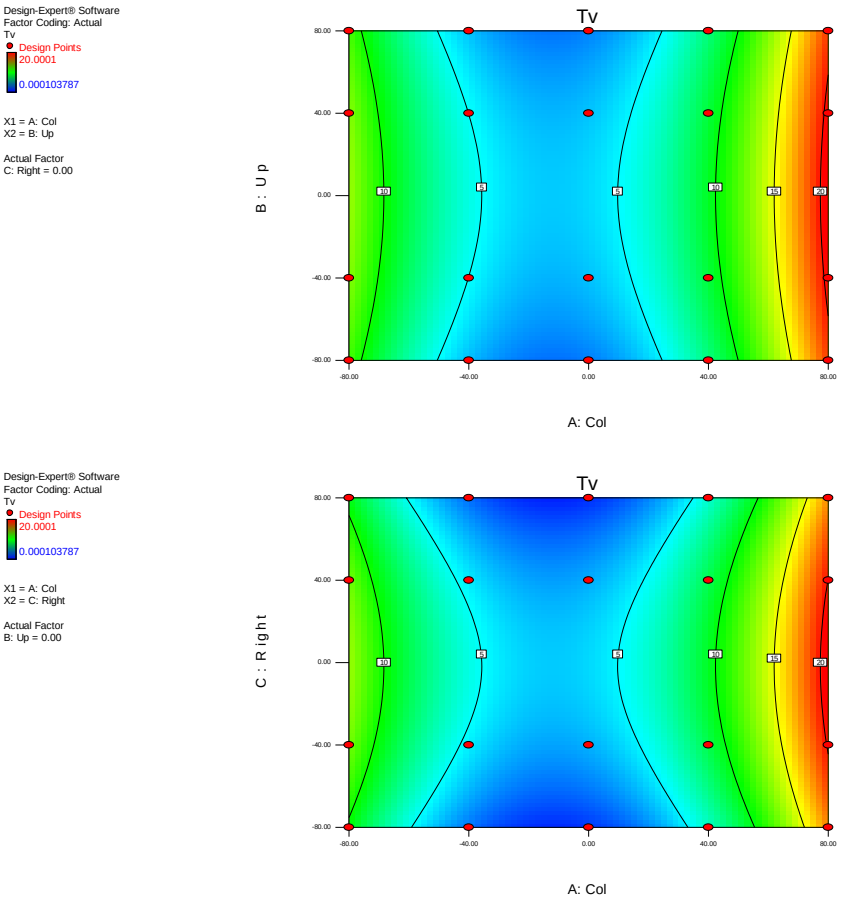

Figure 5.27. The contour plot of T_V for various collective pitch setting, up/down pitch setting (top), and right/left pitch setting (bottom).

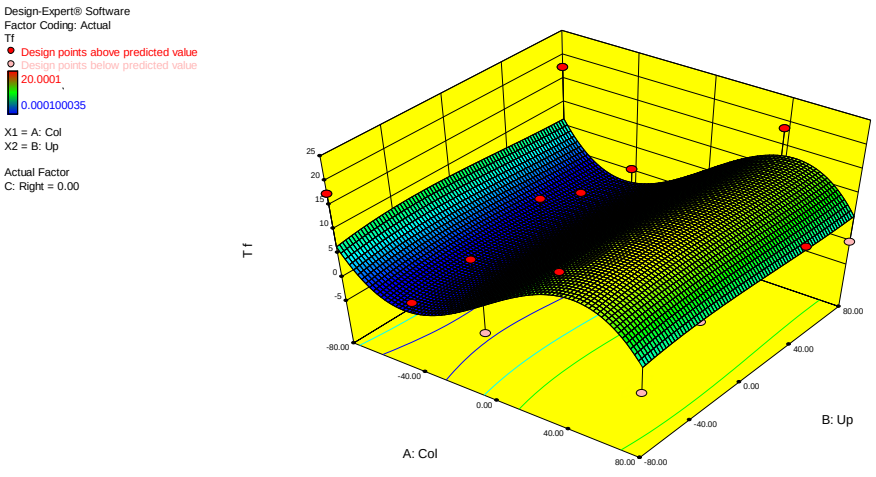

Figure 5.28. The respond surface plot of T_f for various collective and up/down pitch settings which can be represented by the cubic polynomial equation with two variables.

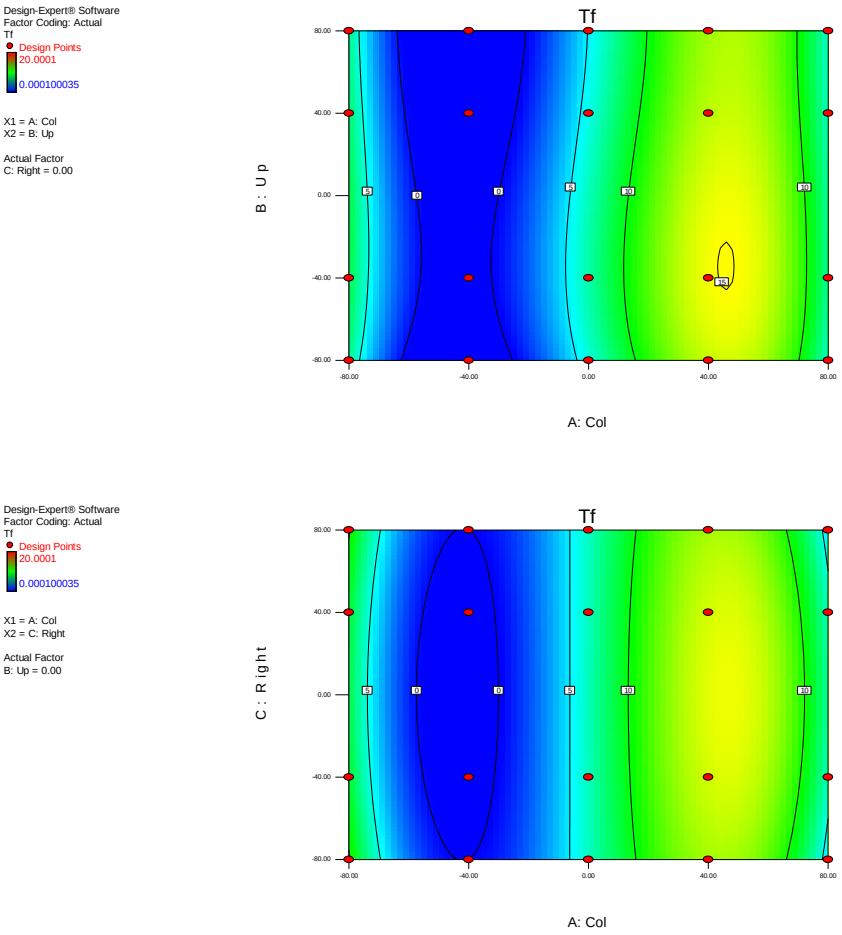

Figure 5.29: The contour plot of T_f for various collective pitch setting, up/down pitch setting (top), and right/left pitch setting (bottom).

5.2 Comparison between Experimental and Numerical Predicted Results for Transverse Thrusts

A comparison was conducted between the experimental and the numerical predicted transverse thrusts. The numerical prediction used the Leishman-Beddoes model to capture the oscillating effect of the blades and the dynamic stall effect. The transverse forces were measured at various pitch settings and advance coefficients, as mentioned in the previous chapter. The transverse forces were numerically predicted at the same conditions as the experiment. The following figures present the experimental results and predicted results in various methods. The first method used the Blade Element Momentum Theory (BEMT), which did not take any unsteady hydrodynamic effects into account. The second method still used the BEMT, but the lift and drag coefficients were modified by considering the oscillating effect of the blades and the separation of the flow. The modification of the life and drag coefficients was performed by each module of the dynamic stall model, as mentioned in the section of the Leishman-Beddoes dynamic stall model. The third method considered the

vortex effect, which was an addition to the third method. The time constants in the second and the third methods were not optimised. The last method is similar to the former method, but all time constants were optimised.

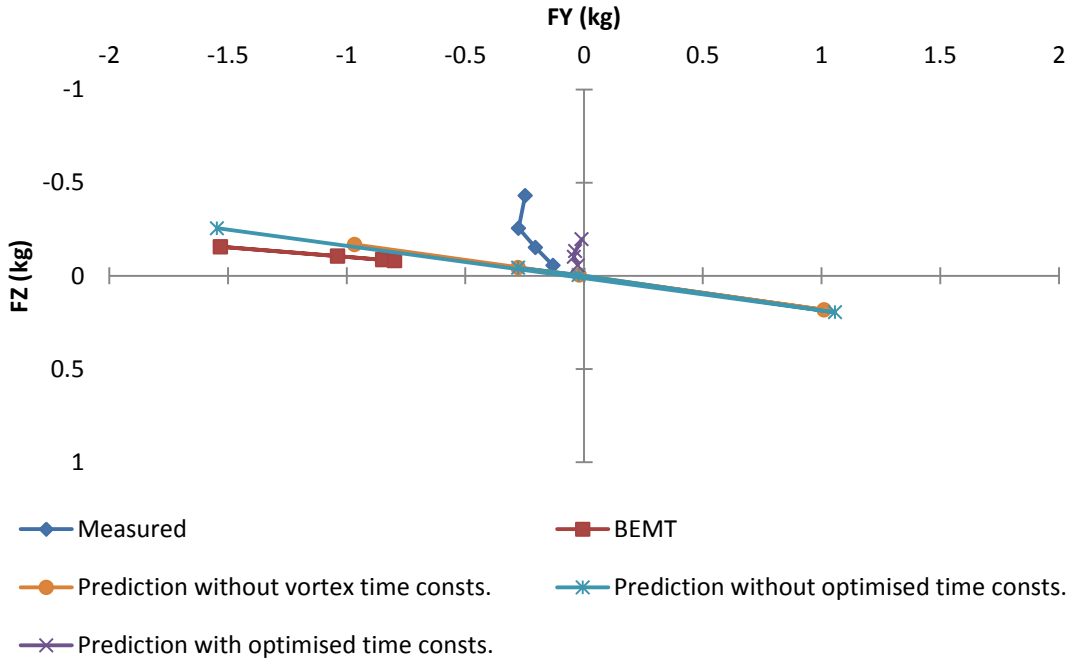

Figure 5.30. Comparison between the predicted results in various methods and the measured results for a collective pitch setting of –80%, an up/down pitch cyclic setting of –80%, and a right/left cyclic pitch setting of –80% at various advance coefficients.

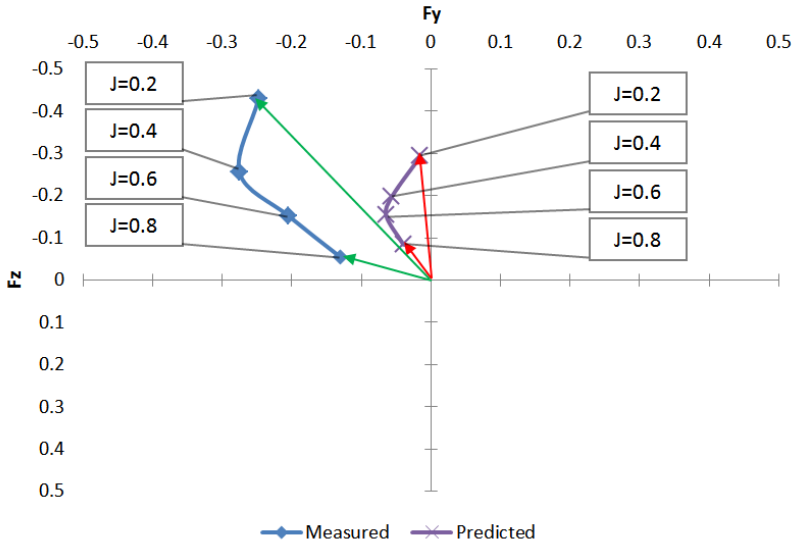

Figure 5.31. Comparison between the predicted results with the optimised time constants and the measured results for a collective pitch setting of –80%, an up/down pitch cyclic setting of –80%, and a right/left cyclic pitch setting of –80% at various advance coefficients.

The first, second, and third prediction methods cannot predict either magnitude or direction of the transverse thrusts, as shown in Figures 5.30, 5.32, 5.34, and 5.36. The BEMT method always overestimated the thrusts, as shown in Figures 5.32, 5.34, and 5.36. In addition, the directions of each predicted thrust at each pitch angle setting were in the same direction, which can be seen in all figures. When the BEMT method was compared with the others, the direction of the predicted transverse thrusts that were predicted by the other methods shifted away from the direction of the predicted thrust estimated by the BEMT method. This is the result of modifying the lift and drag coefficients. The method with the optimised time constants improved the prediction of the thrust. The predicted results with the optimised time constants were not consistent with the experimental results in either magnitude or direction of thrust results when the collective pitch setting was applied, as shown in Figures 5.31 and 5.37. However, these prediction results with the optimised time constants were good in terms of picking up the trends.When the collective pitch setting was kept at zero percent, the prediction results with the optimised time constants have similar magnitudes to the experimental forces, as presented in Figures 5.33 and 5.35.

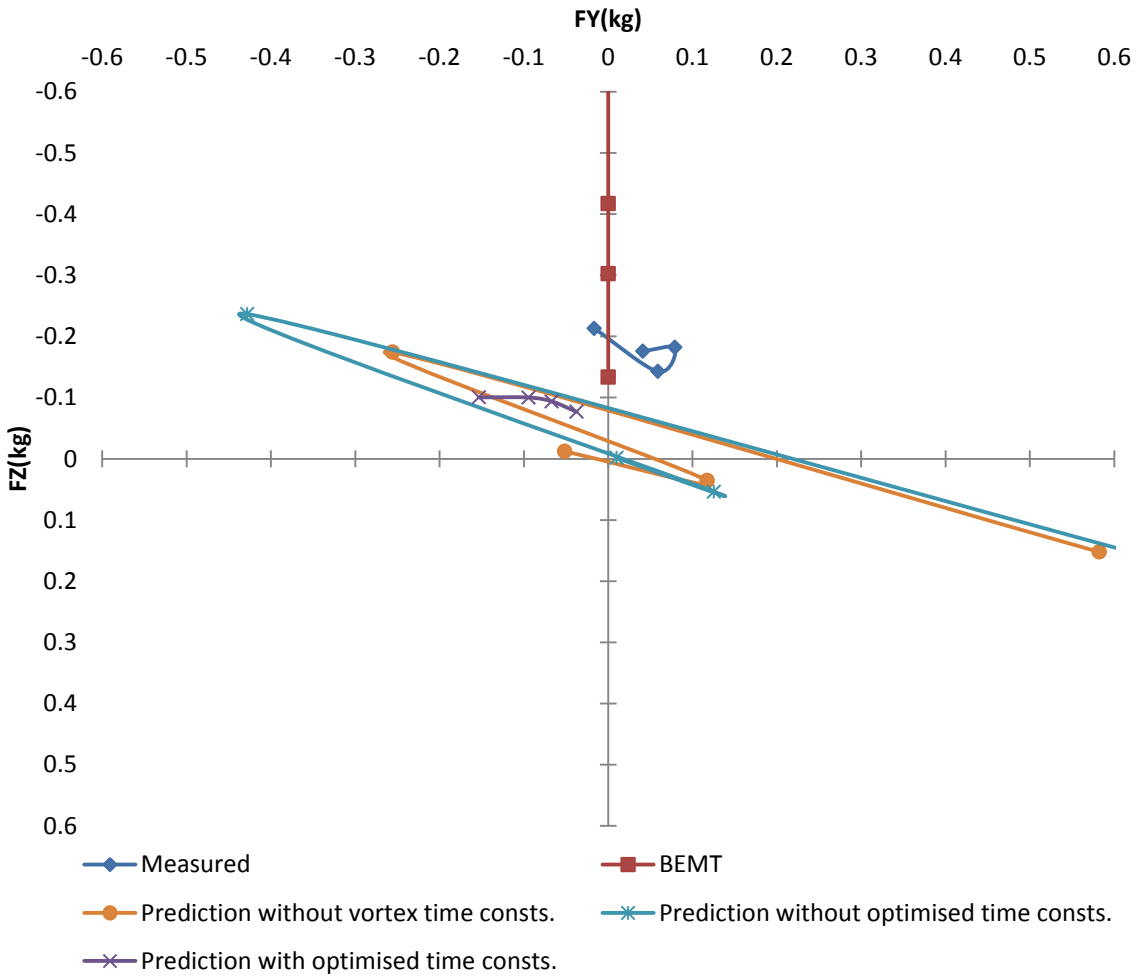

Figure 5.32. Comparison between the predicted results in various methods and the measured results for a collective pitch setting of 0%, an up/down pitch cyclic setting of –80%, and a right/left cyclic pitch setting of 0% at various advance coefficients.

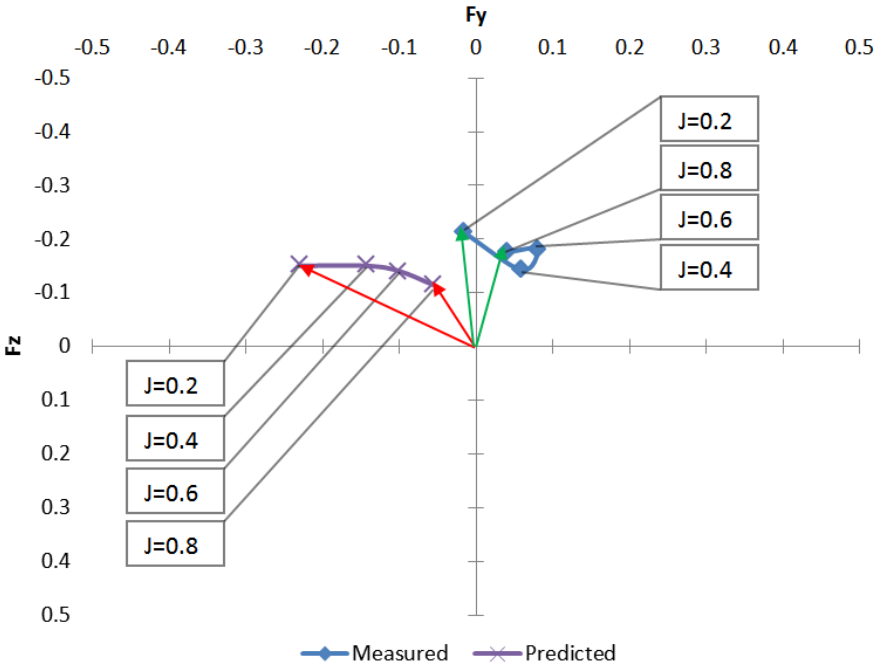

Figure 5.33. Comparison between the predicted results with the optimised time constants and the measured results for a collective pitch setting of 0%, an up/down pitch cyclic setting of –80%, and a right/left cyclic pitch setting of 0% at various advance coefficients.

The shift of the thrust direction can be seen in all cases tested. When the method with the optimized time constants was used, the discrepancy of the direction of the transverse thrusts between the predicted and the experimental thrusts was approximately 30°. In addition, at the lower advance coefficient, the CCPP can generate higher transverse forces as in all figures. The predicted and the experimental transverse thrusts changed in a similar direction as the advance coefficient changed, and this can be observed in the path line of the thrusts in each figure.

The BEMT assumed that the incoming flow was perpendicular to the propeller plane. The incoming flow during the experiment was, however, not perpendicular but it was also affected by the turning propeller collar. This feature could cause the error in the prediction of the thrusts. The incoming flow should be studied in the future by using numerical software, CFD or conducting further experiments.

The numerical model with optimised time constants was unable to predict the experimental results however the trend was clearly similar. Both prediction and experimental results show that the transverse thrust turn into the same direction as the advance coefficient is changed. This result implies that the propeller blades of the CCPP experienced the dynamic stall phenomena. Furthermore, a cause that led to the discrepancy between the predicted and the experimental results is that the time constants could not sufficiently represent the lagged lift force. In the optimization section, the time constraints were studied. However, fitting errors of the response surfaces of optimized time constants exist for variations in pitch settings. This discrepancy could be the cause of the difference between the predicted and the experimental transverse forces. In the future, more experimental data is required to improve the

optimization of the time constants. In addition, the cascade effect might be hydrodynamically significant near the propeller hub and might affect the transverse forces on the propeller. The cascade effect was not included in the prediction program, but future research may include these corrections.

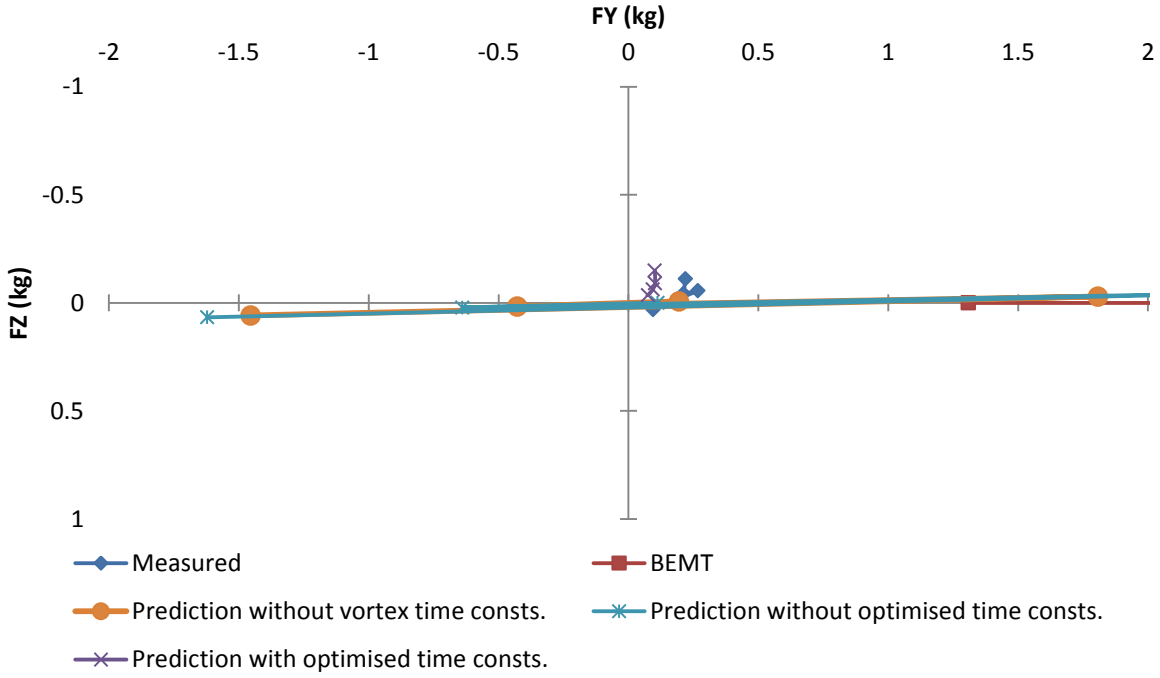

Figure 5.34. Comparison between the predicted results in various methods and the measured results for a collective pitch setting of 0%, an up/down pitch cyclic setting of 0%, and a right/left cyclic pitch setting of –80% at various advance coefficients.

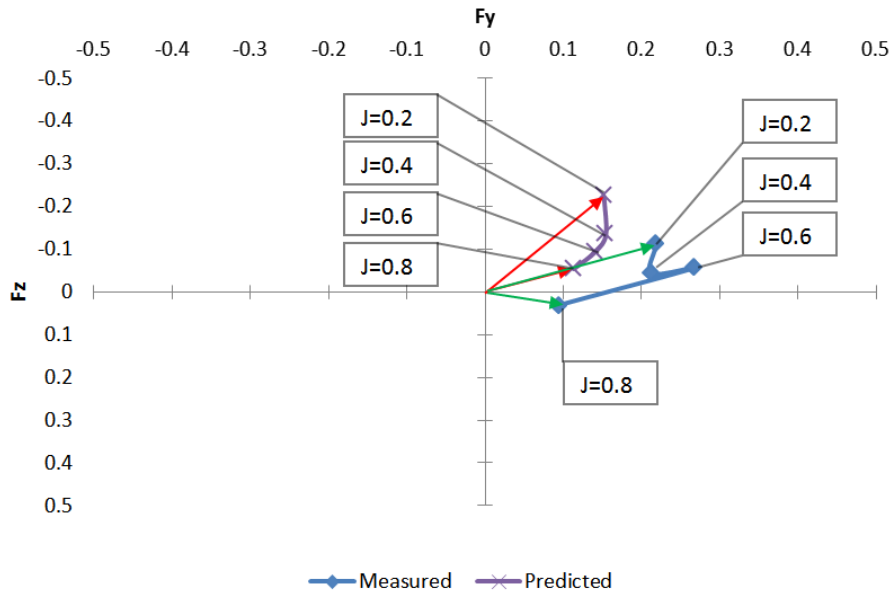

Figure 5.35. Comparison between the predicted results with the optimized time constants and the measured results for a collective pitch setting of 0%, an up/down pitch cyclic setting of 0%, and a right/left cyclic pitch setting of –80% at various advance coefficients.

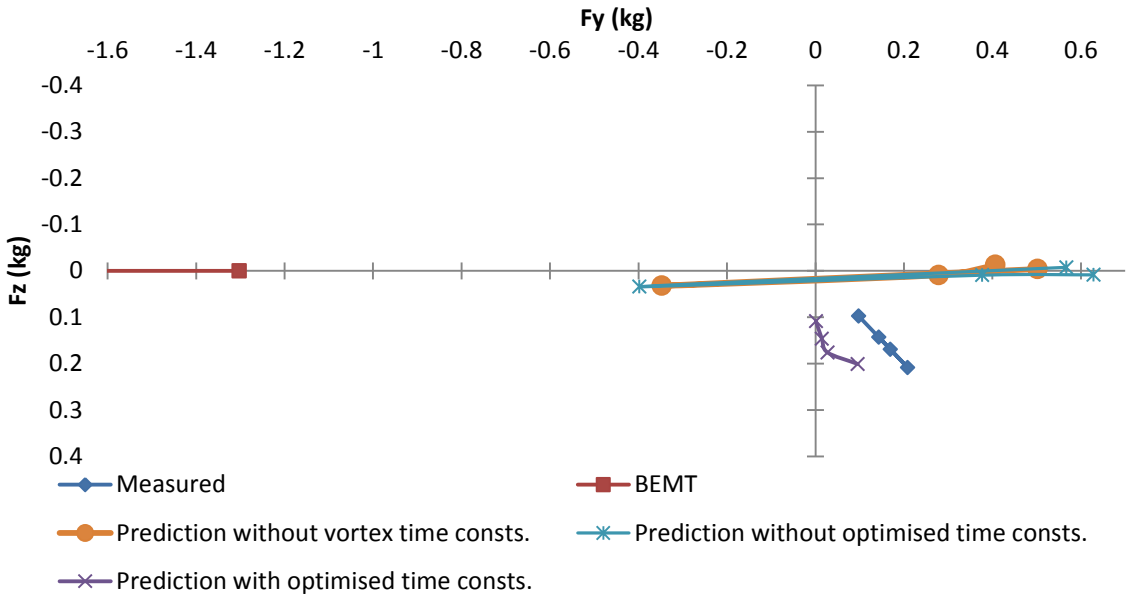

Figure 5.36. Comparison between the predicted results in various methods and the measured results for a collective pitch setting of 80%, an up/down pitch cyclic setting of 0%, and a right/left cyclic pitch setting of 80% at various advance coefficients.

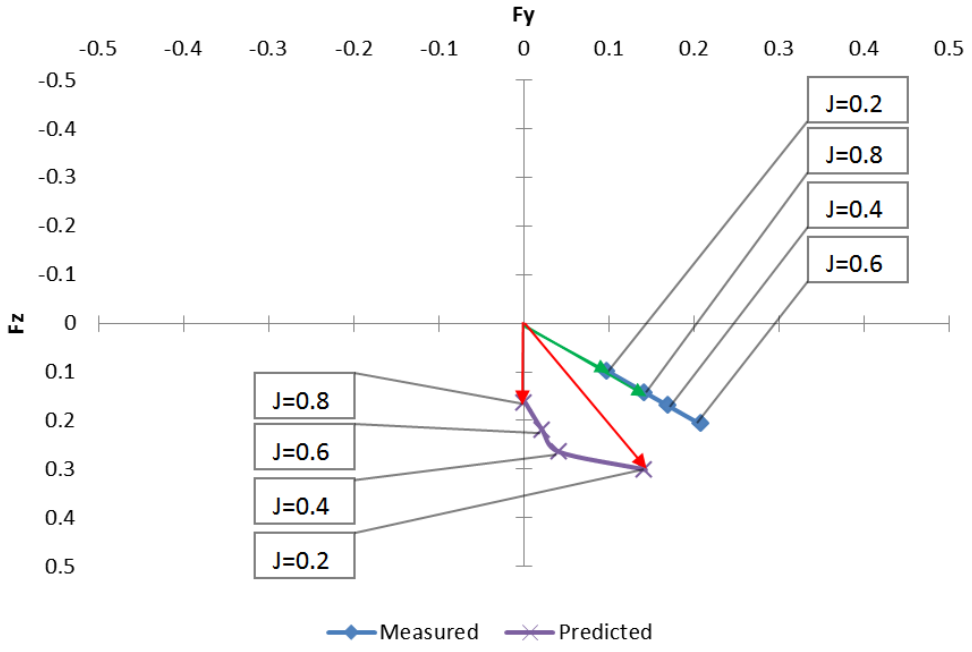

Figure 5.37. Comparison between the predicted results with the optimized time constants and the measured results for a collective pitch setting of 80%, an up/down pitch cyclic setting of 0%, and a right/left cyclic pitch setting of 80% at various advance coefficients.

Chapter Summary

The performance prediction program was implemented using a LabVIEW application software. The BEMT and the Leishman-Beddoes dynamic stall models were used to predict the performance of the CCPP. The convergence of the implemented program was studied to establish a suitable number of elements in the spanwise direction, the step size of azimuth angles, and the number of shaft revolutions to convergence. Furthermore, the time constants in the dynamic stall model were optimized based on the experimental results. In comparison between the predicted and the experimental results, the predicted results did not agree well with the experimental results in cases of the collective pitch setting applied. However, when the collective pitch setting kept at zero, the predicted results have a similar magnitude to the experimental forces. The prediction method with only BEMT cannot provide an accurate result. Furthermore, the prediction method with optimized time constants is great better than the methods without optimized time constants. The incoming flow should be studied in the future by using a numerical software, CFD or conducting an experiment. Furthermore, a cause that led to the discrepancy between the predicted and the experimental results is that the time constants could not sufficiently represent the lagged lift force. In the future, more experimental data is required to improve the optimization of the time constants.

Chapter 6 Simulation Study

The dynamic model of the underwater vehicles was based on the body buildup method as mentioned. The numerical simulation program was developed. The motion control system of the underwater vehicle was designed as mentioned in Chapter 2. The numerical simulation study was used to assess the manoeuvrability of an underwater vehicle equipped with the collective and cyclic pitch propeller (CCPP). In addition, the study demonstrated the capability of an underwater vehicle equipped with only one CCPP. Both open-loop and closed-loop motion controls were studied.

6.1 Manoeuvrability

The term "manoeuvrability" is defined as "the capability of the craft to carry out specific manoeuvres" (Fossen, 2011).

The manoeuvrability of the underwater vehicles was assessed by using the turning circle test, the zigzag manoeuvre test, yaw control, depth, speed control, control, and trajectory tracking control.

6.1.1 Turning Circle Test

The turning circle test was used to assess the turning ability of the underwater vehicle. The turning diameter was determined. In the simulation study, the shaft speed, the collective pitch, the angle, and left/right cyclic pitch angle were varied while the up/down cyclic pitch angle was kept constant at 0%. The testing parameters were varied as shown in Table 6.1.

Table 6.1. Test matrix for the turning circle test (up/down cyclic pitch is constant at 0%)

Parameters	Start	End	Increment
RPM	250	350	100
Collective pitch (%)	50	100	50
Right/left cyclic pitch (%)	−100, −50, −25, −10, 10, 25, 50, 100		

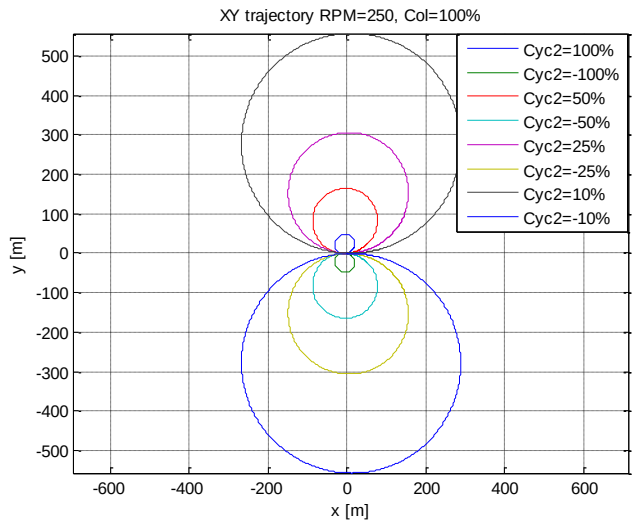

Figure 6.1. Turning circle tests at RPM = 250, collective pitch angle = ±100%, and various left/right cyclic pitch angles.

Figure 6.3 shows turning circles for the shaft speed of 250 RPM, collective pitch angle = 100% and −100%, and various left/right cyclic pitch angles. The initial speed of the underwater vehicle is 0 m/s. From Figure 6.3, it can be seen that the underwater vehicle equipped with CCPP has good turning manoeuvres.

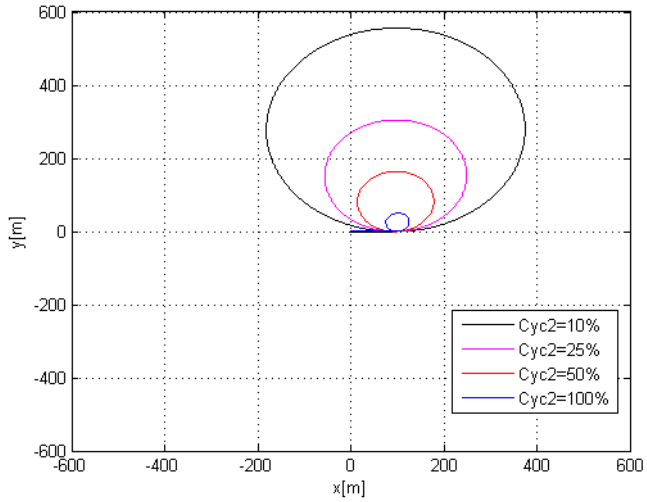

Figure 6.2. Turning circle tests at RPM = 250, collective pitch angle = +100%, and various left/right cyclic pitch angles.

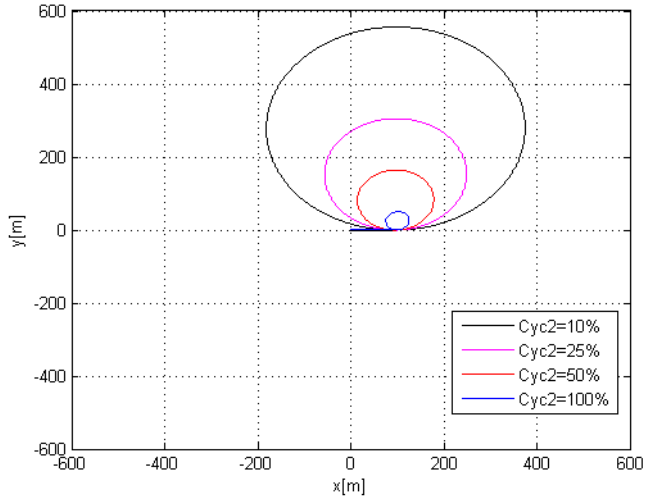

Figure 6.3. Turning circle tests at RPM = 350, collective pitch angle = +100%, and various left/right cyclic pitch angles.

From Figure 6.4, the shaft speed was set to 250 RPM, and the collective pitch angle was set to 100%. The left/right cyclic pitch angle was varied for each run. The initial steady speed of the vehicle was 1.25 m/s. Figure 6.5 shows turning circles for the shaft speed of 250 RPM, collective pitch angle = 100% and –100%, and various left/right cyclic pitch angles. The initial speed of the underwater vehicle was 1.8 m/s. From Figures 6.4 and 6.5, the underwater vehicle equipped with CCPP performed the turning circle test well. The paths of the vehicle are elliptical shape.

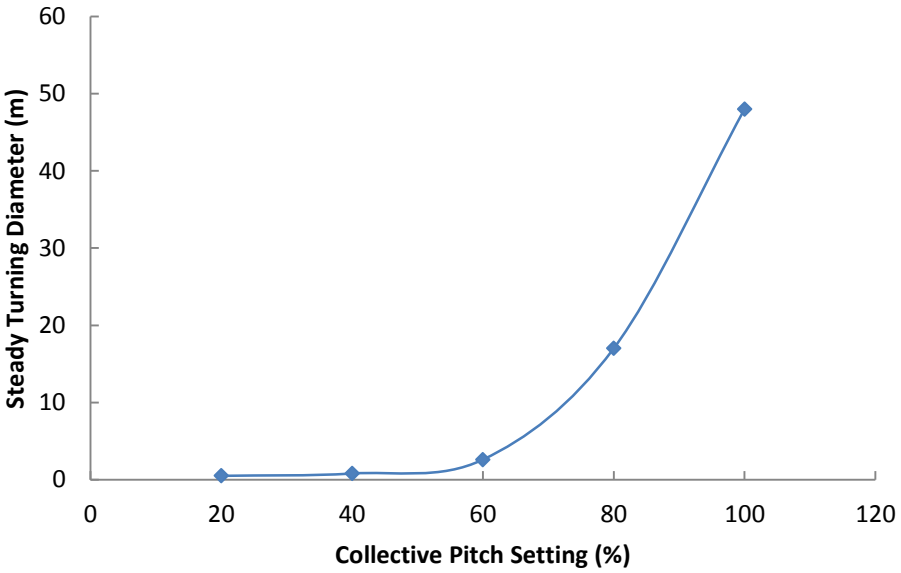

Figure 6.4. Turning circle tests at RPM = 250, at velocity of 0 m/s, left/right cyclic pitch angle = +100%, and various collective cyclic pitch angles.

For comparing turning diameter, the experimental data is required. However, the capability of the CCPP to turn the vehicle at zero speed. In addition, the turning diameter decreases as the collective pitch setting decreases as shown in Figure 6.6.

6.1.2 Zig Zag Manoeuvre Test

The zigzag manoeuvre test was used to assess the initial turning ability and the yaw-checking ability of the underwater vehicle. The initial turning ability is the measure of the ability to respond to the manoeuvring devices. An underwater vehicle operates in both horizontal and vertical planes. Therefore, the zigzag manoeuvre tests included horizontal (yaw) zigzag test and vertical zigzag test. The tests were completed as shown in Figures 6.7 and 6.8, respectively. For horizontal zigzag manoeuvre test, the RPM and collective pitch angle were set constant while the left/right cyclic pitch angle was changed. For the depth zigzag manoeuvre test, the RPM and the collective pitch angle were set constant and the up/down cyclic pitch angle was changed. From Figures 6.7 and 6.8, it is seen that the AUV equipped with the CCPP has good course/depth keeping and changing.

Table 6.2. Test matrix for zigzag manoeuvre test

Parameters	Value	Note
RPM	250	—
Collective pitch (%)	100	—
Right/left cyclic pitch (%)	−50% ←→ +50%	For horizontal zigzag test
Up/down cyclic pitch (%)	−100% ←→ +100%	For vertical zigzag test

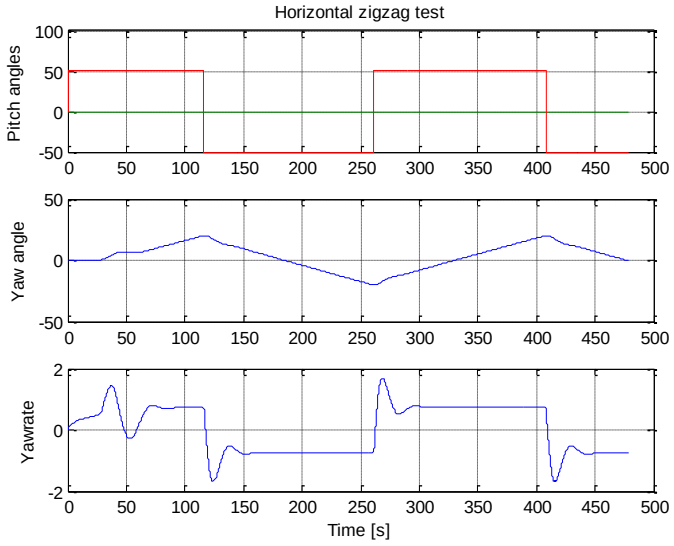

Figure 6.5. Horizontal (yaw) zigzag manoeuvre test.

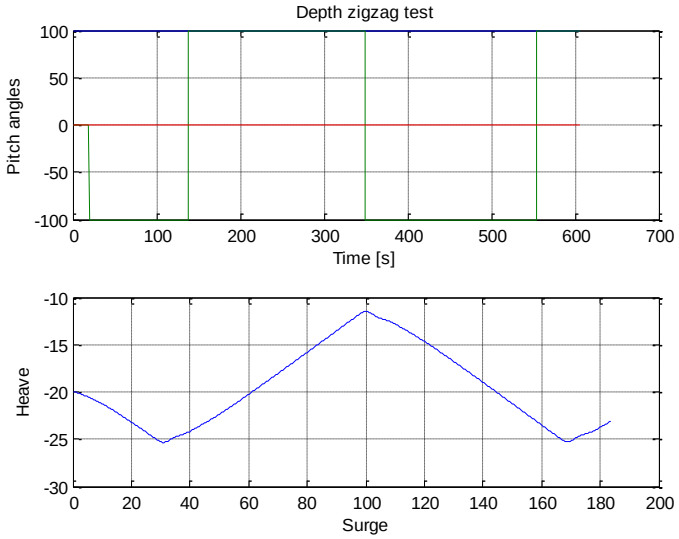

Figure 6.6. Vertical zigzag manoeuvre test.

6.1.3 Yaw Control Test

A PID autopilot was designed for the yaw control. The shaft speed and the collective pitch angle were kept constant while the yaw angle was controlled by adjusting the left/right cyclic pitch angle. The test matrix for yaw control test is presented in Table 6.3. Figure 6.9 shows the desired heading angle and actual heading angle versus time in the upper graph and the left/right cyclic pitch angle versus time in the lower graph. The underwater vehicle has good course-keeping and course-changing abilities; however, the left/right cyclic pitch angle changed dramatically. If this were done in the real world, the components of the CCPP would be worn out very quickly or damaged.

Table 6.3. Test matrix for yaw control test

Parameters	Start	Second	Third	Fourth	Fifth	Sixth	Seventh	End
Yaw angle (°)	0.0	20.0	60.0	90.0	60.0	40.0	20.0	0.0

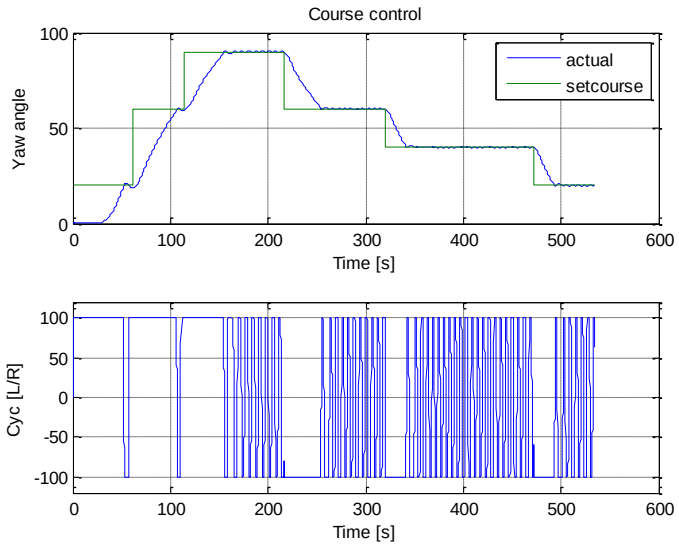

Figure 6.7. Yaw speed control test.

6.1.4 Depth Control Test

An underwater vehicle requires an ability of altering and maintaining depth. The depth control was implemented by a PID controller in which RPM and collective pitch angle were set constant, and the depth maintain and altering were done by the up/down cyclic pitch angle. Figure 6.10 presents the time history of the desired depth, the actual depth in the upper graph, and the up/down cyclic pitch angle in the lower graph. It is seen that the depth was controlled well, but it oscillated because the control gains were not tuned properly and the up/down cyclic pitch angle limits were set at maximum values of –100% and +100%. In addition, the up/down cyclic pitch angle changed dramatically and a lot while keeping the depth constant.

Table 6.4. Test matrix for depth control test (constant RPM)

Parameters	Start	Second	Third	Fourth	Fifth	Sixth	End
Depth (m)	20.0	25.0	15.0	5.0	10.0	30.0	20.00

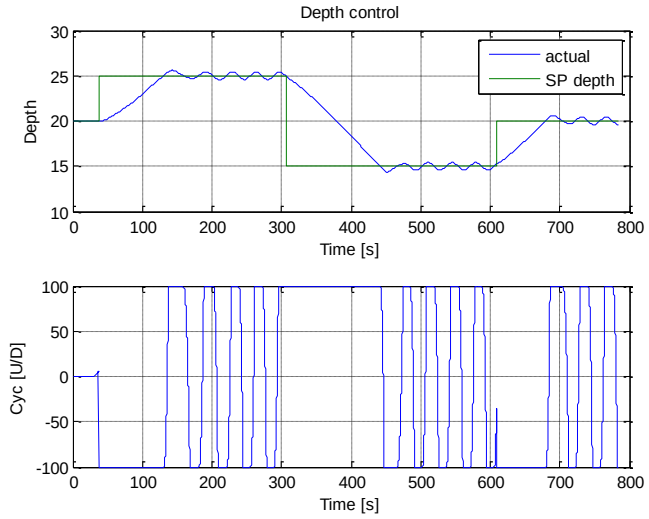

Figure 6.8. Depth control test.

6.1.5 Turning and Diving Test

For the combined turning and diving test, RPM, collective pitch angle, left/right cyclic pitch angle, and up/down cyclic pitch angle were set constant. Figure 6.10 shows the turning and diving trajectory for an RPM of 450, v = 1.33 m/s, up/down cyclic pitch = –100%, and left/right cyclic = 100%. From Figure 6.11, it is seen that the underwater vehicle turns and dives stably.

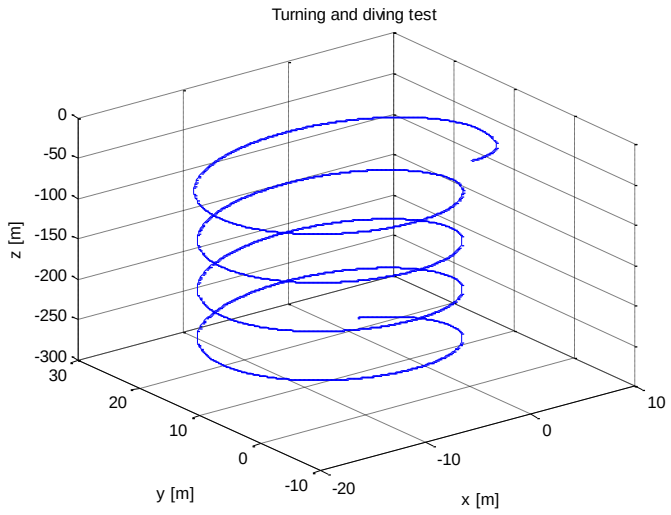

Figure 6.9. Turning and diving control test.

6.1.6 Speed Control Test

A PID controller was designed for both forward and reverse speed controls. During the speed control, the shaft speed (RPM) was set constant, the left/right and up/down cyclic pitch angles were set at zero, and the speed was controlled by the collective pitch angle as shown in Figures 6.12 and 6.13. Both forward and reverse speeds were controlled well. However,

during speed keeping, the speed oscillated a bit, and the collective pitch angle changed very frequently because the limits of the collective pitch angle were set at maximum values of –100% and +100%. Another reason might be that the control gains were not tuned properly.

In the simulation study, the maximum speed of the underwater vehicle could reach 2.2 m/s for forward speed and 1.4 m/s for reverse speed. Some trials were done with speed values beyond the above values, but the simulation programs became unstable.

Table 6.5. Test matrix for speed control test (constant RPM)

Parameters	Start	Second	Third	Fourth	Fifth	Sixth	End
Forward velocity (m/s)	0.00	1.00	1.50	2.00	1.00	0.50	0.00
Reverse velocity (m/s)	0.00	–0.50	–1.00	–1.25	–1.00	–0.50	0.00

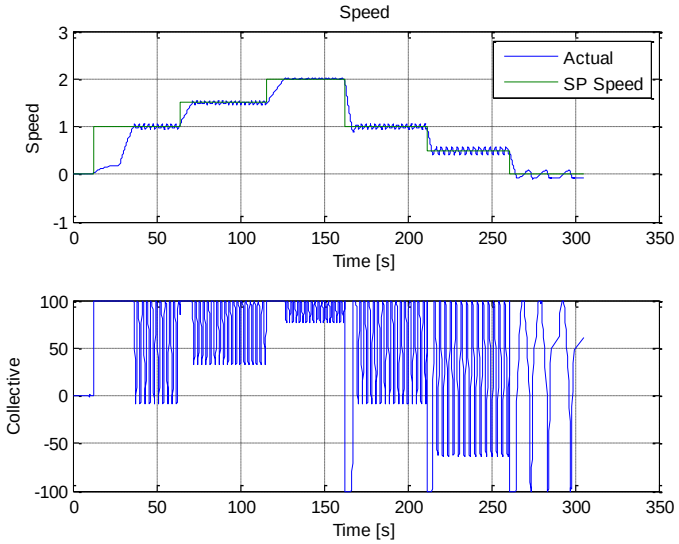

Figure 6.10. Forward speed control.

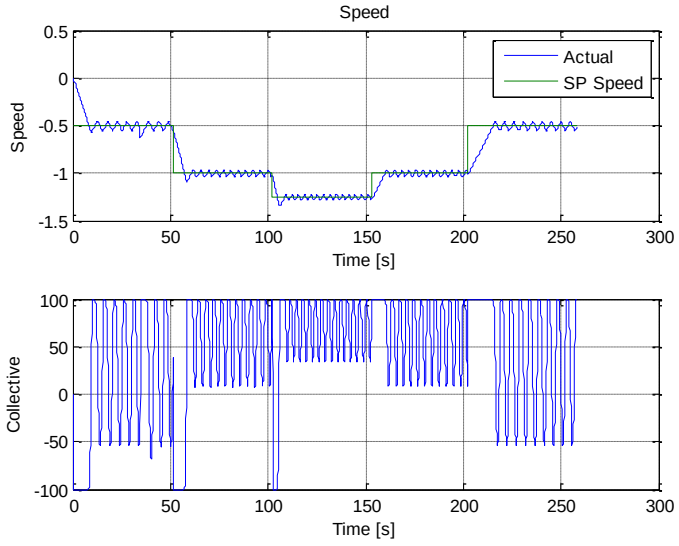

Figure 6.11. Reverse speed control.

6.1.7 Trajectory Tracking Control Test

Trajectory tracking control can be done by four controllers using the PID control law. In simulation, RPM and collective pitch angle were set constant while both left/right, and up/down cyclic pitch angles were varied to keep the underwater vehicle tracking a desired trajectory.

To control position, speed and yaw of an underwater vehicle are very important for underwater missions. The motion control may be station keeping for observing and taking images/photos and position control. In order to verify whether the underwater vehicle equipped with the CCPP is capable of tracking the desired trajectory, simulation for two simple trajectories was done.

The first desired trajectory was a 2-D horizontal trajectory at a depth of 20 meters. The desired speed was set at a constant value. The desired waypoints are (0,0,20), (100,0,20), (200,100,20), (300, 100, 20), (400,0,20), and (500, 0, 20). The simulated results are shown in Figures 6.14 and 6.15, where it is seen that the actual trajectory tracked the desired trajectory and reached every waypoint. The cyclic pitch angle had been changed very frequently.

The second desired trajectory was a 3-D trajectory with waypoints (0,0,20), (100,0,20), (200,100,30), (300, 100, 30), (400,0,20), and (500, 0, 20). The 3-D results are shown in Figure 6.16. From Figure 6.16, it can be seen that the underwater vehicle equipped with the CCPP could track the desired 3-D trajectory well, and it reached all waypoints. The depth control should be improved by an advanced control method or PID control gain tuning.

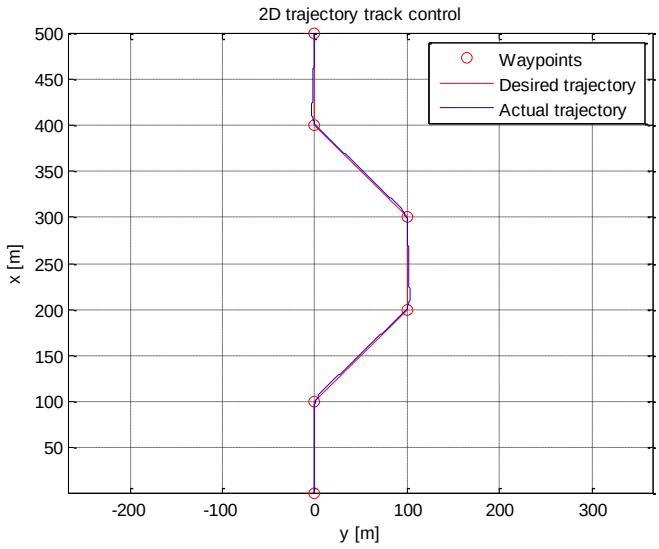

Figure 6.12. The 2-D trajectory track control system.

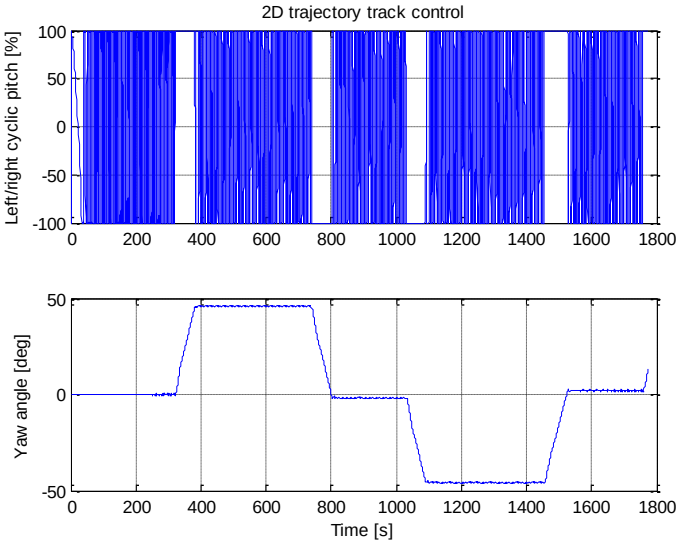

Figure 6.13. Time history of left/right cyclic pitch angle and yaw angle.

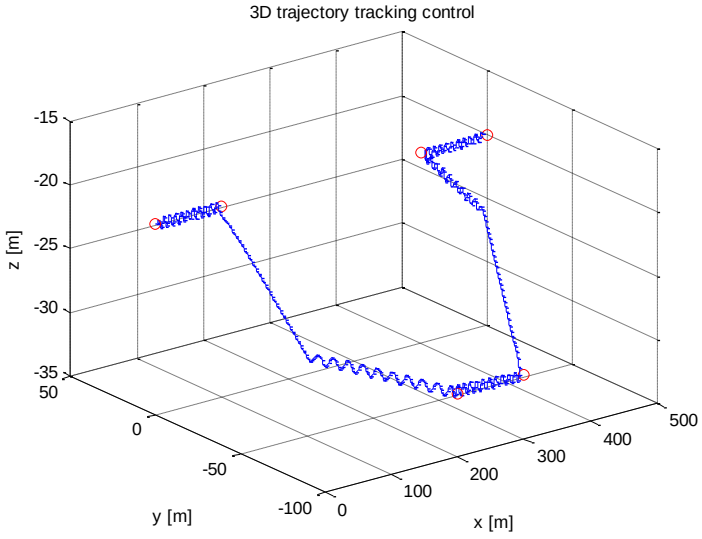

Figure 6.14. The 3-D trajectory tracking control.

Chapter Summary

The motion control system must compromise between stability and manoeuvrability. The performance of the motion control system was assessed by using the simulation study. In addition, the study demonstrated the capability of an underwater vehicle equipped with only one CCPP.

The simulation study showed that from the turning circle test, the underwater vehicle equipped with CCPP sufficiently performed the turning circle test. When the CCPP turning diameter was compared with the control plane turning diameter of the Delphin 2 AUV, the capability of the CCPP to turn the vehicle at a high forward velocity was not as good as the control plane. However, the capability of the CCPP to turn the vehicle was available at zero speed. In contrast, the control plane was ineffective at zero speed. In addition, the turning

diameter decreased as the collective pitch setting decreased. The paths of the vehicle were elliptical when the initial speed was not at zero. The zigzag manoeuvre test showed that the UV equipped with the CCPP possessed good course/depth keeping and changing, and the yaw control test showed that the underwater vehicle possessed good course-keeping and course-changing abilities. The depth control performed well in changing the depth and keeping the depth constant, and the underwater vehicle turned and dove stably.

In the simulation study, the maximum speed of the underwater vehicle reached 2.2 m/s for forward speed and 1.4 m/s for reverse speed. Some trials were performed with speed values beyond the above values, but the simulation programs became unstable.

Trajectory tracking control was developed and implemented by four controllers using the PID control law. In the simulation study, the RPM and collective pitch angle were set constant, whereas both left/right and up/down cyclic pitch angles were varied to keep the underwater vehicle tracking a desired trajectory.

The simulation study verified flexible manoeuvrability, and controllability of the underwater vehicle equipped with only one CCPP. It was possible to control the underwater vehicle in all directions using the CCPP. The performance of the CCPP and the manoeuvring characteristics of the underwater vehicle equipped with the CCPP were quantified and analysed by numerical simulation.

Chapter 7 Conclusions and Future Works

Underwater vehicles were designed for many types of operation, such as ocean exploration, inspection, and leisure activities. A problematic operation for underwater vehicles with a control surface is when underwater vehicles are required to operate at low speed. Their control surfaces become ineffective. A potential solution to this problem is by using the collective and cyclic pitch propeller (CCPP). The CCPP showed its capabilities of generating axial and transverse thrusts. With these useful capabilities, the CCPP became an innovative mechanism to manoeuvre an underwater vehicle at a low-speed operation.

7.1 Research Outcomes

Limited information exists regarding the performance of the CCPP. The uncertainty of the hydrodynamic characteristics of the CCPP causes difficulty in the motion control of the underwater vehicle. Therefore, the true performance of the propeller was sought to be unveiled. An experiment and experimental devices were designed to capture the performance of the CCPP. In this research, a performance in a straight line of the CCPP was assessed by using a captive experiment. Furthermore, a prediction program was developed by using the experimental information to optimize the time constants. After understanding the performance, the control system of the propeller and its simulation were developed. The motion control of the underwater vehicle equipped with the CCPP was based on the conventional PID control law. In order to evaluate the motion control and to study the manoeuvrability of an underwater vehicle equipped with the CCPP, a simulation program was developed in this research.

7.2 The Performance in a straight line of the CCPP on the Experimentation

One of the main objectives of this study was to understand how the CCPP performed in various conditions. The true performance in a straight line of the CCPP behind an underwater vehicle was conducted in the Towing Tank at the Australian Maritime College. The test underwater vehicle and the test apparatus were designed and fabricated. Furthermore, the data logging program and the control program of the CCPP were especially developed in LabVIEW software for the experiment, where the performance of the propeller in each pitch setting was assessed in various advance coefficients.

The useful information from the experiment is the behaviour of the CCPP with the collective pitch setting, which is similar to the typical controllable pitch propeller (CPP). As the collective pitch setting is increased in either positive direction (0% → +100%) or negative direction (0% → –100%), the generated thrust also increases. The propeller with the maximum collective pitch setting could generate the highest forward thrust and the highest backward thrust of 2.85 and 3.51 kg, respectively. In addition, the maximum generated torque

was 0.19 kgf·m. The maximum efficiency of positive pitch settings is approximately 70% on the 60% (17.4°) collective pitch setting, at about an advance coefficient of 0.6.

The performance in a straight line of the CCPP with the various collective pitch settings at different advance coefficients were established in the form of a polynomial equation. The thrust and the torque coefficients of the propeller can be easily determined by inputting a value of the collective pitch setting and a value of the required advance coefficient. The polynomial equation was used in the simulation to estimate the generated forces when the collective pitch setting was applied.

In the experiment, the resistance of the underwater vehicle was measured at various speeds. The measured resistance of the underwater vehicle was utilized to estimate the drag coefficient as a function of the Reynolds number, *Re.* If the drag coefficient can be correctly estimated, it can consequently improve the simulation program to be more accurate. Furthermore, *w*ith the resistance data and the performance equations of the propeller, the shaft speed and the collective pitch setting can be optimized to operate the propeller at a high efficiency for load requirements.

The performance of the propeller with various cyclic pitch settings at various advance coefficients was analysed. Based on the experiment, the direction of a transverse thrust from the propeller with a cyclic pitch setting was influenced by many inputs, such as the amplitude of cyclic pitch angle, the advance coefficient, and the amplitude of collective pitch angle.

The effect of the magnitude of the collective pitch setting was studied. As the magnitude of the collective pitch setting increased, the magnitude of the transverse forces also increased. With regard to the directional control, however, as the magnitude of the collective pitch setting increased, the direction of a generated transverse force rotated. Increasing the magnitude of the collective pitch setting in positive (forward) direction (0% → 100% or 0° → 29°) caused the transverse force to rotate clockwise when looking from the aft. By contrast, increasing the magnitude of the collective pitch setting in the negative (backward) direction (0% → −100%) caused the direction of the transverse thrust to rotate counterclockwise. As the magnitude of the collective pitch setting increased, the maximum angle of attack also increased. The maximum angle of attack was sufficient to cause flow separation. The dynamic stall phenomenon caused the shifting direction of a transverse force. The propeller blades experienced stronger dynamic stall as phenomenal as the higher magnitude of the collective pitch setting.

The influence of the amplitude of R/L cyclic pitch setting on the direction of a transverse thrust was that the direction of the thrust rotated clockwise when viewed from the aft, as the amplitude of R/L cyclic pitch increased in both positive (0% → +100%) and negative (0% → −100%) directions. The magnitude of the transverse thrusts also increased as the amplitude of the cyclic pitch setting increased (0% → ±100%). However, the influence of the amplitude of U/D cyclic pitch setting on the direction of a transverse thrust was that the direction of the thrust rotated counterclockwise when viewed from the aft, as the amplitude of the U/D cyclic pitch increased (0% → ±100%). The magnitude of the transverse thrusts also increased as the

amplitude of the cyclic pitch setting increased. The propeller with the cyclic pitch setting can generate the maximum transverse thrust of 0.53 kg.

7.3 The Performance of the CCPP on the Prediction Program

After understanding the performance of the CCPP, the performance prediction program of the CCPP was developed by using the BEMT, the Leishman-Beddoes dynamic stall model, and the experimental results. The Leishman-Beddoes dynamic stall model was used to estimate the lift and drag coefficients of a blade element when the blade experienced the unsteady flow effects. The blade element experienced unsteady flow when the cyclic pitch setting was applied. The time constants were optimized by using the experimental data as a guide. The optimization of the time constants was not sufficient to produce accurate predictions of the lift and drag characteristics.

The prediction results were compared with the existing experimental results. The prediction program was used to predict the performance of the CCPP at various conditions. When the collective pitch setting was applied, the prediction program with all optimized time constraints did not predict well in either magnitude or direction of thrust results. However, these prediction results with the optimized time constants were good in terms of picking up the trends. When the collective pitch setting was kept at zero percent, the predicted transverse forces possessed magnitudes similar to the experimental forces. The discrepancy of the direction of the transverse thrusts between the predicted and the experimental thrusts was approximately leading 30°. The results of the prediction program could illustrate the effect of the advance coefficients. Moreover, the predicted results were used in the simulation program.

7.4 The Motion Control System of the Underwater Vehicle Equipped with the CCPP

The capability of controlling the direction of the transverse thrust is important for manoeuvring an underwater vehicle. However, the direction of the transverse thrust is difficult to control because of the effect of the above mentioned parameters. Manual control of the transverse thrust is almost impossible; therefore, the development of the control system becomes necessary. In this research, the control system was developed. The mathematical models of the motor and its servo drive were created. In addition, the kinematics of the mechanism of the CCPP were studied and mathematically modelled. The kinematic model was also used to estimate a real-time pitch angle of each propeller blade, and this information was used as a feedback signal to be sent to the CCPP controller. The kinematic model also improved by changing the pitch setting. The transition of a generated thrust was as smooth as the results of the improvement, which made the direction control of the thrust more precise.

The actual control program for the CCPP was also implemented by using the LabVIEW program. In the developed control program, the pitch setting and the RPM of the propeller shaft can be selected between manual control and automatic control. The motion control was used to manipulate the position and ordination of the vehicle. The control algorithm of the blade angles must be able to control the thrust direction as desired. The motion control

system was developed based on the conventional PID control law. In future works, the motion control system can be further developed by using advanced control theories.

7.5 The Manoeuvrability of the Underwater Vehicle in the Simulation Program

For the future development of an underwater vehicle equipped with the CCPP, the development of the simulation program for an underwater vehicle is an essential tool. In this research, the simulation program was used to assess the capability of the motion control system and to demonstrate the proper performance of an underwater vehicle equipped with the CCPP. The LabVIEW software was also used to develop the simulation and control program.

The development of the simulation started from modelling the underwater vehicle. The underwater vehicle used in this research was not yet fully built; therefore, some particulars of the vehicles were based on the C-SCOUT vehicle. The added mass of the test vehicle was determined by using the sensitivity, S, of the response to the variation in geometric parameter (Perrault, 2002). The model for the hull forces was determined by using the method of Jorgensen (1973). Furthermore, the hydrodynamic forces of the CCPP were modelled based on the performance prediction program.

From the turning circle simulation, the underwater vehicle equipped with CCPP performed the turning. When the CCPP turning diameter was compared with the control plane turning diameter, the capability of the CCPP to turn the vehicle at a high forward velocity was not as good as the control plane. However, the capability of the CCPP to turn the vehicle at zero speed was still possible. By contrast, the control plane was ineffective at zero speed. In addition, the turning diameter was related to the magnitude of the collective pitch setting. At zero velocity, the turning diameter decreased as the collective pitch setting decreased.

The zigzag manoeuvre test showed that the underwater vehicle equipped with the CCPP possessed good course/depth keeping and changing, and the yaw control test showed that the underwater vehicle possessed good course-keeping and course-changing abilities. The depth control performed well in changing the depth and keeping the depth constant.

Trajectory tracking control was developed and implemented by four controllers using the PID control law. The simulation study has shown that the underwater vehicle equipped with the CCPP can track a prescribed path. The simulation study verified the flexible manoeuvrability, and controllability of the underwater vehicle equipped with only one CCPP. Using the CCPP, controlling an underwater vehicle equipped with a CCPP in all directions was possible. In the simulation study, the maximum speed of the underwater vehicle reached 2.2 m/s for forward speed and 1.4 m/s for reverse speed. Some trials were performed with speed values beyond the above values, but the simulation programs became unstable.

7.6 Future Works

In future works, the information of the maximum generated torque should be used to design a device or a shape of the vehicle to prevent rolling of the vehicle because of the generated torque.

The performance prediction program requires further development. The discrepancy between the predicted and the experimental results should be lessened, especially when the collective pitch setting is applied. In addition, the prediction program should consider the cascade effect and oblique flow effect.

The simulation program can be improved by having more accurate hydrodynamic coefficients. In future works, the hydrodynamic coefficients of the fully built underwater vehicle should be determined by using either a CFD software or an experiment.

The results from the simulation study were required to be verified by an experiment. For future works, free run tests should be conducted to verify the simulation results and to assess the straight line stability of the vehicle. Therefore, an underwater vehicle equipped with the CCPP should be built for the free run test, and the free run test should be designed. When an underwater vehicle is operating, the observation is limited. The operator cannot see the orientation of the vehicle, and this limitation could cause a disaster to an underwater vehicle. In the future, the developer will need to design a system that provides information of the position and orientation of the vehicle to the operator.

References

ADVANCED MOTION CONTROLS. 2011. Hardware Installation Manual [Online]. 3805 Calle Tecate Camarillo, CA • 93012-5068 USA. Available: http://www.a-m-c.com/download/manual/AMC_AnalogDrives_InstallManual.pdf [Accessed 2 October 2011 2011].

ALLEN, H. J. & PERKINS, E. W. 1951. A Study of Effects of Viscosity on Flow Over Slender Inclined Bodies of Revolution. National Advisory Committee on Aeronautics (NACA).

ANDERSON, B. J., CAMPANELLA, G. F. & WALKER, G. J. 1995. Development of a Horizontal Planar Motion Mechanism for determining Hydrodynamic Characteristics of underwater vehicles. Twelfth Australasian Fluid Mechanics Conference. The University of Sydney, Australia.

BALDURSSON, S. 2005. BLDC Motor Modelling and Control – A Matlab®/Simulink® Implementation. Master thesis, Institutionen för Energi och Miljö.

BENJAMIN, Y. N. C., STEPHEN, K. N., KURT, A. J., DAVID, P.B. & DAVID, C.R. 2008. A Feasibility Study of a Novel Propulsion System for Unmanned Underwater Vehicles. UDT Europe 2008 symposium, June 10-12 2008 Glasgow, UK.

BIJLEVELD, H. 2002. Design of a Cyclic Pitch Propeller for the Autonomous Underwater Vehicle C-SCOUT. Master, Delft University of Technology.

BLIDBERG, D. R. 2001. The Development of Autonomous Underwater Vehicles (AUV): A Brief Summary. Proceedings of the IEEE International Conference on Robotics and Automation (ICRA2001). Seoul, Korea.

BOSE, N. 2008. Marine Powering Prediction and Propulsors, The Society of Naval Architects and Marine Engineers.

BRANDNER, P. 2007. Blade Element Momentum Theory for Propellers. [Accessed 4 May 2012].

CARLTON, J. 2007. Marine Propellers and Propulsion. 2nd ed. 30 Corporate Drive, Suite 400, Burlington, MA 01803, USA: Elsevier Ltd.

CARTA, F., CASELLINI, L., ARCHIDIACONO, P. & ELMAN, H. 1970. Analytical Study of Helicopter Rotor Stall Flutter. 26th Annual Forum of the American Helicopter Society.

CHEN, C.-W., KOUH, J.-S. & TSAI, J.-F. 2013. Modelling and Simulation of an AUV Simulator With Guidance System. IEEE Journal of Oceanic Engineering, Vol. 38(2), pp. 211-225.

CLARK, B. 2010. Modelling dynamic stall of SC-1095 airfoil at high mach numbers. Master of Science, Georgia Institute of Technology.

COLEMAN, H. W. & STEELE, W. G. 2009. Experimentation, Validation, and Uncertainty Analysis for Engineers, Hoboken, New Jersey, John Wiley & Sons, Inc.

CONFERENCE, I. T. T. 2002. ITTC-Recommended procedures and Guidelines-Testing and Extrapolation Methods Propulsion, Performance Propulsion Test. ITTC.

CORPORATION, B. R. 2011. Bluefin-21 [Online]. http://www.bluefinrobotics.com. Available: http://www.bluefinrobotics.com [Accessed 2 October 2011.

EVANS, J. P. 2003. Dynamics Modelling and Performance Evaluation of an Autonomous Underwater Vehicle. Master thesis, McGill University.

FIELD, C. 2010. The story of the submarine from the earliest ages to the present day. Philadelphia, Lippincott; London: General Books LLC.

FOSSEN, T. I. 1991. Nonlinear modelling and control of underwater vehicles. PhD Thesis, Norwegian Institute of Technology.

FOSSEN, T. I. 1994. Guidance and Control of Ocean Vehicles, London, John Wiley and Sons.

FOSSEN, T. I. 2002. Marine control systems - Guidance, navigation and control of ships, rigs and underwater vehicles, Marine Cybernetics, Trondheim.

FOSSEN, T. I. 2011. Handbook of Marine Craft Hydrodynamics and Motion Control, West Sussex, UK., John Wiley and Sons Ltd. .

FROUDE, R. E. 1889. On the part played in the operation of propulsion differences in fluid pressure. vol.30, p.390-405.

FROUDE, W. 1878. On the Elementary Relation Between Pitch, Slip and Propulsive Efficiency. Transactions Royal Institution of Naval Architects, vol.19, p. 47-65.

GADEFELT, G. R. 1961. Swedish Patent.

GANGWANI, S. T. 1983. Synthesized airfoil data method for prediction of dynamic stall and unsteady airloads. the 39th Annual Forum of the American Helicopter Society. St. Louis, Mo.

GORMONT, R. E. 1973. A Mathematical Model of Unsteady Aerodynamics and Radial Flow for Application to Helicopter Rotors. In: U.S. ARMY AIR MOBILITY R&D LABORATORY (ed.). National Technical Information Service.

HASELTON, F. R., WILSON, W. G. & RICE, R. S. 1966. Tandem propeller Concept of Submarine Propulsion and Control. Journal of Aircraft, Vol 3, pp.180-184.

HEASLET, M. A. & SPREITER, J. R. 1952. Reciprocity Relations in Aeradynamics. NACA Report 1119.

HOPKINS, E. J. 1951. A Semiempirical Method for Calculating the Pitching Moment of Bodies of Revolution at Low Mach Numbers. Research Memorandum RM A51C14: National Advisory Committee on Aeronautics (NACA).

HUMPHREY, T. C. 2005. Design and Fabrication of a Collective and Cyclic Pitch Propeller. Master of Engineer, Memorial University of Newfoundland.

HUMPHREY, T. C., BOSE, N. & WILLIAMS, C. 2005. Improving AUV Manoeuverability:Development of a Collective and Cyclic Pitch Propeller Oceanic Engnineering Society, Vol. XXXIX.

ITTC. 2002. Propulsion, Propulsor, Uncertainty Analysis, Example for Open Water Test [Online]. International Towing Tank Conference. Available: http://ittc.sname.org/2002_recomm_proc/7.5-02-03-02.2.pdf [Accessed 3 May 2010].

ITTC. 2006. Testing and Extrapolation Methods, Genera Density and Viscosity of Water [Online]. Available: http://ittc.sname.org/2006_recomm_proc/7.5-02-01-03.pdf [Accessed 3 May 2010].

JANI, R. & HINCHEY, M. 2005 Development of a hydrocopter. Mechatronics and Automation, IEEE International Conference, 29 July-1 Aug. 2005. Vol. 4, pp. 1896-1900.

JESSUP, S. D. 1976. Reduction of Propeller Vibration and Cavitation by Cyclic Variation of Blade Pitch. Master of Science, Massachusetts Institute of Technology.

JOHNSON, W. 1974. Comparison of Three Methods for Calculation of Helicopter Rotor Blade Loading and Stresses Due to Stall. In: AMES RESEARCH CENTRE & U.S. ARMY AIR MOBILITY RESEARCH AND DEVELOPMENT LABORATORY (eds.). National Technical Information Service.

JONES, D. A., CLARKE, D.B. , BRAYSHAW, I.B. , BARILLON, J.L. AND ANDERSON, B.A. 2000. The calculation of Hydrodynamic Coefficients for underwater vehicles. AME CRC.

JOOSEN, W. P. A., MANEN, J. D. & WALLE, F. 1963. Large Hub to Diameter Ratio Propellers with Programmed Blade Control. International Shipbuilding Progress, Vol.10, pp.3-11.

JORGENSEN, L. H. 1973. Prediction of Static Aerodynamic Characteristic for Space-Shuttle-Like and Other Bodies at Angles of Attack from 0° to 180°. NASA TN D-6996. NASA.

KIM J., K., K., CHOI, H.S., SEONG, W. & LEE, K.Y 2002. Estimation of Hydydronamic Coefficients for an AUV Using Nonlinear Observers. IEEE Journal of Oceanic Engineering, Vol. 27.

LEISHMAN, J. G. 1989. Modelling Sweep Effects on Dynamic Stall. Journal of the American Helicopter Society, Volume 34, Number 3, pp. 18-29(12).

LEISHMAN, J. G. 2002. Challenges in Modelling the Unsteady Aerodynamics of Wind Turbines. 21st ASME Wind Energy Symposium and the 40th AIAA Aerospace Sciences Meeting, p. 19.

LEISHMAN, J. G. 2006. Principles of helicopter aerodynamics, New York, Cambridge University Press.

LEISHMAN, J. G. & BEDDOES, T. S. 1989. A Semi-Empirical Model for Dynamic Stall. Journal of the American Helicopter Society, Volume 34, Number 3, pp. 3-17(15).

LEYLAND, J. A. 1993. Kinematics and Constraints Associated with Swashplate Blade Pitch Control. [Accessed 1 Apr 2012].

LINDAHL, C. A. 1965. A ship Propeller with separately turntable blades. Swedish patent application No.201106.

MATHWORKS. 2013. DC Motor Model [Online]. MathWorks. Available: http://www.mathworks.com.au/help/physmod/elec/ug/example--modelling-a-dc-motor.html [Accessed 14 January 2013].

MCCROSKEY, W. J. 1981. The phenomenon of dynamic stall. NASA TM-81264.

MCCROSKEY, W. J., CARR, L. W. & MCALISTER, K. W. 1976. Dynamic Stall Experiments on Oscillating Airfoils. AIAA Journal, vol. 14, pp.57-63.

MOLLAND, A. F., TURNOCK, S. R. & HUDSON, D. A. 2011. Ship Resistance and Propulsion: Practical Estimation of Propulsive Power, 32 Avenue of the Americas, New York, NY 10013-2473, USA, Cambridge University Press.

MUN & NRC-IOT. 2003. Canadian Self Contained Off-the-shelf Underwater Testbed (C-SCOUT) [Online]. Newfoundland, Canada: Memorial University of Newfoundland,

MUNK, M. M. 1924. The Aerodynamic Forces on Airship Hulls. Report No. 184. National Advisory Committee on Aeronautics (NACA).

MURRAY, B. & FRASER, J. 1994. Applications of Cyclic Pitch Thrusters. Propellers/Shafting '94 Symposium. Virginia Beach, Virginia: The Society of Naval Architects and Marine Engineers.

MYERS, R. H., MONTGOMERY, D. C. & ANDERSON-COOK, C. M. 2011. Response Surface Methodology : Process and Product Optimization Using Designed Experiments. 3 Ed. Hoboken: Wiley.

NAGASHIMA, Y., TAGUCHI, N., ISHIMATSU, T. & MIZOKAMI, T. Development of a Compact Autonomous Underwater Vehicle Using Variable Vector Propeller. Proceedings of The Twelfth(2002) International Offshore and Polar Engineering Conference, May 26-31, 2002 2002 Kitakyushu,Japan.

NATIONAL INSTRUMENTS. 2011. Product Information: What is NI LabVIEW [Online]. LabVIEW. Available: http://www.ni.com/labview/products/ [Accessed 1 February 2011].

NESIMI, E. 2002. LabVIEW for electric circuits, machines, drives and laboratories, Pearson Education.

NGUYEN, H. D. 2008. Multitask Automatic Manoeuvring Systems Using Recursive Optimal Control Algorithms. Proceedings of the Second International Conference on Communications and Electronics, Hoi An, Vietnam. pp. 54-59.

NGUYEN, H.D., NIYOMKA, P., BOSE, N. & BINNS, J. 2013. Performance Evaluation of an Underwater Vehicle Equipped with a Collective and Cyclic Pitch Propeller. 9th IFAC Conference on Control Applications in Marine Systems, 2013 Osaka, Japan.

NIYOMKA, P., BINNS, J., BOSE, N. & NGUYEN, H.D. 2013. Experimental characterization of collective and cyclic pitch propulsion for an underwater vehicle. The 3rd International Symposium on Marine Propulsors,. Launceston, Tasmania, pp 542-552, 5-8 May 2013.

NIYOMKA, P. 2009. Designing the tests for a Collective and Cyclic Pitch Propeller. Bachelor of Engineering Final year thesis, Australian Maritime College.

PALMER, A. R. 2009. Analysis of the Propulsion an Manoeuvring Characteristics of Survey-Style AUVs and the Development of a Multi-Purpose AUV. Doctor of Engineering, University of Southampton.

PARKER MOTION. 2011. K Series Kit Motors [Online]. 5500 Business Park Drive, Rohnert Park, CA 94928. Available: http://divapps.parker.com/divapps/emn/pdf/Frameless_Motor_Brochure.pdf [Accessed 11 December 2011].

PEREIRA, R., SCHEPERS, G. & PAVEL, M. D. 2012. Validation of the Beddoes–Leishman dynamic stall model for horizontal axis wind turbines using MEXICO data. Wind Energy, 16, p. 207-219.

PERRAULT, D. E. 2002. Autonomous underwater vehicles (AUV) sensitivity of motion response to geometric and hydrodynamic parameters and AUV behaviours with control plane faults. PhD Thesis, The Memorial University of Newfoundland.

RADM MOONEY, B., COLLINS, D. & BOSTMAN, J. 2001. Review of Autonomous Underwater Vehicle(AUV) Developments. In: COMMAND, N. M. A. O. (ed.).

RANKINE, W. J. M. 1865. On the Mechanical Principles of the Action of Propellers. Transactions Royal Institution of Naval Architects, vol.6, p.13-35.

RAPIN, M. & ORTUN, B. 2007. 3D rotational correction in ONERA Aeroelastic predictions of NREL wind Turbine. 45th AIAA Aerospace Sciences Meeting and Exhibit.

SCIENCE DAILY. 2012. Bioinspired Robot Meets Fish: Robotic Fish Research Swims Into New Ethorobotics Waters [Online]. Available: http://www.sciencedaily.com/releases/2012/11/121120122051.htm [Accessed 19 May 2012].

SHENG, W., GALBRAITH, R. A. M. & COTON, F. N. 2006. A new stall onset criterion for low speed dynamic stall. Journal of Solar Energy Engineering [Online]. [Accessed 14 Jan 2011].

SIMONSSON, P. The Pinnate Propeller. Propellers 81 Symposium, May 1981 Viginia Beach. Society of Naval Architects and Marine Engineers, pp.41–48.

SIMONSSON, P. Report on Full-Scale tests with Pinnate Propeller in Swedish Navy Patrol Boat. Propellers 84 Symposium, May 15-16 1984 Virginia Beach. Society of Naval Architects and Marine Engineers, pp.1-8.

SNAME 1950. Nomenclature for Treating the Motion of a Submerged Body Through a Fluid. Technical and Research Bulletin N0. 1-5. New York: The Society of Naval Architects and Marine Engineers.

SNEL, H., HOUWINK, R., VAN BUSSEL, G. & BRUINING, A. 1993. Sectional Prediction of 3D Effects for Stalled Flow on Rotating Blades and Comparison with Measurements. Proceedings of the European Community Wind Energy Conference, pp. 395-399.

STEENSON, L. V., PHILLIPS, A.B., FURLONG, M., ROGERS, E. AND TURNOCK, S.R. 2011. Maneuvering of an over-actuated autonomous underwater vehicle using both through-body tunnel thrusters and control surfaces. *17th International Undersea Untethered Submersible Technology Conference.* United States.

THE PAST FOUNDATION. 2009. The Development of ROV Technology [Online]. Available: http://pastfoundation.org/previous-programs/DeepWrecks/ROVTechnology.htm [Accessed 21 December 2009].

TRUONG, V. K. 1996. Prediction of helicopter rotor airloads based on physical modelling of 3-D unsteady aerodynamics. 22nd European Rotorcraft Forum. Brighton, UK.

WAGNER, H. 1925. Über die Entstehung des dynamischen Auftriebes von Tragflügeln. Journal of Applied Mathematics and Mechanics, vol. 5, pp.17-35.

WALSH, D. 2008. Underwater vehicles [Online]. @McGraw-Hill Companies. Available: http://accessscience.com/content/Underwater-vehicles/720550 [Accessed 26 September 2011].

WILBY, P. G. 1979. The aerodynamic characteristics of some new rae blade sections and their potential influence on rotor performance. 5th European Rotorcarft Forum. Amsterdam, The Netherlands.

WRIGHT, J. R. & COOPER, J. E. 2008. Introduction to Aircraft Aeroelasticity and Loads. John Wiley & Sons.

Appendix A1

Measurement of Pitch Angle

The measuring method is indirect. The position of the leading edge was recorded while turning the propeller shaft. Then, the positions of the leading edge at every angular position were converted into the pitch angle.

A1.1 Objective

1. Verify the kinematic model, which has used to control blade angles of CCPP.

A1.2 Apparatus

1. The Collective and Cyclic Pitch Propeller
2. The electronic control box
3. A personal computer

A1.3 Data Acquisition Instruments

1. A digitizer
2. A laptop with Rhinoceros software

Figure A1.0.1. Setup of measuring pitch settings

A1.4 Measuring Procedures

1. Calibrate the digitizer with two orthogonal lines, known lengths and on the same plane as the propeller plane, as seen in Figure A1.0.2.

Figure A1.0.2. Orthogonal lines are marked on the front plate

2. Commence the measurement as the following plan.

A1.5 Measuring Plan

1. Check collective blade angle

Step 1. Assign a blade angle as seen in Table A1.0.1.

Step 2. Continually measure at a leading edge.

Table A1.0.1. Blade angle to be measured

Collective. Pitch setting Set [%]
-100
-80
-60
-40
-20
0
20
40
60
80
100

2. Check cyclic blade angle

Step 1. Assign a blade angle as seen in Table A1.0.2.

Step 2. Continually measure at a leading edge.

Table A1.0.2. Blade angle to be measured

Col. Pitch Set	Cyc1 Pitch Set	Cyc2 Pitch Set
-100	-100	-100
-50	-50	-50
0	0	0
50	50	50
100	100	100

A1.6 Conversion Measured Data into Blade Angle

The data for each pitch setting is the path of the leading edge at r/d =0. 25 when the propeller shaft turns one revolution. The measure paths of each pitch setting are required to convert into the blade angle an each angular position. The conversion was implemented in 3D modelling software, Rhinoceros version 4.

A1.6.1 Procedures to Convert Measured Data into Blade Angle

1. Create a path line of leading edge by using a create line by cloud points function and then repeat for every pitch angle setting.
2. Create a surface by using the path line in the first step, and then repeat for every blade angle setting.
3. Create a circle with a radius of 52.114 mm., which is a distance from a shaft centre line to a pivot point of the blades and the centre of the circle coincides with the centre of a created surface only at a blade angle setting of collective pitch 0%, cyclic pitch 0% and cyclic pitch 0%.
4. Create lines, which are drawn from the centre of the created circle to the rim of the circle at every 45 degrees
5. Create tangent line at the intersection of the rim of the circle and the created line in step 4
6. Create a surface of the propeller plane by using the circle in step 3.
7. Create 8 spheres at the intersection of the rim of the circle and the created line in step 4. Spheres has a radius of 11 mm., which is a distance from the pivot point to the leading edge point.
8. Create intersected lines between the created spheres and a created surface in step 6.
9. Create lines from the intersection points of the rim of the circle and the created line in step 4 to the intersection points in step 8.
10. Measure blade angles, which is between the lines in step 9 and the tangent lines at step 5. Repeat this measurement for every blade angle setting.

Appendix A2

Uncertainty Analysis of the Measurement of Pitch Angle

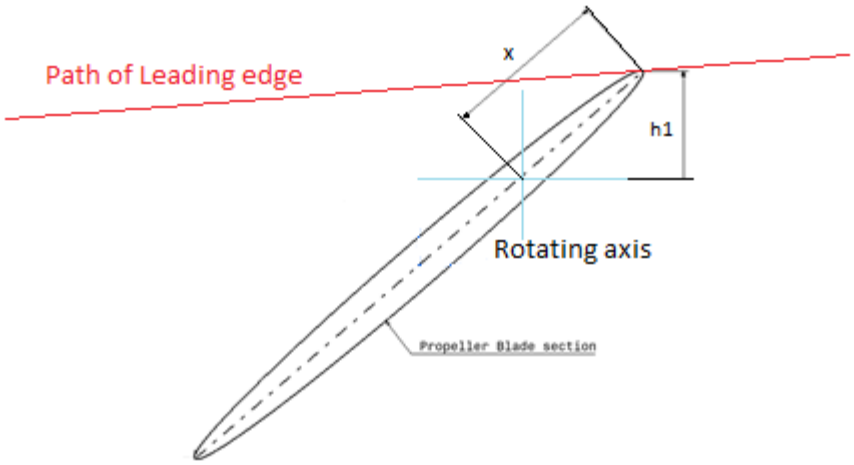

Figure A2.0.1. The diagram of measuring the pitch angle

The angle of the propeller blades can be determined by measuring the height of the leading edge, h_1, and the distance from the leading edge to the rotating axis of the propeller blade, x, and using the following equation.

$$e° = \sin^{-1}\left(\frac{h_1}{x}\right) \tag{A2.1}$$

The above equation is a data reduction equation. The general uncertainty analysis expression was derived as follows:

$$\frac{Ue^2}{e^2} = \frac{Uh_1^2}{\arcsin\left(\frac{h_1}{x}\right)^2 \cdot x^2 \cdot \left(1-\frac{(h_1)^2}{x^2}\right)^2} + \frac{(h_1)^2 \cdot Ux^2}{\arcsin\left(\frac{h_1}{x}\right)^2 \cdot x^4 \cdot \left(1-\frac{(h_1)^2}{x^2}\right)^2} \tag{A2.2}$$

The uncertainty magnification factor (UMF) indicates the influence of the uncertainty of each measured parameter on the uncertainty in the result. If a UMF value is more than 1, it indicates that the uncertainty in the parameter is magnified as it propagates through the data reduction equation into the result. If a UMF value is less than 1, it indicates that the uncertainty in the parameter diminishes as it propagates through the data reduction equation into the result. The uncertainty magnification factors of each parameter are shown as follows.

The uncertainty magnification factor of the trailing edge height;

$$UMF_{h_1} = -\left(\frac{1}{x\sqrt{1-\frac{(h_2-h_1)^2}{x^2}}} \right) \cdot \left(\frac{h_1}{e} \right) = 0.955 \quad \text{(A2.3)}$$

The uncertainty magnification factor of the chord length;

$$UMF_x = -\left(\frac{(h_1)}{x^2\sqrt{1-\frac{(h_1)^2}{x^2}}} \right) \cdot \left(\frac{x}{e} \right) = 1.103 \quad \text{(A2.4)}$$

The influences of the uncertainty of the measurement of the height of the leading edge are not magnified into the result.

The h_1, and x measurement had uncertainties of 0.23 mm. Figure A2.0.2 shows the uncertainty of the measured results at different angles of the propeller blades. The trend lines of the uncertainties of the measuring pitch angle increased when measuring the high angle.

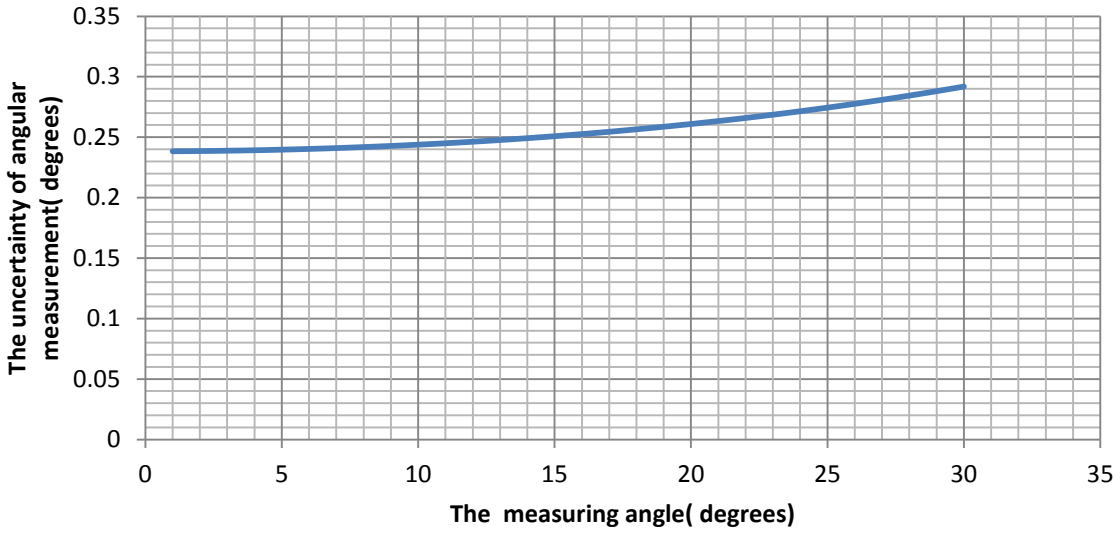

Figure A2.0.2. The uncertainty of the angular measurement with respects to the measuring angle

Appendix A3

Optimised Time Constants

Table A3.0.1. The Optimised Time Constants from simulating the middle range of time constants.

Cases			Optimised Time Constants			
Collective	Cyclic Up/Down	Cyclic Right/Left	T_{vl}	T_V	T_P	T_f
-80	-80	-80	0.000	3.927	20.000	10.111
-80	-80	-40	13.237	20.000	19.379	0.000
-80	-80	0	18.017	8.949	13.638	17.661
-80	-40	-80	0.000	3.354	19.464	9.586
-80	-40	-40	15.780	12.774	17.963	7.133
-80	-40	0	4.101	3.983	14.961	3.455
-80	0	-80	0.000	3.622	20.000	9.737
-80	0	-40	0.020	7.840	18.035	11.080
-40	-80	-80	13.844	0.013	10.590	0.889
-40	-80	-40	16.969	0.116	4.398	0.958
-40	-80	0	1.676	7.684	9.192	0.461
-40	-40	-80	18.399	10.964	6.014	1.446
-40	-40	-40	17.126	0.449	5.708	1.163
-40	-40	0	0.000	20.000	3.801	2.036
-40	0	-80	0.000	20.000	3.801	2.036
-40	0	-40	17.377	0.503	4.786	1.265
0	-80	-80	19.836	0.005	0.049	0.044
0	-80	-40	19.994	0.006	0.000	0.000
0	-80	0	20.000	0.004	0.000	0.000
0	-40	-80	20.000	0.000	0.000	0.011
0	-40	-40	20.000	0.014	0.000	0.009
0	-40	0	1.139	0.000	0.000	20.000
0	0	-80	20.000	0.000	0.000	0.081
0	0	-40	0.000	19.770	0.000	20.000
80	80	80	0.520	0.000	0.000	20.000
80	80	40	20.000	0.117	0.000	0.001
80	80	0	20.000	0.092	0.000	0.003
80	40	80	20.000	0.092	0.000	0.003
80	40	40	19.975	0.000	0.000	0.000
80	40	0	20.000	0.015	0.001	0.000
80	0	80	20.000	0.075	0.000	0.000
80	0	40	20.000	0.000	0.000	0.005
40	80	80	13.127	20.000	20.000	7.045
40	80	40	19.954	0.001	20.000	19.996
40	80	0	4.000	16.000	16.000	4.000
40	40	80	10.870	0.000	20.000	9.125
40	40	40	10.167	0.000	11.554	20.000
40	40	0	20.000	6.120	20.000	18.741
40	0	80	20.000	3.997	20.000	19.954

40	0	40	20.000	3.739	20.000	20.000
0	80	80	6.714	20.000	20.000	18.644
0	80	40	10.741	19.998	0.000	0.000
0	80	0	19.705	20.000	20.000	6.452
0	40	80	20.000	20.000	20.000	6.512
0	40	40	10.647	17.422	0.000	0.000
0	40	0	11.045	19.999	0.000	0.000
0	0	80	20.000	19.361	14.040	5.644
0	0	40	11.052	19.998	0.031	0.000

Appendix A4

Uncertainty Analysis of the Captive Experiment of the Collective and Cyclic Pitch Propeller

A4.1Uncertainty Sources

A4.1.1 Geometric Uncertainty

The propeller blade of the CCPP unit was manufactured to be same as the designed propeller. The error might be in diameter, thickness of the blades, and shape of the blade section.

A4.1.2 Installation Uncertainties

For the Big Force Transducer(Yacht Dynamometer)
The uncertainties relate to the underwater vehicle installation and alignment. The axis of the vehicle body must be parallel to the calm water surface, the direction of movement, and the horizontal axis of the big force transducer (yacht dynamometer).

The heights of the front and the back poses were measured and corrected to make them similar. Therefore, the axis of the vehicle aligned with the vertical plane and the horizontal plane of the big force transducer. The horizontal plane of the big force transducer (yacht dynamometer) was also arranged parallel to the calm water surface. The precise spiritlevel was used to assess the alignments.

To align the vehicle to a moving direction of the carriage, first, the propeller blades were turned into the axis of the vehicle body. Second, the two distances were measured from the position of load cell number 2 to a side of the carriage rail, and from the position of load cell number 3 to a side of the carriage rail. The two measurements were used to align the big force transducer (yacht dynamometer) to the direction of movement. The alignment of the axis of the vehicle to the moving direction was checked again by using the measurement of the forces from the big force transducer (yacht dynamometer).

For the Small Force Transducer(Internal Load Cell)
The small force transducer directly measured forces and moments that were generated by the CCPP. Therefore, the axis of the propeller shaft aligned with the axis of the small force transducer. In addition, the vertical and horizontal planes of the propeller and the small force transducer aligned with each other. The process of installing the propeller unit and the small force transducer to the main underwater vehicle was necessary, and this process could induce a misalignment of the two components. To reduce the misalignment of the two components, the small force transducer and the propeller unit were assembled first, and their alignments were checked before the whole unit was attached to the main body of the underwater vehicle.

For the Depth of the Underwater Vehicle

To avoid air drawn from the water surface during an experiment, an immersion depth of the propeller at 1.5 diameters was recommended by ITTC 7.5-0.2-03-02.2 (2002). The immersion depth of the vehicle was at 940 mm or approximately 3 diameters of the propeller.

A4.2 Bias Limits, B

A4.2.1 Propeller Geometry

According to the propeller drawing, the tolerance of the propeller diameter was given +/-0.01 in or +/-0.0245 mm. The bias error limit is B_D=0.00002 m. corresponding to 0.008% of the nominal propeller diameter of 0.305943m.

A4.2.2 Temperature

By assuming the calibrating error in the thermometer to be within +/- 0.5 ˚C, the bias limit is B_{t° =0.5 ˚C.

A4.2.3 Water Density

Calibration:

According to the ITTC Procedure 7.5-02-01-03 (2006) 'Density and Viscosity of Water' for g=9.81 m/s^2

$$\rho = 1000.1 + 0.0552 \cdot t^{\circ 2} + 0.00004 \cdot t^{\circ 3}$$

$$\left|\frac{\partial \rho}{\partial t^\circ}\right| = \left|0.0552 - 0.0154 t^\circ + 0.000120 \cdot t^{\circ 2}\right|$$

With t˚=20.5 ˚C and B_{t° =0.5 ˚C the bias $B_{\rho 1}$ can be calculated according to :

$$B\rho 1 = \left|\frac{\partial \rho}{\partial t^\circ}\right| Bt^\circ = 0.21007 \cdot 0.5 = 0.105035 \; kg/m^3$$

Data reduction:

The error due to converting the temperature to a density can be calculated as two times the SEE of the curve fit the density/temperature values for the whole temperature range. The bias error, $B_{\rho 2} = 0.070 kg/m^3$.

Conceptual:

The nominal density according to the ITTC-78 method is $\rho = 1000 kg/m^3$. Using ITTC-78 method introduces a bias limit as the difference between $\rho(20.5°C) = 1000 kg/m^3$ and $\rho = 1000 kg/m^3$ such that $B_{\rho 3} = 1000 - 998.34028 = 1.65972 kg/m^3$

Total bias limit of the density can be calculated as following;

$$B_\rho = \sqrt{\left(B_{\rho 1}\right)^2 + \left(B_{\rho 2}\right)^2 + \left(B_{\rho 3}\right)^2} = \sqrt{(0.105035)^2 + (0.070)^2 + (1.65972)^2} = 1.6645\ kg/m^3$$

The bias limit for the density is $B_2 = 1.6645\ kg/m^3$ corresponding to 0.1664% of $\rho(20.5°C) = 1000 kg/m^3$

A4.2.4 Carriage Speed

The carriage velocity was used in calculation advance coefficient, thrust coefficient and torque coefficient. The bias limit, Bv is 5% of the nominal speed of 1 m/s, reading 0.05 m/s.

A4.2.5 Propeller Rate of Revolution

The bias limit, Bn is 0.1% of the nominal rate of revolution of 8.33 rps or reading 0.08 rps.

A4.2.6 The Vertical Distance between the Centre Line of the CCPP and the Centre of YDM

The uncertainty of vertical distance between the centre of YDM and the bottom joint plate of YDM, U_{h1}= +/- 0.1mm.

The uncertainty of height of the adaptive joint, $Uh2 = \pm 1mm$.

The uncertainty of the vertical distance from the bottom of the adaptive joint to the top of the CCPP, $Uh3 = \pm 1.5mm$.

The uncertainty of the diameter of the CCPP, $Uh4 = 0.02mm$.

Thus, the total uncertainty of vertical distance between the centre line of the CCPP and the centre of YDM, U_h can be calculated as follows;

$$\begin{aligned} B_h &= \sqrt{\left(B_{h1}\right)^2 + \left(B_{h2}\right)^2 + \left(B_{h3}\right)^2 + \left(B_{h4}\right)^2} \\ &= \sqrt{(0.1)^2 + (1)^2 + (1.5)^2 + (0.02)^2} \\ &= 1.8057mm\ or\ 0.0018057\ m \end{aligned}$$

The total bias limit associated with the vertical distance is $Bh = 0.0018057$ m corresponding to 0.1237 % of the measured vertical distance of 1.460 m.

A4.2.7 The Parallel between the Longitudinal Axis of the Vehicle and the Horizontal Plane of the YDM

The error is manifested in the difference of the vertical distance of the two struts which connects the vehicle to the YDM. The vertical distance is the distance between the axial line of the CCPP and the centre of YDM. The maximum incline angle of the vehicle occurs when the vertical distance of the forward strut is 1.8057mm longer, or the vertical distance of the aft strut is 1.8057 mm shorter. The maximum difference of heights at the forward strut and

the aft strut is 3.6114 mm. The distance from the forward strut to the aft strut is 600 mm. The maximum pitch angle, B_{pitch1} will be $arctan(3.6114/600)=0.3448 degrees$.

A4.2.8 The Parallel of the Horizontal Plane of the YDM to the Clam Water Surface

Calibration:

The precise engineering spirit level was used to assess the parallel of the YDM to the calm water surface. The manufacturer of the precise engineering spirit level guarantees the accuracy of 0.42mm/m or 0.0241 degrees. $B_{pitch2} = \pm 0.0241 degrees$.

Therefore, total bias limit of pitch angle of the vehicle

$$B_{pitch} = \sqrt{(B_{pitch1})^2 + (B_{pitch2})^2} = \sqrt{(0.3448)^2 + (0.0241)^2} = 0.3456 \ degrees.$$

A4.2.9 The Yaw Angle of the Vehicle which References to the Longitudinal Axis of the YDM

The yaw angle of the vehicle should be zero. However, the error during the manufacture could occur, for instance the forward strut holder is offset to the aft strut holder or vice versa.

With the measured offset of +/-5 mm, the error of the yaw angle equal to $arctan(5/600) = 0.4775 degrees$.

A4.2.10 Total Forces/Moments Measurement by Using Only the YDM

The total bias errors for forces and moments measurement including bias errors from calibration and data acquisition are presented in Table A4.0.1.

Table A4.0.1. Force balance errors after rotating the axis

Force/Moment	Max Error	Min Error	Assumed Error
X	0.840636 N	-0.78965 N	+/-0.81514 N
Y	1.189217 N	-1.22454 N	+/-1.20688 N
Z	2.093543 N	-1.98812 N	+/-2.04083 N
L	0.640139 Nm	-0.54718 Nm	+/-0.59366 Nm
M	1.635472 Nm	-1.40779 Nm	+/-1.52163 Nm
N	0.659547 Nm	-0.67313 Nm	+/-0.66634 Nm

The second error is manifested in the vehicle misalignment. The bias limit for the measured forces and moments are accounting for the effect of the yaw angle and pitch angle of the orientation of the vehicle. The effect of the orientation can be estimated by using the following equations:

$$B_{FX} = B_{Resistance} = B_{thrust} = F_X - F_X \cos(0.4775) - F_X \cos(0.3456)$$

$$B_{FY} = F_Y - F_Y \cos(0.4775) - F_Y \cos(0.3456)$$

$$B_{FZ} = F_Z - F_Z \cos(0.3456)$$

$$B_{MX} = M_X - M_X \cos(0.4775) - M_X \cos(0.3456)$$

$$B_{MY} = M_Y - M_Y \cos(0.4775) - M_Y \cos(0.3456)$$

$$B_{MZ} = M_Z - M_Z \cos(0.3456)$$

A4.2.11 Forces/Moments Generated by the Propeller (Using Only the YDM)

The forces/moments generated only by the propeller can be determined by using the following equation:

$$F = \textit{The forces}_{(\textit{propeller operating})} - \textit{The forces}_{(\textit{propeller blades align with the flow})}$$

$$M = \textit{The moments}_{(\textit{propeller operating})} - \textit{The moments}_{(\textit{propeller blades align with the flow})}$$

After the propeller blades are adjusted to align with the water flow, the forces/moments acting on the vehicle must be in the same condition as testing the propeller, such as the same water speed. The forces and the moment were measured. The measured data from the test of the propeller blades align with the flow shows the forces/the carriage speed relationship and the moments/the carriage speed relationship as shown in Figure A4.0.1 and Figure A4.0.2, respectively.

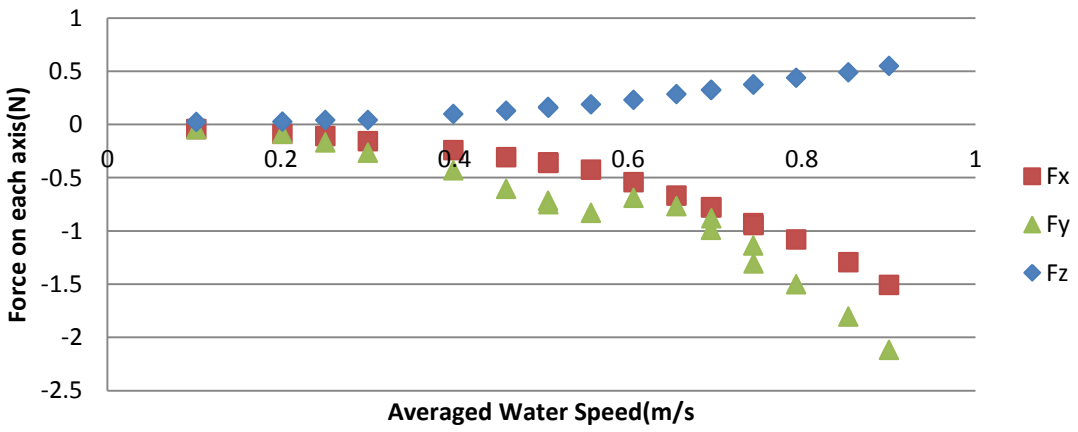

Figure A4.0.1. The relationship of forces and averaged carriage speeds

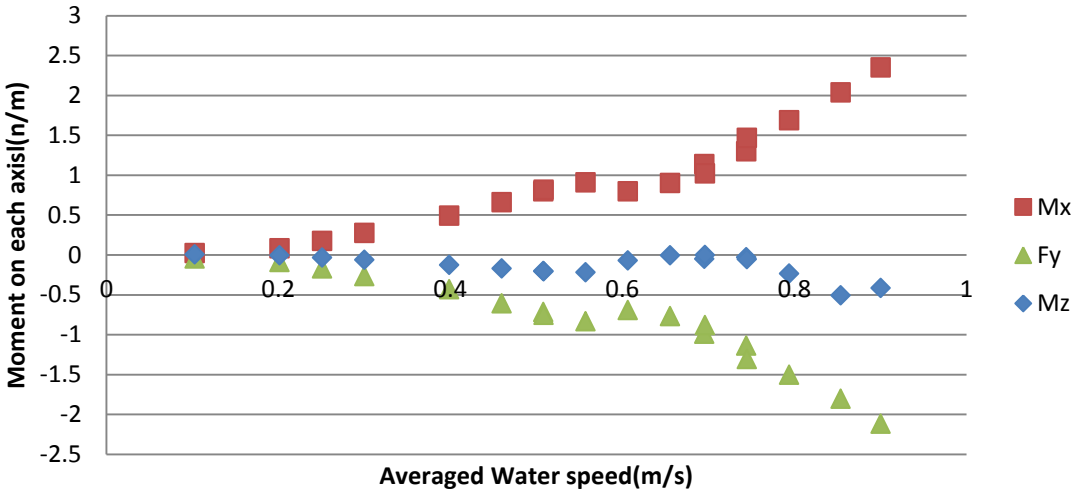

Figure A4.0.2. The relationship of moments and averaged carriage speeds

The mathematical models for each curve fit are shown in Table A4.0.2.

A bias for each curve fit equals to 2x(SEE), proposed by Coleman and Steele (2009). The regression curve will contain approximately 95% of the data points within the band of +/- 2(SEE).

$$SEE = \sqrt{\frac{\sum_{i=1}^{N}\left(Y_i - f\left(X_i\right)\right)^2}{N-2}}$$

Table A4.0.2. The bias limits of forces and moments on each axis (align with the flow)

Forces/	Math. Models	SEE	2XSEE, Bias limit
F_X	$F_X = 1.8397x^3 - 0.1269x^2 + 0.2766x + 0.0214$	0.01374	0.02748
F_Y	$F_Y = -7.6115x^3 + 8.7541x^2 - 4.5252x + 0.4395$	0.10355	0.20710
F_Z	$F_Z = -0.3231x^3 + 1.3199x^2 - 0.369x + 0.0489$	0.00612	0.01224
M_X	$M_X = 7.6873x^3 - 8.6291x^2 + 4.6611x - 0.4776$	0.10178	0.20355
M_Y	$M_Y = -1.6054x^3 - 0.2427x^2 - 0.4548x + 0.0247$	0.01259	0.02518
M_Z	$M_Z = -21.696x^4 + 37.24x^3 - 20.512x^2 + 3.7217x - 0.1895$	0.07569	0.15138

The bias limit can be expressed as:

$$\left(B_{Fi\ prop}{}'\right)^2 = \left[\frac{\partial Fi'}{\partial F_{i\ propeller\ operating}} B_{F\ propeller\ operating}{}'\right]^2 + \left[\frac{\partial Fi'}{\partial F_{i\ propeller\ blades\ align\ with\ the\ flow}} B_{Fi\ propeller\ blades\ align\ with\ the\ flow}{}'\right]^2$$

$$\left(B_{Mi\ prop}{}'\right)^2 = \left[\frac{\partial Mi'}{\partial M_{i\ propeller\ operating}} B_{M\ propeller\ operating}{}'\right]^2 + \left[\frac{\partial Mi'}{\partial M_{i\ without\ propeller\ blades}} B_{Mi\ propeller\ blades\ align\ with\ the\ flow}{}'\right]^2$$

Partial derivatives

$$\frac{\partial Fi'}{\partial F_{i\ propeller\ operating}'} = 1$$

$$\frac{\partial Fi'}{\partial F_{i\ propeller\ blades\ align\ with\ the\ flow}'} = 1$$

$$\frac{\partial Mi'}{\partial M_{i\ propeller\ operating}'} = 1$$

$$\frac{\partial Mi'}{\partial M_{propeller\ blades\ align\ with\ the\ flow}'} = 1$$

The bias limit for the forces and the moment will be

$$B_{Fi\ prop}' = \sqrt{\left[\frac{\partial Fi'}{\partial F_{i\ propeller\ operating}} B_{F\ propeller\ operating}'\right]^2 + \left[\frac{\partial Fi'}{\partial F_{i\ propeller\ blades\ align\ with\ the\ flow}} B_{Fi\ propeller\ blades\ align\ with\ the\ flow}'\right]^2}$$

$$B_{Mi\ prop}' = \sqrt{\left[\frac{\partial Mi'}{\partial M_{i\ propeller\ operating}}, B_{M\ propeller\ operating}'\right]^2 + \left[\frac{\partial Mi'}{\partial M_{i\ propeller\ blades\ align\ with\ the\ flow}}, B_{Mi\ propeller\ blades\ align\ with\ the\ flow}'\right]^2}$$

Note: the mark (‘) means the forces and the moments after rotating the axis

A4.2.12 Total Forces/Moments Measurement by Using Only the Internal Force Transducer

The total bias errors for forces and moments measurement including bias errors from calibration and data acquisition are presented in Table A4.0.3.

Table A4.0.3. Internal force transducer errors

Force/Moment	Max Error	Min Error	Assumed Error
X	0.14438 N	-0.37839 N	+/- 0.26138 N
Y	1.58969 N	-0.05265 N	+/- 0.82117 N
Z	1.58969 N	-0.05265 N	+/- 0.82117 N
L	0.04188 Nm	-0.00658 Nm	+/-0.02423 Nm
M	0.07701 Nm	-0.01625 Nm	+/-0.04662 Nm
N	0.12548 Nm	-0.04639 Nm	+/-0.08593 Nm

The second error is manifested in the misalignment between the propeller unit and the small force transducer. The bias limits for the measured forces and moments are accounting for the

misalignment between the axis of the propeller unit and the axis of the force transducer. In addition, the bias limit also took the angle between the vertical plane of the propeller unit and the vertical plane of the small force transducer.

The bias limit accounting for the misalignment between the axis of the propeller unit and the axis of the force transducer.

In x direction B_x is 0.001m. In y direction B_y is 0.001m.

The bias limit accounting for the angle between the vertical plane of the propeller unit and the vertical plane of the small force transducer.

B_{roll} is 1 degree.

The effect of the orientation can be estimated by using the following equations:

$$B_{FX'} = F_{X'}$$

$$B_{FY'} = F_{Y'}\cos(1) + F_{Z'}\sin(1)$$

$$B_{FZ'} = F_{Z'}\cos(1) - F_{y'}\sin(1)$$

$$B_{MX'} = M_{X'} + B_{FY'}(0.001) + B_{FZ'}(0.001)$$

$$B_{MY'} = M_{Y'} + B_{Fx'}(0.001)$$

$$B_{MZ'} = M_{Z'} + B_{Fx'}(0.001)$$

Appendix A5

A5.1 Experimental Results in Various Conditions

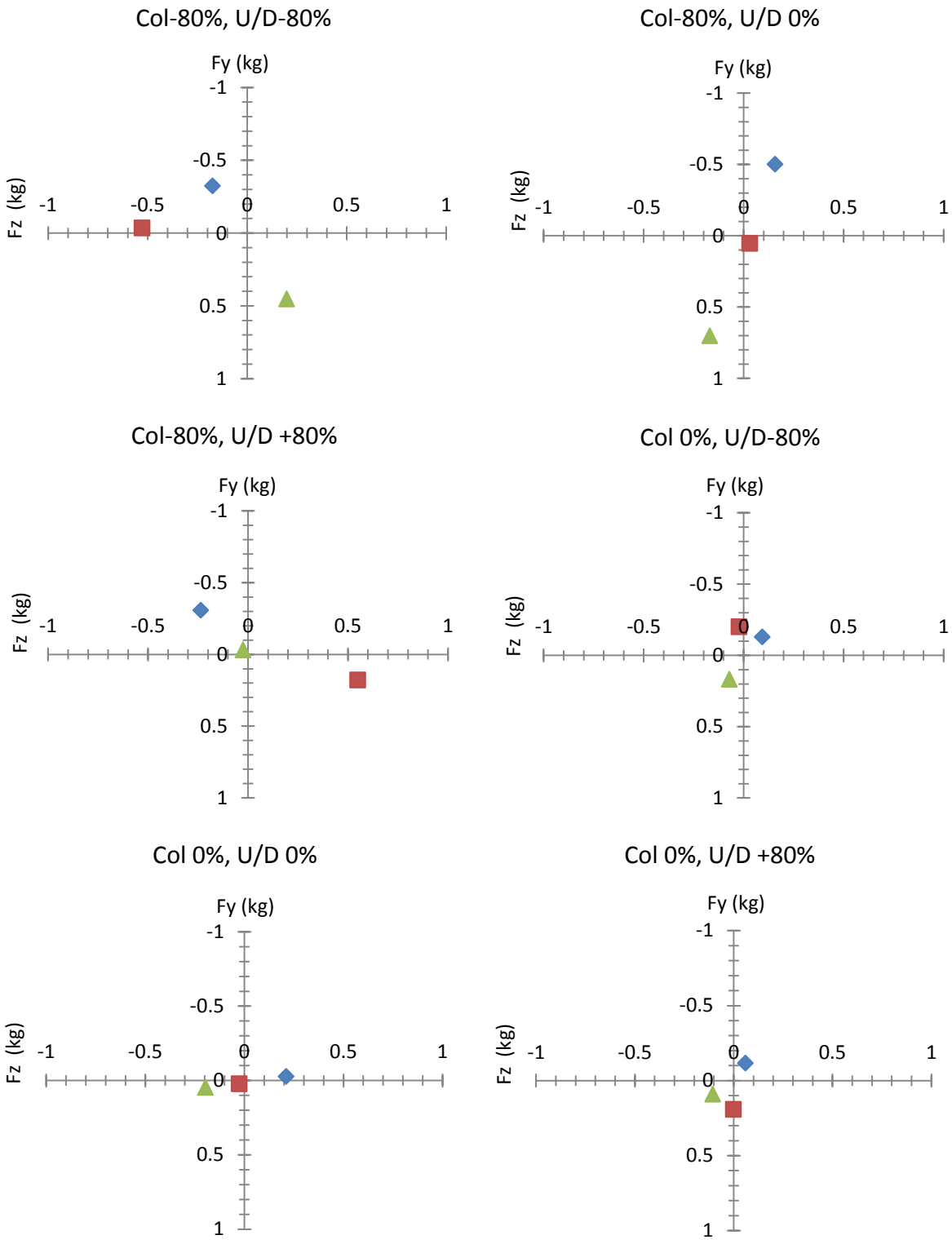

Figure A5.0.1. Magnitude and direction of transverse forces acting on the small 6-DOF force transducer with various right/left pitches (blue = -80%, red =0%, green=+80%), J=0.

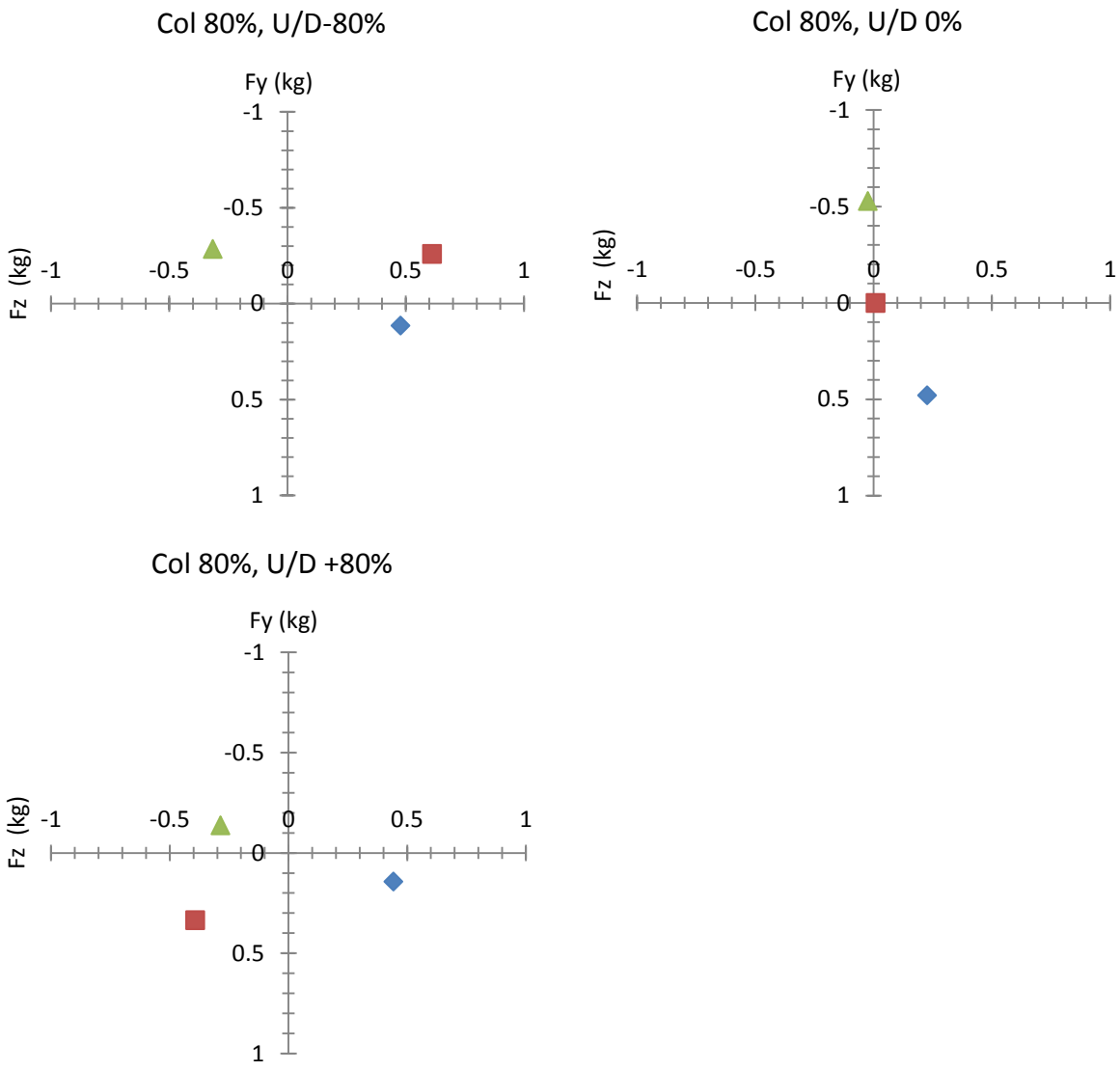

Figure A5.0.2. Magnitude and direction of transverse forces acting on the small 6-DOF force transducer with various right/left pitches (blue = -80%, red =0%, green=+80%), J=0.

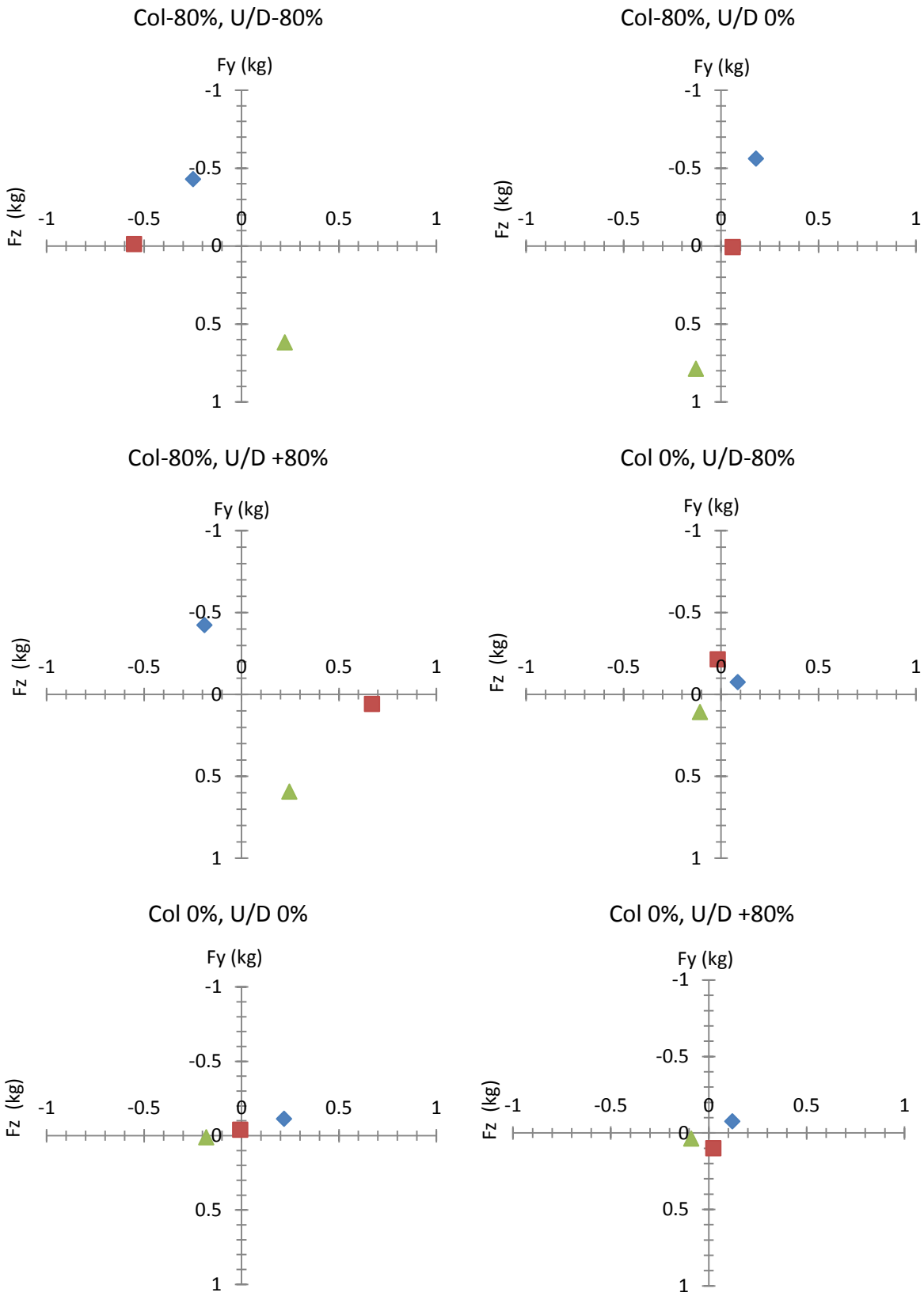

Figure A5.0.3. Magnitude and direction of transverse forces acting on the small 6-DOF force transducer with various right/left pitches (blue = -80%, red =0%, green=+80%), J=0.25.

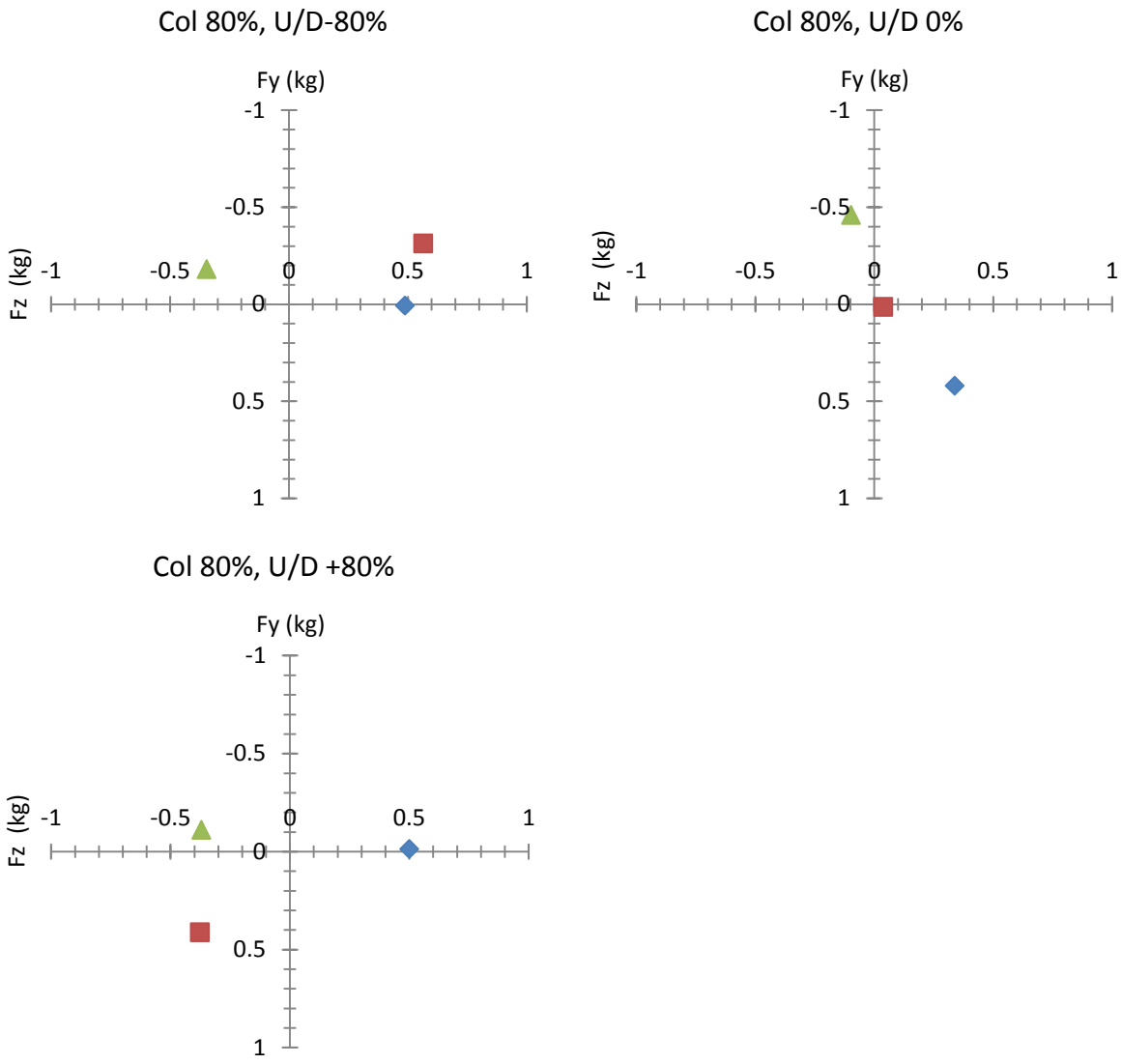

Figure A5.0.4. Magnitude and direction of transverse forces acting on the small 6-DOF force transducer with various right/left pitches (blue = -80%, red =0%, green=+80%), J=0.25.

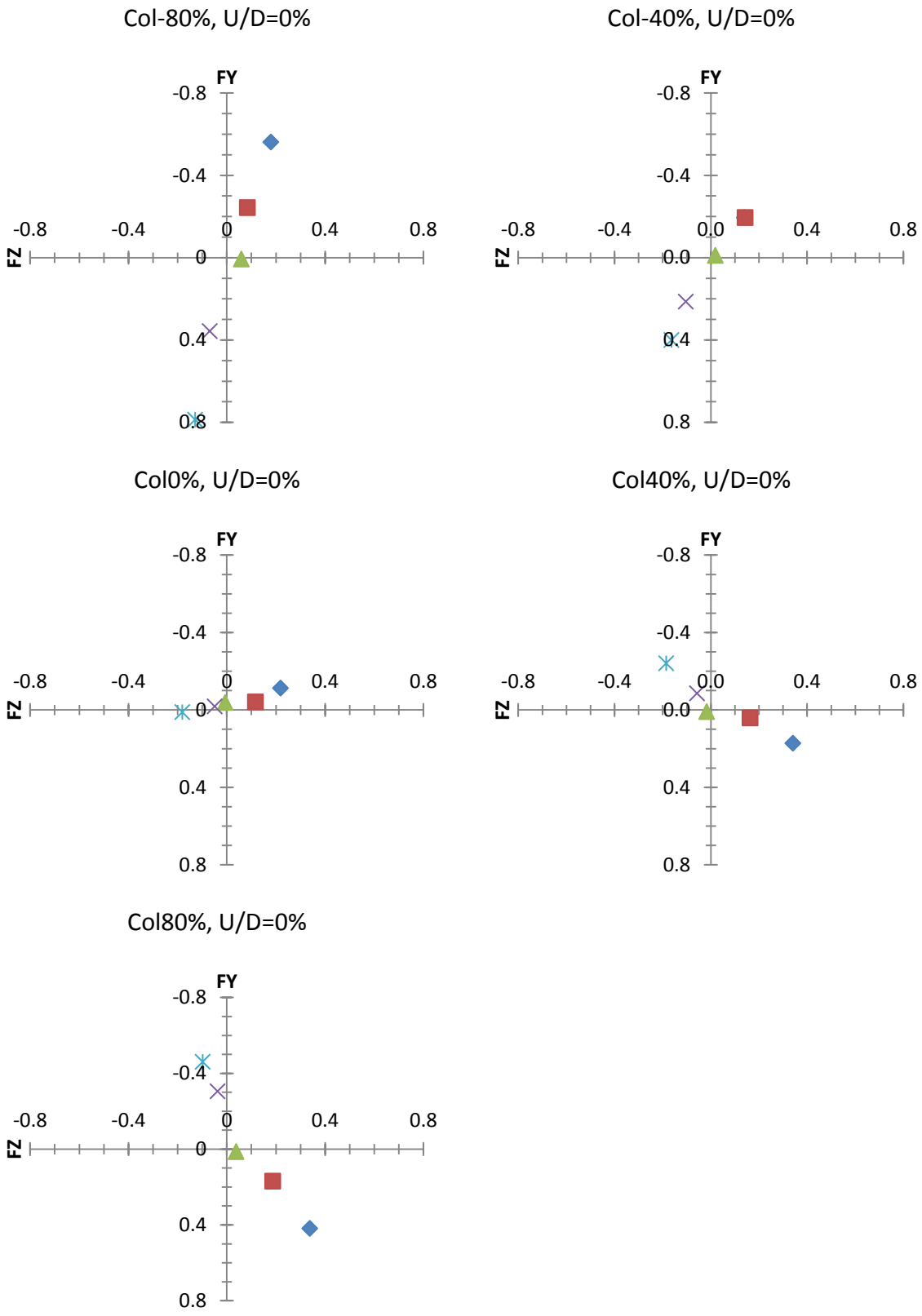

Figure A5.0.5. Magnitude and direction of transverse forces acting on the small 6-DOF force transducer with various right/left pitches (blue = -80%, red =-40%, green=0%, purple cross =+40%, light blue cross=+80%), J=0.25.

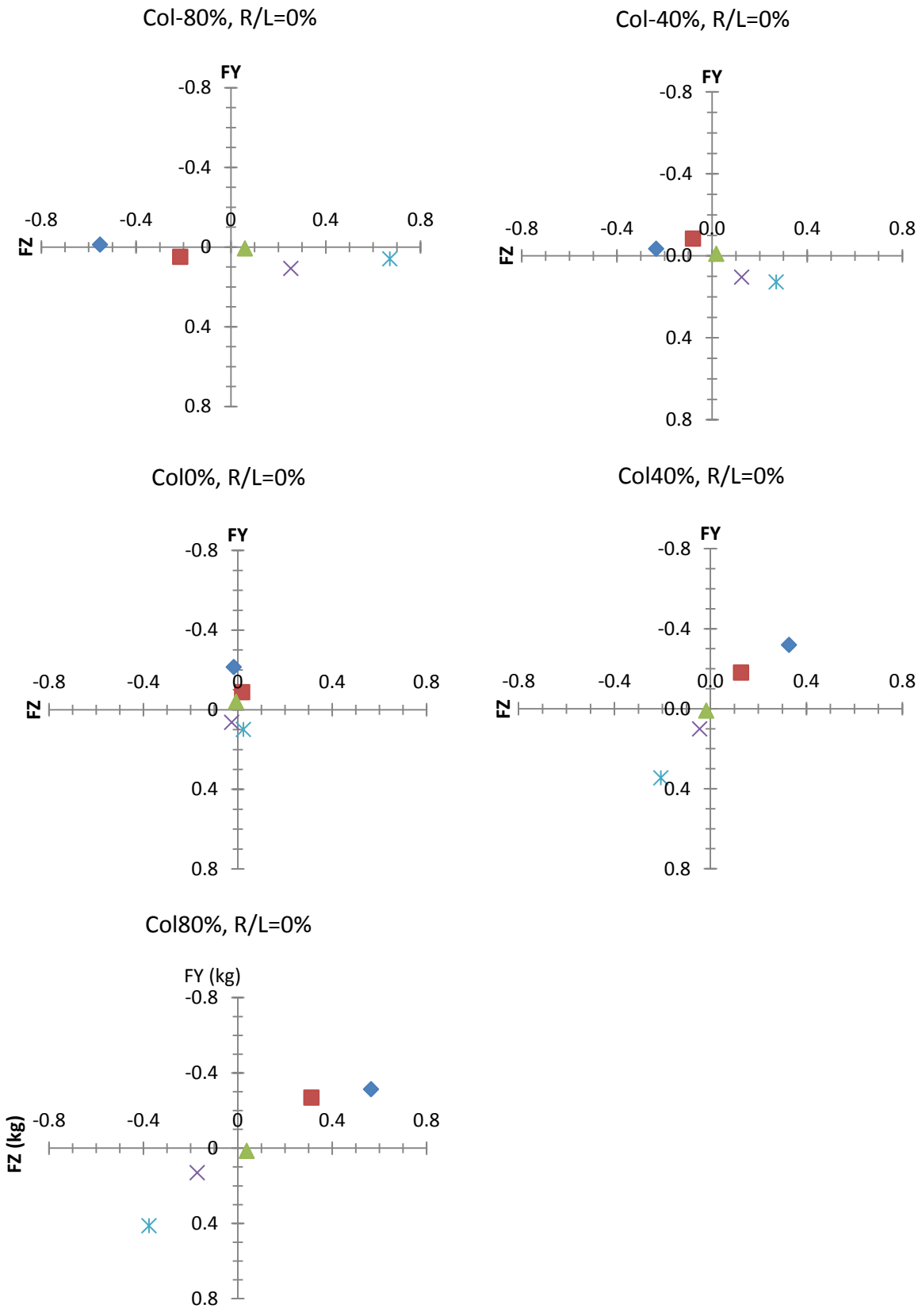

Figure A5.0.6. Magnitude and direction of transverse forces acting on the small 6-DOF force transducer with various up/down pitches (blue = -80%, red =-40%, green=0%, purple cross =+40%, light blue cross=+80%), J=0.25.

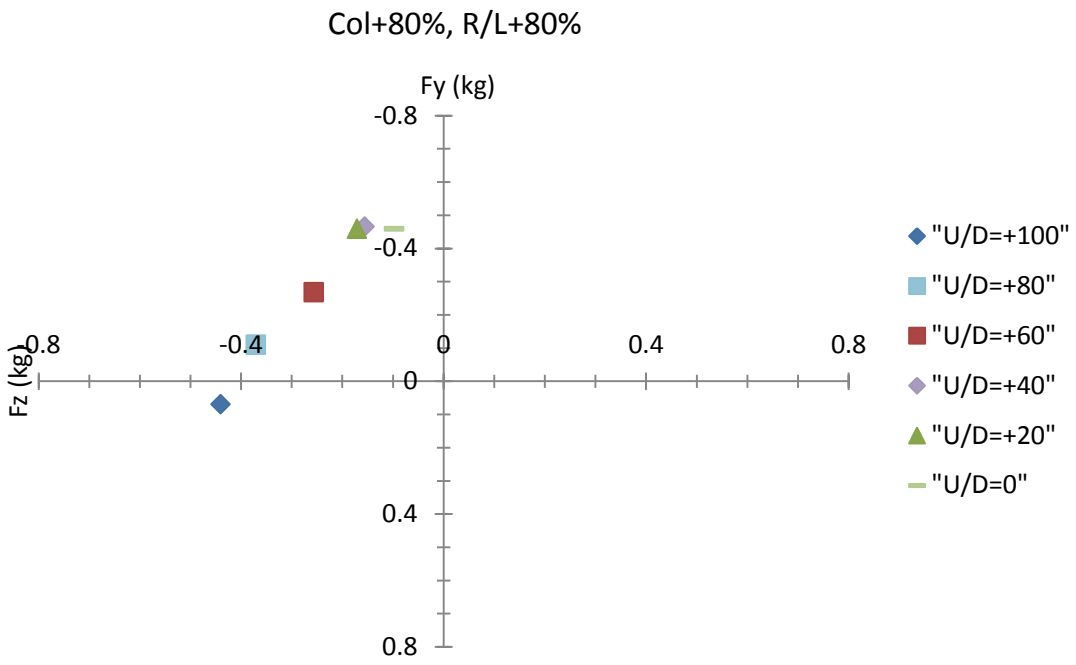

Figure A5.0.7. Magnitude and direction of transverse forces acting on the small 6-DOF force transducer with various up/down pitches (blue = +100%, light blue squre= +80%, red=+60%, purple =+40%, green tri=+20%, green bar=0%), J=0.25.

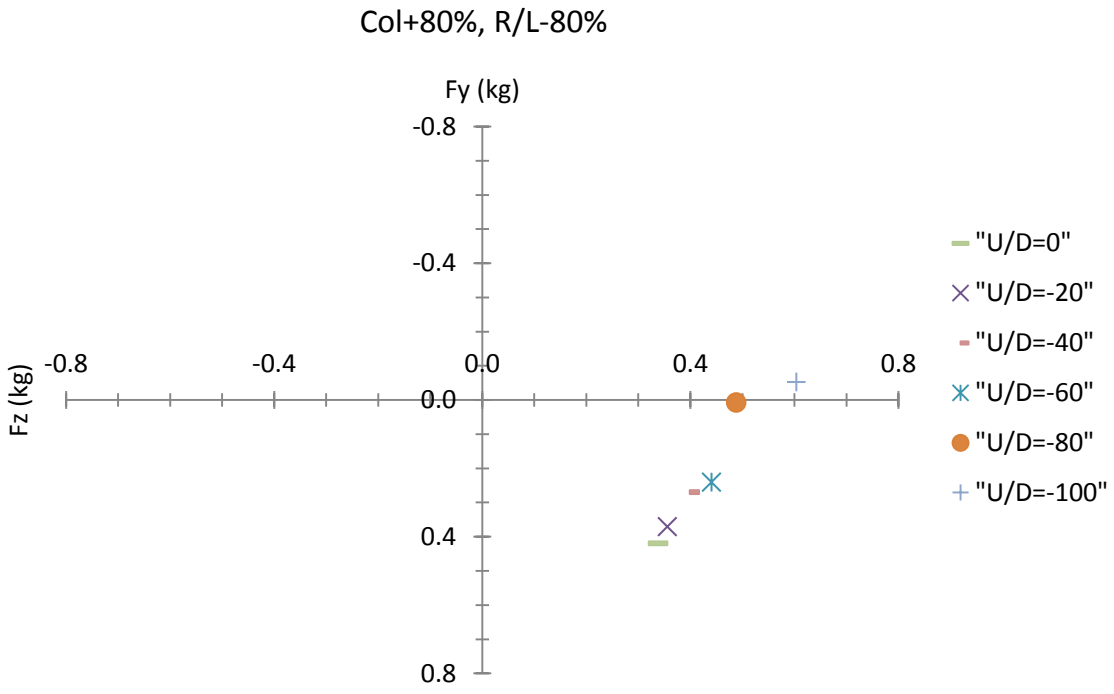

Figure A5.0.8. Magnitude and direction of transverse forces acting on the small 6-DOF force transducer with various up/down pitches (green bar=0%, purple cross = -20%, orange bar = -40%, blue cross =-60%, orange circle =-80%, blue plus=-100 %,), J=0.25.

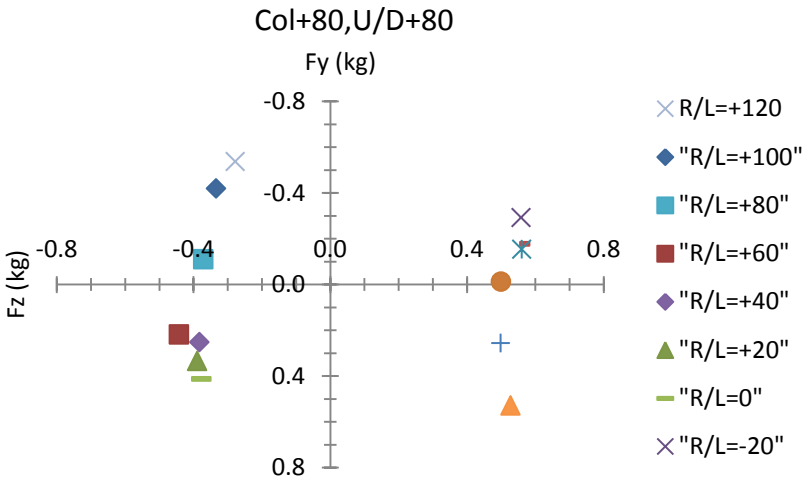

Figure A5.0.9. Magnitude and direction of transverse forces acting on the small 6-DOF force transducer with various right/left pitches, J=0.25.

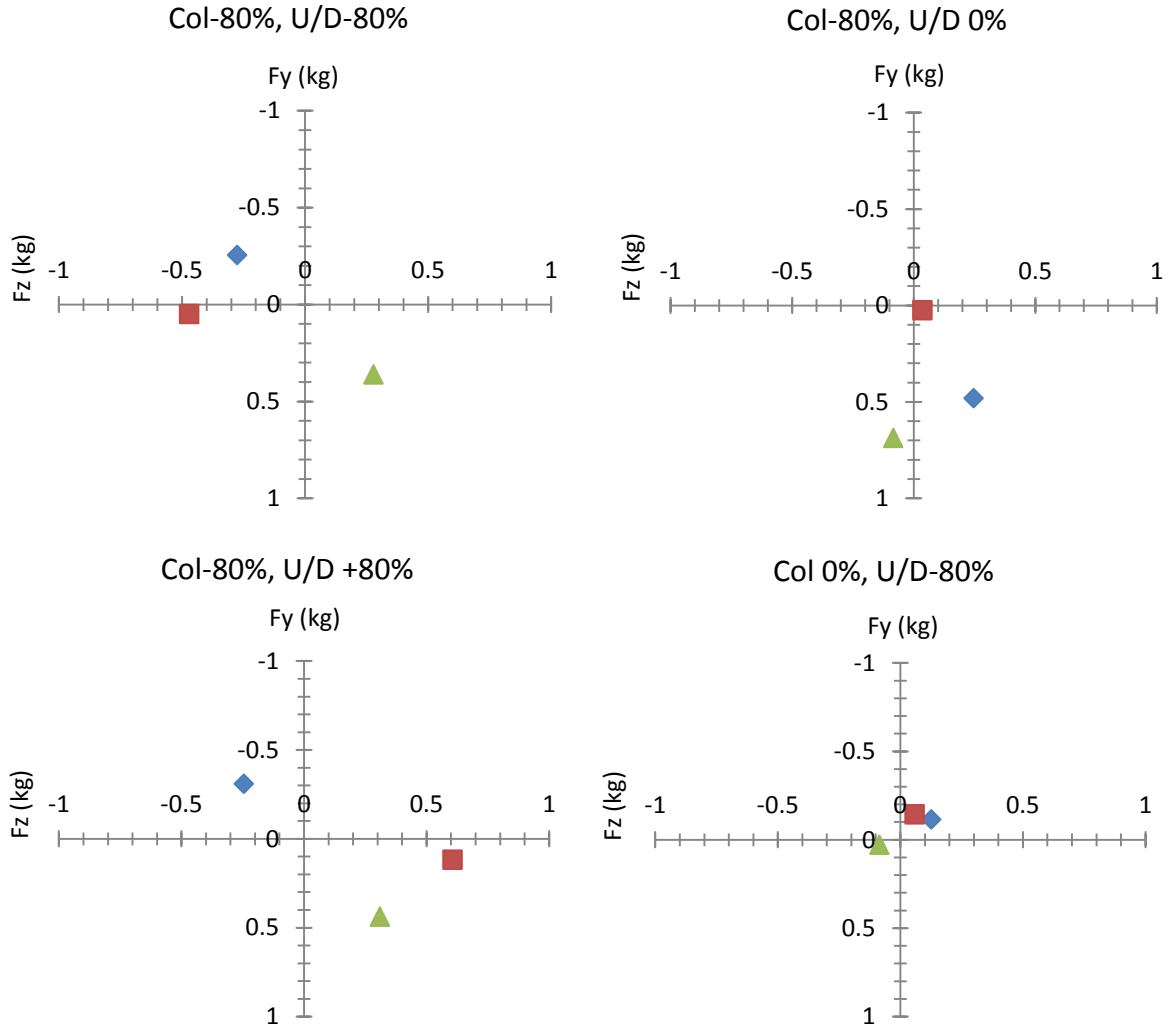

Figure A5.0.10. Magnitude and direction of transverse forces acting on the small 6-DOF force transducer with various right/left pitches (blue = -80%, red =0%, green=+80%), J=0.50.

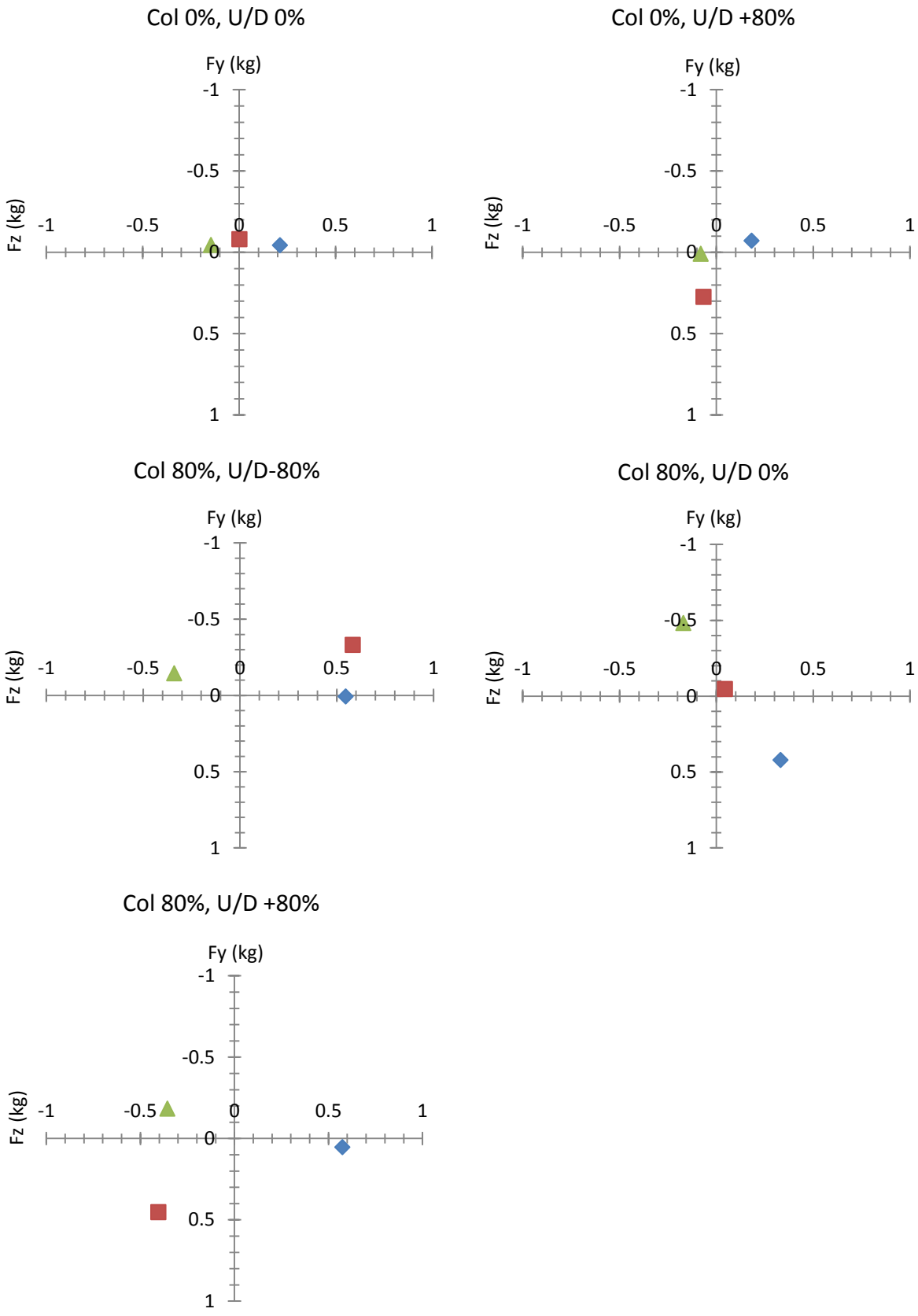

Figure A5.0.11. Magnitude and direction of transverse forces acting on the small 6-DOF force transducer with various right/left pitches (blue = -80%, red =0%, green=+80%), J=0.50.

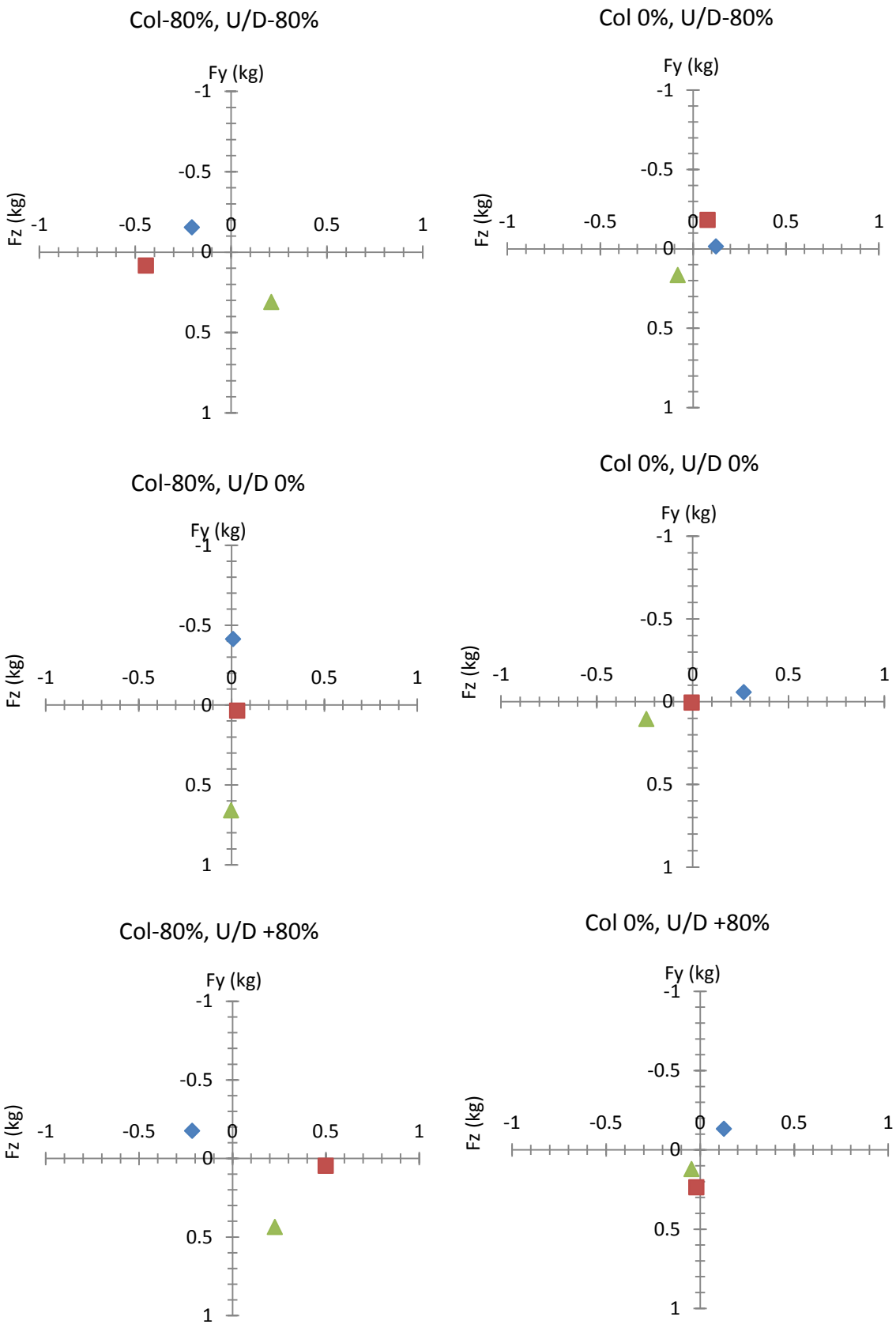

Figure A5.0.12. Magnitude and direction of transverse forces acting on the small 6-DOF force transducer with various right/left pitches (blue = -80%, red =0%, green=+80%), J=0.75.

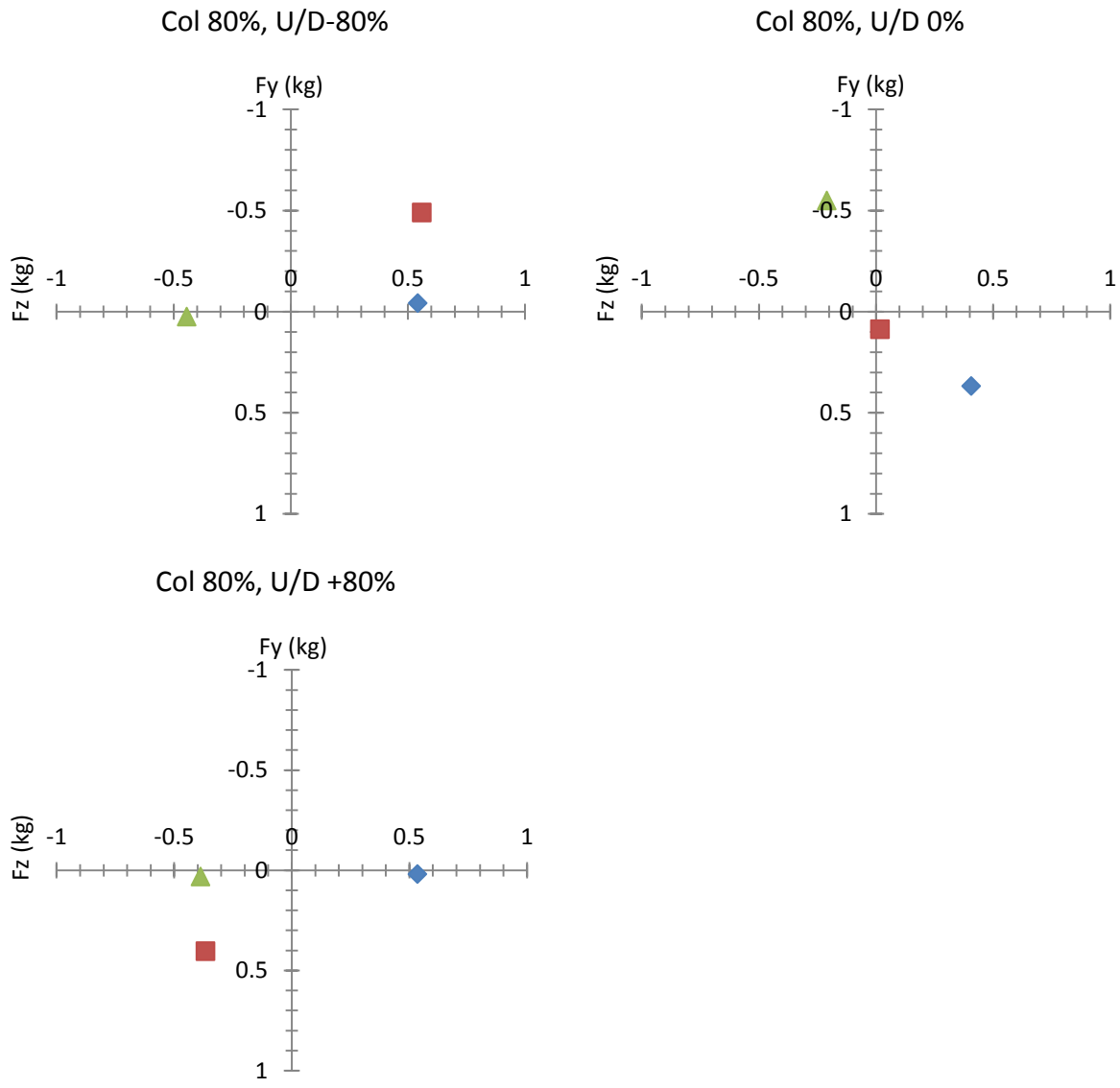

Figure A5.0.13. Magnitude and direction of transverse forces acting on the small 6-DOF force transducer with various right/left pitches (blue = -80%, red =0%, green=+80%), J=0.75.

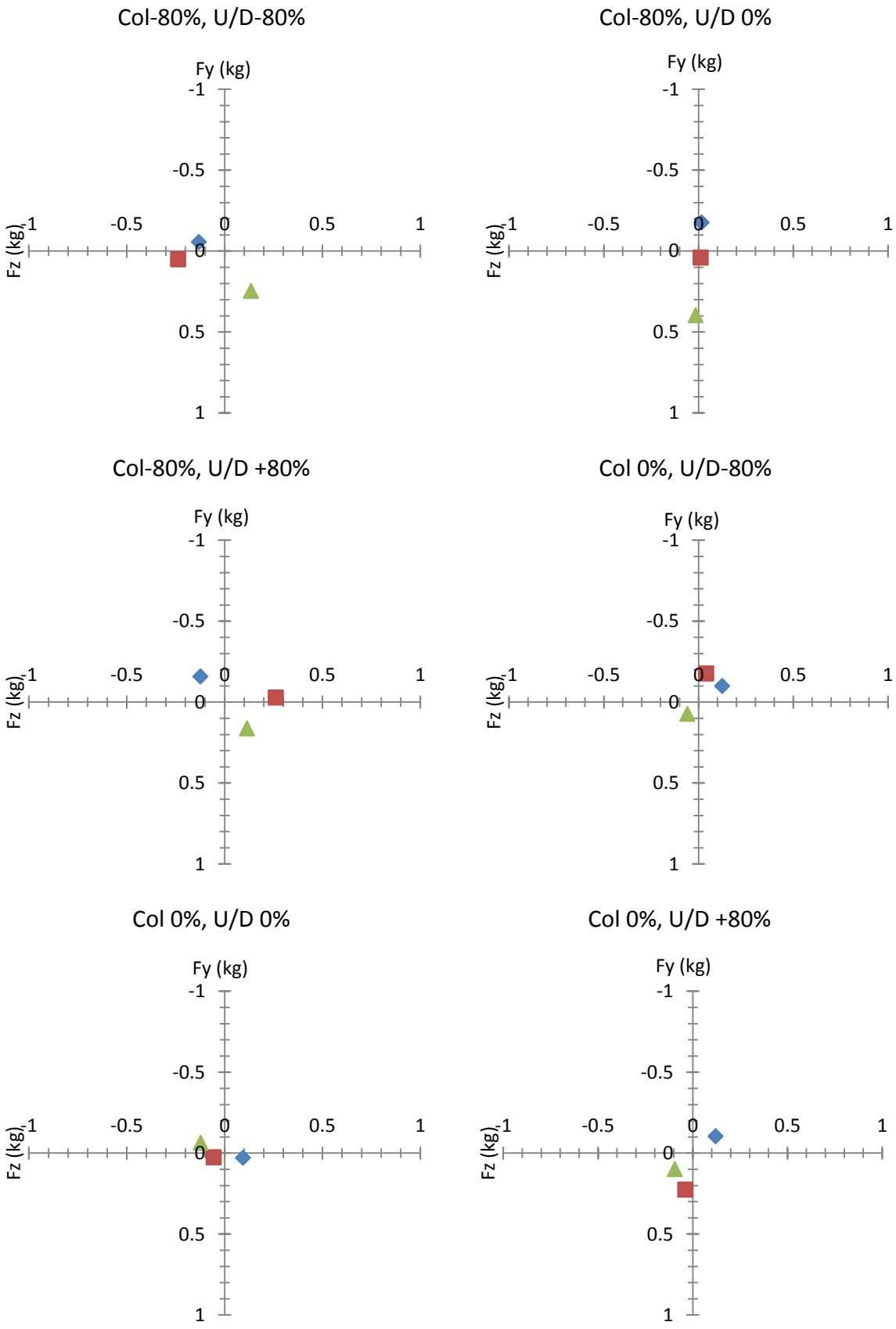

Figure A5.0.14. Magnitude and direction of transverse forces acting on the small 6-DOF force transducer with various right/left pitches (blue = -80%, red = 0%, green= +80%), J=0.8.

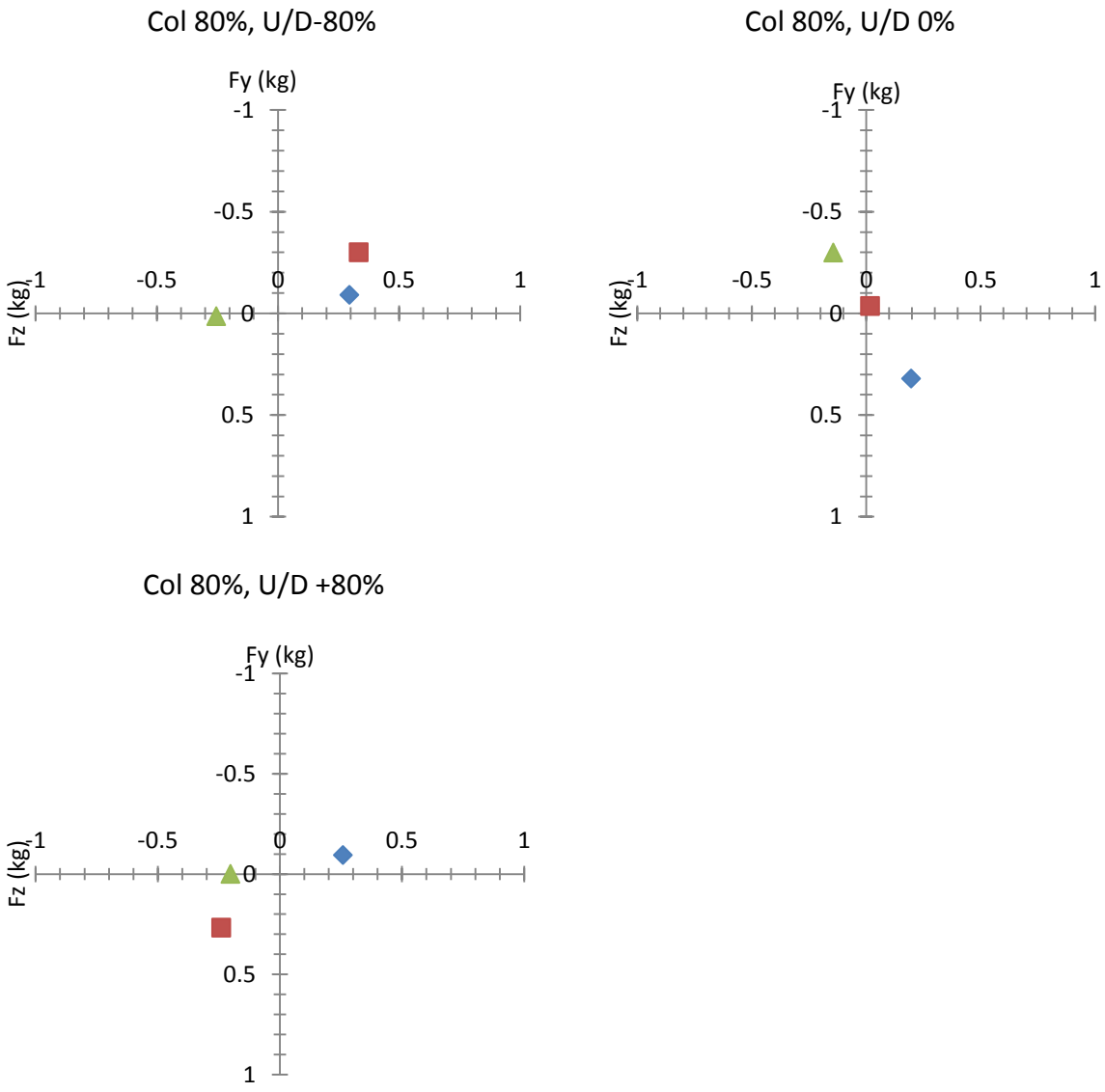

Figure A5.0.15. Magnitude and direction of transverse forces acting on the small 6-DOF force transducer with various right/left pitches (blue = -80%, red = 0%, green= +80%), J=0.8.

Appendix A6

A6.1 Numerical values for calculating a hull static drag

Table A6.0.1. The values of C_{Dc} in a function of the Reynolds number, Rn

Rn	C_{Dc}
0	1.2
59300	1.2
119000	1.2
178000	1.16
237000	1.1
296000	0.95
356000	0.74
415000	0.28
474000	0.26
533000	0.28
593000	0.3
652000	0.32
711000	0.32
770000	0.33
830000	0.33
889000	0.34
948000	0.35
1010000	0.38
1070000	0.39
1130000	0.41
1190000	0.44
1240000	0.45
1300000	0.48
1360000	0.49
1420000	0.5
1480000	0.51

Table A6.0.2. The numerical values for calculating hull static drag

S_b	0.128 m^2
A	2.285 m^2
A_p	0.979 m^2
$C_{DF(\alpha=0°)}$	0.00135
η	0.64
V_B	0.16m^3
X_m	1.284 m.
X_p	1.296 m.
L_{tot}	2.335 m.
$(k_2 - k_1)$	0.89
C_O	0.189 m.
C_B	0 m.

A6.2 Numerical values of coefficients (p_{1i}, p_{2i} and p_{3i}) in the equations of the displacement of actuator

Table A6.0.3. The numerical values of coefficients

	Equation *L1*	Equation *L1*	Equation *L1*
i	p_{1i}	p_{2i}	p_{3i}
1	-0.000059371	-0.000513070	-0.003414267
2	-0.268200000	-0.268044444	-0.269644444
3	-0.001200000	-0.300481481	0.300796296
4	0.347129630	-0.173296296	-0.173648148
5	-0.005824407	-0.006598452	-0.002267316
6	0.001195201	-0.006716099	-0.005483003
7	-0.003942054	0.005323117	-0.011051630
8	0.032803922	-0.028352941	0.028588235
9	0.005392157	-0.016411765	-0.016254902
10	0.065587464	0.001509804	-0.005352941
11	-0.038000000	-0.056289459	0.058565242
12	-0.118492308	-0.033406268	-0.032764672
13		0.032882051	-0.033989744
14		0.019374359	0.019210256
15		0.058512821	0.059825641
16		0.101774359	-0.102635897